CLARKSON UNIVERSITY

Oceanographic Modeling with Hyperspectral Satellite Imagery

A Dissertation

By

Sean Jason Kramer

Department of Mathematics

Submitted in partial fulfillment of the requirements

for the degree of

Doctor of Philosophy, Mathematics

May 15, 2013

Accepted by the Graduate School

_____, _____

Date, Dean

The undersigned have examined the thesis/dissertation entitled **"Oceanographic Modeling with Hyperspectral Satellite Imagery"** presented by **Sean Jason Kramer**, a candidate for the degree of **Doctor of Philosophy** (**Mathematics**), and hereby certify that it is worthy of acceptance.

_____
Date

_____
Erik Bollt (Advisor)

_____
Daniel ben-Avraham

_____
Katie Fowler

_____
Joseph D. Skufca

_____
Jie Sun

Abstract

Phytoplankton form the basis of the food chain in the Earth's oceans and are ultimately responsible for providing nourishment for marine life further up the food chain [1]. Seasonal environmental heterogeneities such as nutrient replenishment, predation, and temperature induce recurring algal blooms, often called spring blooms [2–4]. Certain bloom events, especially harmful algal blooms, elicit widespread repercussions on regional communities such as human sickness, shellfish poisoning, and fish kills [5]. Models for near-shore algal blooms would be extremely valuable for forecasting during such events and might help inform short-term management decisions. Algal blooms are visible in their entirety through remote sensors mounted on ocean-observing satellites. Such data is capable of informing model-fitting techniques for short-term ecological forecasts. The primary task of this work is to develop new techniques for model fitting and forecasting from observed data within the framework of synchronization. We assume vertical concentrations to be homogeneous and examine two-dimensional systems of PDEs with spatially dependent parameters. Several new developments in parameter and model fitting are demonstrated, including spatially dependent parameters in reaction-diffusion-advection systems. Obstacles including sparsity in data and cloud cover are addressed. The new techniques are proven by demonstrating a Lyapunov functional [6] or by estimating conditional Lyapunov exponents [7] when required.

Contents

List of Tables

List of Figures

xv

Chapter 1

Introduction

Phytoplankton form the basis of the trophic web in the Earth's oceans, providing nourishment for marine life further up the food chain [1]. Phytoplankton generate roughly half of the Earth's oxygen through photosynthesis [15] and also absorb half of the Earth's carbon dioxide. As such, phytoplankton are efficient scrubbers of the Earth's atmosphere, contributing significantly to the Earth's carbon cycle [15, 16]. Due to the growing consumption of fossil fuels, the carbon cycle has been altered with large amounts of carbon pumped into the atmosphere [17]. Phytoplankton absorb carbon through photosynthesis, eventually die, and subsequently sink to the bottom of the ocean, in a sense cycling the Earth's carbon [16, 18–20]. Therefore the modeling of phytoplankton is a progressively important problem, especially considering the mounting interest in the Earth's climate.

Seasonal environmental heterogeneities such as nutrient replenishment, predation, and temperature induce recurring algal blooms, often called spring blooms [2–4, 21]. More localized bloom events are commonly observed in estuaries and coastal regions [22]. Certain bloom events, especially harmful algal blooms, elicit widespread repercussions on regional communities such as human sickness, shellfish poisoning, and fish kills [5]. These harmful algal blooms are detrimental to regional ecology and

economies through fishing losses and tourism depletion [5].

Sources contributing to phytoplankton growth include nutrients, sunlight, and regions of upwelling or wind mixing that transport nutrients to the surface [8]. The processes by which these events occur are not well understood, in part due to the many complexities involved [2]. Models for near-shore algal blooms would be extremely valuable for forecasting during bloom events and might help inform short-term management decisions.

Phytoplankton are grazed upon by zooplankton, animals that can be either herbivores or predators [23]. Zooplankton are incredibly efficient grazers, and are primarily responsible for controlling seasonal spring phytoplankton blooms [3, 24]. Since zooplankton are such efficient grazers, they are an important consideration in modeling algal ecology and are very frequently included in even basic models [2–4, 15, 25–37].

Plankton are often studied either empirically or theoretically. We aim to blend the two approaches by fitting established theoretical models to observed data for ecology on the mesoscale. However, modeling an oceanic ecosystem over the mesoscale requires ample empirical data over a widespread geographic region; a study on the mesoscale is an ambitious endeavour. We focus on a passive technique to gather empirical data over the scale at which we aim to fit models and provide forecasts.

Remote sensing provides a relatively new and powerful tool in observing algal blooms in real-time over the mesoscale. Therein, certain geophysical quantities of interest such as wave speed, algae, or ocean salinity are observed through instruments including RADAR, LIDAR, or multispectral instruments [8]. Specifically, algal blooms may be studied using satellite-mounted ocean-observing multispectral instruments toward building models to represent observed ecology and short-term forecasts. Hyperspectral instruments mounted on satellites are capable of capturing an entire algal bloom, thereby permitting the observation and analysis of the comprehensive biological system [23]. We work with three particularly useful instruments for ob-

serving ocean ecology and explain their characteristics in some detail. We describe the satellites on which they are mounted, some of the detrimental phenomena, including sun glint and atmospheric scattering, and a basic ocean color algorithm to infer phytoplankton density. We aim to fit models informed by data, as opposed to first principles, requiring that our models must match observed data regardless of underlying physics.

Model fitting in ODEs and PDEs has developed into a vast field in applied mathematics and control engineering. For models representing important physical processes, accurate estimates of appropriate model parameters help facilitate short-term forecasting. However, to forecast a system one requires not only accurate parameter estimates, but also full knowledge of the initial state of the system. There are widely varying and powerful methods for parameter estimation of spatio-temporal systems including, but certainly not limited to, Kalman filter methods [38–40], multiple shooting methods [41, 42], and adjoint methods [43]. Parameter estimation based on synchronization has drawn substantial interest [44–54]. Applications include communications and cryptography [46], electronics and circuit dynamics [45,55], and cardiac cell dynamics [51] to name just a few.

The mathematical study of synchronization between chaotic systems emerged with the seminal work of Pecora and Carroll [56]. They discovered the counter-intuitive phenomena of synchronization between two chaotic dynamical systems. In fact, due to inherent exponential divergence of nearby initial conditions, one would expect that model states of two chaotic systems with nearby initial states would rapidly diverge. In practice, noise persists both in transmitted data and in measurement error. Therefore a receiver accepting a noisy chaotic signal from a transmitter should experience exponential divergence. However, Pecora and Carroll demonstrated [57] that, with a specific coupling between two chaotic systems, they will inevitably synchronize.

Synchronization was observed between one-dimensional systems of PDEs in [55]

and two-dimensional systems in [52], where the authors considered the Grey-Scott and Barkley reaction-diffusion systems respectively. In these works, the authors observed synchronization of an infinite-dimensional system by coupling the drive and response systems at only a finite number of grid points. The authors observe single-species assimilation as they drive the PDE system to identical synchronization while coupling with only one species [52].

Parameter estimation techniques were then developed by exploiting the tendency of chaotic systems to synchronize. Synchronization acts as a regularizing force in the parameter fitting process [52]. Given two systems, a drive and response, parameters of the drive system may be identified by minimizing the misfit between response model prediction and drive model observations. Since perfect parameters will yield a perfect fit, one need only search through R^n to correctly estimate parameters.

Autosynchronization is a special variation of synchronization methods rooted in an approach to force a response model to adapt to observed data by developing additional equations for the parameters that depend on the model error [44, 49]. If coupled properly, the drive and response parameters will synchronize while the two systems themselves synchronize, thus the term "autosynchronization" [44]. Further work [52] examines parameter estimation for PDE systems using optimization over the synchronization error surface. However, none of these address autosynchronization in the PDE setting.

In this work, we build upon the results in [44], including parameter estimation through autosynchronization. We extend the method of autosynchronization between chaotic ODEs to spatiotemporally chaotic PDEs. We first demonstrate the ability of the PDEs to synchronize, then demonstrate synchronization by sampling only one species. Next, we demonstrate autosynchronization such that scalar model parameters are estimated. Furthermore, we demonstrate autosynchronization for spatially dependent parameters. Optimization techniques require complex tools when estimat-

ing spatially-dependent model parameters, requiring a minimization over a function space. Autosynchronization provides a simple framework with which to estimate parameters over a function space. We show that autosynchronization is observed by sampling only one species. Finally, we demonstrate autosynchronization for spatially dependent parameters over a reaction-diffusion-advection system including spatially dependent parameters.

These methods are performed on benchmark models to demonstrate their efficacy. However, for a guarantee to properly function in practice, some analysis is required in determining exactly under what conditions synchronization or autosynchronization will be observed. There are classically two approaches to analyzing this phenomena, the Lypaunov direct method [6] and the estimation of conditional Lyapunov exponents [7]. Using these tools, we analyze the synchronization between the benchmark systems and prove conditions under which synchronization and parameter estimation are observed.

An outline of this work is as follows. In Chapter 2 we study the remote sensing instruments we aim to use for observing ocean ecology, including algal blooms. We discuss their properties in detail, including particular characteristics of each instrument. We detail data processing techniques to filter noise-inducing atmospheric effects, ending with the ocean color algorithms for inferring plankton densities from multispectral data.

In Chapter 3 we introduce the benchmark model to be used in the twin experiments performed in later chapters to demonstrate synchronization. The benchmark model is a system of partial differential equations representing phytoplankton-zooplankton ecology which, after spiral-producing transients, results in spatiotemporal chaos [15]. We describe the numerical techniques used to simulate the reaction-diffusion system. We next introduce a reaction-diffusion-advection system based on the former reaction-diffusion system and describe the numerical techniques used to

simulate the new system.

Chapter 4 is a demonstration of the reaction-diffusion system to synchronize. We discuss a first demonstration of autosynchronization, including spatially dependent parameter estimation. These results are repeated assuming sampling of one species to include model state estimation. Lastly, the problem of incomplete observation data is addressed including sampling by local averaging, temporal subsampling, and cloud coverage over the observed domain.

We study the dynamics in phase space in Chapter 5 with an analysis by the Lyapunov direct method [6] when available. Here, we describe the Lyapunov direct method for systems of ODEs and demonstrate how the method is extended from stability analysis on one dynamical system to analyze synchronization between two dynamical systems. We next extend the method from systems of ODEs to PDEs, gaining knowledge of the basin of attraction of the synchronization manifolds for the different systems shown in Chapter 4.

Later in Chapter 3, we discuss Lyapunov exponents, their geometric interpretation, and their numerical calculation. We define conditional Lyapunov exponents (CLEs) and estimate CLEs on the ODE analogs of the PDEs with which we observed synchronization and parameter estimation. The estimation of CLEs provides an analysis of the stability of the synchronization manifold whence we are unable to use the Lyapunov direct method. Finally, we extend the CLEs from the aforementioned ODE systems to the system representing the numerical approximation to the PDEs used in Chapter 4.

In Chapter 6, we extend synchronization between the reaction-diffusion systems studied in Chapter 4 to reaction-diffusion-advection systems with advection governed by a flow field resulting in rigorous mixing over the domain [58–62]. That is, we study a benchmark problem including complex mixing to mimic expected behavior over turbulent coastal regions. Finally, we demonstrate synchronization and parameter

estimation by sampling one species.

In Chapter 7 we merge synchronization with a relatively new development in transport analysis in time-dependent dynamical systems [63], wherein *coherent sets* for a dynamical system are uncovered. As noted, an algal bloom may be observed in its entirety by multispectral satellite data. By viewing the system on the mesoscale, we fit models and also analyze the underlying dynamics governing density transport near coastal regions. The underlying dynamics, typically including ocean currents which transport plankton [15], might partition a domain into mostly coherent regions, or regions between which there is not much mixing [63]. Synchronization and autosynchronization are shown to be more efficient when performed over mostly-coherent sets as opposed to the entire domain.

Finally, we discuss future work including expectations for exploiting these techniques toward modeling ocean ecology with hypersectral satellite data given by the instruments discussed in Chapter 2. Some concluding remarks follow.

Chapter 2

Remote Sensing

Remote sensing provides an extremely effective means of modeling mesoscale dynamics. Data obtained by remote sensing allow for prediction, assimilation, and forecasting of oceanic dynamics and weather. Remote sensing is defined as the use of electromagnetic radiation to learn information about the ocean, land, and atmosphere without having physical contact with the object or phenomenon under investigation [8]. In contrast to direct, or in-situ, measurements, remote sensing measures large regions and the quantity under investigation is inferred from reflected or emitted radiation. Examples of remote sensing include but are not limited to radar, lidar, particle image velocimetry (PIV), and hyperspectral satellite imagery. Remote sensors infer a broad array of geophysical quantities of interest. Our work will include remote sensing of geophysical quantities from hyperspectral imagers mounted on earth-observing satellites.

Hyperspectral imagers measure the characteristics of light coming from the surface of the Earth. Such imagers can view the ocean in three electromagnetic wavelength bands, the visible, infrared, and microwave [8]. Both visible and infrared can be obscured by cloud cover, but microwave wavelengths can be viewed through clouds. There are two types of microwave observations, active and passive. Hyperspectral

imagers fall under the passive category as they observe only reflected solar radiation or naturally emitted radiation [8]. Active measurements are made by instruments such as Radar, in which directed pulsed beams are emitted and inferences are made based on reflected backscatter. We begin by describing how orbiting multispectral imagers collect information, starting with what multispectral imagers actually observe, electromagnetic radiation. We then describe how electromagnetic radiation interacts with the Earth's atmosphere, followed by how radiance incident on the ocean is reflected, transmitted, and absorbed. Next, we discuss important definitions and characteristics of multispectral satellites, followed by how data is captured and is subsequent processed. Finally, we discuss the imagers we will be using in this work toward ocean modeling and their features along with the algorithms used to infer data. This provides a somewhat rigorous background as to how these sensors are able to infer information about plankton density in the ocean from space.

2.1 Electromagnetic Spectrum

Electromagnetic radiation is a form of energy propagation characterized by either wavelength or frequency. The electromagnetic spectrum is divided into several sections based on either frequency or wavelength. One end of the spectrum contains the high frequency range, with what are called X-rays. Next, with a slightly lower frequency, is ultraviolet radiation. What follows is the visible spectrum in which the colors visible to the human eye are found. Next, the infrared wavelengths are found. Finally, the longest wavelengths discussed consist of microwaves and radio waves. Table 2.1 describes these regions along with respective abbreviations for future reference. The sun is the source of the bulk of observed electromagnetic radiation with respect to satellite remote sensors.

Any object emits thermal radiation based on certain properties such as its tem-

Table 2.1: Regions of the electromagnetic spectrum with abbreviations, adapted from Martin, 2004 [8].

Name	Abbreviation	Wavelength band
Ultraviolet	UV	10-400 nm
Ultraviolet-B	UV-B	280-320 nm
Visible	V	400-700 nm
Near Infrared	NIR	0.7-3.5 μ m
Visible/Near Infrared	VNIR	0.4-3.5 μ m
Thermal Infrared	TIR	3.5-20 μ m
Visible/Infrared	VIR	0.4-20 μ m

perature. To properly understand the relationship between absorbance and emission, some definitions and laws are required from thermodynamics. First, we define some useful terms as found in [64].

Definition 2.1.1. Radiation *is the energy emitted by matter in the form of electromagnetic waves as a result of the changes in the electronic configurations of the atoms or molecules.*

Definition 2.1.2. *The* emission efficiency, *denoted* ϵ, *describes the efficiency of an object to emit thermal radiation. The* emission efficiency *takes values* $0 \leq \epsilon \leq 1$, *with 0 denoting no emission and 1 denoting the highest possible emission.*

Definition 2.1.3. *The* absorption efficiency, *denoted a, describes the efficiency of an object to absorb radiation. The value of a is found by dividing the absorbed radiation by the incident radiation. The* absorption efficiency *takes values* $0 \leq a \leq 1$, *with 0 denoting complete reflection and 1 denoting complete absorption.*

In 1859, Gustav Kirchhoff discovered a relationship between emission efficiency and absorption efficiency.

Theorem 2.1.4. Kirchhoff's law of radiation *states that the emissivity and the absorptivity of an object are equal at the same temperature and wavelength. That is* $a = \epsilon$.

Theoretically, a body could have the property of maximum absorption, in which case Kirchhoff's law implies it would also have maximum emission. Such an idealized object is called a *blackbody*. The radiation emitted by a blackbody also has a special name, called *blackbody radiation*.

Next, we describe how the temperature of an object depends on the the amount of radiation emitted by a body with the Stephan-Boltzmann law.

Theorem 2.1.5. *The* Stefan-Boltzmann law *states that the radiation emitted by an object is expressed as*

$$\dot{Q}_{emit} = \epsilon \sigma A T_S^4, \tag{2.1}$$

where A is the surface area under consideration and $\sigma = 5.67 \times 10^8 \ W/m^2 \cdot K^4$ is the Stephan-Boltzmann constant.

Therefore, thermal radiation intensity increases exponentially with respect to an increase in temperature. Next, we explore how changes in temperature are related to changes in emission by Planck's equation.

Theorem 2.1.6. (Martin, 2004 p.58) Planck's equation *states that the spectral radiance emitted from a blackbody at a given wavelength is described by*

$$\dot{Q}_\lambda = \frac{2hc^2}{\lambda^5 \exp[(hc/k\lambda T) - 1]}, \tag{2.2}$$

where λ is the emission wavelength, $h = 6.625 \times 10^{-34} \ J$ is Planck's constant, c is the speed of light, and $k = 1.38 \times 10^{-23} \ J \ K^{-1}$ is the Boltzmann constant.

This equation is useful for remote sensing because spectral emission properties of bodies can be calculated from their spectral efficiency. Finally, an equation describing the maximum wavelength of an emission spectrum in terms of the temperature is given by Wein's Displacement law.

Theorem 2.1.7. (Martin, 2004 p.58) Wein's displacement law *states that the wavelength of maximum radiance in Planck's equation is proportional to 1/T,*

$$\lambda_{max} = \frac{C}{T}, \tag{2.3}$$

where $C = 0.3$ cm K.

Thus, warm bodies emit maximum radiation at shorter wavelengths than colder bodies.

2.2 Atmospheric Influences on Radiation

The Earth's atmosphere greatly influences radiation as it passes from the sun or is emitted or reflected from the Earth. The atmosphere reflects, scatters, and absorbs passing radiation. This interference means that there exist but a few windows in the electromagnetic spectrum appropriate for Earth observation [8].

With respect to remote sensing, there are several atmospheric phenomena that contribute to interference. The first is water, which can occur in the form of vapor, rain, snow, or ice crystals in clouds. Another is atmospheric aerosols, which are made up of small particles from the Earth such as dust or urban pollution. The ozone is a part of the atmosphere that absorbs certain intervals of the electromagnetic spectrum, particularly ultraviolet rays. Among the sources of atmospheric interference, clouds are the worst, as they completely block passive sensing of the Earth and are masked in an image. Finally, free electrons generated in the Earth's ionosphere are a component of the atmosphere that affect passing radiation [8]. All of these sources of interference contribute to diffuse scattering of radiation in the atmosphere, called *atmospheric scattering*. Atmospheric scattering can be described as either *Rayleigh* or *Mie* scattering.

Definition 2.2.1. (Martin, 2004 p.84) Rayleigh scattering *refers to molecular scattering, or scattering from particles that are small relative to the wavelength of incident radiation.*

Definition 2.2.2. (Martin, 2004 p.86) Mie scattering *refers to aerosol scattering, or scattering from particles that are larger than or of comparable size to the wavelength of incident radiation. These particles include water droplets, aerosols, and ice crystals.*

The atmosphere also emits radiation itself in certain spectral bands by two processes known as *Lorenz* and *Doppler* broadening [8]. Lorenz broadening occurs due to molecular collisions within a gas such as the atmosphere and Doppler broadening is an artifact of the Doppler shift that occurs due to the motion of molecules within a gas.

As noted, atmospheric interference varies with wavelength. In particular, transmittance is highest in the visible spectrum. In higher wavelengths, including those at which the Earth emits radiation, we find narrow bands of transmittance. Wavelengths smaller than ultraviolet are almost completely absorbed and are mostly useless for remote sensing.

2.3   Reflectance, Absorbance, and Transmission

Once through the atmosphere, radiation interacts with the surface of the Earth or, for ocean observing, the boundary between the ocean and the atmosphere. Electromagnetic radiation interacts with a body in three ways. It can be reflected, absorbed, or transmitted depending on the properties of the body. Different bodies have different surface and material properties, allowing to distinguish between them based on their interaction with radiation.

We will discuss these three interactions and their impacts on remote sensing, beginning with reflection. Things that affect the how an object reflects radiation

are the angle of incidence of radiation upon the object and surface topography of the object. There are two different types of reflectance. If the surface is flat, the reflection of incident radiance is mirror-like and the angle if reflection equals the angle of incidence. This type of reflectance is called *specular*. The second type of reflectance is called *Diffuse*. Diffuse reflectance occurs on rough surfaces in which case incident radiance is reflected uniformly in all directions. The two types of reflections are contrasted in Figure 2.1.
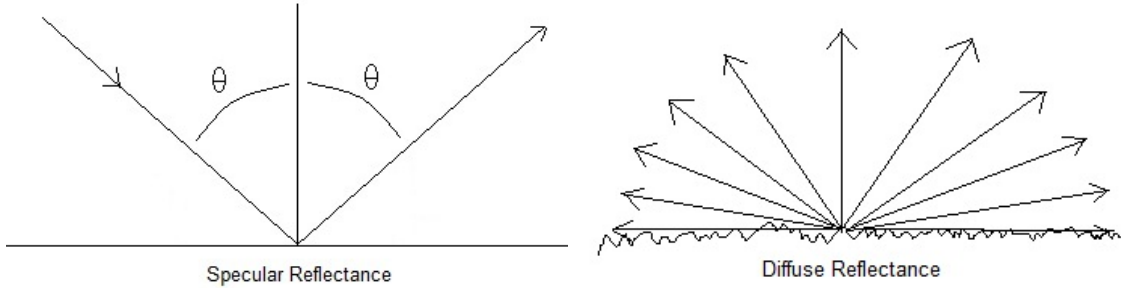
Figure 2.1: Two types of reflectance based on roughness properties of reflecting surface.

Figure 2.1 does not tell the entire story. As a flat surface increases in roughness, specular reflection will begin to directionally diffuse in the direction opposite of incidence. That is, the reflected radiation will be anisotropic in a biased direction at first, but will become isotropic as the surface continues to roughen.

Furthermore, surface reflection depends on the particular wavelength of incident radiation, which can be described by the Rayleigh roughness criterion [8].

Definition 2.3.1. *Suppose radiation with wavelength λ interacts with a surface at incidence angle θ, then the scattering is* specular *if*

$$\frac{\sigma_n \cos(\theta)}{\lambda} < \frac{1}{8}, \tag{2.4}$$

where σ_n denotes the root mean square surface height.

14

The Rayleigh roughness criterion, which gives bounds for specular scattering, says that as the wavelength of incident radiation increases, the surface roughness becomes decreasingly important.

Since we are interested in the remote sensing of ocean ecology, we now discuss the reflectance properties of seawater. For pure seawater, the scattering coefficient exponentially decreases with increasing wavelength [8].

Radiation incident upon the surface of the ocean is in fact both reflected and transmitted through the surface. Radiation transmitted through a surface is said to be *refracted*.
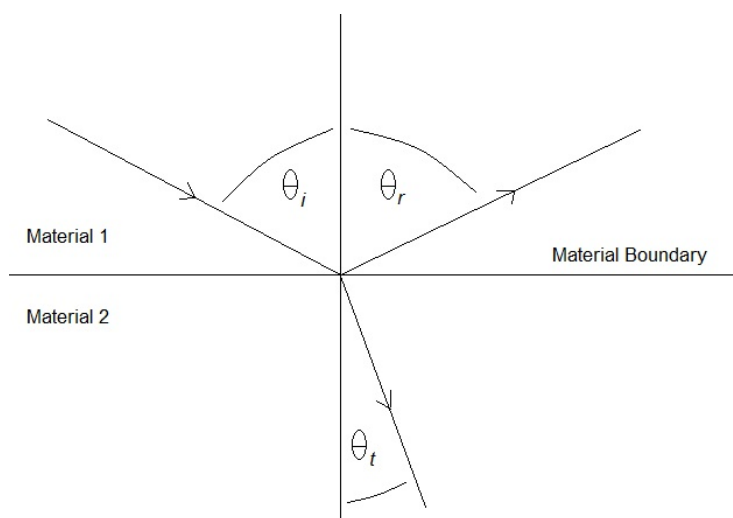
Figure 2.2: Reflection and refraction at material boundary between two different materials. Angle of incident radiation is θ_i, angle of reflected radiation is θ_r, and angle of transmitted or refracted radiation is θ_t.

Figure 2.2 shows radiation incident on a boundary being both reflected with refracted at different angles. Here, θ_i is the angle of incident radiation, $theta_r$ is the angle of reflected radiation, and θ_t is the angle of transmitted, or refracted, radiation. Snell's law described how these angles are related given radiation incident upon the boundary between two different materials.

Theorem 2.3.2. (Halliday et al, p.819) *Suppose the angle of incident radiation is*

denoted θ_i and the angle of reflected radiation is denoted θ_r, as shown in Figure 2.2. The law of reflection *states that the angle of incidence and angle of reflection are equal and opposite for specular reflection, that is $\theta_i = -\theta_r$.*

Theorem 2.3.3. (Halliday et al, p.819) *Suppose the angle of incident radiation is denoted θ_i and the angle of transmitted radiation is denoted θ_t, as shown in Figure 2.2. Snell's law states that the radiation is refracted by an angle θ_t as*

$$n_2 \sin(\theta_t) = n_1 \sin(\theta_i), \tag{2.5}$$

where n_1 is the index of refraction for material 1 and n_2 is the index of refraction for material 2.

The relationship between the magnitudes of reflected and refracted radiances can be described by the *Fresnel equations*. To describe the Fresnel equations, first we define the *radiance reflectance*.

Definition 2.3.4. (Martin, 2004 p.109) *Suppose the angle of incident radiation is denoted θ_i and the angle of reflected radiation is denoted θ_r. The* radiance reflectance $r(\lambda, \theta_r)$, *is defined as*

$$r(\lambda, \theta_r) = \frac{L_r(\lambda, \theta_r)}{L_i(\lambda, \theta_i)}, \tag{2.6}$$

where $L(\lambda, \theta_i)$ is the radiance of incident radiation at a given wavelength and $L(\lambda, \theta_r)$ is the radiance of reflected radiation.

Now the transmitted radiance $r(\theta_i)$ can be written as (Martin, 2004)

$$r(\theta_i) = \frac{1}{2} \left(\left(\frac{\sin(\theta_i - \theta_t)}{\sin(\theta_i + \theta_t)} \right)^2 + \left(\frac{\tan(\theta_i - \theta_t)}{\tan(\theta_i + \theta_t)} \right)^2 \right), \tag{2.7}$$

where $\theta_i = -\theta_r$ by Snell's law. Here θ_i is the angle of incident radiation, θ_r is the angle of reflectance, and θ_t is the angle of transmittance as shown in Figure 2.1.

However, the atmosphere-ocean boundary is not an idealized mirror-like interface. The wavy ocean surface causes diffuse reflectance, or a scattering of solar radiance, called *sun glint.* Sun glint is an important issue as it is observed by a sensor and can overwhelm the radiance both reflected and emitted by the ocean surface and therefore must be filtered, or masked [8]. Finally, another type of reflection to be considered is the reflection from foam caused by breaking waves. This type of reflection is assumed to be diffuse in nature and deserves consideration in remote sensing algorithms [8].

The ocean has a particularly high absorbency at many wavelengths. Absorption and emission are confined to the top $1 - 100\mu$m in the infrared and to the top $1 - 3$ mm in the microwave [8]. Thus, in these regions of the spectrum, we are only concerned with scattering and reflection. However, the same is not true of the visible wavelengths, in which both direct and diffuse reflections occur [8]. Absorption in pure seawater as a function of wavelength has a minimum in the region between 300-600 nm [8]. As a result absorption has a strong maximum when seen as a function of water depth in the region between 320-570 nm, wherein absorption is greater than 10 m [8]. This is the basis for Raman's argument that the color of the ocean is determined by scattering within the water column, since the 320-570 nm range is heavily blue-green biased.

Water-leaving radiance occurs whence radiation is transmitted into the water column and subsequently scattered, being partially transmitted back across the boundary between the atmosphere and ocean. This is sometimes referred to as *backscattering.* Water-leaving radiance is a product of diffuse reflections and is extremely important to consider in remote sensing over the visible wavelengths [8].

2.4 Satellite Characteristics

We now discuss some characteristic differences between satellite-borne multispectral imagers and define relevant terms. Particularly, we will discuss different satellite orbits and imaging techniques. The orbit of a satellite can be broken into two parts, the motion of the satellite relative to the Earth's center of mass and the orbit of the satellite relative to the rotating Earth. First, it is necessary to define some terms.

Definition 2.4.1. *A satellite's position along its orbit is called the satellite* ephemeris.

The ephemeris can be projected onto the surface of the Earth and that time-dependent location is called the satellite's *ground track*.

Definition 2.4.2. *A satellite's* ground track *is the intersection of the Earth's surface with the line between the satellite and the Earth's center of mass.*

Information about the satellite's ground track is often of greater interest than it's particular position in orbit. We take as an illustrative example, the orbit of many satellites launched at Cape Canaveral, FL including the Hubble Space Telescope [9]. Cape Canaveral is located at roughly 28.5° North and the resulting orbit has an angle of inclination of 28.5° from the equator as shown in Figure 2.3.

If the Earth were not rotating, this sort of orbit would produce a ground track resembling a giant circle that would be represented by a sine wave on a Mercator projection of the Earth. A trajectory of the Hubble Space Telescope for the non-rotating Earth is shown in Figure 2.4, where the same regions on Earth would be repeatedly viewed by the orbiting satellite.

However, reality dictates that the Earth is rotating along with the orbital movement of a satellite. If the rotation of the Earth is different from the orbital period of the satellite, the sine plot will be shifted steadily over the Mercator projection. For example, the Hubble Space Telescope takes just 96 minutes to orbit the Earth
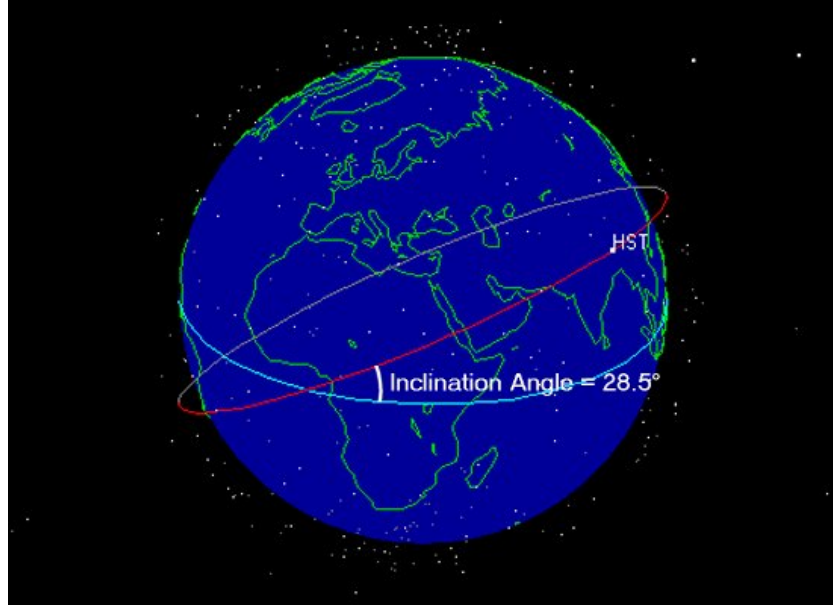
Figure 2.3: Illustration of the orbit of the Hubble Space Telescope with respect to the equator, launched from Cape Canaveral, FL [9].
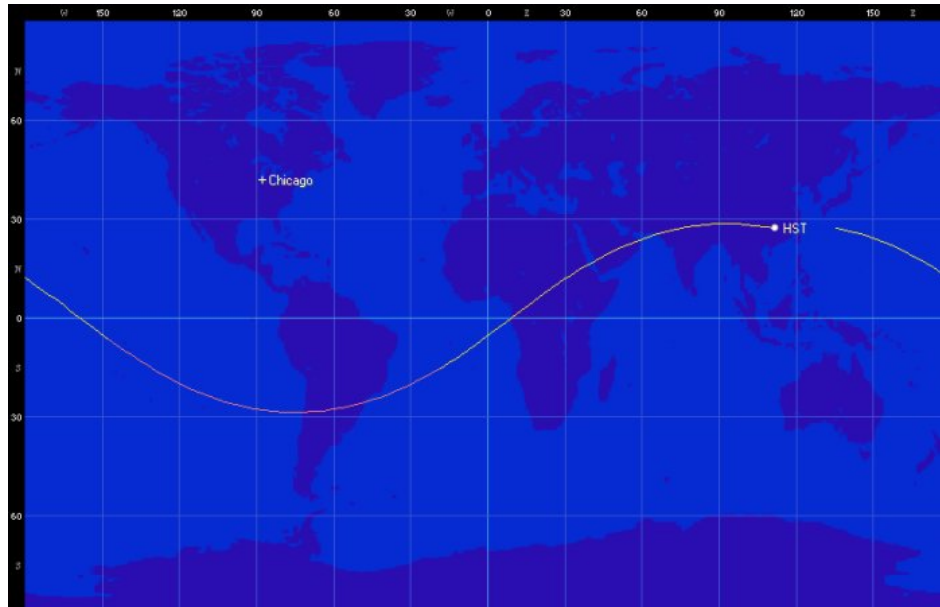
Figure 2.4: Example trajectory of Hubble Space Telescope for non-rotating Earth resulting in a single repeated trajectory [9].

compared with the 1440 minutes it takes the Earth to rotate [9]. Therefore, the path of the satellite resembles a family of sine waves when viewed on a Mercator projection

of the Earth as shown in Figure 2.5.
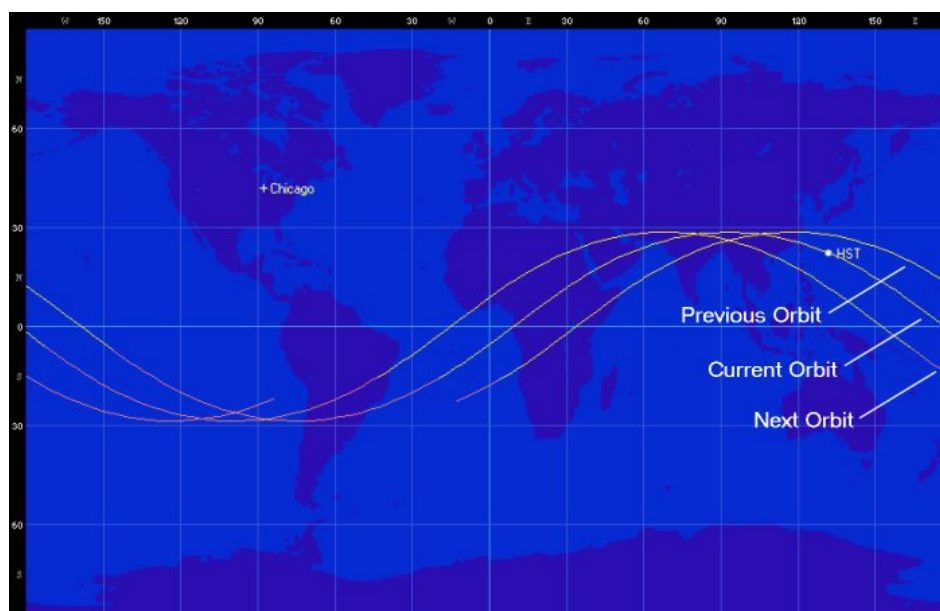
Figure 2.5: Realistic trajectory of Hubble Space Telescope for rotating Earth resulting in a steady shift west of the orbit track [9].

There are three common types of satellite orbits used in remote sensing called *geosynchronous*, *sun-synchronous*, and *near equatorial low inclination* [8]. Each type of orbit presents advantages over the others and no particular type is preferred for all forms of Earth observation. Thus the choice of orbit often depends on the desired utilization of a particular remote sensor.

Geosynchronous orbits are located at roughly an altitude of 36,000 kilometers above the surface of the Earth. Geosynchronous orbits are by far the largest in circumference of the three mentioned. A satellite requires 24 hours to make a full orbit around the Earth at roughly 36,000 kilometers. Geostationary orbits are a subset of geosynchronous orbits, wherein the satellite's orbit lies in the equatorial plane such that the satellite remains at a fixed location over the Earth's surface. The more general geosynchronous orbits allow a tilt in the orbit relative to the equator so that its ground path may look like a figure eight centered about the equator [8]. An obvious disadvantage with geosynchronous orbits is that the satellite must pass

20

through the Earth's shadow. Another disadvantage with such satellites is the spatial resolution can be quite low due to its relative distance from the Earth's surface. Geosynchronous satellites are limited to a spatial resolution of about 1 square kilometer. Geosynchronous satellites are often used for weather observation, communication, and near-equatorial observations of sea surface temperature [8].

Sun-synchronous orbits are much closer to the Earth's surface at altitudes ranging from 300 to 1,400 kilometers. Therein lies an advantage over geosynchronous satellites; spatial resolutions range from medium to high. The sun-synchronous period is roughly 90 minutes which results in 16 orbits per day [8]. With each subsequent orbit, the satellite is able to view a different section of the Earth in a narrow band, which is not again visited for a few days. Thus, the geosynchronous satellites have a vast temporal advantage when interested in a fixed geographic location [10]. The orbit plane of a sun-synchronous satellite remains at a fixed angle to the line between the sun and the Earth. Thus, the sun-synchronous orbit plane slowly drifts such that it rotates once per year [8]. Sun-synchronous satellites make daily observations of chlorophyll or sea surface temperature at the same time of day every day. This is due to the fact that the satellite will always cross the equator at the same local time of day. Therefore, the effect of the diurnal cycle is removed from the phenomena under investigation allowing for easy comparison. Another advantage for ocean observations is the fact that these satellites can be forced to cross an area of interest at a favorable time of day. For example, cloudiness increases over the ocean throughout the day and the orbit of a sun-synchronous satellite can be chosen to minimize the cloudiness during observation [8]. Therefore, these orbits are most commonly found in ocean-observing satellites. Three ways of describing sun-synchronous orbits are "early morning", "mid-morning", and "early afternoon". Finally, a disadvantage to sun-synchronous satellites is their inability to cover the poles, with what is called the "hole at the pole" [8].

Finally, the near equatorial low inclination orbit has the lowest altitude at 350 kilometers. The orbit covers roughly half of the Earth and is capable of hourly temporal observations of a given geographic location, an improvement over sun-synchronous orbits. This type of orbit is used for tropical monitoring of rainfall and sea surface height [8]. An illustration of these different orbital paths is shown in Figure 2.6 as found in [10]
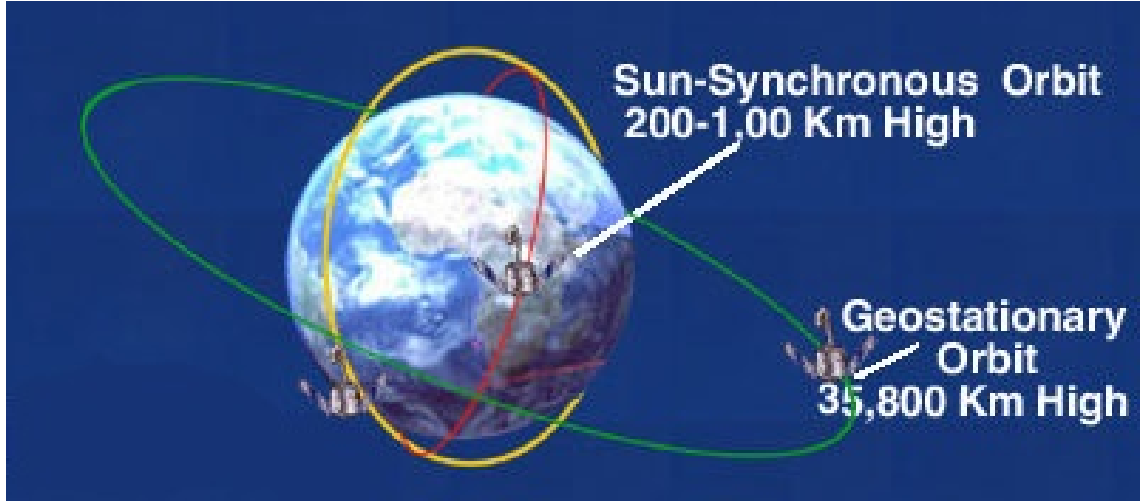
Figure 2.6: Two different types of orbits shown with respective altitudes [10].

2.5 Imaging

The second property of satellite imagery to consider is the particular imaging technique used. Different techniques include *cross-track* or *wiskbroom*, *alongtrack* or *push-broom*, and a hybrid technique called a *hybrid wiskbroom* [8].

We now discuss some important terminology with respect to satellite imaging.

Definition 2.5.1. *The* zenith *is the direction pointing directly overhead of a geographic location.*

Definition 2.5.2. *The* nadir *is the direction pointing directly below a geographic location. The nadir points in the same direction as gravitational pull.*

Definition 2.5.3. *The* scan point *is the location on Earth observed by an instrument.*

Definition 2.5.4. *The* view angle *or* scan angle*, denoted θ_v is the angle between the nadir line and the instrument look direction.*

Definition 2.5.5. *The angle between the look direction and the local normal to the scan point is the* zenith incidence*, also called the* look angle*.*

Definition 2.5.6. *The angle between the line from the Earth's surface to the sun and the local normal to the Earth's surface is called the* solar zenith angle*, denoted θ_v.*

Definition 2.5.7. *the surface area of Earth that the instrument observes is called the* instrument field-of-view *or the* instantaneous field-of-view*.*

If the instrument is looking directly downward toward the Earth, also called *nadir view*, the field-of-view is a circle. However, if the satellite is looking at off-nadir angles, the field-of-view is an ellipse [8]. The angles described above are shown in Figure 2.7

Definition 2.5.8. *As sun-synchronous satellites orbit the Earth, they view a region over the satellite's nadir path, the width of which is called the* swath width*.*

The swath width is determined by the sensor's full angular field-of-view.

We now describe three scanning techniques used by sensors that are looking in the visible and infrared regions of the electromagnetic spectrum. The first type of scanning technique we discuss is the *cross-track* or *wiskbroom* technique. The cross-track technique uses a rotating mirror to sweep across the scene in a "sideways" motion relative to the sensor's nadir path. The term "wiskbroom" provides the mental picture of the back-and-forth sweeping motion when using a broom. This technique is shown in Figure 2.8. A calibration source is held at a constant radiance such that after each surface scan, the sensors are calibrated. An advantage of the cross-track technique is that a calibration is made after every revolution or oscillation of the mirror [8].
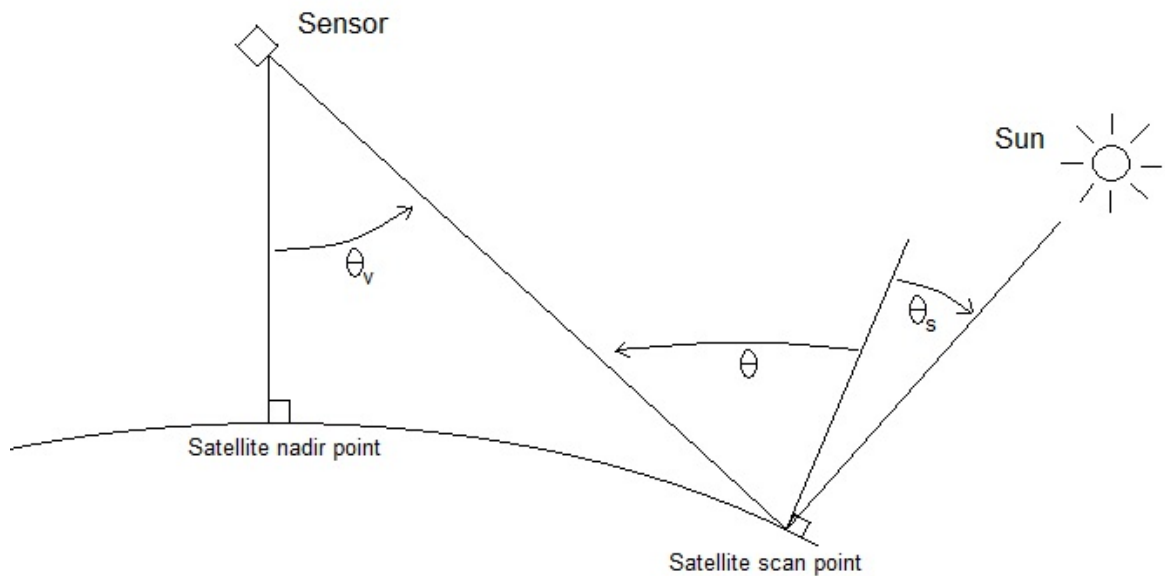
Figure 2.7: Angles defined to describe satellite view angle and the solar angle with respect to the Earth, figure adapted from [8]. Here θ_s is the solar zenith angle, θ is the instrument look angle, and θ_v is the instrument scan angle, all relative to the local normals to the Earth.

An example of an instrument that uses cross-track scanning is the Sea-viewing Wide Field-of-View Sensor (SeaWiFS).

The second technique is called *along-track* or *pushbroom* scanning. The mental picture for this method is that of cleaning a floor with a wide pushbroom using forward sweeps. For this technique, the sensor contains a stationary line of sensors arranged to observe the surface in the cross track direction as the sensor orbits, thus the scan is in the direction of the sensor's nadir path. The along-track method has one advantage over the cross-track method in that the time interval for which the sensor is focused on a particular geographic location is greater. This allows for a higher spatial resolution than is available to sensors using the cross-track technique [8]. A disadvantage of the along-track technique is that multiple sensors can lose their relative calibrations, causing the instrument to be less accurate than a well-calibrated cross-track instrument. Furthermore, the wider the swath, the more cumbersome the

line of sensor arrays becomes on the instrument [8]. The Medium Resolution Imaging Spectrometer (MERIS) on the ENVISAT satellite uses the along-track technique. This method is shown in Figure 2.8with thick arrows pointing in the satellite ground track direction.
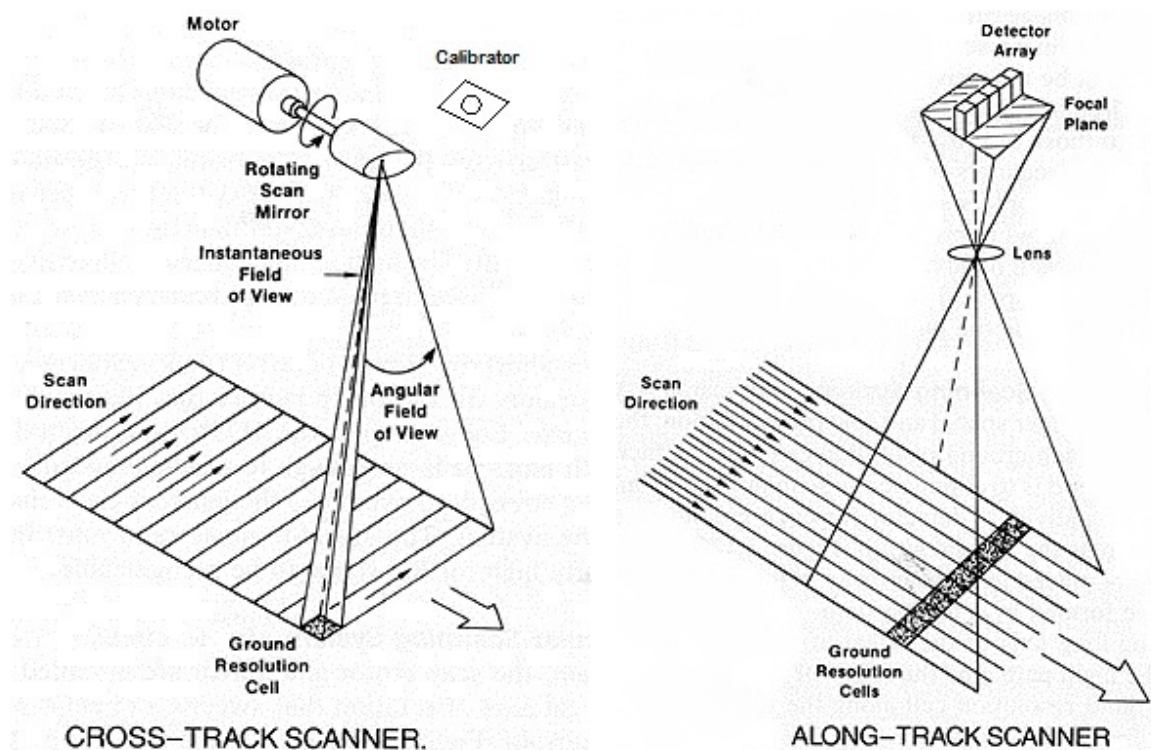
Figure 2.8: Comparison of cross-track and along-track scanning methods. Figures taken from [11].

The third technique commonly used in remote sensing is called the *hybrid cross-track scanner*. Users require wide-swath high resolution images, so a hybrid technique combining both methods was developed. The hybrid technique lines sensors up in the nadir-direction, orthogonal to the direction of the sensors in the along-track arrangement. This gives an oblong instantaneous field-of-view in the instrument's nadir direction. This arrangement is then oscillated as in the cross-scan method such that the sensors move orthogonally to the nadir-track. The hybrid technique provides a higher resolution image due to the longer time interval over which a particular

geographic location is observed. Furthermore, the sensors are calibrated after each rotation, thus combining the benefits from both techniques. The hybrid cross-track scanning method is currently used by the Moderate Resolution Imaging Spectrora-diometer (MODIS) on the NASA-owned TERRA and AQUA satellites.
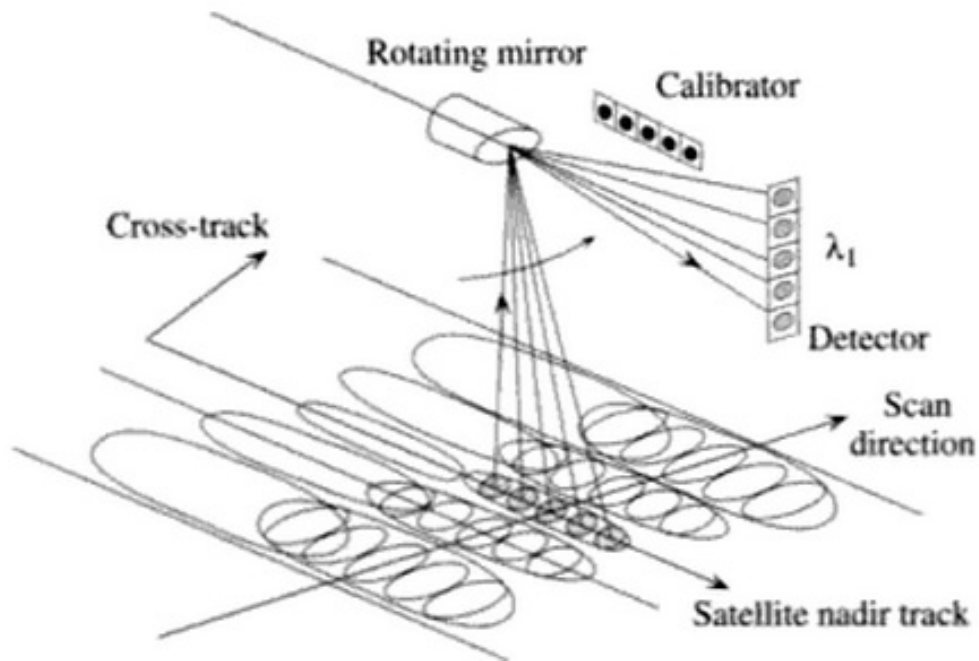
Figure 2.9: The hybrid cross-track scanning method. Figure taken from Figure 1.12 of [8].

2.6 Data Processing

As data are collected from remote sensors, they are fed through a series of steps, called processing levels. There are four levels of processing in which data may be found. These processing levels are defined as follows:

Definition 2.6.1. Level 0 *data are completely raw as collected by the sensor.*

Level 0 data are usually not distributed to the public. Most users have no need for Level 0 data.

Definition 2.6.2. Level 1A *data are presented at full resolution in files that contain time references, calibration values, and geo-referencing values. This data have been corrected for variations within the sensor, sometimes called radiometric correction.*

Definition 2.6.3. Level 1B *data contain image swaths that have been corrected for errors in the geometry of the product.*

Level 1B data corrections include, for example, correction for oblique viewing angles and non-uniform pixel sizes. These files are in a more user-friendly format.

Definition 2.6.4. Level 2 *data are processed to yield geophysical data products, including sea surface temperature, chlorophyll, or colored dissolved organic matter in a swath format. Level 2 data have been mapped to a standard map projection at which point the data is called "geo-referenced".*

Here the image is registered to a base map by aligning several ground control point from both the image and the map. At this point the image geometry will match the geometry of the base map. There is a considerable amount of processing done between Level 1 and Level 2 data products.

Definition 2.6.5. Level 3 *data are gridded to the base map in both time and space. Level 3 data often consists of multiple day averages of, for example, sea surface temperature.*

Most data is distributed in either Level 1 or Level 2 format and Level 2 or Level 3 data are most often used for analysis of geophysical quantities of interest. As noted, Level 0 data is very difficult to obtain, and is cumbersome for most remote sensing data users. If obtained in Level 1 format, data can be processed by the user for specific products or geophysical quantities of interest using software packages. It may then be mapped to a uniform grid, or geo-referenced for comparison over time with subsequent images or for Level 3 processing. The Level 2 product we require

is chlorophyll concentration, which provides inferences for plankton densities in the ocean, as will be discussed.

2.7   Hyperspectral Imagers

We collect data from three remote sensors mounted on earth-observing satellites. The first instrument we use is the European Space Agency's Medium Resolution Imaging Spectrometer (MERIS). This instrument is mounted on the Envisat satellite. The spatial resolution is often 1200 meters, but can be as fine as 300 meters on the coast [65]. The instrument orbits the Earth such that it observes the entire planet once every three days. MERIS collects data in 15 spectral bands, selectable across a range from 390 nm to 1040 nm [65]. Data taken from MERIS is unavailable to the public so we receive processed data with much gratitude from Dr. Nick Tufillaro at the College of Earth, Ocean, and Atmospheric Sciences (COAS) at Oregon State University. Two images from MERIS of the Oregon coast, including the Columbia River mouth, are shown in Figure 2.10. On the left is a quasi-true color image reconstructed from data received by MERIS on December 12, 2009. To the right is the processed image; it has been mapped to a uniform grid such that subsequent images can be directly compared and their respective domains contain matching coordinates. Furthermore, chlorophyll has been inferred from the spectral bands in the original dataset and is shown with higher densities corresponding to dark red and purple. During this time period there was a high level of bloom activity off the coast of Oregon and the bloom is even visible as a slight discoloration of the water in the quasi-true color image.

The second instrument we use is the NASA-owned Moderate Resolution Imaging Spectroradiometer (MODIS), mounted on both AQUA and TERRA satellites. The instrument was launched in 1999 on board NASA's Terra satellite and was deemed useful enough to be subsequently launched on board NASA's Aqua satellite in 2002.
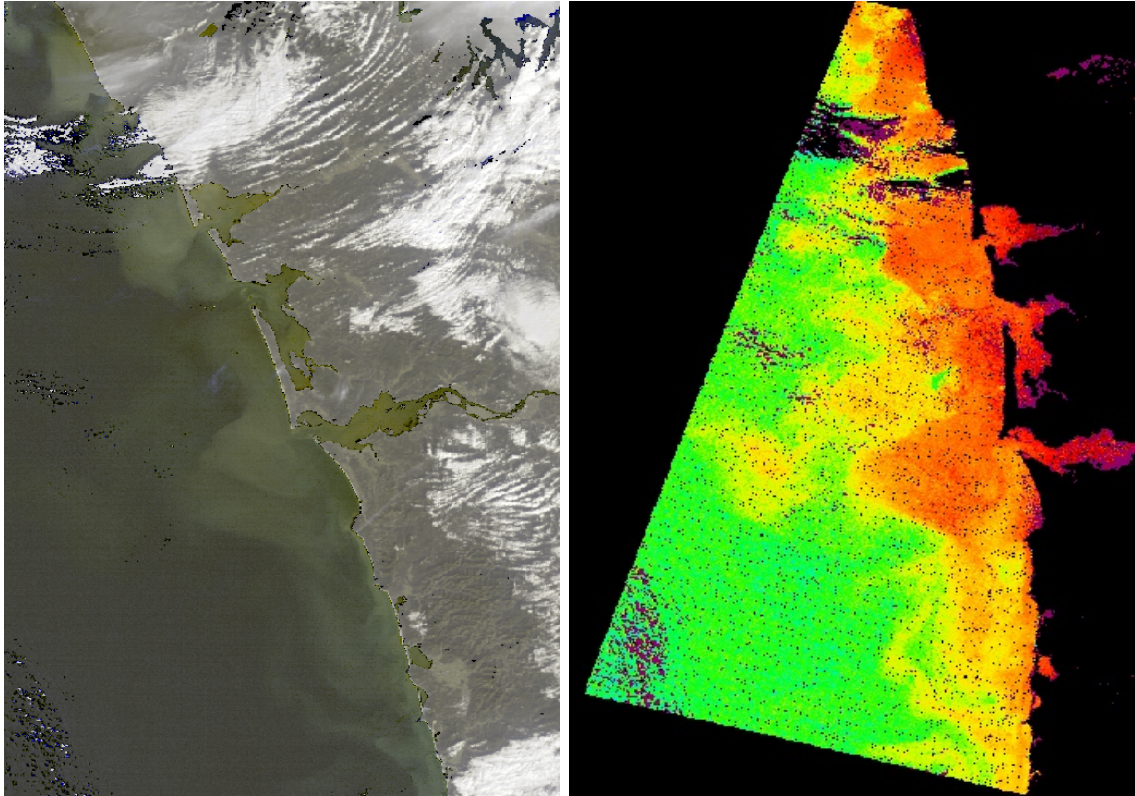
Figure 2.10: Quasi-true color image of the Oregon Coast on the left with processed level 3 image on the right. Relatively high levels of chlorophyll are indicated by dark red and purple. Image was taken by MERIS on December 12, 2009.

These satellites orbit the Earth such that they observe the entire planet once every 24-48 hours. Data are acquired in 36 spectral bands, of which eight are relevant for ocean observing. The spatial resolution over the bands useful for oceanic remote sensing is 1000 meters. Bandwidths are fixed and vary between 10 and 15 nanometers [66]. The data taken by this sensor is archived at [67] in many different forms for use in a wide variety of research. In Figure 2.11, two images are shown in the same order as in Figure 2.10. The quasi-true color image shows a bloom mixed with sediment run-off from the Louisiana delta region, with the bloom activity and sediment clearly visible as a discoloration of the coastal water. On the right the image has been processed for chlorophyll, indicating higher levels of phytoplankton near shore. This image was taken by MODIS on November 10, 2009 and was obtained using [67].
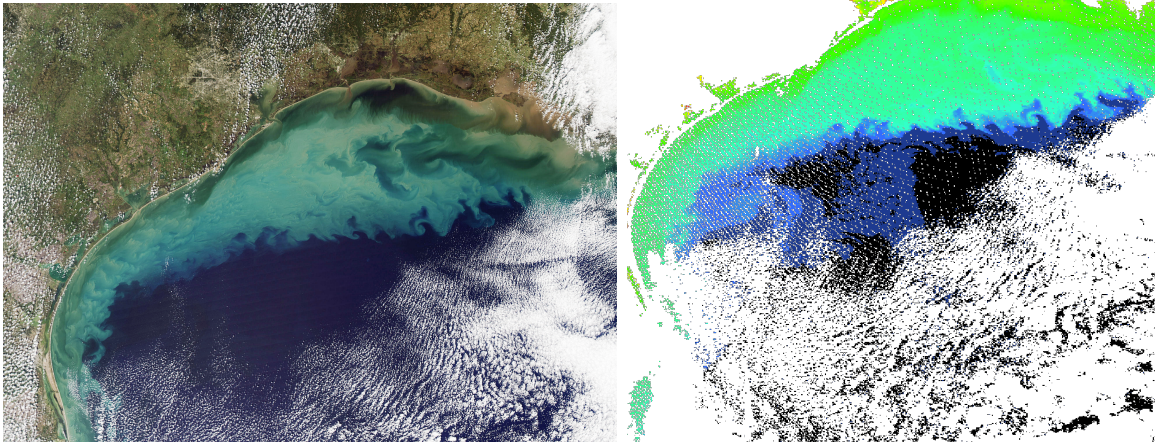
Figure 2.11: Quasi-true color image of the Gulf coast on the left with processed level 3 image on the right. Relatively high levels of chlorophyll are indicated by green and yellow. Image was taken by MODIS on November 10, 2009.

Finally, our goal is to use data from the Hyperspectral Imager for the Coastal Ocean (HICO), mounted on the Japanese Experiment Module Exposed Facility (JEM-EF) on the International Space Station. HICO is revolutionary in that it is the first orbiting spectrometer specifically designed to sample the coastal ocean [14]. The data from HICO provides an unprecedented level of detail with which to study the Earth's oceans. Launched in 2009, the instrument was originally sponsored by the Office of Naval Research and is currently supported by NASA's International Space Station program [14]. HICO collects data from 380 to 960 nm with 128 bands in 5.7 nm bandwidths. Thus, the bandwidth discretization far outperforms the former sensors. Furthermore, HICO samples the coastal ocean at 90 meters, producing about 2000 images yearly from around the world. HICO samples the Earth spatially at ten times that of the former sensors. HICO data are archived at Oregon State University's COAS, which acts as the primary repository of the data to the public. Figure 2.12 compares a MERIS image of the Oregon coast with a HICO image. The MERIS image is the same as shown in Figure 2.10 and the HICO image shows the Columbia River mouth in extraordinary detail.
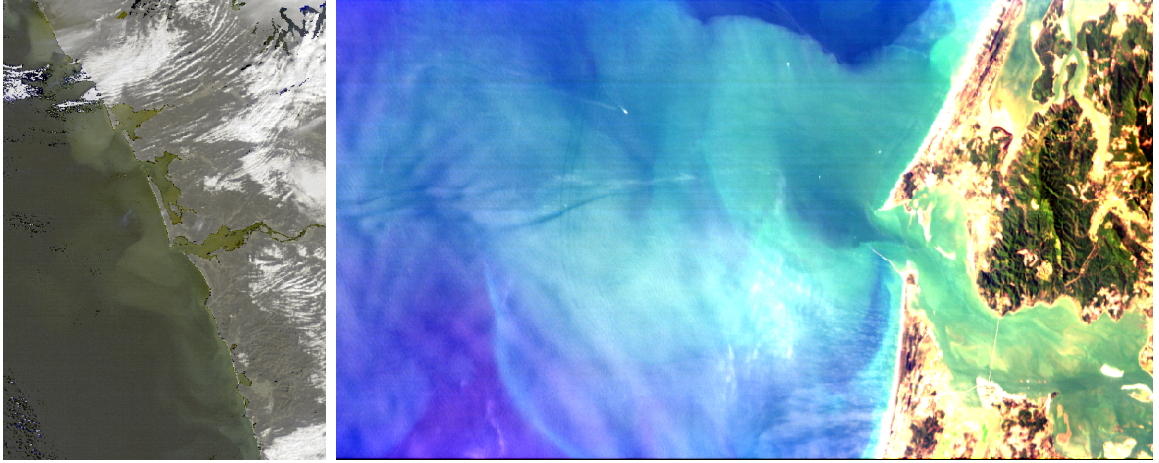
Figure 2.12: Quasi-true color image of the Oregon coast from MERIS on the left compared with HICO on the right. The comparison shows the ability to reconstruct better quasi-true color images and shows off the spatial resolution of HICO relative to previous instruments.

Images of the three sensors are shown in Figure 2.13, wherein the top two images show the satellites on which the sensors are mounted and the bottom image shows the HICO instrument.

2.8 Filtering Radiation to Detect Ocean Ecology

Certain algal blooms are so dense that they visibly change the color of seawater. In this sense, algal blooms can be seen in the visible spectrum, a phenomena earning many algal blooms the name *red tides*. Other sources of ocean color include colored dissolved organic matter (CDOM), also called yellow matter, and suspended particulate matter [8]. CDOM is produced near-shore by run-off and in the open ocean as a consequence of organisms grazing on phytoplankton. CDOM particles absorb mostly in the blue range, thus causing a yellow-brown coloring of the water, hence the term "yellow matter".

Due to the variety of sources of ocean color, the ocean is divided into either case 1 or case 2 waters.
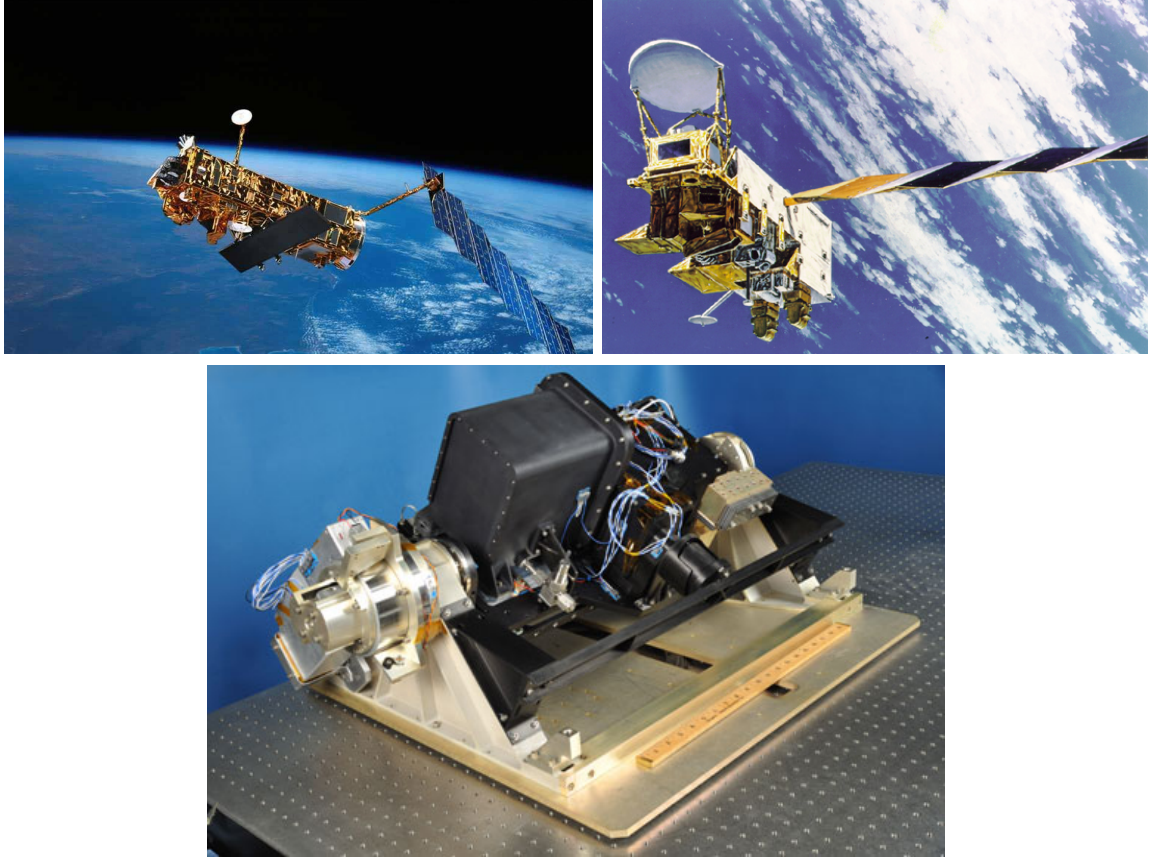
Figure 2.13: Top Left: ENVISAT satellite on which MERIS is housed. Top Right: Aqua Satellite on which MODIS is housed. BOTTOM: HICO Instrument, currently mounted on the International Space Station.

Definition 2.8.1. Case 1 *waters refer to open ocean waters in which phytoplankton are the main cause of ocean color.*

Definition 2.8.2. Case 2 *waters refer to waters in which suspended sediments and CDOM dominate ocean color. Near-shore waters commonly fall under the case 2 classification.*

As noted, case 2 waters are commonly found near-shore due to land run-off, river mouths, or suspended sediments in shallow water. Our work is primarily focused on modeling in case 2 waters since they directly concern coastal economies and ecologies through fishing, tourism, and shipping.

We are interested in phytoplankton inferences from satellite imagery, so we now

discuss how phytoplankton absorb radiation, or the *spectral signature* of phytoplankton. An important feature of phytoplankton is the chlorophyll pigment contained within the algae. Thus, to study phytoplankton in the ocean, we analyze the spectral signature of chlorophyll, particularly chlorophyll-*a*, denoted Chl-*a*. Chlorophyll-*a* has classically two absorption peaks, a blue peak near 440 nm and a red peak near 665 nm. The blue peak is significantly larger than the red peak. The absorption as a function of wavelength for Chl-*a* is shown in Figure 2.14, the absorption is at a minimum in the 550-650 nm range, explaining the associated green coloring characteristic of chlorophyll-dense waters.
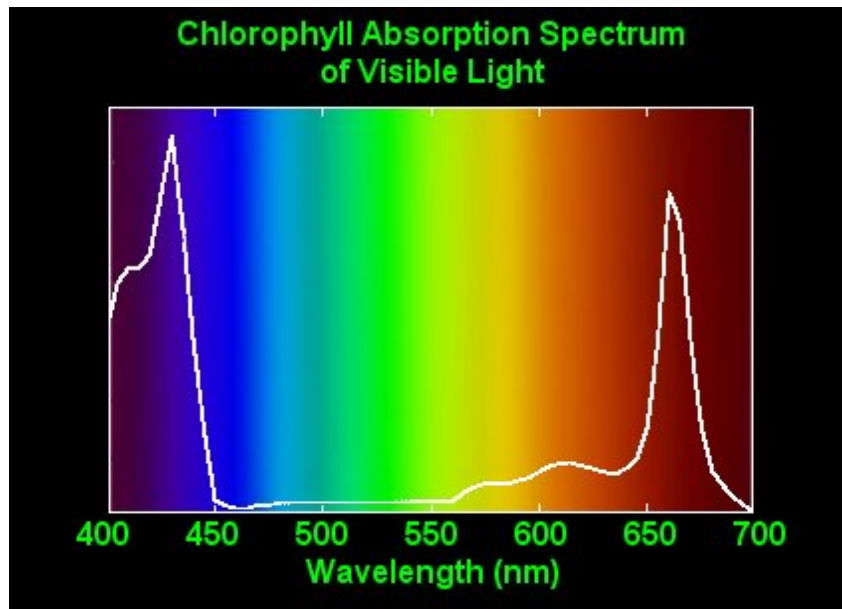
Figure 2.14: The absorption properties of phytoplankton using the absorptive and reflective properties of Chlorophyll-*a*. Both absorption peaks are clearly visible as is the interval of higher reflection accounting for the characteristic greenish color of chlorophyll. Figure taken from [12]

Various organisms in the water column are responsible for scattering. As described in Martin(2004), the smallest living organisms present are viruses. Viruses have diameters of 10-100 nm and are small enough that they are responsible for Rayleigh scattering. Bacteria have a diameter of 0.1-1 μm and are responsible for absorption

of radiation in the blue wavelengths. Phytoplankton range from 2-200 μm, which are mostly Mie scatters because of their larger size. Finally, zooplankton are the largest organisms considered here with a size of 100 μm to 20 mm. Inorganic material, such as CDOM or sediments, can range in sizes from 1 μm to roughly 10 μm. Certainly, larger organisms exist in the ocean but occur infrequently enough such that they do not affect scattering or absorption on the scale of satellite observation.

From here on, for the sake of example, we will consider and explore the algorithms used in MODIS. The algorithm used for remote sensing on MODIS begins with determining whether a pixel in the image is cloud-free. Band 1 is at 660 nm and band 2 is at 870 nm and the ratio of the two bands determines whether or not clouds are present in combination with a threshold test for the amount of reflectance in band 2. For detection of high cirrus clouds, MODIS uses two bands, band 26 and band 18. These wavelengths are 1.375 μm and 936 nm respectively.

The sensors receive radiation from several sources that need to separated and filtered in the algorithm. The total radiance $L_T(\lambda)$ received by the sensor is broken down as

$$L_T(\lambda) = t_D(\lambda)L_W(\lambda) + t_D(\lambda)L_F(\lambda) + t(\lambda)L_G(\lambda) + L_R(\lambda) + L_A(\lambda) + L_{RA}(\lambda), \quad (2.8)$$

where $t_D(\lambda)$ is the diffuse transmittance, $L_F(\lambda)$ is the radiance reflected by foam, $L_G(\lambda)$ is sun glint, $L_R(\lambda)$ is atmospheric Rayleigh scattering, $L_A(\lambda)$ is aerosol atmospheric scattering, and $L_{RA}(\lambda)$ is mixes Rayleigh-aerosol scattering. Following the presentation in Martin, we now describe how these terms are calculated.

For wavelenths in the range of 500-700 nm, the ozone is assumed to be strictly absorbing and thus does not contribute to scattering. The Total Ozone Mapping Spectrometer is used to find the spatiotemporal distribution of ozone.

As already discussed, sun glint is a function of sun angle and wind speed. There-

fore, a sun glint mask is applied to MODIS data using numerical weather models from NOAA at a temporal resolution of 3-6 hours. Since gusts of wind occur at much smaller time scales, a further examination of the NIR radiances is used to mask pixels if radiances exceed a threshold value.

Reflection from foam depends much less on the solar angle and more on wind speed. Recall that reflection from foam is more diffuse than specular, therefore the angle of the sun does not affect reflected radiation as much as amount of foam present due to higher wind speeds. Therefore, $L_F(\lambda)$ is often nearly constant across large regions of an image. In processing, if $L_F(\lambda)$ is too large, then the image is not used. However, often times the contribution to $L_T(\lambda)$ from $L_F(\lambda)$ is quite small.

The largest contributor to $L_T(\lambda)$ is often Rayleigh radiance. This term is estimated largely using numerical weather models since the surface pressure and wave information are required.

The aerosol scattering term, $L_A(\lambda)$, is estimated using the NIR bands, which allow aerosol inferences and their wavelength dependence. Basically, since seawater absorption is much larger for wavelengths greater than 700 nm than in the visible range, the NIR reflectance from below the surface and water-leaving radiances are negligible. Therefore, $L_W(\lambda) = 0$ for 765 nm and 865 nm bands. First $L_G(\lambda)$, $L_R(\lambda)$, $L_F(\lambda)$, and ozone absorption are removed from all bands. For the two bands mentioned in which $L_W(\lambda) = 0$, this gives both $L_A(765)$ and $L_A(865)$. These observations are compared with several different numerically calculated values for benchmarking. If these values agree, then the aerosol radiances are extrapolated to the visible range.

Once $L_W(\lambda)$ are removed from all bands, the final step in the process is to remove the diffuse transmittance $L_W(\lambda)$. This term is either calculated using the assumption of diffuse distribution of radiance at the surface or from a numerical approximation based on an aerosol model.

After dealing with the scattering from the atmosphere and the ocean-atmosphere

interface, we consider the reflectance properties of chlorophyll-laden seawater. For wavelengths less than 500 nm, the reflectance decreases as chlorophyll concentration increases. For wavelengths greater than 500 nm the reverse occurs and reflectance increases with increasing chlorophyll concentration. This behavior results in a *pivot point* at a wavelength of about 500 nm, where the reflectance remains the same regardless of chlorophyll concentration [68]. Therefore, the spectral signature for different concentrations of phytoplankton behaves in this somewhat inverse manner.

Sometimes a body tends to emit radiance of a higher wavelength when subject to radiation of a given wavelength.

Definition 2.8.3. Fluorescence *is the emission of light by a body that has absorbed some form of electromagnetic radiation.*

Importantly, chlorophyll-containing phytoplankton tend to fluoresce at a well-known 683 nm peak. Figure 2.15 shows both the aforementioned absorption peak and the fluorescence peak for chlorophyll-a. This fluorescence peak exists for all chlorophyll densities but increases in intensity with increasing concentration [8].

The measurement of fluoresce provides another means to estimate chlorophyll-a by remote sensing and is an important consideration in ocean color algorithms. Such an algorithm requires three bands at 667, 678, and 748 nm at a 10 nm bandwidth [8]. The product given by this measurement is called the fluorescence line height (FLH). Also, while absorption measurements may be skewed by CDOM, fluorescence is not as CDOM does not fluoresce. MODIS, MERIS, and HICO all have a spectral resolution sufficient to observe this product. The fluorescence properties of chlorophyll allow for two algorithms to determine chlorophyll concentration from satellite imagery. The first makes use of the blue-green absorptive properties of phytoplankton and the second observes the fluoresce line height to infer plankton densities. Both will now be discussed in detail.
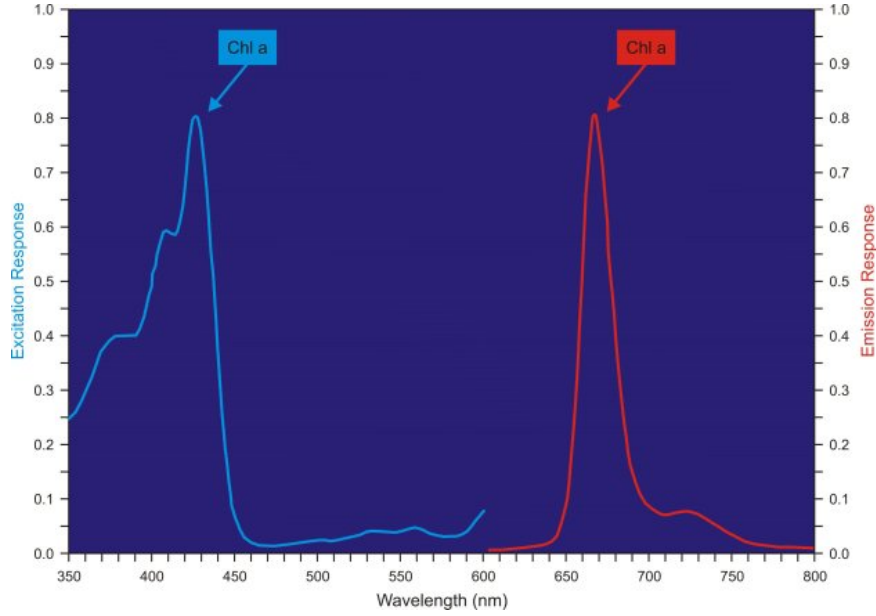
Figure 2.15: Composite of absorption peak and fluorescence peak for chlorophyll taken from [13]

2.9   Ocean Color Algorithms

We now discuss two algorithms used by MODIS for monitoring chlorophyll densities by multispectral satellite data. These are divided into the 400-550 nm wavelengths and the 683 nm region for monitoring absorption and fluorescence respectively. There are yet two types of algorithms for data in the 400-550 nm interval. There is what is called an *empirical* algorithm, in which satellite inferences of $L_W(\lambda)$ are matched with in-situ measurements of chlorophyll-a. The empirical algorithm presented here is suitable for only case-1 waters.

Also there is an *semianalytic* algorithm for chlorophyll detection in which models of the relationship of the reflectance observed by the satellite to the backscatter/absorption ratio are combined with in-situ models. This allows for seasonal variation, changes in geography, and changes in sea surface temperature [8]. This algorithm has the advantage of use in case-1 and case-2 waters as chlorophyll can be extracted from CDOM.

We begin with the empirical algorithm used for MODIS data. The remote sensing reflectance $R_r s(\lambda)$ is given by

$$R(\lambda) = \frac{T^2 R(\lambda)}{n^2 Q} = \frac{G T^2 b_{bT}(\lambda)}{n^2 Q a_T(\lambda)}, \tag{2.9}$$

where $R(\lambda)$ is the subsurface reflectance. Recall that $R(555)$ does not depend on chlorophyll concentration, at least approximately. Therefore, the reflectances are given as ratios with respect to their intensity at 555 nm

$$\frac{R_{rs}(\lambda)}{R_{rs}(555)} \equiv \frac{[L_W(\lambda)]_N F_S(555)}{[L_W(555)]_N F_S(\lambda)} = \frac{R(\lambda)}{R(555)} = \frac{b_{bT}(\lambda) a_T(555)}{b_{bT}(555) a_T(\lambda)}, \tag{2.10}$$

as given in [8]. The MODIS empirical algorithm, called OC3M is

$$R_L = \log_{10}\left(\max\left[R_{rs}\text{-ratio}\left(\frac{443}{551}, \frac{488}{551}\right)\right]\right), \tag{2.11}$$

$$\log_{10}(C_a) = 0.283 - 2.753 R_L + 0.659 R_L^2 + 0.649 R_L^3 - 1.403 R_L^4, \tag{2.12}$$

where C_a is concentration of chlorophyll-a and $\max[R_{rs}\text{-ratio}\left(\frac{443}{551}, \frac{488}{551}\right)]$ is an operation that chooses the maximum band ratio [8].

Next we consider the semianalytic algorithm. This algorithm is written with contributions from empirical formulas for absorptions and backscatter dependence on sediments, CDOM, and chlorophyll along with theoretical models similar to Equations eq. (2.9) and eq. (2.10). This algorithms uses

$$\frac{R_{rs}(\lambda)}{R_{rs}(555)} = \frac{b_{bT}(555)[a_W(\lambda) + a_\phi(\lambda) + a_{CDOM}(\lambda)]}{b_{bw}(\lambda) + b_{bp}(\lambda)}, \tag{2.13}$$

where a_W is absorption from pure water, a_ϕ is absorption from phytoplankton, a_{CDOM} is absorption from CDOM, b_{bw} is backscatter from seawater, and b_{bp} is backscatter

from particulates [8].

Given these algorithms, it is even possible to distinguish between certain different species of phytoplankton. Species that may be singled out by satellite imagery include coccolithophores, Karenia brevis, and phycoerythrin-containing species [8]. Karenia brevis are a toxic red-tide-inducing species in which we are particularly interested in modeling.

Atmospheric influences and other noise-inducing phenomena are important to understand when sensing the electromagnetic spectrum. Different satellites have several discriminating characteristics including how they record images and process data. We have access to data from three hyperspectral imagers that inform algorithms to detect ocean ecology. Much of the work to be done in this thesis is intended to develop new methods toward modeling with this data, and it is important that we understand the characteristics inherent in the data with which we aim to build models. The remainder of this thesis will examine many of the new techniques toward model fitting with an ideal benchmark dataset, progressively representative of what might be observed by remote sensing; many limiting features of remote sensing data will be subsequently included in the benchmark dataset.

Chapter 3

Numerical Techniques

3.1 Model Dataset

Satellite data of plankton blooms often reveal complex mesoscale structures such as ocean gyres and eddies [8, 15]. As a synthetic dataset, a spatiotemporal model for plankton ecology should have the capability to render such mesoscale structures. Our benchmark model, from Medvinksi, et al, [15] describes a two-component predator-prey model for phytoplankton and zooplankton ecology, over a rectangular two-dimensional region.

Given perturbed initial conditions, the model exhibits spiral patterns on a spatial scale comparable to that which is observed in nature by satellite data [15]. By observing snapshots from the numerical solution of this model, we emulate a satellite image dataset. We further complicate the synthetic dataset by including spatially varying parameters. This is a valid consideration when modeling mesoscale ocean ecology [15]. Consider the system of two PDEs as given in [15],

$$
\begin{aligned}
\frac{\partial P}{\partial t} &= \triangle P + P(1 - P) - \frac{PZ}{P + h}, \\
\frac{\partial Z}{\partial t} &= \triangle Z + k\frac{PZ}{P + h} - mZ,
\end{aligned}
\tag{3.1}
$$

on a compact connected two-dimensional domain, Ω, with zero-flux boundary conditions. Zero-flux, or Neumann, boundary conditions enforce that

$$\frac{\partial P}{\partial \mathbf{n}}(x, y) = 0,$$
$$\frac{\partial Z}{\partial \mathbf{n}}(x, y) = 0, \ \ \forall x, y \in \Omega,$$

(3.2)

where $\mathbf{n}$ is the normal to the boundary $\partial\Omega$.

In terms of the biology of the model, the system represents a dimensionless reaction-diffusion model for phytoplankton-zooplankton predator prey dynamics in a horizontal layer where vertical distributions of plankton are considered uniform. For simulations shown here, we choose Ω to be a rectangle of size 900×300. Although shown in dimensionless form, the model is derived from principles in which phytoplankton concentrations obey a logistic growth and are grazed upon by zooplankton, following a Holling-type II functional response. First classified by Holling, [69], the Holling-type II functional response assumes a decelerating growth rate such that the predator, or consumer, is limited by its ability to efficiently process food. Zooplankton grow at a rate proportional to phytoplankton mortality and are subject to a natural mortality rate.

In dimensionless form, the growth and death rates for phytoplankton are absorbed in the parameters k and m. For a range of parameter values, e.g., $k = 2$, $h = 0.4$, and $m = 0.6$, this system gives rise to transient spiral pattern behavior on its way to spatiotemporal chaos [15]. For homogeneous initial plankton distributions, the system remains in a homogeneous state for all time so we apply the perturbed initial conditions found in [15],

$$P(x, y, 0) = P_* - (2 \times 10^-7)(x = 0.1y - 225)(x - 0.1y - 675),$$

$$Z(x, y, 0) = Z_* - (3 \times 10^-5)(x - 450) - (1.2 \times 10^-4)(y - 150),$$

where,

$$P_* = \frac{rh}{1-r},$$

$$Z_* = (1 - u_*)(h + u_*),$$

$$r = \frac{m}{k}.$$

The numerical solution of this system defines our benchmark dataset for the entirety of the work here. The initial conditions for the drive system for every simulation performed herein will be the above.

The system Eq (3.1) is modified as found in [15] by allowing the parameters to be nonnegative $C^0(\Omega)$ functions. Generally, we may allow $\Omega \subset \mathbf{R}^2$ to be a compact domain such as a rectangle for simplicity or a realistic domain representing a coastal region obtained from a satellite.

An example domain is shown in Figure 3.1, where a high concentration of phytoplankton is shown by a greenish coloring of the water. This is a quasi-true color image taken from the HICO (Hyperspectral Imager for the Coastal Ocean) instrument mounted on the International Space Station. It is the first such imaging spectrometer specifically designed to sample the coastal ocean [14]. Shown is the Columbia River mouth bordering Oregon and Washington, taken on July 8, 2010. The domain is large enough to capture mesoscale and small scale patterns, which may result from complex intra-species and fluid dynamics. We note that Neumann boundary conditions are very difficult to compute properly when using finite differences over a domain as shown in Figure 3.1. Therefore, for simulation over such domains, the finite element method should be used. However, our domain is a simple rectangle, allowing for boundary conditions to be easily handled numerically.
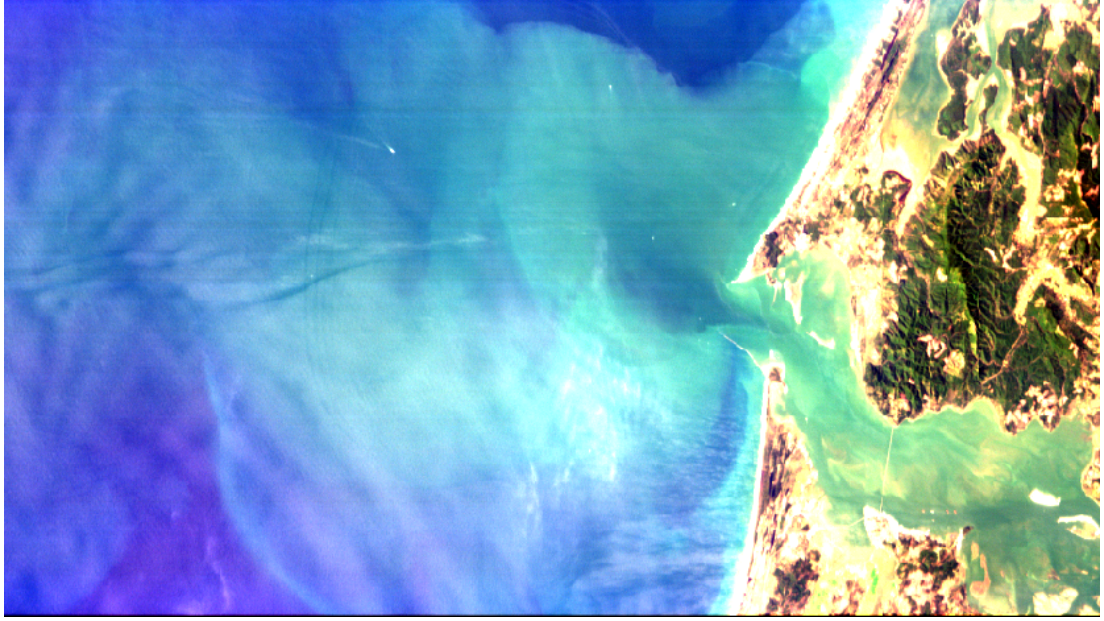
Figure 3.1: A quasi-true color satellite image from HICO instrument, [14], of the Columbia River mouth taken on July 8, 2010. High plankton densities shown by green coloring of the water. Spatial resolution is fine enough that a boat is clearly visible in the upper half of the image.

We further complicate the benchmark model by adding advection as,

$$
\begin{aligned}
\frac{\partial P}{\partial t} &= \Delta P - \nabla \cdot (\mathbf{v}P) + P(1-P) - \frac{PZ}{P+h}, \\
\frac{\partial Z}{\partial t} &= \Delta Z - \nabla \cdot (\mathbf{v}Z) + k\frac{PZ}{P+h} - mZ,
\end{aligned}
\tag{3.3}
$$

where $\mathbf{v}$ is a non-autonomous, divergence-free, spatially dependent vector field. Boundary conditions remain of type zero-flux. We next discuss how this system is discretized and solved numerically for simulation over a rectangular domain. We begin with the reaction-diffusion equation Eq (3.1) as it is used often as a benchmark system. We then discuss how we handle advection and subsequently simulate Eq (3.3).

3.2 Discretization

There are several available methods for discretization and subsequent numerical simulation of PDEs, including explicit, implicit, semi-implicit, first-order and second-order methods to name a few [70,71]. We use a simple first order forward difference scheme to estimate temporal derivatives. Spatial derivatives require a little more work, but we find that a simple method will suffice.

For notational purposes, we will write the general form of the PDE problem we simulate as

$$\frac{\partial u}{\partial t} = \Delta u - \mathbf{v} \cdot \nabla u + f(u), \tag{3.4}$$

$$g(u) = 0 \text{ on } \partial \Omega,$$

$$u = u_0 \text{ on } \Omega,$$

where $u(x, y, t)$ can be considered a vector in order that this is a PDE system. We disctretize the domain $[\Omega \times t_F]$ spatially and temporally, resulting in grid points (x_i, t_n), where $x_i = ih$ and $t_n = nk$. Here $h = dx$ is the space step and $k = dt$ is the time step. Let the numerical approximation to the solution at a grid point (x_i, t_n) be denoted by $U_i^n \approx u(x_i, t_n)$.

Spatial derivatives are calculated using a centered difference approximation. Therefore, the differencing scheme we will be using for the majority of our simulations is forward difference in time and centered difference in space. Figure 3.2 shows a stencil for this differencing scheme. This scheme is said to be first order accurate in space and second order accurate in time [71].

Figure 3.2 indicates the space-time discretization in one dimension. However, we will be solving PDEs in two dimensions, and thus we require a 3-point stencil to estimate the Laplacian in two-dimensions. This stencil is shown in Figure 3.3 where the stencil is applied at time step n and the temporal derivative requires data at time
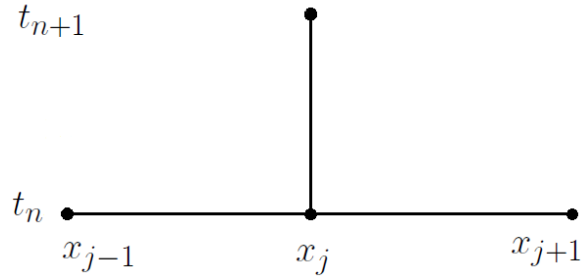
Figure 3.2: Stencil for the forward difference in time and centered difference in space in one space dimension.

step $n+1$. This stencil represents the preferred method of numerical solution for the system Eq (3.1).
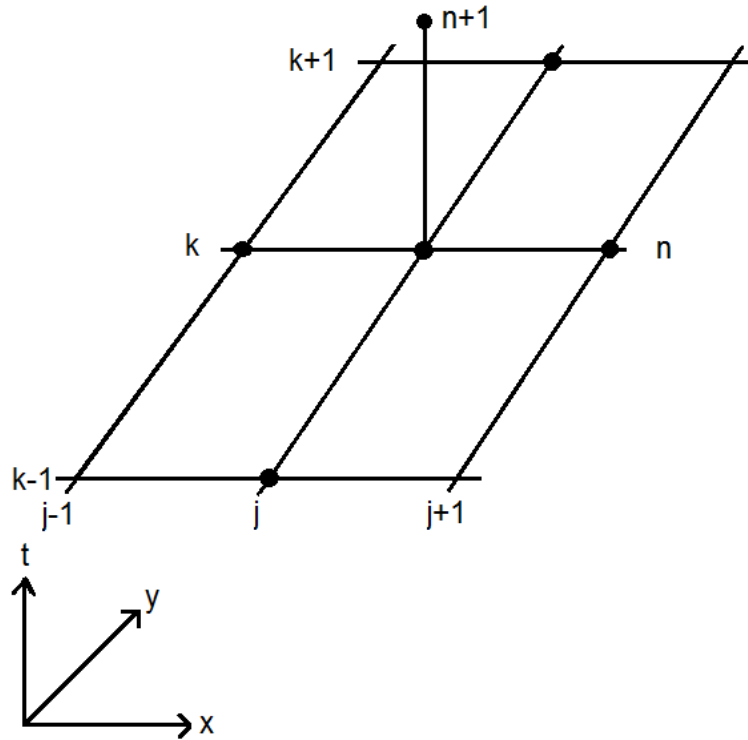
Figure 3.3: Stencil for the forward difference in time and centered difference in space in two space dimensions.

We discretize the modified system, Eq (3.1), with explicit finite differences, using a three-point center difference stencil for spatial derivatives and forward Euler time

stepping. That is, we use the discretization

$$\frac{P^{n+1} - P^n}{dt} - \frac{P^n_{i,j+1} - 2P^n_{i,j} + P^n_{i,j-1}}{dx^2} - \frac{P^n_{i+1,j} - 2P^n_{i,j} + P^n_{i-1,j}}{dy^2} = f_1(P^n_{i,j}), \qquad (3.5)$$

$$\frac{Z^{n+1} - Z^n}{dt} - \frac{Z^n_{i,j+1} - 2Z^n_{i,j} + Z^n_{i,j-1}}{dx^2} - \frac{Z^n_{i+1,j} - 2Z^n_{i,j} + Z^n_{i-1,j}}{dy^2} = f_2(Z^n_{i,j}),$$

where

$$f_1(P^n_{i,j} Z^n_{i,j}) = P^n_{i,j}(1 - P^n_{i,j}) - k\frac{P^n_{i,j} Z^n_{i,j}}{P^n_{i,j} + h}, \qquad (3.6)$$

$$f_2(P^n_{i,j} Z^n_{i,j}) = k\frac{P^n_{i,j} Z^n_{i,j}}{P^n_{i,j} + h} - mZ^n_{i,j},$$

for notational simplicity. The system Eq (3.5) is solved for simulation as

$$P^{n+1}_{i,j} = P^n_{i,j} + dt\left(\frac{P^n_{i,j+1} - 2P^n_{i,j} + P^n_{i,j-1}}{dx^2} + \frac{P^n_{i+1,j} - 2P^n_{i,j} + P^n_{i-1,j}}{dy^2} + f_1\right), \qquad (3.7)$$

$$Z^{n+1}_{i,j} = Z^n_{i,j} + dt\left(\frac{Z^n_{i,j+1} - 2Z^n_{i,j} + Z^n_{i,j-1}}{dx^2} + \frac{Z^n_{i+1,j} - 2Z^n_{i,j} + Z^n_{i-1,j}}{dy^2} + f_2\right),$$

with boundary conditions

$$\frac{\partial P}{\partial x} = 0, \qquad \frac{\partial P}{\partial y} = 0,$$

$$\frac{\partial Z}{\partial x} = 0, \qquad \frac{\partial Z}{\partial y} = 0,$$

that are discretized using the second-order centered difference in space as

$$\frac{P^n_{i,L+1} - P^n_{i,L-1}}{dx} = 0, \qquad \frac{P^n_{i,1} - P^n_{i,-1}}{dx} = 0, \qquad (3.8)$$

$$\frac{P^n_{M+1,j} - P^n_{M-1,j}}{dy} = 0, \qquad \frac{P^n_{1,j} - P^n_{-1,j}}{dy} = 0,$$

where $0 \leq x \leq L$ and $0 \leq y \leq M$.

In one space dimension, a discretization such as the forward time centered space method is typically discussed within the framework of a nearly symmetric, tridiagonal matrix solve [70]. That is, suppose we are to solve the discretization shown in Eq (3.7) in one dimension only, and consider only the phytoplankton equation. Let $r = \frac{dt}{dx^2}$, and rewrite the equation as

$$P_j^{n+1} = P_j^n + r \left(P_{j+1}^n - 2P_j^n + P_{j-1}^n + f_1(P_j^n) \right) \tag{3.9}$$
$$= rP_{j+1}^n + P_j^n(1 - 2r) + rP_{j-1}^n + hf_1(P_j^n).$$

This can be written as a matrix operator update for a given time n [71]

$$dt \begin{pmatrix} f_1(P_0^n) \\ f_1(P_1^n) \\ f_1(P_2^n) \\ \vdots \\ f_1(P_{L-1}^n) \\ f_1(P_L^n) \end{pmatrix} + \begin{pmatrix} -2r & 2r & 0 & 0 & 0 & 0 \\ r & -2 & r & 0 & 0 & 0 \\ 0 & r & -2 & r & 0 & 0 \\ 0 & 0 & \ddots & \ddots & \ddots & 0 \\ 0 & 0 & 0 & r & -2 & r \\ 0 & 0 & 0 & 0 & 2r & -2r \end{pmatrix} \begin{pmatrix} P_0^n \\ P_1^n \\ P_2^n \\ \vdots \\ P_{L-1}^n \\ P_L^n \end{pmatrix} = \begin{pmatrix} P_0^{n+1} \\ P_1^{n+1} \\ P_2^{n+1} \\ \vdots \\ P_{L-1}^{n+1} \\ P_L^{n+1} \end{pmatrix}, \tag{3.10}$$

where boundary conditions are included in the matrix and reaction terms are accounted for in the left-most vector.

We use a different approach to solving Eq (3.9), by taking the convolution of a matrix with a finite difference kernel. Let $g(x - \hat{x}, y - \hat{y})$ bet the convolution kernel, represented by the coefficients of a two-dimensional finite difference scheme such as shown in Figure 3.3. Let $f(x, y, t)$ be the solution of the PDE at time t. We suppose f has compact support for simplicity and since Ω is compact. We compute the Laplacian

by taking the convolution

$$[f * g](x, y) = \int_{\Omega} f(\hat{x}, \hat{y}, t) g(x - \hat{x}, y - \hat{y}) d\hat{x} d\hat{y}. \tag{3.11}$$

For simulation over the discretized domain, we require discrete two-dimensional convolution. Let $A(t) \in \mathbb{R}^{m \times n}$ be the image representing the discretized solution of a PDE at a given time t. Let $G \in \mathbb{R}^{p \times p}$ be the discretized convolution kernel given by the coefficients of a finite difference scheme. For our work we let

$$G = \begin{pmatrix} 0 & 1 & 0 \\ 1 & -2 & 1 \\ 0 & 1 & 0 \end{pmatrix}, \tag{3.12}$$

so the discretized version of Eq (3.11) is

$$[A * G](m, n) = \sum_{\hat{m} \in \Omega} \sum_{\hat{n} \in \Omega} A(\hat{m}, \hat{n}, t) G(m - \hat{m}, n - \hat{n}), \tag{3.13}$$

where $\hat{m}$ and $\hat{n}$ range over all pixels in the image. Typically the image is extended to handle boundary conditions. Since we are using a five-point stencil, the image must be extended such that an extra row is added to the top and bottom of A and an extra column is added to the left and right side of A. To handle zero-flux boundary conditions, the values are extended symmetrically from the image boundary.

Eq (3.13) describes how the Laplacian is computed in two-dimensions for the reaction-diffusion equations solved here. The method is essentially identical to building matrices, however, this is clearly much simpler to handle notationally and is in fact how our numerical simulations are coded.

3.3 Advection

Thus far we have studied the numerical approximation of systems of reaction-diffusion equations. However, we require methods to solve models that include advection. A general pure advection equation is written as [72]

$$u_t + \nabla \cdot (\mathbf{a}u) = 0, \tag{3.14}$$

for some velocity field $\mathbf{a}$, and given initial data $u(x, 0) = u_0$ and boundary conditions. Since we are assuming a divergence-free velocity field, $\mathbf{a}$, Eq (3.14) simplifies to

$$u_t + \mathbf{a} \cdot \nabla u = 0, \tag{3.15}$$

To solve the advection equation, one might prefer the upwinding method [71, 72]. We discretize this equation by forward differences in time, and upwinding in space [71]. For the general problem, we have two choices for an asymmetric discretization and the explicit algorithm is written as

$$U_j^{n+1} = U_j^n - \frac{ak}{h}(U_j^n - U_{j-1}^n), \text{ or} \tag{3.16}$$
$$U_j^{n+1} = U_j^n - \frac{ak}{h}(U_{j+1}^n - U_j^n),$$

which are first order accurate in space. Since the time discretization is also first order accurate, this method is first order accurate in both space and time [71].

The choice of discretization in Eq (3.16) is dictated by the sign of a. If $a > 0$, the solution travels to the right while if $a < 0$ the solution travels to the left. Given that we are using non-autonomous gyre-like vector fields, a is both positive and negative at any given time over Ω. When solving advection equations we estimate derivatives with data in the direction opposite of advection so the numerical method is stable [71].

In fact, symmetric approximations like those used in Section 3.2 are unstable, in the sense of Von Neumann stability, when applied to the advection problem [71]. Therefore, we solve advection by upwinding and combine with the approximations to the second derivative noted in Section 3.2 to solve the more comprehensive problem.

3.4 Reaction-Diffusion-Advection

We combine the methods in Sections 3.2 and 3.3 to simulate a reaction-diffusion-advection system as a model for ocean ecology over a compact connected two-dimensional domain. That is, we solve systems of equations of the form

$$\frac{\partial \mathbf{u}(x,y,t)}{\partial t} + \nabla \cdot (\mathbf{a}(x,y,t)\mathbf{u}(x,y,t) - \nabla D\mathbf{u}(x,y,t)) = \mathbf{f}(\mathbf{u}(x,y,t)), \qquad (3.17)$$

where $D \in \mathbb{R}^1$ is the diffusion coefficient, $\mathbf{a}(x,y,t) \in C^1 \times C^1$ is a spatially-dependent non-autonomous vector field, and $\mathbf{f}(\mathbf{u}(x,y,t)) : C^2 \times C^2 \to C^2 \times C^2$ is the reaction term for the species. Further, we require initial conditions $\mathbf{u}(x,y,0) = \mathbf{u}_0$ and Neumann boundary conditions $\frac{\partial \mathbf{u}}{\partial \mathbf{n}} = \alpha$. We impose the scientific prior of a divergence-free vector field on Eq (3.17) such that it may be rewritten as

$$\frac{\partial \mathbf{u}}{\partial t} + \mathbf{a} \cdot \nabla \mathbf{u} - D\Delta \mathbf{u} = \mathbf{f}(\mathbf{u}), \qquad (3.18)$$

omitting the independent variables, where the diffusion term is assumed scalar. Diffusion is treated using a centered difference in space and advection with the upwinding scheme. For the time derivative, we use the forward difference method.

Our benchmark equations, now including advection, are transformed to

$$\frac{\partial P}{\partial t} = D\Delta P - \mathbf{v} \cdot \nabla P + f_1(P,Z), \qquad (3.19)$$
$$\frac{\partial Z}{\partial t} = D\Delta Z - \mathbf{v} \cdot \nabla Z + f_2(P,Z),$$

where

$$f_1 = P(1 - P) - \frac{PZ}{P + h},$$

$$f_2 = k\frac{PZ}{P + h} - mZ,$$

and **v** is a non-autonomous divergence-free vector field. We discretize the system in time and space and simulate Eq (3.19) in two-dimensions. That is, we combine forward difference in time, centered difference in space, and upwinding to build the difference equations

$$\frac{P^{n+1} - P^n}{dt} + I(P^n_{i,j}) - \frac{P^n_{i,j+1} - 2P^n_{i,j} + P^n_{i,j-1}}{dx^2} - \frac{P^n_{i+1,j} - 2P^n_{i,j} + P^n_{i-1,j}}{dy^2} = f_1(P^n_{i,j}),$$

$$(3.20)$$

where

$$I(P^n_{i,j}) = \begin{cases} \frac{v_{i,j}}{dx}(P^n_{i,j} - P^n_{j-1}), & \text{if } v^n_{1_{i,j}} \geq 0, \\ \frac{v_{i,j}}{dx}(P^n_{i,j+1} - P^n_{i,j}), & \text{if } v^n_{1_{i,j}} < 0, \\ \frac{v_{i,j}}{dx}(P^n_j - P^n_{j-1}), & \text{if } v^n_{2_{i,j}} \geq 0, \\ \frac{v_{i,j}}{dx}(P^n_{j+1} - P^n_j), & \text{if } v^n_{2_{i,j}} < 0, \end{cases} \qquad (3.21)$$

and we are only showing the phytoplankton equation. The zooplankton equation is discretized in the same way. The scheme quickly becomes unwieldy when simulating in two-dimensions. Eq (3.20) is solved in the same way as Eq (3.7) and evolved forward given initial and boundary conditions. The domain over which the equations are solved is $\Omega = 300 \times 900$. The spatial and temporal step sizes are chosen as $dx = 2$ and $dt = .1$.

This is a nonlinear system enforcing that the methods for stability based on linear PDEs are not applicable. We verified stability numerically by spatially and temporally refining the grid and noting the qualitative similarity of solution behavior.

51

The model that produces our observed data is built upon aforementioned biological and physical assumptions. The basic methods of discretization are examined, including the method of approximating solution behavior to build an observed dataset. Spatially-dependent model parameters and advection are included in the model, culminating in the reaction-diffusion-advection system described. This system represents the most general model for which we aim to develop our methods.

Chapter 4

Synchronization

The phenomena of synchronization between two chaotic oscillators has been extensively explored over the past few decades [7, 44–54, 56, 57, 73–75]. This study aims to advance the utility of synchronization techniques toward observability for modeling spatiotemporal geophysical quantities with hidden or unobserved data in both time and space.

The chapter begins with a brief introduction into the field of synchronization, including necessary definitions. We next demonstrate that a benchmark reaction-diffusion model representing ocean ecology will exhibit synchronization with several different coupling choices. We provide a first demonstration that synchronization can be extended to *autosynchronization* as we are able to estimate model parameters while concurrently estimating model states for the PDE system. Next, we extend these results to show that synchronization and parameter estimation is demonstrated when one system state is unobservable, a very important development for practical use with the data described in chapter 2. Furthermore, the unobserved state is synchronized such that the entire state of the observed system is known.

Remote sensing data provides a challenge in that data may be missing, or hidden, in either time, space, or even both. Such is the result of temporal sparsity

in measurements and the spatial sparsity governed by an instrument's ground sampling distance [8]. We show that both synchronization and parameter estimation by autosynchronization are robust to temporal and spatial subsampling. Finally, we consider the formidable problem of clouds occluding regions of the domain and describe how the method is altered to demonstrate synchronization when observing clouds.

We begin with some mathematical definitions and terms commonly used in the field of synchronization. First we formally define synchronization for two ODE systems [7].

Definition 4.0.1. (Pecora, Carroll, Johnson, Mar, & Heagy, 521) *Let $\dot{\boldsymbol{u}} = \mathbf{f}(\mathbf{u}, \mathbf{p})$ and $\dot{\boldsymbol{v}} = \mathbf{g}(\mathbf{u}, \mathbf{v}, \mathbf{p})$ be two systems of ordinary differential equations wherein sates of $\dot{\boldsymbol{u}}$ are coupled with, or fed into, $\dot{\boldsymbol{v}}$. Let $\boldsymbol{p} \in \mathbb{R}^n$ be a vector of parameters. The systems $\dot{\boldsymbol{u}}$ and $\dot{\boldsymbol{v}}$ are said to* synchronize identically *if*

$$\|\boldsymbol{u} - \boldsymbol{v}\| \to 0 \ as \ t \to \infty. \tag{4.1}$$

Here we take the vector norm to be the standard Euclidean norm. We note the broader idea of *generalized synchronization* [7] allows for the existence of a map from one phase space to the other such that knowledge of the state of one system allows for knowledge of the state of the other, however we are only interested in the special case of identical synchronization.

Definition 4.0.2. (Perko, 104) *An* n-dimensional differentiable manifold, M*, is a connected metric space with an open covering U_α, i.e., $M = \cup_\alpha U_\alpha$, such that*

1. *for all α, U_α is homeomorphic to the open unit ball, B, in $\mathbb{R}^n$, and*

2. *if $U_\alpha \cap U_\beta \neq \emptyset$ and $\mathbf{h}_\alpha : U_\alpha \to B, \mathbf{h}_\beta : U_\beta \to B$ are homeomorphisms, then $\mathbf{h}_\alpha(U_\alpha \cap U_\beta)$ and $\mathbf{h}_\beta(U_\alpha \cap U_\beta)$ are subsets of $\mathbb{R}^n$ and the map*

$$\mathbf{h} = \mathbf{h}_\alpha \circ \mathbf{h}_\beta^{-1} : \mathbf{h}_\beta(U_\alpha \cap U_\beta) \to \mathbf{h}_\alpha(U_\alpha \cap U_\beta)$$

54

is differentiable and for all $\mathbf{x} \in \mathbf{h}_\beta(U_\alpha \cap U_\beta)$, *the Jacobian determinant* $D\mathbf{h}(\mathbf{x}) \neq 0$.

Intuitively, an n-dimensional manifold is a set that "looks" locally like $\mathbb{R}^n$ [6]. With the definition of manifold, we now describe the *synchronization manifold* [76, 77].

Definition 4.0.3. (Josic, 3054) and (Sun, Bollt, & Nishikawa, 204) *Let* $\dot{\boldsymbol{u}} = \mathbf{f}(\mathbf{u}, \mathbf{p})$ *and* $\dot{\boldsymbol{v}} = \mathbf{g}(\mathbf{u}, \mathbf{v}, \mathbf{p})$ *be two systems with* $\boldsymbol{u} = [u_1, u_2, ..., u_n]^T$ *and* $\boldsymbol{v} = [v_1, v_2, ..., v_n]^T$. *The* synchronization manifold *is the set* $\{((u_1, u_2, ..., u_n), (v_1, v_2, ..., v_n)) | \boldsymbol{u} = \Phi(\boldsymbol{v})\}$.

Stating the manifold in terms of identical synchronization, we alter the Definition 4.0.3 such that the synchronization manifold is the set $\{(u_1, u_2, ..., u_n), (v_1, v_2, ..., v_n) | ((u_1, u_2, ..., u_n) = (v_1, v_2, ..., v_n)\}$ and Φ is the identity function.

Stating the synchronization problem in the ODE setting, we require a drive system

$$\dot{\mathbf{u}} = \mathbf{f}(\mathbf{u}, \mathbf{p}), \tag{4.2}$$

from which we are able to sample data with parameters $\mathbf{p} \in \mathbf{R^m}$. Then we must state a response system

$$\dot{\mathbf{v}} = \mathbf{g}(\mathbf{u}, \mathbf{v}, \mathbf{q}) \tag{4.3}$$

with the same model form as the drive system. By *same* we mean in as far as possible by our understanding of the underlying physics. Then the goal is that when $\mathbf{u}$, Eq 4.2, is coupled forward into $\mathbf{v}$, Eq 4.3, then Eq 4.3 will synchronize with Eq 4.2 and $\mathbf{v} \to \mathbf{u}$ as $t \to \infty$ [44].

The coupling between the systems shown in Eq 4.2 and Eq 4.3 is called *unidirectional coupling*, as opposed to *bidirectional coupling*, wherein $\mathbf{v}$ would be fed into $\mathbf{f}$ [7].

There are two ways to unidirectionally couple two systems, via *complete replacement* coupling and *diffusive coupling*. In complete replacement coupling, the model

states from the drive system are directly fed into, and hence completely replace, the corresponding model states from the response system [7]. The response system is updated along with the drive system while states from the drive are fed into the response. Diffusive coupling includes an extra term added to the response system accounting for the error between the drive and response [7]. The diffusive term, under appropriate conditions, forces the response system toward the drive system based on model misfit [7]. Often, either one or the other is used in experimental work [7, 48–50, 52, 55, 57, 73], but we have found that combining the two methods of unidirectional coupling produces synchronization which was not observed when using either method alone [78].

Synchronization was extended from systems of ODEs to one-dimensional systems of PDEs in [55] and two-dimensional systems in [52], where the authors considered the Grey-Scott and Barkely reaction-diffusion systems respectively. In these works, the authors observed synchronization of an infinite-dimensional system by coupling the drive and response systems at only a finite number of grid points. To state formally, we define synchronization between two systems of PDEs in a way similar to [79].

Definition 4.0.4. *Let* $\mathbf{u_t}(x, y, t) = \mathbf{f}(\mathbf{u}(x, y, t), \mathbf{p})$ *and* $\mathbf{v_t}(x, y, t) = \mathbf{g}(\mathbf{u}(x, y, t), \mathbf{v}(x, y, t), \mathbf{p})$ *be two systems of partial differential equations wherein sates of* $\boldsymbol{u}(x, y, t)$ *are coupled with, or fed into,* $\boldsymbol{v}_t(x, y, t)$*. Let* $\boldsymbol{p} \in \mathbb{R}^n$ *be the parameter vector for the systems. The PDE systems* $\boldsymbol{u}_t(x, y, t)$ *and* $\boldsymbol{v}_t(x, y, t)$ *are said to* synchronize identically *if*

$$\|\boldsymbol{u}(x, y, t) - \boldsymbol{v}(x, y, t)\|_{L_2} \to 0 \ as \ t \to \infty. \tag{4.4}$$

The synchronization manifold for identical synchronization between two PDEs is extended from the ODE definition in a similar way.

Thus, we investigate observed data from the PDE drive system

$$\mathbf{u_t}(x, y, t) = \mathbf{f}(\mathbf{u}(x, y, t), \mathbf{p}) \tag{4.5}$$

with parameters $\mathbf{p} \in \mathbb{R}^n$ and a response system

$$\mathbf{v_t}(x, y, t) = \mathbf{g}(\mathbf{u}(x, y, t), \mathbf{v}(x, y, t), \mathbf{p}). \tag{4.6}$$

with the goal that $\mathbf{v}(x, y, t) \to \mathbf{u}(x, y, t)$ as $t \to \infty$.

4.1 Sampling Both Species

Our methods are validated on the benchmark model from Chapter 4. We restate the model here,

$$
\begin{aligned}
\frac{\partial P}{\partial t} &= \triangle P + P(1 - P) - \frac{PZ}{P + h}, \\
\frac{\partial Z}{\partial t} &= \triangle Z + k\frac{PZ}{P + h} - mZ,
\end{aligned}
\tag{4.7}
$$

solved on a compact connected two-dimensional domain, $\Omega = [300, 900]$, with zero-flux boundary conditions. Model parameters chosen result in spiral patterns on spatial scales consistent with observations from satellite data, subsequently exhibiting spiral break-up into complex spatiotemporal behavior [15].

We are only able to observe time series data Eq 4.5 as a movie and the model form of Eq 4.7 is known. We begin by demonstrating the capability of the systems to synchronize. We next assume known model form and wish to estimate the parameters used to create the observed data while the systems synchronize. The system in Eq 4.7 will be taken as the drive system and we form a response system to be synchronized to the observations.

4.1.1 Synchronization

We begin by stating a response model with diffusive coupling for both components in the system,

$$\frac{\partial \hat{P}}{\partial t} = \triangle \hat{P} + \hat{P}(1 - \hat{P}) - \frac{\hat{P}\hat{Z}}{\hat{P} + h} + \kappa(P - \hat{P}), \qquad (4.8)$$

$$\frac{\partial \hat{Z}}{\partial t} = \triangle \hat{Z} + \hat{k}\frac{\hat{P}\hat{Z}}{\hat{P} + h} - \hat{m}\hat{Z} + \kappa(Z - \hat{Z}),$$

where we assume $\hat{P}(x, y, 0) \neq P(x, y, 0)$ and that $\hat{Z}(x, y, 0) \neq Z(x, y, 0)$. To derive Eq (4.8), a diffusive coupling term is added to each equation in Eq (4.7) accounting for the error between the drive and response values with a coupling strength, κ. These additional terms drive $\hat{P} \to P$ and $\hat{Z} \to Z$, so that the PDEs will synchronize after a short time. We have found that synchronization is of identical type and dependent upon the choice of κ, as is the synchronization rate of convergence.

Importantly, for all results shown in this work, we enforce that

$$\hat{P} = \begin{cases} \hat{P} & : \quad 0 < \hat{P} < 2 \\ 0 & : \quad \hat{P} \leq 0 \\ 2 & : \quad \hat{P} \geq 2 \end{cases} \quad \text{and} \quad \hat{Z} = \begin{cases} \hat{Z} & : \quad 0 < \hat{Z} < 2 \\ 0 & : \quad \hat{Z} \leq 0 \\ 2 & : \quad \hat{Z} \geq 2 \end{cases}$$

to avoid values outside the normal range of Eq4.7 during the simulation. We evolve Eq 4.7 forward and count the output as observations which are then fed into Eq 4.8 With the response model stated, synchronization is observed between the two systems as their globally-averaged relative misfit shrinks quickly.

Time-instances from a simulation are shown in Figures 4.1a-4.1f with drive model state shown above response model state in each sub-figure. The response model initial conditions are set to $\hat{P}(x, y, t) = \hat{Z}(x, y, t) = 2$. The first column row, Figures 4.1a, 4.1c, and 4.1e, shows phytoplankton and the right column, Figures 4.1b, 4.1d, and 4.1f, shows zooplankton. Both columns show states at $t = 0$, $t = 0.4$, and $t = 3.6$

respectively. By $t = 3.6$, the model states are within an error of $e_P(t) < 1.0 \times 10^{-12}$, from Eq (4.9), and the synchronization manifold is evidently asymptotically stable.

Our simulations are carried out in the discretized spatiotemporal domain so to conveniently compare systems, we prefer matrix norms rather than to estimate function space norms. The globally-averaged relative synchronization errors in this work are calculated over time by the Frobenius norm,

$$e_P(t) = \frac{1}{|\Omega|} \frac{\|P - \hat{P}\|_F}{\|P\|_F}, \tag{4.9}$$

$$e_Z(t) = \frac{1}{|\Omega|} \frac{\|Z - \hat{Z}\|_F}{\|Z\|_F}.$$

where $\frac{1}{|\Omega|}$ denotes averaging by the Lebesgue measure [80] of the domain.

Furthermore, we choose coupling strength $\kappa = 5$ noting that coupling plays a role in the rate at which the systems synchronize, as is often observed with diffusive coupling [7].

In Figure 4.2, the errors in Eq (4.9) are calculated as the simulation is run and shown on a log scale. Here verification of the synchronization between model states is provided by the small value for both $e_P(t)$ and $e_Z(t)$ by the end of the simulation.
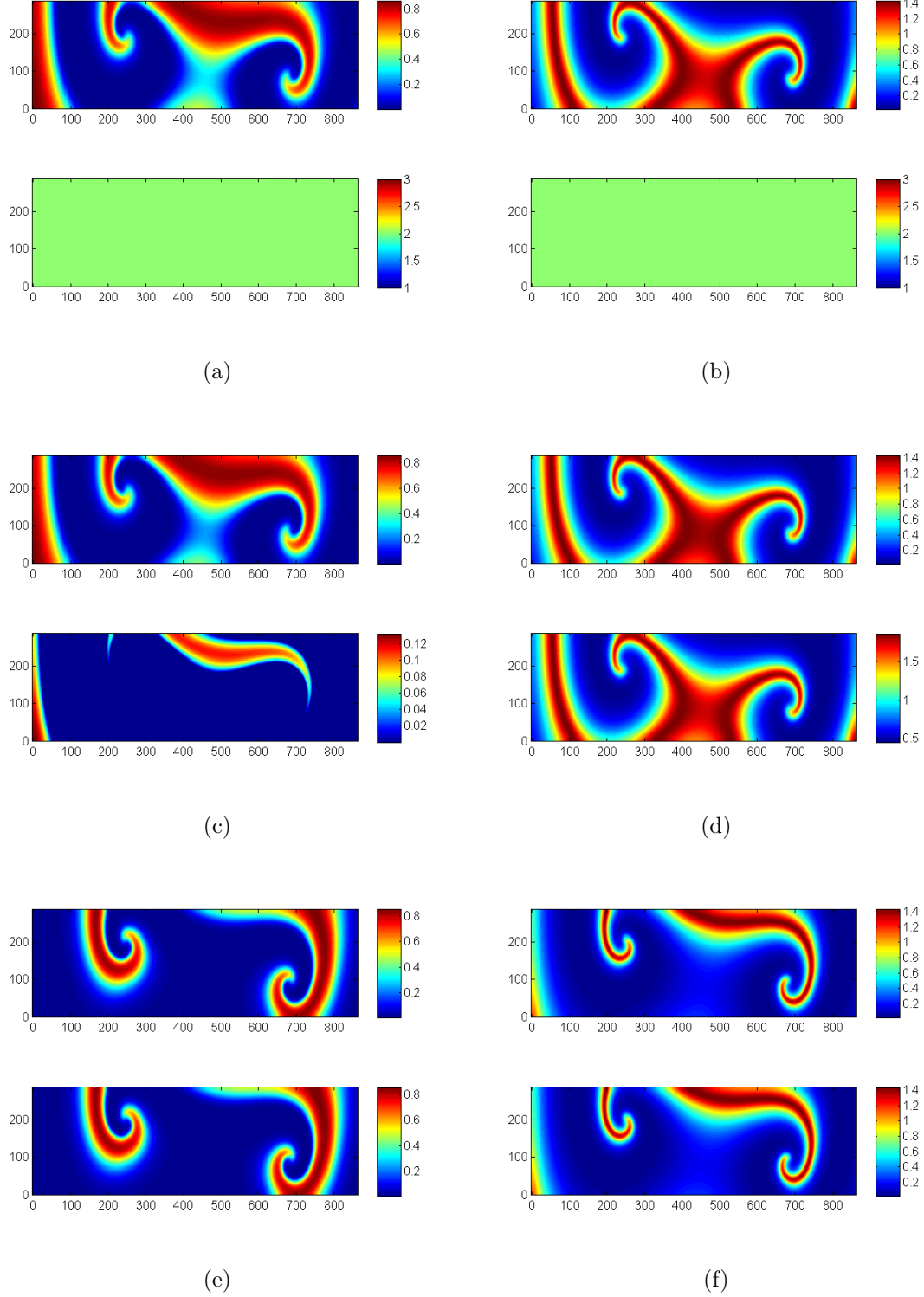
Figure 4.1: A comparison of model states at different times as systems are evolved with response given by Eq 4.8. Each sub-figure shows actual model state (drive system component) on top with response model state on bottom. The left column shows phytoplankton at $t = 0$ for 4.1a, $t = 0.4$ for 4.1c, and $t = 3.6$ for 4.1e. The times are same for zooplankton in the right column.
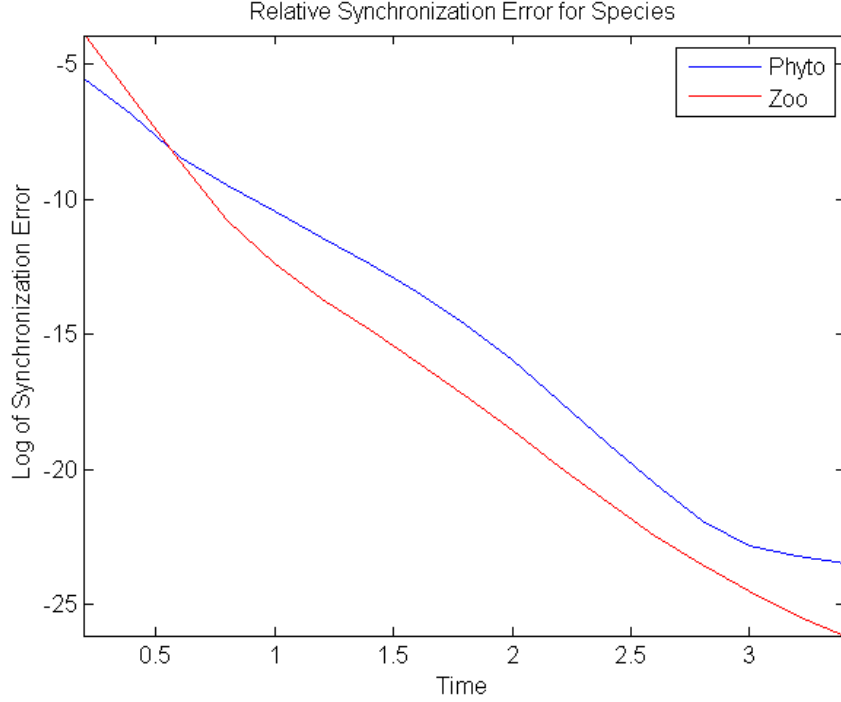
Figure 4.2: Relative error between drive and response system components, with errors calculated by Eq (4.9), plotted on a log scale. Relative error for both species has dropped to less than 1.0×10^{-12} by $t = 3.6$.

Since this system is shown to exhibit spatiotemporal chaos [15], this is a surprising, but not necessarily novel result [52]. However, We now consider the problem of model fitting for forecasting. To do so requires accurate parameter estimates as well as model states for forward prediction. We extend a parameter estimation method [44] within the synchronization framework.

4.1.2 Autosynchronization

To synchronize model states along with model parameters, a technique named autosynchronization was introduced in [44], wherein parameters are dynamically updated by drive-response disagreement. If coupled properly, the drive and response parameters will synchronize while the system states synchronize, thus the term *autosynchronization* [44].

We exploit this special feature of synchronization toward parameter estimation for PDEs. This work, [78], is a first demonstration of parameter estimation by autosynchronization on a system of PDEs. We begin with a formal definition of autosynchronization on PDEs.

Definition 4.1.1. *Let $\boldsymbol{u}_t(x, y, t) = \mathbf{f}(u(x, y, t), \mathbf{p})$ and $\boldsymbol{v}_t(x, y, t) = \mathbf{g}(\mathbf{u}(x, y, t), \mathbf{v}(x, y, t), q)$ be two systems of ordinary differential equations wherein sates of $\boldsymbol{u}(x, y, t)$ are coupled with, or fed into, $\boldsymbol{v}_t(x, y, t)$. Let $\boldsymbol{p}, \boldsymbol{q} \in \mathbb{R}^n$ be parameter vectors for $\boldsymbol{u}_t$ and $\boldsymbol{v}_t$ respectively. The systems $\boldsymbol{u}_t$ and $\boldsymbol{v}_t$ are said to* autosynchronize *if*

$$\|\boldsymbol{u}(x, y, t) - \boldsymbol{v}(x, y, t)\|_{L_2} \to 0 \ and \ \|\boldsymbol{p} - \boldsymbol{q}\| \to 0 \ as \ t \to \infty. \tag{4.10}$$

Here, we choose the Euclidean vector norm to compare the parameters and the L_2-norm to compare model states.

Stating an autosynchronization problem in the PDE setting [78], we require a drive system

$$\mathbf{u}_t(x, y, t) = \mathbf{f}(\mathbf{u}(x, y, t), \mathbf{p}), \tag{4.11}$$

from which we are able to sample data with (unknown to us) parameters $\mathbf{p} \in \mathbb{R}^n$. Then we must state a response system

$$\mathbf{v}_t(x, y, t) = \mathbf{g}(\mathbf{u}(x, y, t), \mathbf{v}(x, y, t), \mathbf{q}) \tag{4.12}$$

with the same model form as the drive system if $\mathbf{q} = \mathbf{p}$. Again, the goal is that when $\mathbf{u}(x, y, t)$ is coupled forward into Eq 4.12, then Eq 4.12 will synchronize with Eq 4.11 and $\mathbf{u}(x, y, t) \to \mathbf{v}(x, y, t)$. Concurrently, parameter ODEs are given by

$$\mathbf{q}_t = \mathbf{h}(\mathbf{u}(x, y, t), \mathbf{v}(x, y, t), \mathbf{q}) \tag{4.13}$$

so that $(\mathbf{v}, \mathbf{q}) \to (\mathbf{u}, \mathbf{p})$ as $t \to \infty$. The schematic diagram for this type of simulation
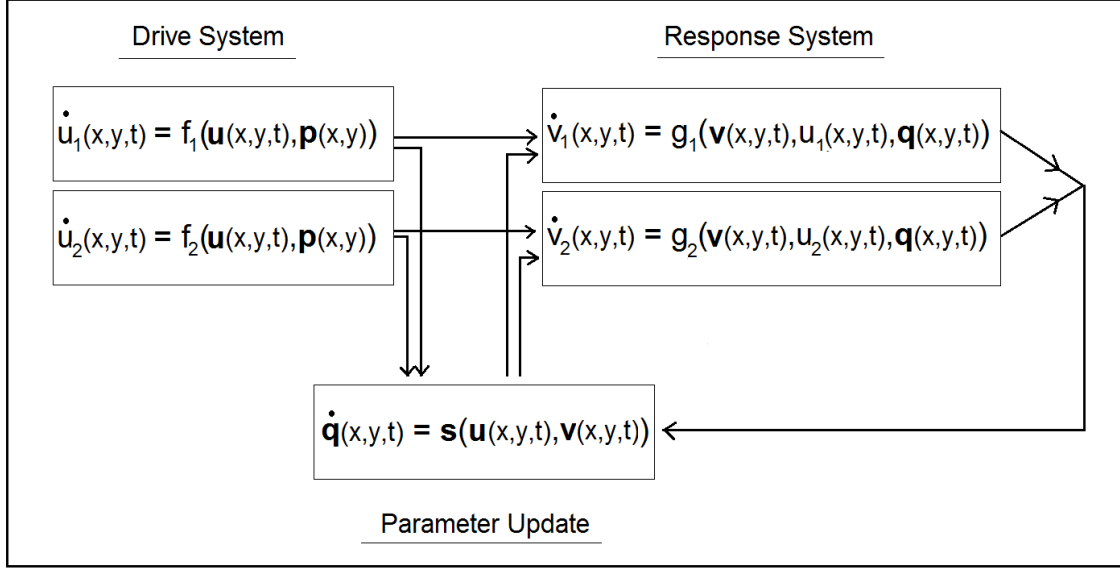
Figure 4.3: Diagram for autosynchronization of two-component PDE system such as described by Eqs (4.7) and (4.14).

is shown in Figure 4.3.

We state the response model with parameter equations,

$$\frac{\partial \hat{P}}{\partial t} = \triangle \hat{P} + \hat{P}(1 - \hat{P}) - \frac{\hat{P}\hat{Z}}{\hat{P} + h} + \kappa(P - \hat{P}), \tag{4.14}$$

$$\frac{\partial \hat{Z}}{\partial t} = \triangle \hat{Z} + \hat{k}\frac{\hat{P}\hat{Z}}{\hat{P} + h} - \hat{m}\hat{Z} + \kappa(Z - \hat{Z}),$$

$$\frac{d\hat{k}}{dt} = -s\frac{1}{|\Omega|}\int_\Omega (P - \hat{P})d\Omega,$$

$$\frac{d\hat{m}}{dt} = -s\frac{1}{|\Omega|}\int_\Omega (Z - \hat{Z})d\Omega,$$

where $\frac{1}{|\Omega|}$ denotes averaging by the Lebesgue measure [80] of the domain and we

assume

$$\hat{P}(x, y, 0) \neq P(x, y, 0),$$

$$\hat{Z}(x, y, 0) \neq Z(x, y, 0),$$

$$\hat{k}(0) \neq k,$$

$$\hat{m}(0) \neq m,$$

$$s > 0.$$

In Eq (4.14), the globally-averaged error between species is added to determine how the parameters are updated in time. The ansatz system Eq (4.14) was chosen after testing multiple forms. The goal is to estimate the model parameters k and m by allowing $\hat{k}$ and $\hat{m}$ to vary in time such that they are driven to the identical synchronization manifold [77]

$$M = \{(P, Z, k, m), (\hat{P}, \hat{Z}, \hat{k}, \hat{m}) \mid P = \hat{P}, Z = \hat{Z}, k = \hat{k}, m = \hat{m}\} \qquad (4.15)$$

The parameter equations are evolved simultaneously with $\hat{P}$ and $\hat{Z}$ with a forward-Euler discretization and the same time step. The model form of Eq 4.14 was chosen after testing several forms and we have found that there exist other forms for which synchronization is possible. Once the model form was chosen, a parameter search was performed to find $s = 30$ and $\kappa = 1.25$. As we vary s and κ, the synchronization manifold may lose stability, a common situation with diffusively coupled systems [7]. Parameters may be updated as reaction-diffusion PDEs, by adding a diffusion term, however we then must restrict parameters to be nonnegative $C^2(\Omega)$ functions and numerical stability may be adversely affected.

To begin the simulation, response system initial conditions were arbitrarily set to

$$
\begin{aligned}
\hat{P}(x, y, 0) &= 2, & \text{(4.16)} \\
\hat{Z}(x, y, 0) &= 2, \\
\hat{k}(0) &= 5, \\
\hat{m}(0) &= 5.
\end{aligned}
$$

Eq 4.7 is evolved forward and the model output serves as observed data. Results are shown in Figures 4.4a - 4.4f. The parameter equations force the parameters to synchronize and parameters are estimated to $e_P(t) < 1.0 \times 10^{-12}$.
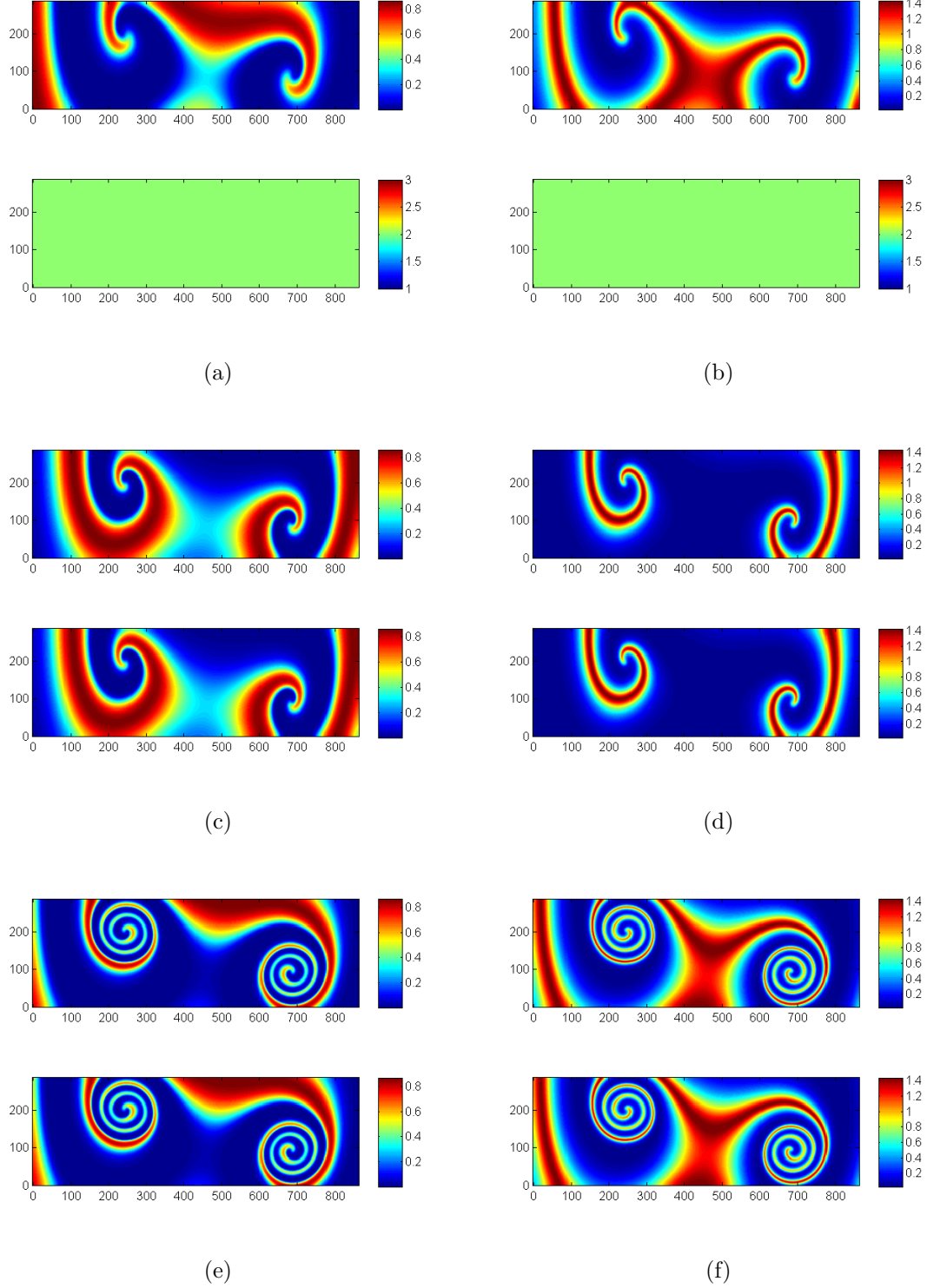
Figure 4.4: A comparison of model states at different times as systems are evolved with response given by Eq (4.14). Each sub-figure shows actual model state (drive system component) on top with response model state on bottom. The left column shows phytoplankton at $t = 0$ in 4.4a, $t = 10$ in 4.4c, and $t = 118$ in 4.4e. The times are the same for zooplankton, shown in right column.
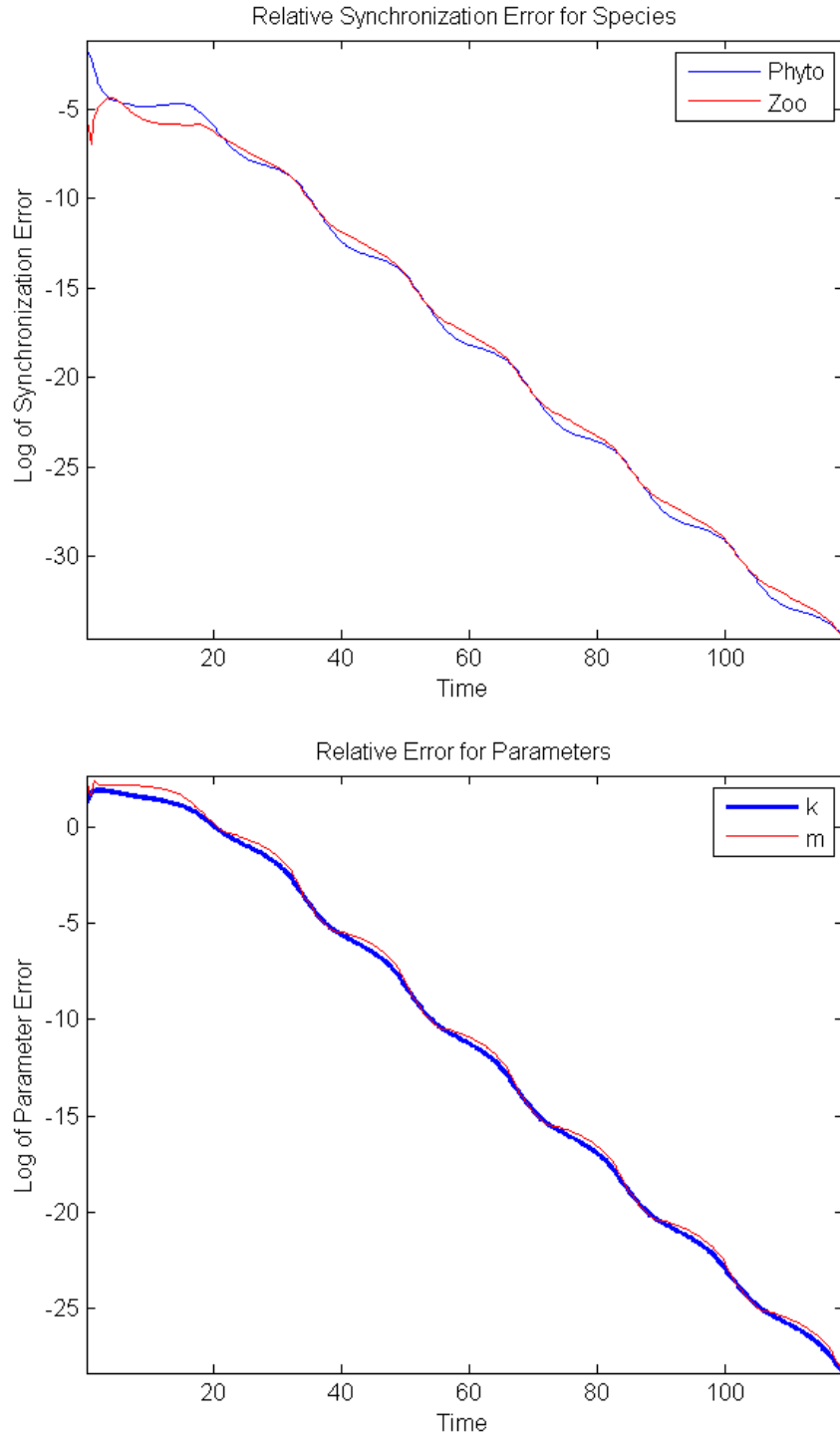
Figure 4.5: Relative error between drive and response system components, with errors given on a log scale. Relative error for both species drops to within nearly 1.0×10^{-15} by $t = 118$. Relative error for parameters drops to less than 1.0×10^{-12}. For these results, $\kappa = 1.25$ and $s = 30$.

Figure 4.5 indicates the globally-averaged relative synchronization errors, Eq (4.9), between species as a function of time on a log scale. The relative parameter errors are shown beneath as a function of time on a log scale. The plots demonstrate that the relative error between both species drops to less than 1.0×10^{-15}. Also, the relative error between both parameters drops to less than 1.0×10^{-12}.

4.1.3   Spatially Dependent Parameters

In many systems, it is very reasonable to expect that model parameters need not be spatially homogeneous. For example, taking our problem of interest, spatial inhomogeneity in parameter values may be an important theoretical assumption when constructing models for coastal algal blooms, since plankton growthrate is affected by near-shore nutrient runoff and upwelling [15, 81, 82]. More to that point, ocean fronts and eddies cause flow-induced long-term inhomogeneities in the ocean which results in a formidable spatial structure for density profiles in the ocean [15]. Whether inhomogeneities be the result of the flow dynamics or of boundary conditions from nutrient runoff, they are an important consideration for modelling ecology over large coastal domains. Thus it is reasonable to expect that a biophysics-based model over the mesoscale should accept spatially dependent parameters.

Many methods have been proposed to estimate scalar parameters as mentioned in Chapter 1. A drawback to Kalman filtering and multiple shooting methods, is that they do not consider spatially dependent parameter values, a priority noted in [38]. Parameter estimation by filtering methods adapted for PDEs can be computationally expensive [42]. Furthermore, we have found that some filtering methods suffer during periods of exponential growth, such as might be expected during plankton blooms. Optimizing the time-averaged synchronization error in some function space is far more complicated than the finite-dimensional alternative with scalar parameters as demonstrated in [52]; optimization methods may not be practical.

Our work aims to extend the method of parameter estimation for spatiotemporal PDE systems by autosynchronization, especially including autosynchronization with spatially dependent parameters. Formally, we investigate observed data from the PDE drive system

$$\mathbf{u_t}(x, y, t) = \mathbf{f}(\mathbf{u}(x, y, t), \mathbf{p}(x, y)) \tag{4.17}$$

with parameters $\mathbf{p}(x, y) \in C^0(\Omega)$, and a response system

$$\mathbf{v_t}(x, y, t) = \mathbf{g}(\mathbf{u}(x, y, t), \mathbf{v}(x, y, t), \mathbf{q}(x, y, t)). \tag{4.18}$$

We formulate an associated system of PDEs for the parameters of Eq (4.18)

$$\mathbf{q_t}(x, y, t) = \mathbf{h}(\mathbf{u}(x, y, t), \mathbf{v}(x, y, t)) \tag{4.19}$$

with the goal that $\|\mathbf{u}(x, y, t) - \mathbf{v}(x, y, t)\|_{L_2} \to 0$ and $\|\mathbf{p}(x, y) - \mathbf{q}(x, y, t)\|_{L_2} \to 0$ as $t \to \infty$.

We modify the system Eq (4.7) as found in [15] by allowing the parameters to be non-negative $C^0(\Omega)$ functions. Here Ω is the domain, which in the case of our simulations, $\Omega \subset \mathbf{R}^2$ is a compact domain such as a rectangle or even a domain shaped as the Gulf of Mexico, in some examples here.

First, we develop synthetic datasets with spatially varying parameters to challenge our methods. Spatially dependent parameters are chosen to be in the range given in [15] for spatially irregular behavior. Three different functional forms for the parameters are tested for variety. First, we define a Gaussian parameter function,

$$
\begin{aligned}
k_1(x, y) &= a e^{-\left(\frac{(x-n/2)^2}{2\sigma^2} + \frac{(y-m/2)^2}{2\sigma^2}\right)}, \\
m_1(x, y) &= c e^{-\left(\frac{(x-n/2)^2}{2\sigma^2} + \frac{(y-m/2)^2}{2\sigma^2}\right)},
\end{aligned}
\tag{4.20}
$$

where $a = 2, c = 0.6, m = 300, n = 900$, and $\sigma = 400$. Appropriate parameters are chosen to maintain $m(x, y)$ and $k(x, y)$ in the target range. For example, Eq (4.20) is displayed in Figure 4.6a and Figure 4.6b respectively. Next, we define,

$$
\begin{aligned}
k_2(x, y) &= a \ \cos(bx + d)\sin(by) + s, & (4.21) \\
m_2(x, y) &= c \ \cos(bx + d)\sin(by) + t,
\end{aligned}
$$

where $a = 0.2, b = \pi/(m/2), c = 0.6, d = \pi/2, s = 0.5$, and $t = 1.5$, to test the quality of the autosynchronization method to resolve fine spatial structures in model parameters. The surfaces produced by Eq (4.21) are displayed in Figure 4.6c and in Figure 4.6d respectively.

Finally, we build a swirly parameter function in order to simulate spiral-like behavior in parameter values as might be expected in turbulent near-coastal regions. Thus time instance is taken from a simulation of the original PDE, Eq (4.7), is scaled appropriately, and is treated as a parameter function. These spiral parameters, $k_3(x, y)$ and $m_3(x, y)$, are shown in Figure 4.6e and Figure 4.6f respectively.
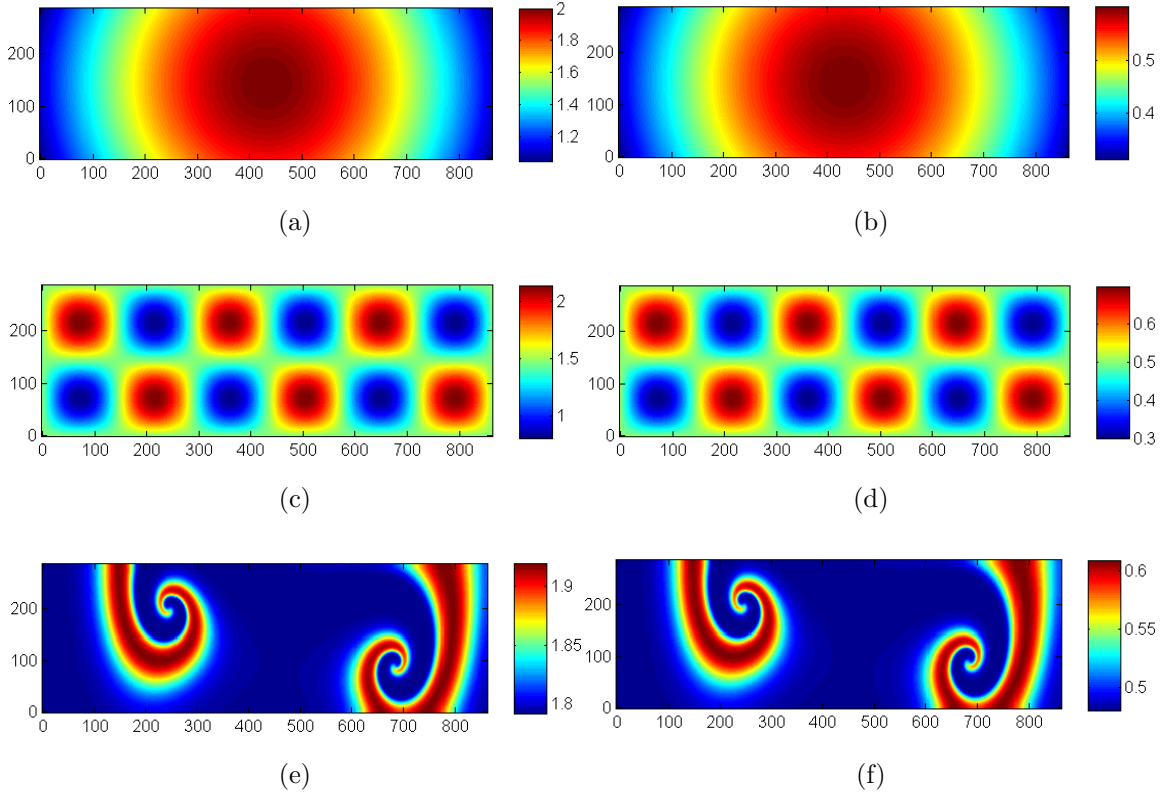
Figure 4.6: The three different sets of spatially dependent parameters used in simulations. Figures 4.6a and 4.6b are described by Eq (4.20), with $k(x, y)$ on the left and $m(x, y)$ on the right. Below, with the same ordering, are the parameters described by Eq (4.21). Finally, the swirly parameters are shown in Figures 4.6e and 4.6f.

We state the response model with parameter equations, now themselves PDEs, as

$$\frac{\partial \hat{P}}{\partial t} = \triangle \hat{P} + \hat{P}(1 - \hat{P}) - \frac{\hat{P}\hat{Z}}{\hat{P} + h} + \kappa(P - \hat{P}), \qquad (4.22)$$

$$\frac{\partial \hat{Z}}{\partial t} = \triangle \hat{Z} + \hat{k}\frac{\hat{P}\hat{Z}}{\hat{P} + h} - \hat{m}\hat{Z} + \kappa(Z - \hat{Z}),$$

$$\frac{\partial \hat{k}}{\partial t} = -s(P - \hat{P}),$$

$$\frac{\partial \hat{m}}{\partial t} = -s(Z - \hat{Z}),$$

where we assume,

$$\hat{P}(x, y, 0) \neq P(x, y, 0),$$

$$\hat{Z}(x, y, 0) \neq Z(x, y, 0),$$

$$\hat{k}(x, y, 0) \neq k(x, y),$$

$$\hat{m}(x, y, 0) \neq m(x, y),$$

$$s > 0.$$

To begin the simulation, response system initial conditions are set to the extension of Eq (4.16)

$$
\begin{aligned}
\hat{P}(x, y, 0) &= 2, \\
\hat{Z}(x, y, 0) &= 2, \\
\hat{k}(x, y, 0) &= 5, \\
\hat{m}(x, y, 0) &= 5.
\end{aligned}
\tag{4.23}
$$

We observe solution data at every time step relative to the response system, Eq 4.22 to drive $(\hat{P}, \hat{Z}) \to (P, Z)$ and $(\hat{m}(x, y), \hat{k}(x, y)) \to (m(x, y), k(x, y))$ as $t \to \infty$. The parameters defined by Eq 4.20, Eq 4.21, and the spiral parameters are estimated and compared with ground truth. We observe autosynchronization for each test set of parameters and the spatial inhomogeneities in each test set are effectively resolved; the Gaussian test parameters are estimated in Figure 4.8 while the species are shown in Figure 4.7. This is a first demonstration of the utility of autosynchronization for parameter estimation of spatially dependant parameters and thus allows for parameter estimation over function spaces.

Figures 4.7 and 4.8 display time instances of the simulation of Eq (4.22), as the response, and Eq (4.8), as the drive, with spatially dependent model parameters ren-
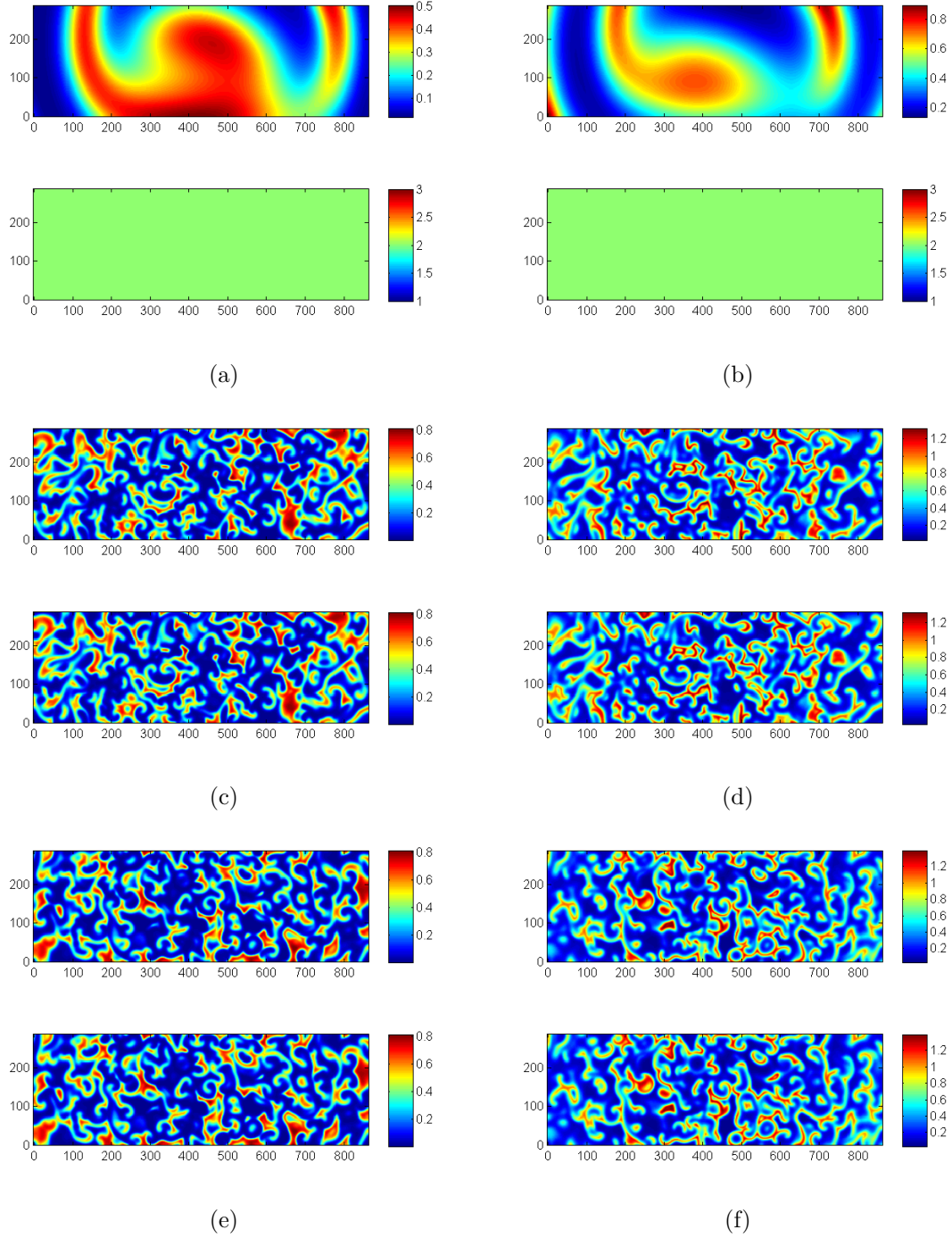
Figure 4.7: Autosynchronization of species in response system in Eq(4.22). Each figure shows drive (top) and response (bottom) pairs. $P(x, y, 0)$ and $\hat{P}(x, y, 0)$ in 4.7a, $P(x, y, 1000)$ and $\hat{P}(x, y, 1000)$ in 4.7c, and $P(x, y, 4788)$ and $\hat{P}(x, y, 4788)$ in 4.7e. $Z(x, y, 0)$ and $\hat{Z}(x, y, 0)$ in 4.7b, $Z(x, y, 1000)$ and $\hat{Z}(x, y, 1000)$ in 4.7d, and $Z(x, y, 4788)$ and $\hat{Z}(x, y, 4788)$ in 4.7f.

(a)

(b)

(c)

(d)

(e)

(f)
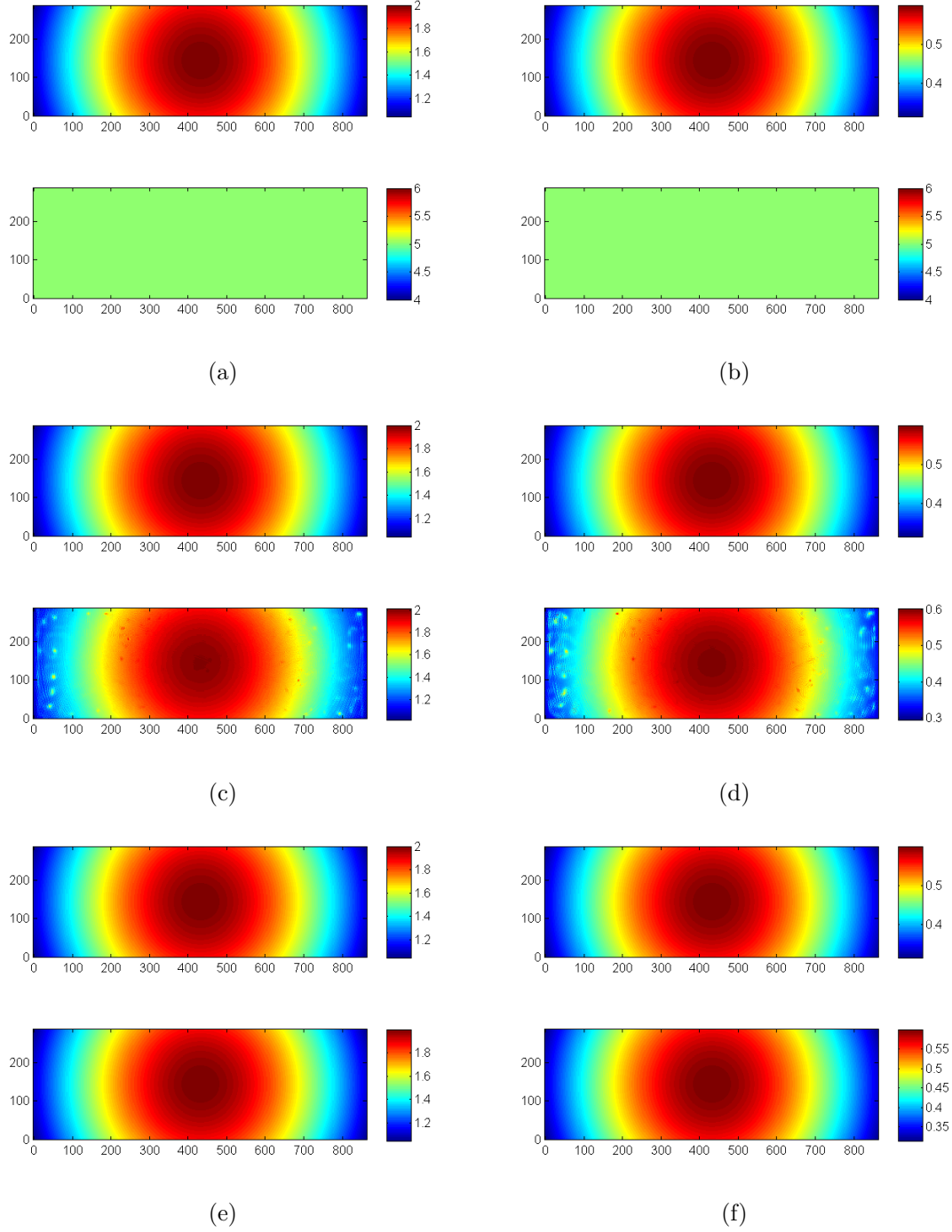
Figure 4.8: Autosynchronization of response parameters in Eq(4.22). Each figure shows drive (top) and response (bottom) pairs. $k(x, y)$ and $\hat{k}(x, y, 0)$ in 4.8a, $k(x, y)$ and $\hat{k}(x, y, 1000)$ in 4.8c, and $k(x, y)$ and $\hat{k}(x, y, 4788)$ in 4.8e. $m(x, y)$ and $\hat{m}(x, y, 0)$ in 4.8b, $m(x, y)$ and $\hat{m}(x, y, 1000)$ in 4.8d, and $m(x, y)$ and $\hat{m}(x, y, 4788)$ in 4.8f.

dered by Eq (4.20). Figure 4.7a shows the initial conditions, $P(x, y, 0)$ over $\hat{P}(x, y, 0)$, Figure 4.7c represents $P(x, y, 1000)$ over $\hat{P}(x, y, 1000)$, and Figure 4.7e represents $P(x, y, 4788)$ compared to $\hat{P}(x, y, 4788)$. Figure 4.7b shows the initial conditions, $Z(x, y, 0)$ over $\hat{Z}(x, y, 0)$, Figure 4.7d represents $Z(x, y, 1000)$ over $\hat{Z}(x, y, 1000)$, and Figure 4.7f represents $Z(x, y, 4788)$ compared to $\hat{Z}(x, y, 4788)$.

Likewise, Figure 4.8a shows the initial conditions, $k(x, y)$ over $\hat{k}(x, y, 0)$, Figure 4.8c represents $k(x, y)$ over $\hat{k}(x, y, 1000)$, and Figure 4.8e represents $k(x, y)$ compared to $\hat{k}(x, y, 4788)$. Figure 4.8b shows the initial conditions, $m(x, y)$ over $\hat{m}(x, y, 0)$, Figure 4.8d represents $m(x, y)$ over $\hat{m}(x, y, 1000)$, and Figure 4.8f represents $m(x, y)$ compared to $\hat{m}(x, y, 4788)$. Further results will be presented in the same way throughout the chapter.

The simulation is terminated once the relative error between the parameters k and $\hat{k}$ reach a threshold of $e_k(t) < 1.0 \times 10^{-5}$. The globally averaged relative errors are the extension of Eq (4.9),

$$e_P(t) = \frac{1}{|\Omega|} \frac{\|P - \hat{P}\|_F}{\|P\|_F}, \tag{4.24}$$

$$e_Z(t) = \frac{1}{|\Omega|} \frac{\|Z - \hat{Z}\|_F}{\|Z\|_F},$$

$$e_k(t) = \frac{1}{|\Omega|} \frac{\|k - \hat{k}\|_F}{\|k\|_F},$$

$$e_m(t) = \frac{1}{|\Omega|} \frac{\|m - \hat{m}\|_F}{\|m\|_F},$$

where $\frac{1}{|\Omega|}$ denotes averaging by the Lebesgue measure [80] of the domain.

In Figure 4.9, the globally-averaged relative error, Eq (4.24), between phytoplankton terms in the drive and response system is demonstrated to be driven to less than 3.0×10^{-9} and the error between the zooplankton profiles is driven below 2.0×10^{-8}. The globally-averaged relative error between both sets of true and estimated param-

Relative Synchronization Error for Species

(a)

Relative Error for Parameters

(b)
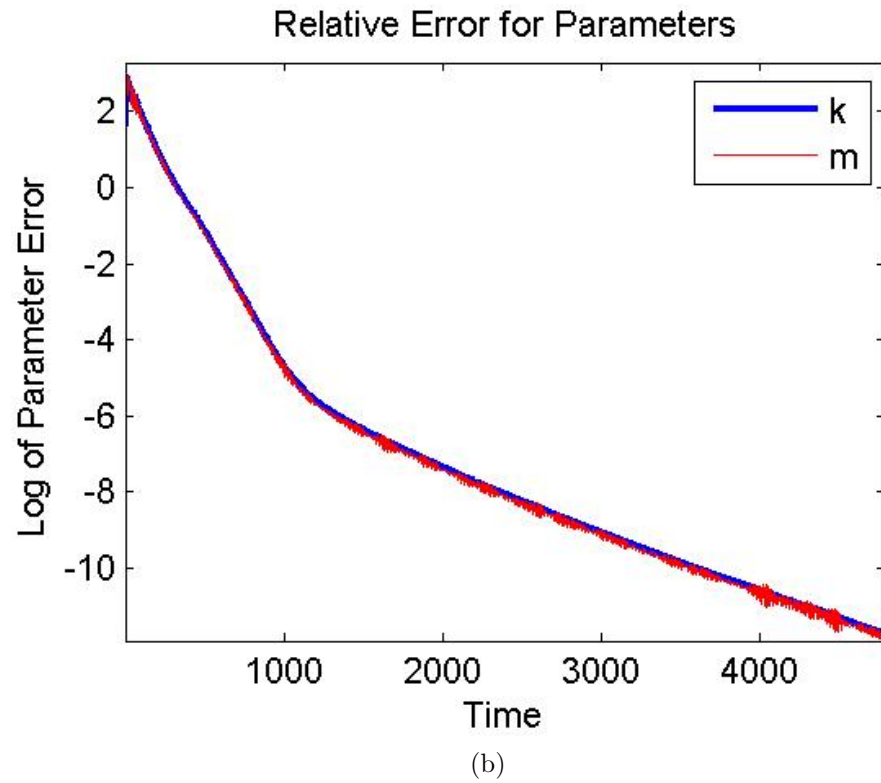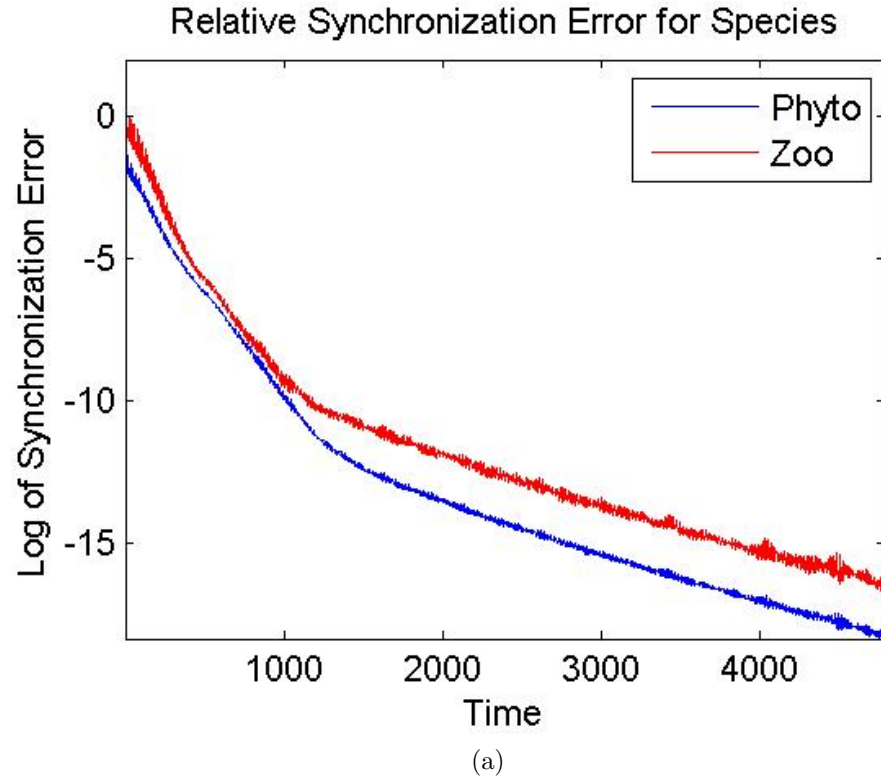
Figure 4.9: Globally-averaged relative synchronization error between drive and response PDE components and parameters on a log scale and with parameters built by Eq 4.20. These errors represent simulations shown in Figures 4.7a - 4.8f

.

eters is driven below 1.0×10^{-5}. The plots correspond to the simulation shown in Figures 4.7 and 4.8, respectively. Interestingly, the results show a change of synchronization rate midway through the simulation. For these results, we choose $\kappa = 2.4$ and $s = 30$.

Next, to really test the ability of the method to resolve fine structures in parameters, we show simulation results with parameters rendered by Eq (4.21). In, Figures 4.10 and 4.11, the results of autosynchronization follow the same pattern of Figures 4.7 and 4.8. Reconstructed parameters are compared with their true counterparts at three different times, $t = 0$, $t = 1000$, and $t = 10660$. This simulation highlights the spatial efficacy of parameter reconstruction. Similar results were found by testing parameters that vary spatially according to Figures 4.6e and 4.6f.

In Figure 4.12, we observe globally-averaged relative errors corresponding to the simulations shown in Figures 4.10 and 4.11. These results, although novel, are not practical for use in model fitting and forecasting with multi-component models informed by remote sensing. Thus, we require some advancements for use in our target application.

4.2 Synchronization by Sampling One Species

An important criticism of the stated autosynchronization method is that one requires samples of both species to drive the response model and parameters. As mentioned, our interest in autosynchronization for parameter estimation stems from work with ocean models for phytoplankton-zooplankton ecology. In fact, hyperspectral satellite imagery provides phytoplankton density inferences but provides no data for zooplankton [8]. In this case, parameter estimation using the response model Eq (4.22) will fail since we have no zooplankton observables with which to drive the response. Even assuming correct model parameters, it is impossible to forecast the model since zoo-
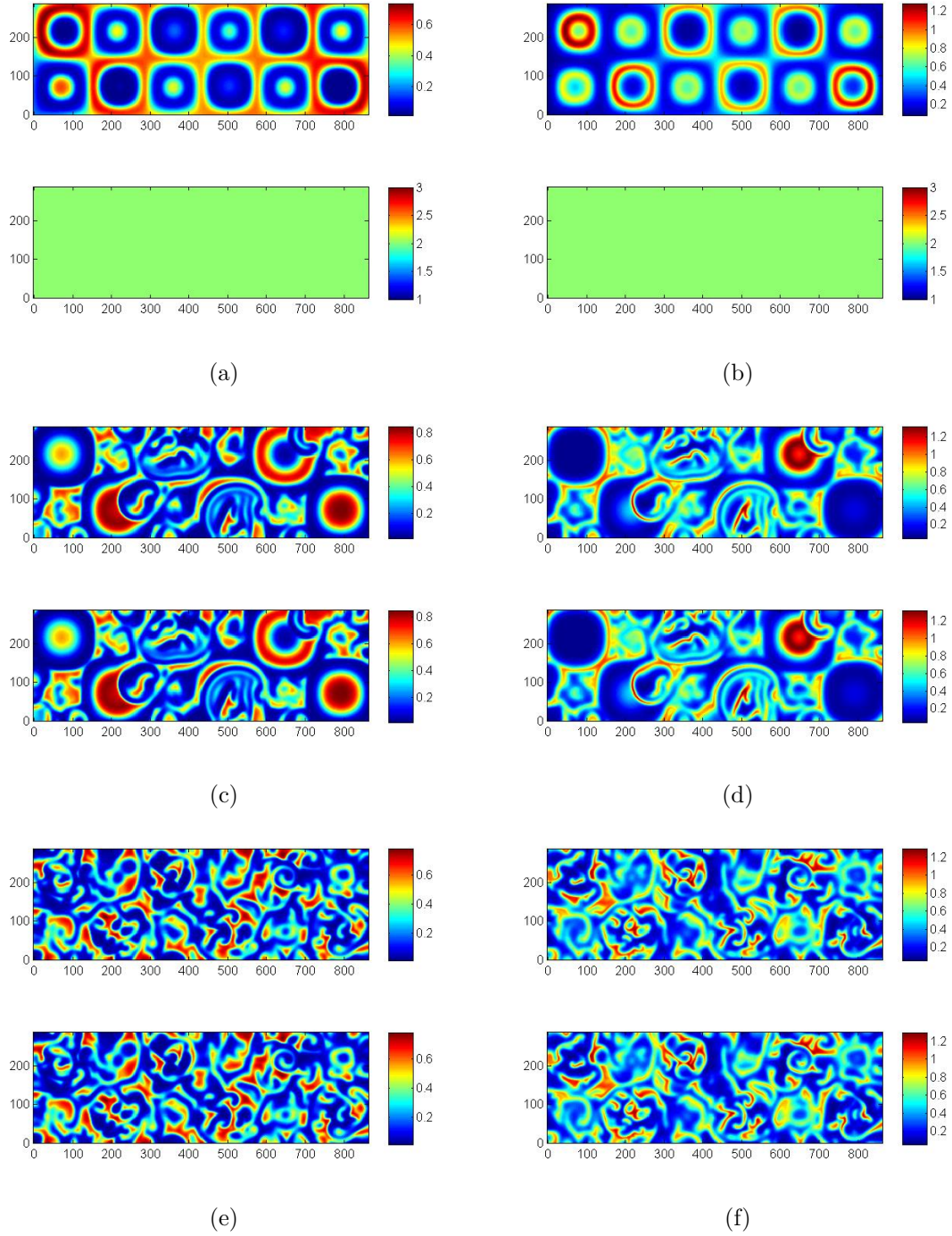
Figure 4.10: Autosynchronization of species in response system Eq(4.22). Each figure shows drive (top) and response (bottom) pairs. $P(x, y, 0)$ and $\hat{P}(x, y, 0)$ in 4.10a, $P(x, y, 1000)$ and $\hat{P}(x, y, 1000)$ in 4.10c, and $P(x, y, 10660)$ and $\hat{P}(x, y, 10660)$ in 4.10e. $Z(x, y, 0)$ and $\hat{Z}(x, y, 0)$ in 4.10b, $Z(x, y, 1000)$ and $\hat{Z}(x, y, 1000)$ in 4.10d, and $Z(x, y, 10660)$ and $\hat{Z}(x, y, 10660)$ in 4.10f.

Figure 4.11: Autosynchronization of response parameters in Eq (4.22). Each figure shows drive (top) and response (bottom) pairs. $k(x,y)$ and $\hat{k}(x,y,0)$ in 4.11a, $k(x,y)$ and $\hat{k}(x,y,1000)$ in 4.11c, and $k(x,y)$ and $\hat{k}(x,y,10660)$ in 4.11e. $m(x,y)$ and $\hat{m}(x,y,0)$ in 4.11b, $m(x,y)$ and $\hat{m}(x,y,1000)$ in 4.11d, and $m(x,y)$ and $\hat{m}(x,y,10660)$ in 4.11f.

79
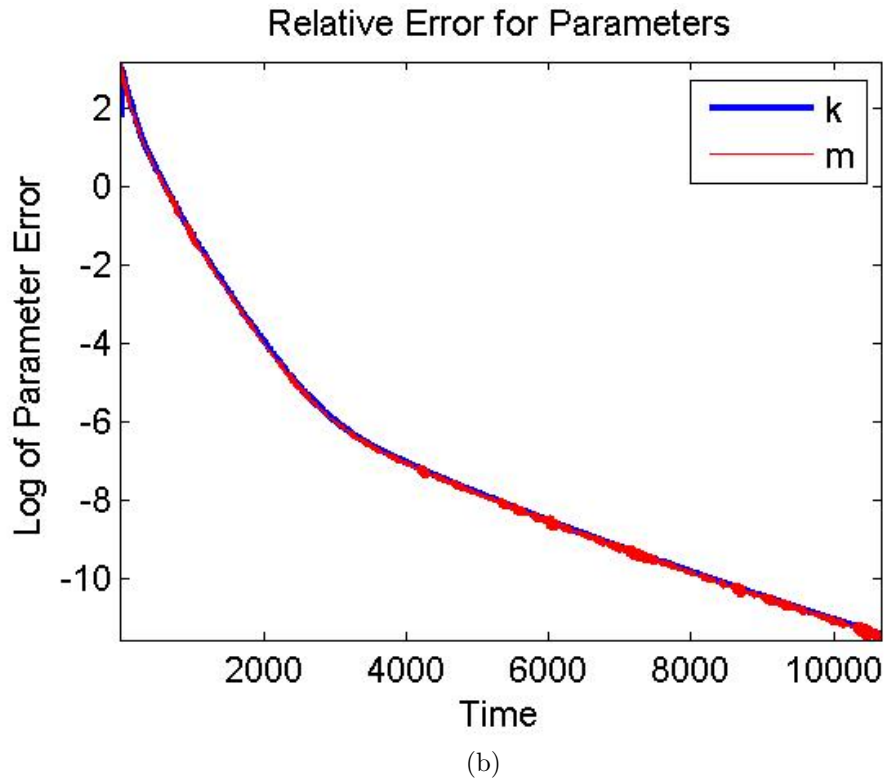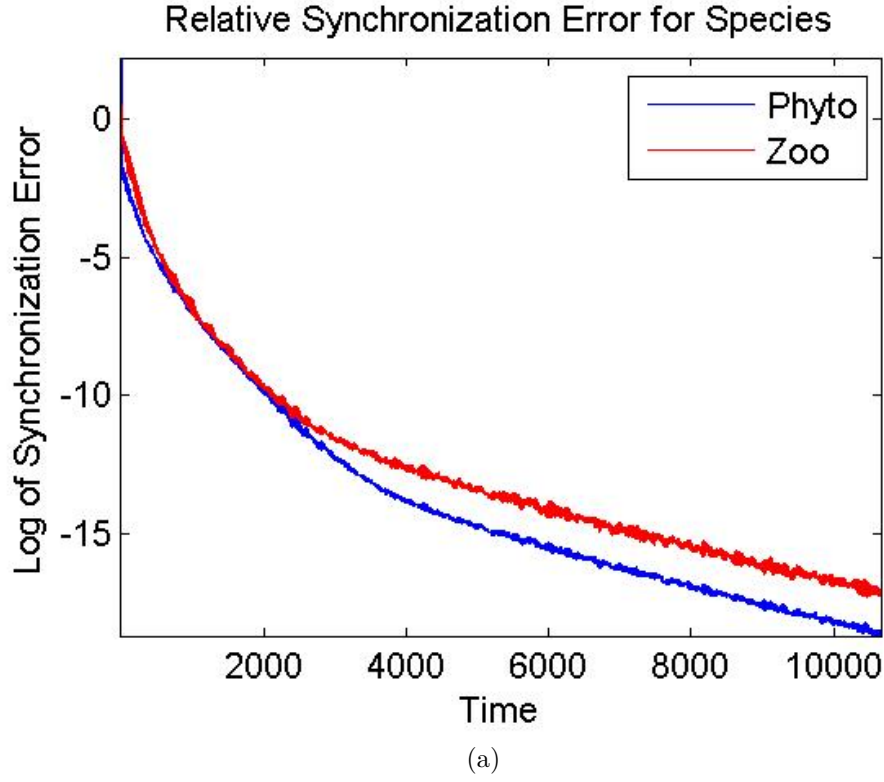
Figure 4.12: Globally-averaged relative synchronization error between drive and response PDE components and parameters on a log scale for parameters built by Eq (4.21). The errors represent simulations shown in Figures 4.10 and 4.11.

plankton initial conditions are not supplied. Our problem of interest requires that we somehow estimate zooplankton initial conditions based on phytoplankton observations.

4.2.1 Synchronization

We find that, by a modification of Eq (4.22), it is possible to drive zooplankton density to its true state by sampling phytoplankton alone. This is a first demonstration of the possibility of simulating this system with only partial knowledge.

We first state a response model using diffusive coupling and sampling only phytoplankton from the drive system. We state the response model,

$$
\begin{aligned}
\frac{\partial \hat{P}}{\partial t} &= \triangle \hat{P} + \hat{P}(1 - \hat{P}) - \frac{\hat{P}\hat{Z}}{\hat{P} + h} + \kappa(P - \hat{P}), \\
\frac{\partial \hat{Z}}{\partial t} &= \triangle \hat{Z} + k\frac{\hat{P}\hat{Z}}{\hat{P} + h} - m\hat{Z},
\end{aligned}
\tag{4.25}
$$

where the diffusive coupling term in the second component is removed. Note that zooplankton is not sampled anywhere in Eq (4.25). Results are shown in Figure 4.13, where simulation snapshots are shown at $t = 0$, $t = 10$, and $t = 227$. This demonstrates that it is possible to observe zooplankton density based on sampling only one species, an extremely useful result toward our target application.
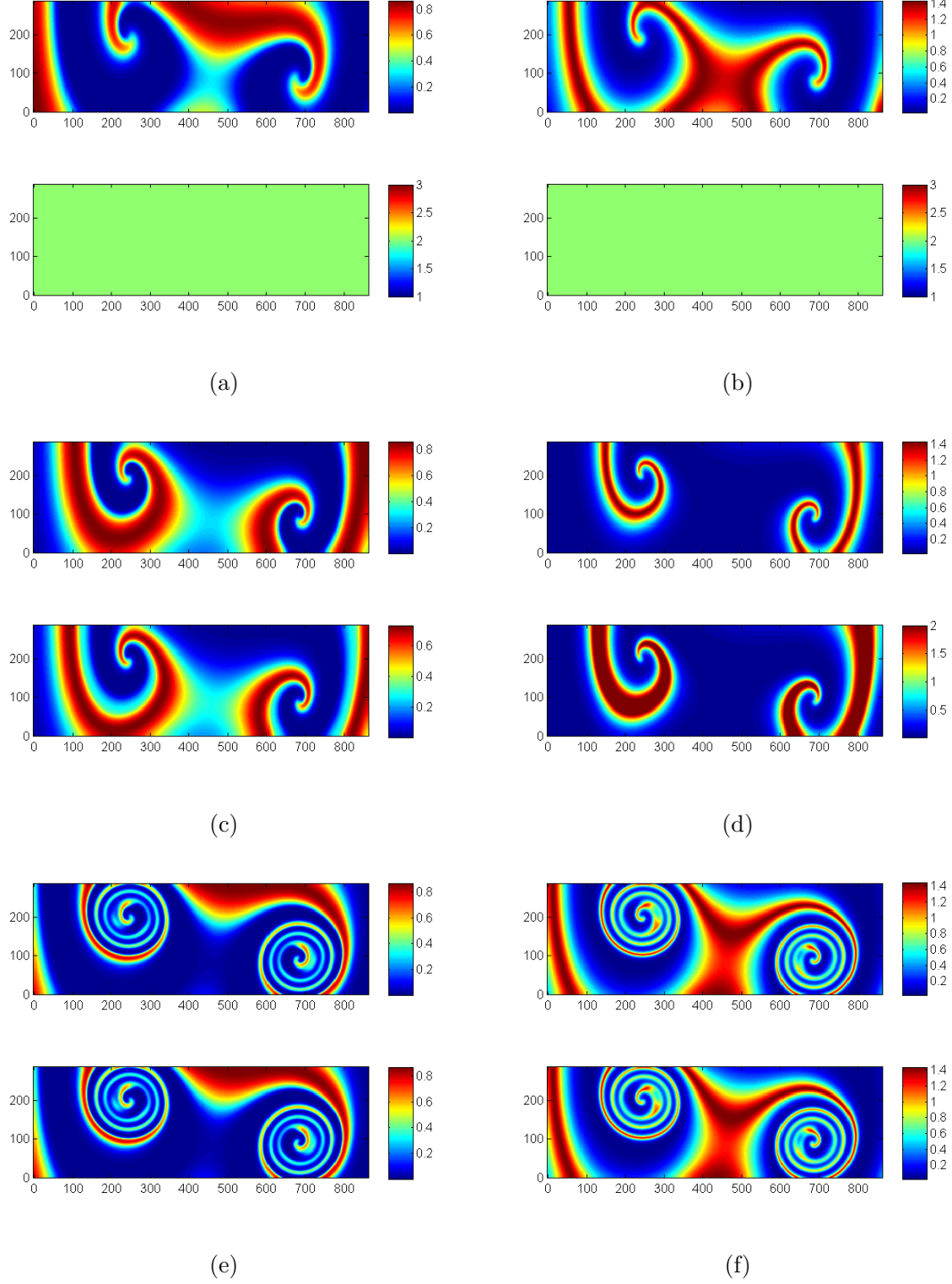
Figure 4.13: A comparison of model states at different times as systems are evolved with response given by Eq (4.25). Each figure shows drive (top) and response (bottom) pairs. $P(x, y, 0)$ and $\hat{P}(x, y, 0)$ in 4.13a, $P(x, y, 10)$ and $\hat{P}(x, y, 10)$ in 4.13c, and $P(x, y, 152)$ and $\hat{P}(x, y, 152)$ in 4.13e. $Z(x, y, 0)$ and $\hat{Z}(x, y, 0)$ in 4.13b, $Z(x, y, 10)$ and $\hat{Z}(x, y, 10)$ in 4.13d, and $Z(x, y, 152)$ and $\hat{Z}(x, y, 152)$ in 4.13f.
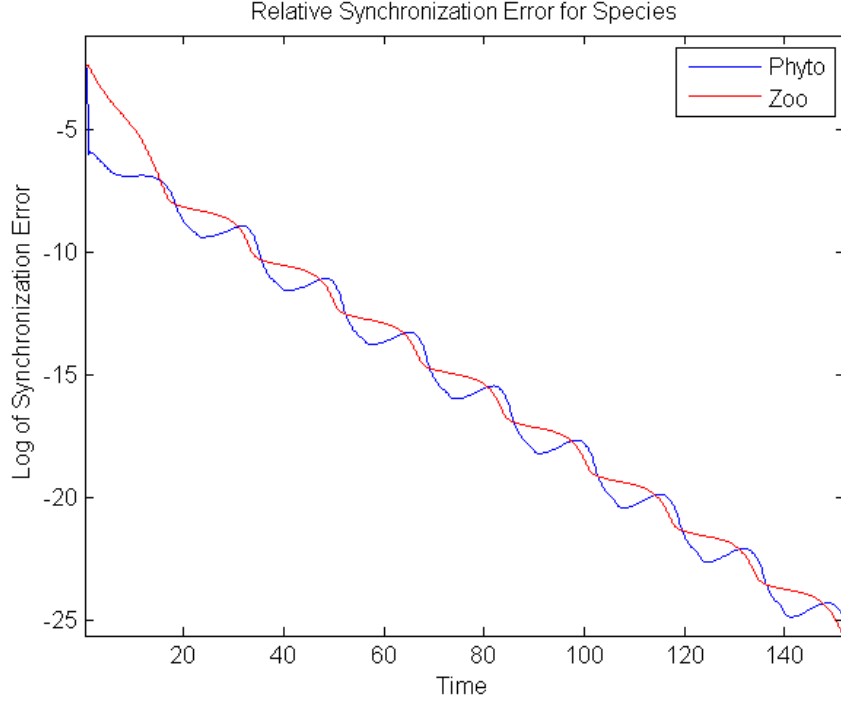
Figure 4.14: Relative error between drive and response system components, with errors given on a log scale. Relative error for both species has dropped to less than 1.0×10^{-12} by $t = 152$, a longer epoch than when sampling both species.

Figure 4.14 demonstrates that globally-averaged relative error between both species has dropped to within 1.0×10^{-12} of ground truth although after a longer time epoch than when sampling both species. The simulation of Eq (4.25) is halted after the globally averaged relative errors reach a threshold of $e_P(t) < 1.0 \times 10^{-12}$.

We note that this coupling scheme need not be unique for observing synchronization when coupling one species. An example including diffusive and complete replacement coupling is given by,

$$
\begin{aligned}
\frac{\partial \hat{P}}{\partial t} &= \triangle \hat{P} + \hat{P}(1 - \hat{P}) - \frac{\hat{P}\hat{Z}}{\hat{P} + h} + \kappa(P - \hat{P}), \qquad (4.26) \\
\frac{\partial \hat{Z}}{\partial t} &= \triangle \hat{Z} + k\frac{\hat{P}\hat{Z}}{P + h} - m\hat{Z},
\end{aligned}
$$

where the absence of the "hat" in the second equation denotes complete replacement of

$P(x, y, t)$. Figure 4.15 describes the results of synchronization for the stated response system. The simulation is halted once the relative synchronization error is less than 1.0×10^{-12}, which this time occurs by $t = 89$. We observe that the synchronization speed may be substantially increased not only with different coupling strengths but with different coupling methods.
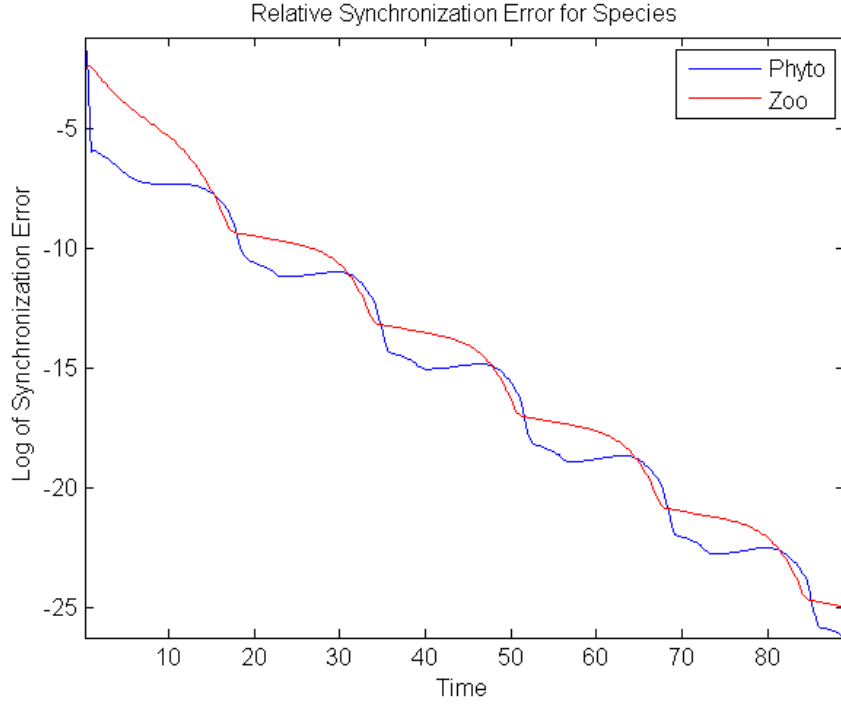
Figure 4.15: Globally-averaged relative error, Eq (4.24), between drive and response system components, with errors shown on a log scale. Relative error between both pairs of species has dropped to less than 1.0×10^{-12} by $t = 89$, a substantially shorter epoch than in Figure 4.14 using Eq (4.25).

4.2.2 Autosynchronization with Spatially Dependent Parameters

We next study parameter estimation by autosynchronization when able to sample only one species. As such, we do not know the initial model states, are able to only partially sample the drive model, and wish to recover the remainder of the drive model and spatially varying parameters, $m(x, y)$ and $k(x, y)$. A box diagram for this
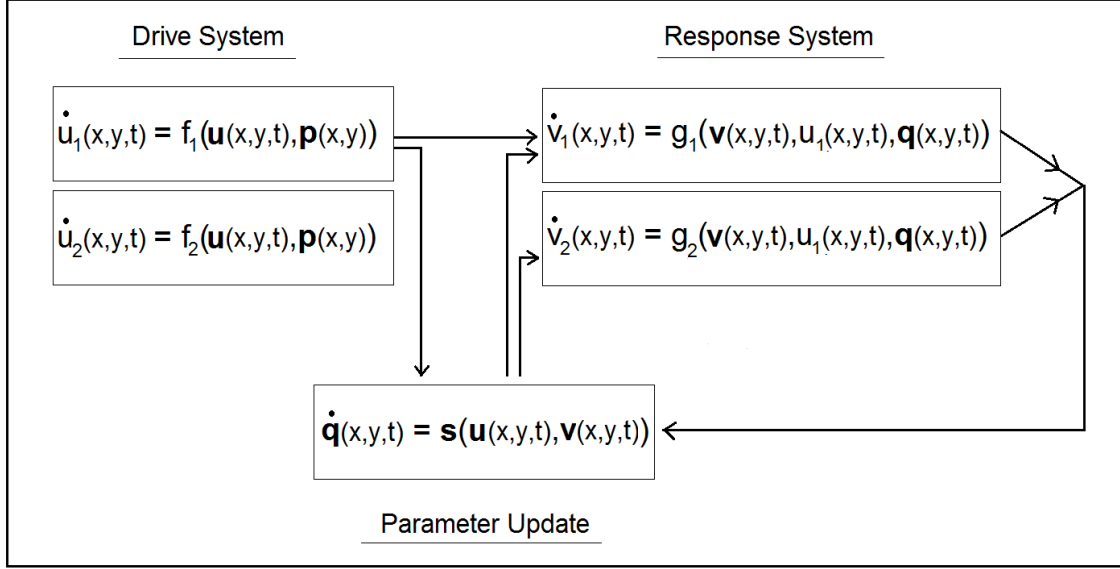
Figure 4.16: Diagram for autosynchronization of two-component PDE system by sampling only one species such as described by Eqs (4.7) and (4.27).

type of observation is shown in Figure 4.16, with respect to the problem formation described in Eq (4.17) - Eq (4.19). Note the arrow between the second component of the system has been dropped since it is unobservable.

Therefore, we must state a response model for which autosynchronization is observed for spatially dependent parameters from which we sample only one species. We state a response model,

$$
\begin{align}
\frac{\partial \hat{P}}{\partial t} &= \triangle \hat{P} + \hat{P}(1 - \hat{P}) - \frac{\hat{P}\hat{Z}}{\hat{P} + h} + \kappa(P - \hat{P}), \tag{4.27} \\
\frac{\partial \hat{Z}}{\partial t} &= \triangle \hat{Z} + \hat{k}\frac{\hat{P}\hat{Z}}{P + h} - \hat{m}\hat{Z}, \\
\frac{\partial \hat{k}}{\partial t} &= s_1(P - \hat{P}) \\
\frac{\partial \hat{m}}{\partial t} &= s_2(P - \hat{P})\hat{P},
\end{align}
$$

with $s_1 = 0.2$, $s_2 = 0.6$, and $\kappa = 0.3625$. The parameter equations are evolved simultaneously with $\hat{P}$ and $\hat{Z}$ using a forward Euler discretization. We combine diffusive

and complete replacement coupling in the response PDE to observe autosynchronization. Again, the ansatz system Eq (4.27) was chosen after testing multiple forms. Figures 4.17 and 4.18 provide three time instances from a simulation of Eq (4.27) demonstrating that zooplankton and parameters are well-estimated. All initial conditions for the response system are the same as for the previous simulations, Eq (4.23). The simulation is terminated, at $t = 633$, once the parameter $k(x, y)$ is estimated such that $e_k(t) < 1.0 \times 10^{-5}$.

Figure 4.18 shows reconstructed parameters compared with drive model parameters at three different times, $t = 0$, $t = 100$, and $t = 633$. This simulation demonstrates the spatial effectiveness of parameter reconstruction and is a first demonstration of parameter estimation for spatially dependent parameters by autosynchronization when only partially observing the drive system.

Globally-averaged relative errors corresponding to the simulations described by Figures 4.17 and 4.18 are described in Figure 4.19, with parameters corresponding to Eq (4.21). The globally-averaged synchronization error between model species is less than 1.2×10^{-5} and less than 1.4×10^{-5} for both parameters. Importantly, we note zooplankton density profiles are synchronizing over time. Therefore, we need not sample zooplankton to observe autosynchronization and we find the true zooplankton density profile and model parameters such that model simulations may be initialized by observing only one species. Thus we have developed a technique based on partial observation to estimate parameters and to initialize a full model for short term forecasts.

We note that these results hold for uniform random initial conditions and synchronization speed is again affected by choice of coupling. In Figures 4.20 and 4.21, we see simulation results assuming swirly parameters given by Figures 4.6e and 4.6f. These results demonstrate that autosynchronization is observed even when initializing the response system with uniform random noise.
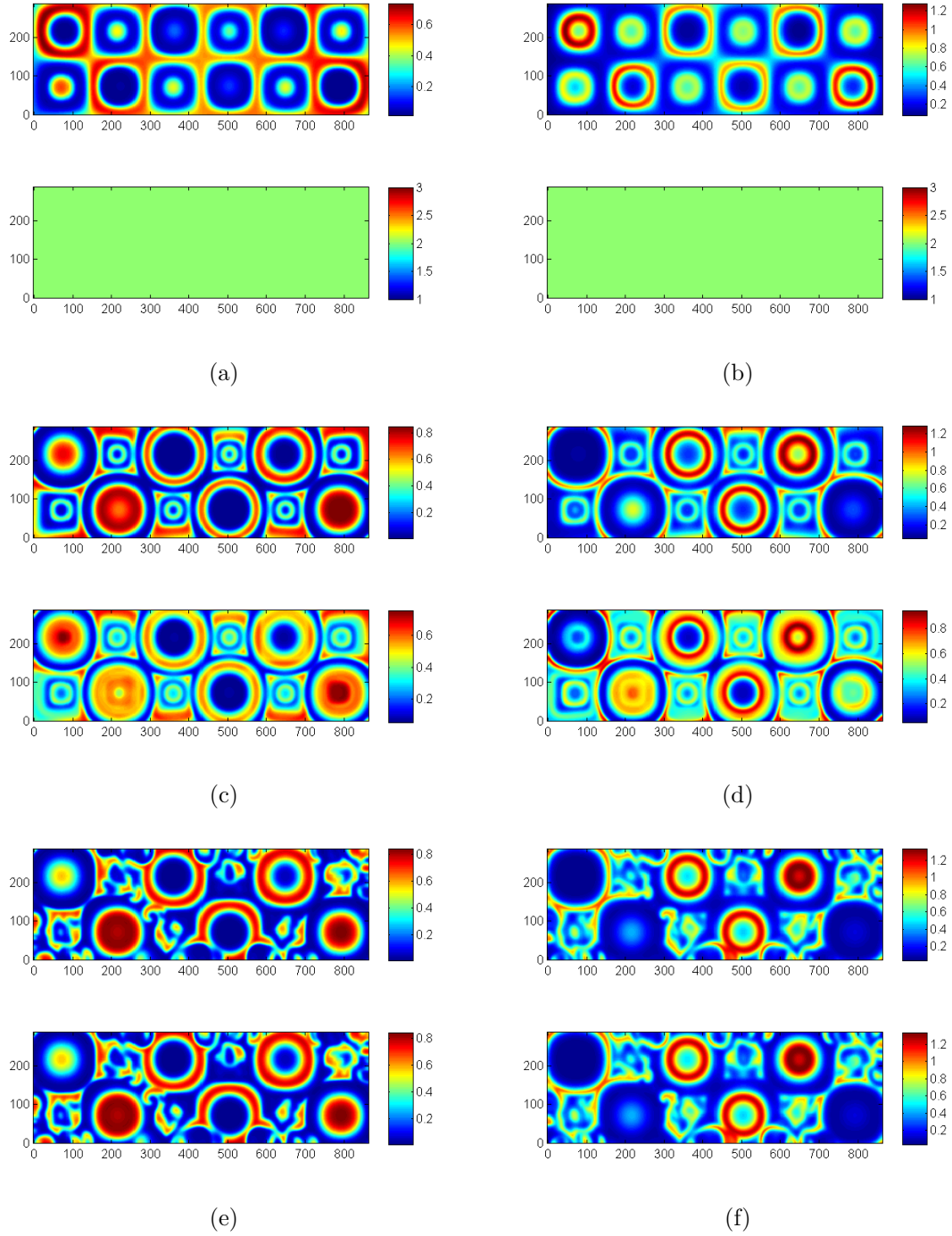
Figure 4.17: Autosynchronization of species where only phytoplankton are observed. Each figure shows drive (top) and response (bottom) pairs. $P(x, y, 0)$ and $\hat{P}(x, y, 0)$ in 4.17a, $P(x, y, 100)$ and $\hat{P}(x, y, 100)$ in 4.17c, and $P(x, y, 633)$ and $\hat{P}(x, y, 152)$ in 4.17e. $Z(x, y, 0)$ and $\hat{Z}(x, y, 0)$ in 4.17b, $Z(x, y, 100)$ and $\hat{Z}(x, y, 100)$ in 4.17d, and $Z(x, y, 633)$ and $\hat{Z}(x, y, 633)$ in 4.17f.
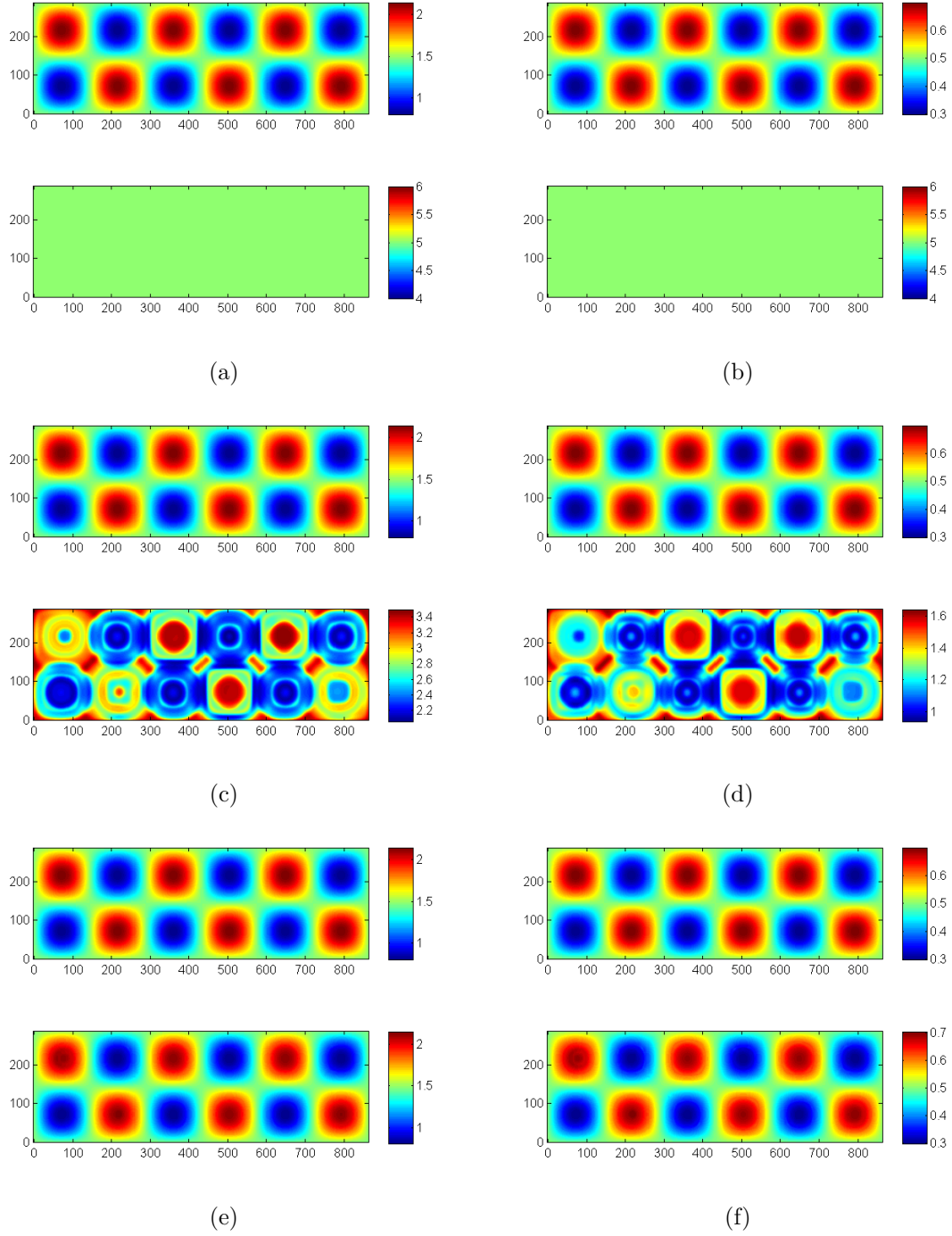
Figure 4.18: Autosynchronization of spatially dependent parameters. Each figure shows drive (top) and response (bottom) pairs. Model parameters given by $k_2(x,y)$ and $m_2(x,y)$ and only phytoplankton are observed. $k(x,y)$ and $\hat{k}(x,y,0)$ in 4.18a, $k(x,y)$ and $\hat{k}(x,y,100)$ in 4.18c, and $k(x,y)$ and $\hat{k}(x,y,152)$ in 4.18e. $m(x,y)$ and $\hat{m}(x,y,0)$ in 4.18b, $m(x,y)$ and $\hat{m}(x,y,100)$ in 4.18d, and $m(x,y)$ and $\hat{m}(x,y,633)$ in 4.18f.
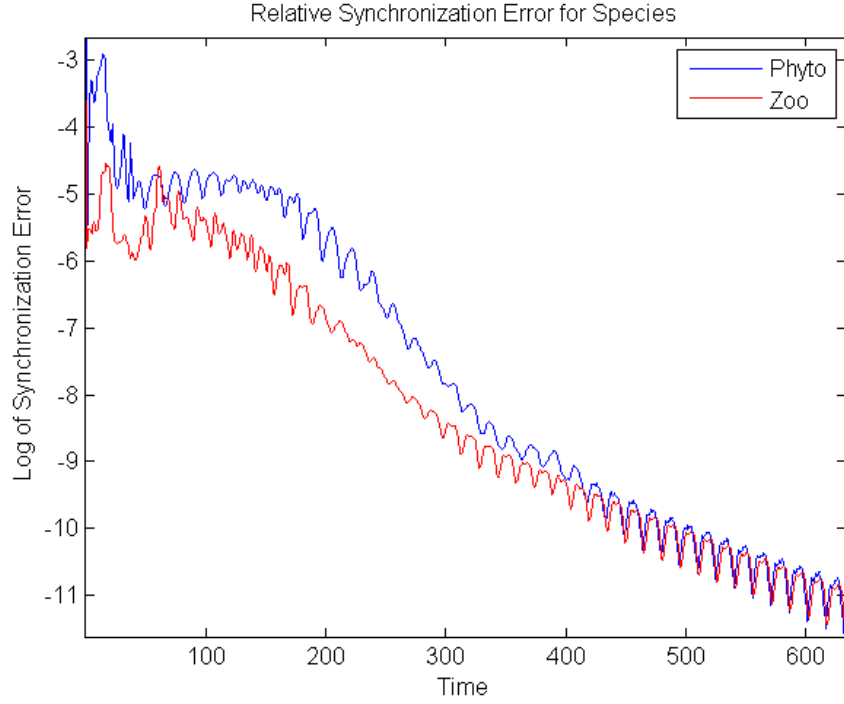
(a)
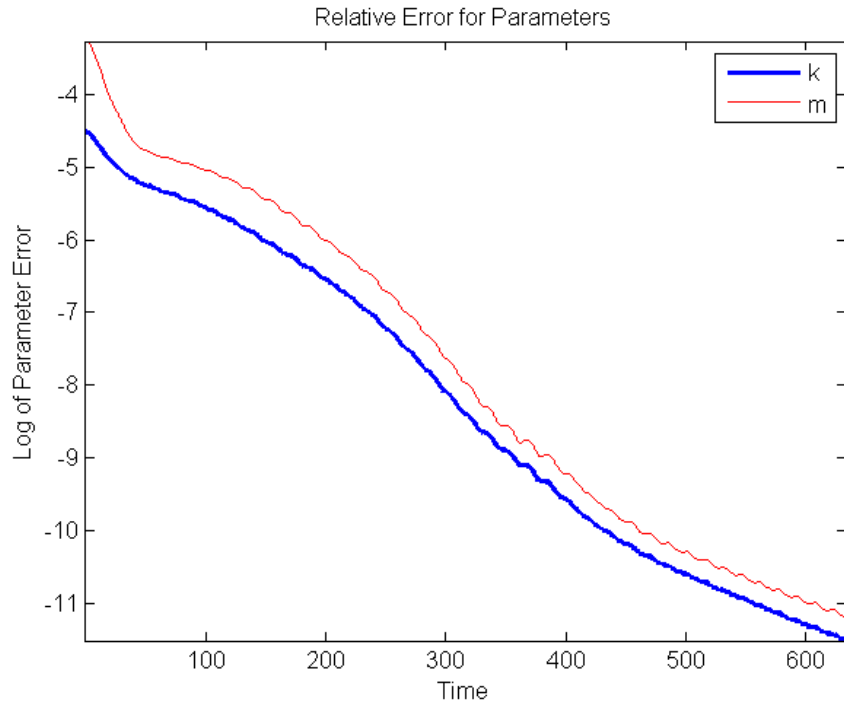
(b)

Figure 4.19: Globally-averaged relative synchronization error Eq (4.24) between drive and response PDE species and parameters on a log scale for parameters built by Eq (4.21). The errors represent simulation in Figures 4.17 and 4.18.
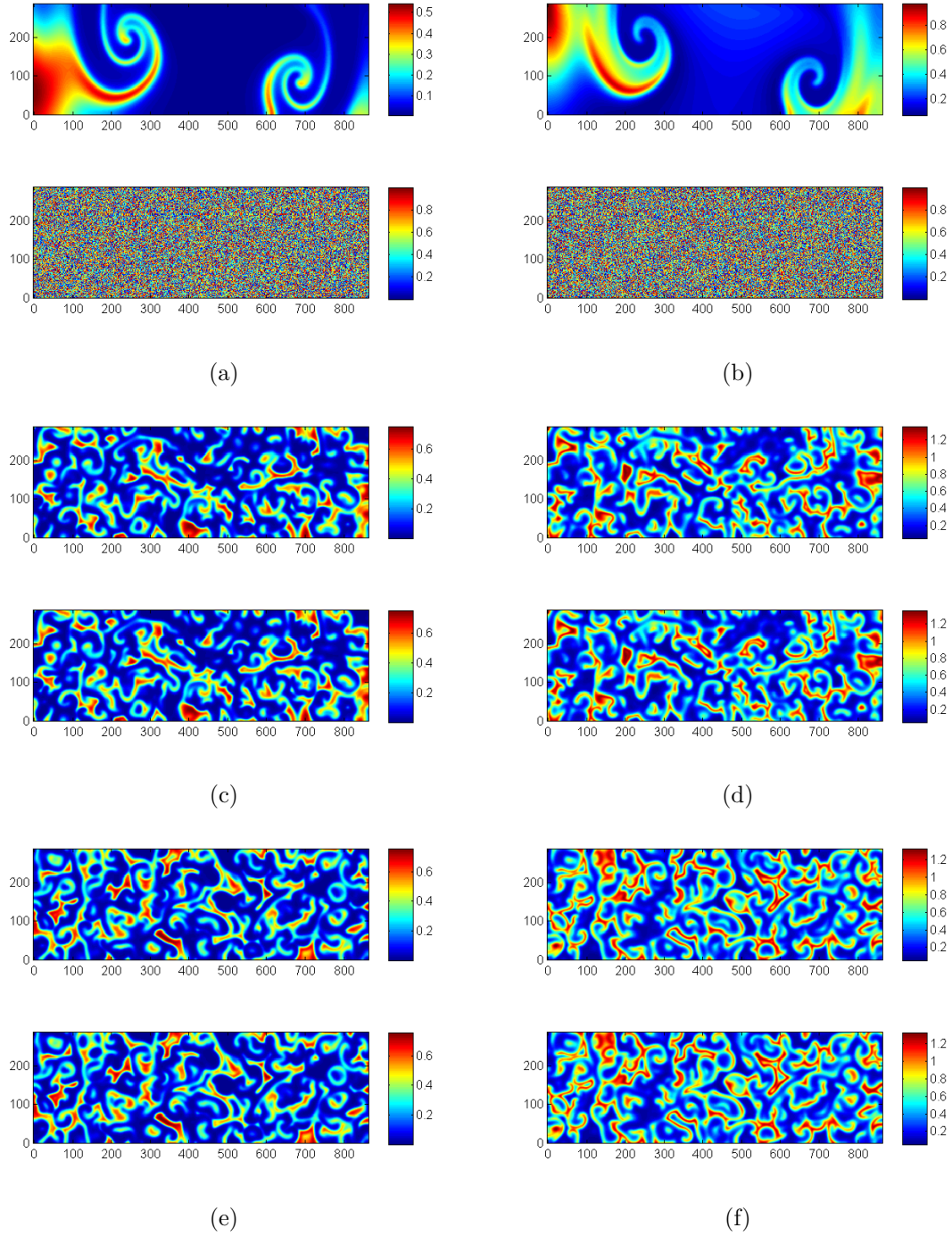
Figure 4.20: Autosynchronization of species where only phytoplankton are observed. Each figure shows drive (top) and response (bottom) pairs. $P(x, y, 0)$ and $\hat{P}(x, y, 0)$ in 4.20a, $P(x, y, 4000)$ and $\hat{P}(x, y, 4000)$ in 4.20c, and $P(x, y, 9360)$ and $\hat{P}(x, y, 9360)$ in 4.20e. $Z(x, y, 0)$ and $\hat{Z}(x, y, 0)$ in 4.20b, $Z(x, y, 4000)$ and $\hat{Z}(x, y, 4000)$ in 4.20d, and $Z(x, y, 9360)$ and $\hat{Z}(x, y, 9360)$ in 4.20f.
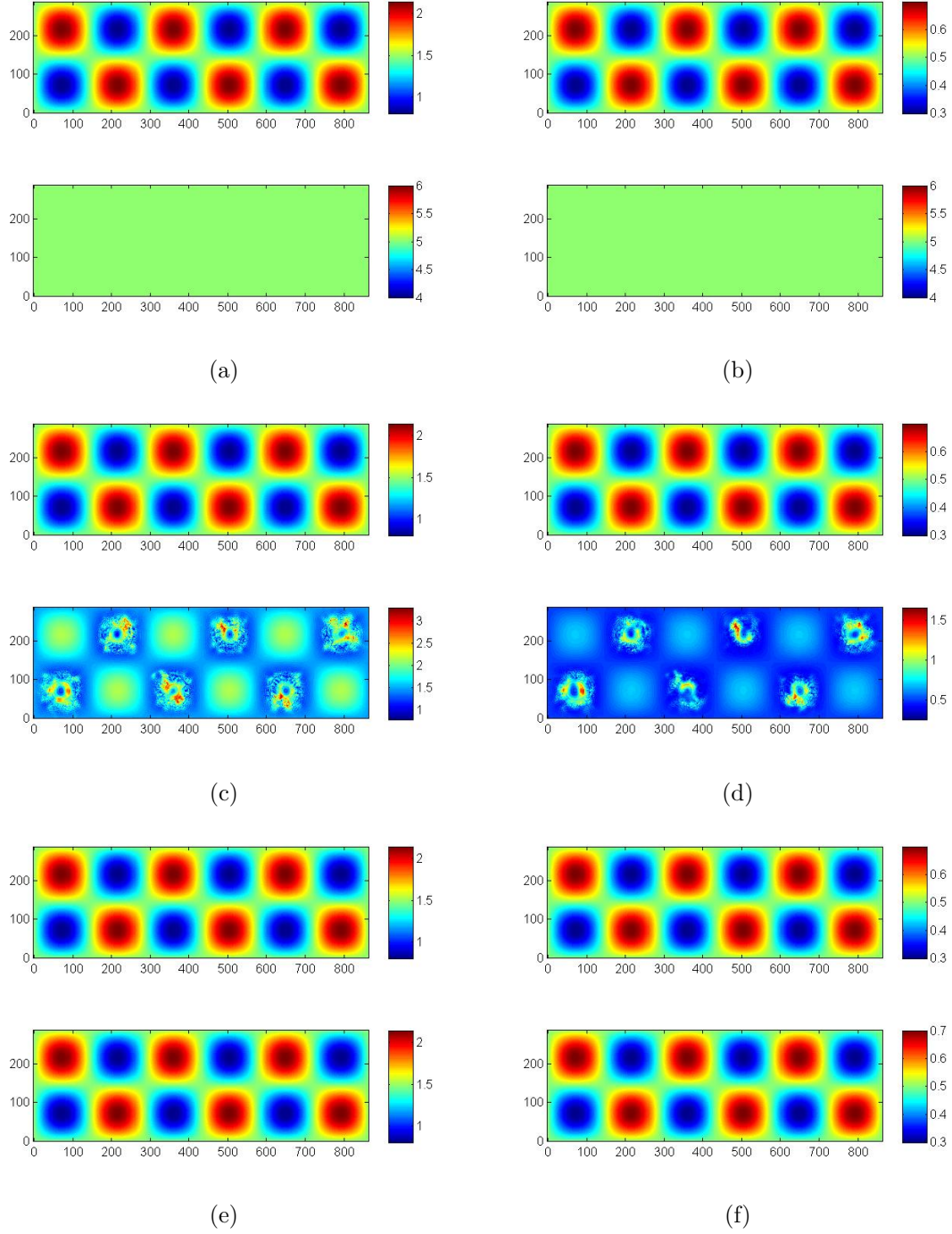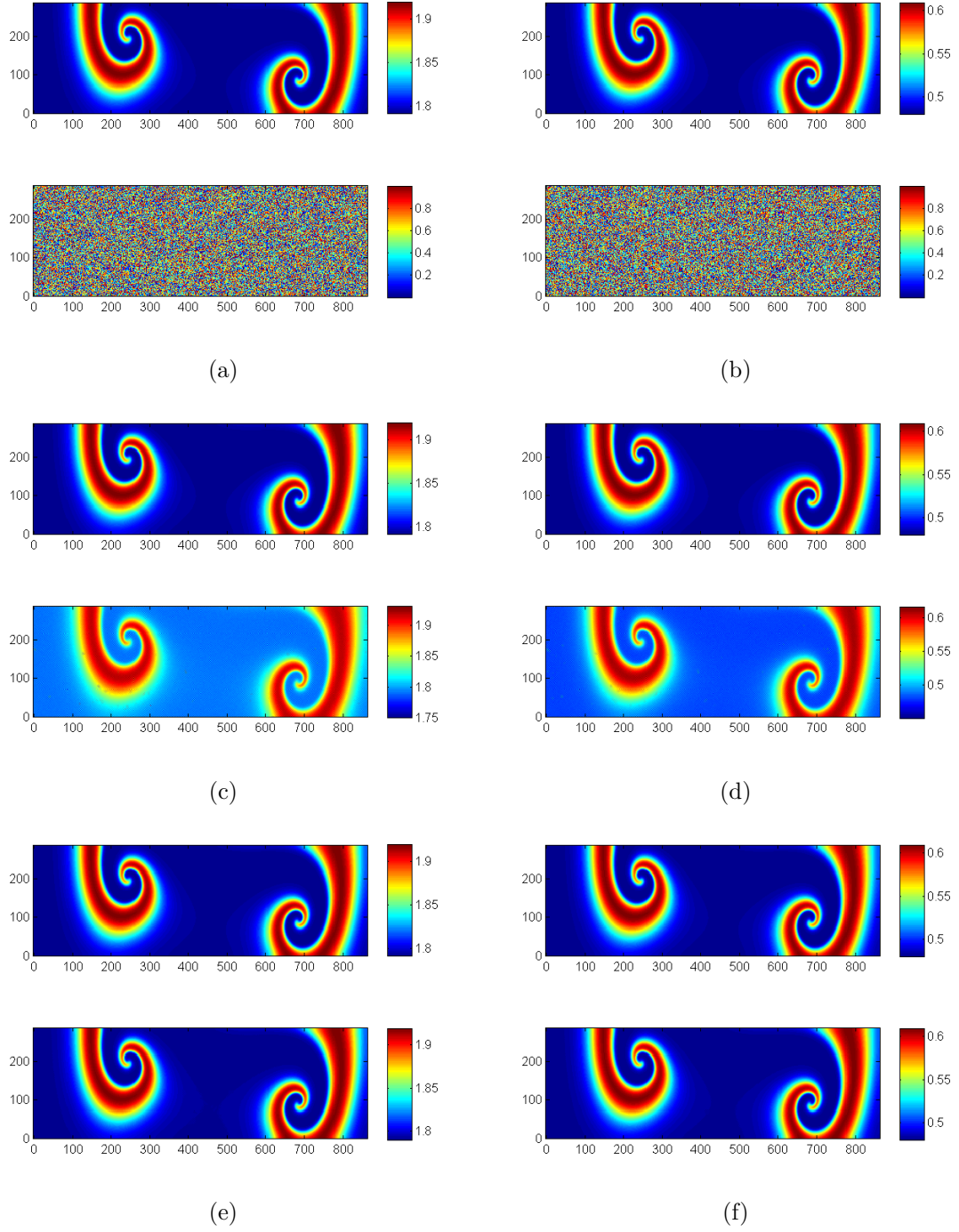
Figure 4.21: Autosynchronization of spatially dependent parameters given by spiral model parameter shown in Figures 4.6e and 4.6f and only phytoplankton are observed. Each figure shows drive (top) and response (bottom) pairs. $k(x, y)$ and $\hat{k}(x, y, 0)$ in 4.21a, $k(x, y)$ and $\hat{k}(x, y, 4000)$ in 4.21c, and $k(x, y)$ and $\hat{k}(x, y, 9360)$ in 4.21e. $m(x, y)$ and $\hat{m}(x, y, 0)$ in 4.21b, $m(x, y)$ and $\hat{m}(x, y, 4000)$ in 4.21d, and $m(x, y)$ and $\hat{m}(x, y, 9360)$ in 4.21f.

91

Drive and response model species are shown in Figure 4.20 and parameters are demonstrated in Figure 4.21, demonstrating the ability to estimate swirly parameters befitting for the ocean on the mesoscale. Simulation snapshots are shown at $t = 0$, $t = 4000$, and $t = 9360$. The simulation is terminated once the parameters k and $\hat{k}$ are synchronized to within $e_k(t) < 1.0 \times 10^{-5}$

Thus, despite rather noisy initial guesses for model parameters and states, the spiral parameters are effectively resolved. We have found that synchronization is substantially faster when initial guesses are sufficiently smooth or even constant.

In Figure 4.22, globally averaged errors are shown to diminish over time as the coupled systems evolve, however at the slowest rate yet. When able to sample at every point in a desired grid, we observe autosynchronization of realistic spatially-dependent model parameters and states.

We remark here that we observe evidence for the convergence of the drive and response systems to the identical synchronization manifold and preceding results are shown as a first demonstration. Convergence for some of these systems is rigorously analyzed in Chapter 5, however for others we rely on numerical evidence for stability.

In summary, we have extended the autosynchronization method from scalar parameters on a system of partially-observable ODEs to spatially dependent model parameters for a system of partially-observable PDEs. However, in application, one may not be able to sufficiently sample a domain such that simulations remain numerically stable. Furthermore, data might only be experimentally available in locally averaged discrete "patches" [52], requiring further development of these methods.

4.3   On Incomplete Observation Data

Our target application for these methods is to model ocean ecology based on remote sensing, in particular hyperspectral satellite imagery. We now consider an innate
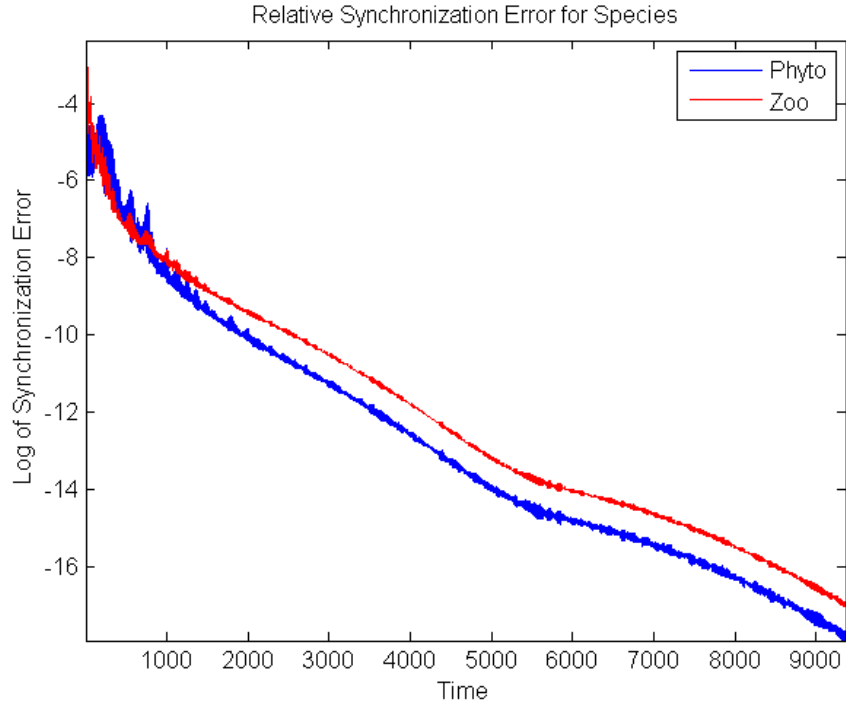
(a)
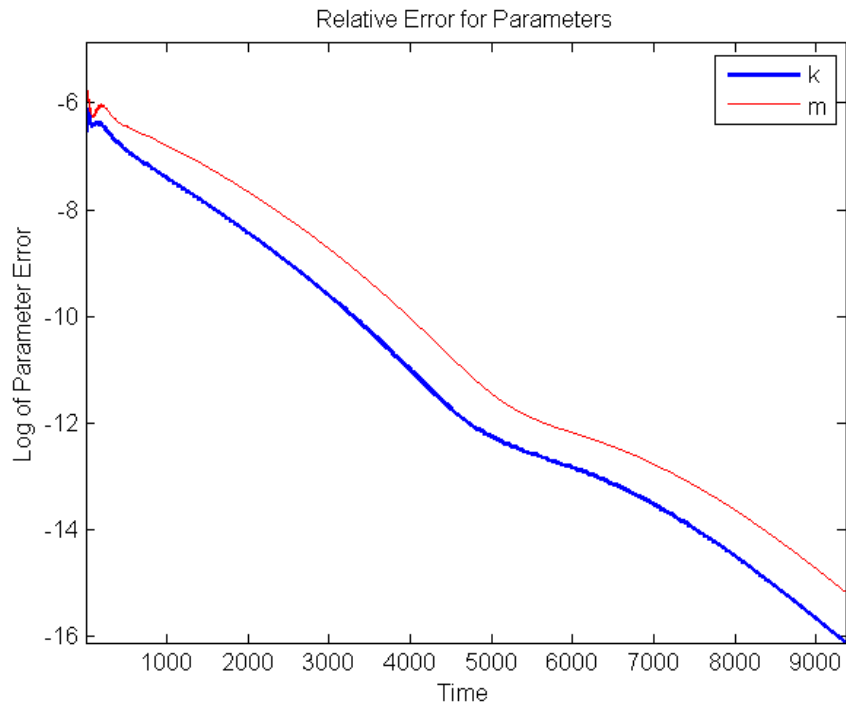
(b)

Figure 4.22: Globally-averaged relative synchronization error between drive and response PDEs on a log scale in 4.22a. Globally-averaged synchronization error between drive and response parameters on a log scale in 4.22b. Errors correspond to simulation shown in Figures 4.20 and 4.21, and estimating perhaps more realistic spiral parameters.

93

complication with fitting and assimilating a PDE model informed by experimental data.

In real experimental situations, data is often sampled at discrete locations, providing perhaps local averages on a coarsened subset of the domain [52]. In order to apply the methods discussed directly one might subsample the observed data by interpolation to a desired refined grid. Interpolation might perform quite well, if given the assumption of smooth solutions. Sans interpolation, our method should to be adapted for sampling by local averaging over the observable domain. Therefore, we now show that our techniques are robust by partially observing only one species in locally-averaged patches throughout the domain.

4.3.1 Synchronization by Local Averaging

We sample a coarsened subset of the discretized domain and take local averages to be the driving signal, in the same way as [52]. An example domain over which we sample is shown in Figure 4.23, where the domain is sampled in 3×3 patches with a spacing of 3 grid points between patches. That is, the systems are coupled unidirectionally, with "sensors" representing the local sampling of observables, and "controllers" representing local coupling in the response model [52]. Relevant parameters are the grid spacing and size of the sensors and controllers in the domain, now in addition to the coupling strength.

The following work is quite "ad hoc" in contrast to the preceding work that is theoretically analyzed in Chapter 5. Although techniques included in the following section are quite successful, further analysis is required to obtain bounds on errors or prove convergence results.

Synchronization is robust to spatial subsampling by local averaging by changing the response system to include only diffusive coupling, described by Eq (4.28),
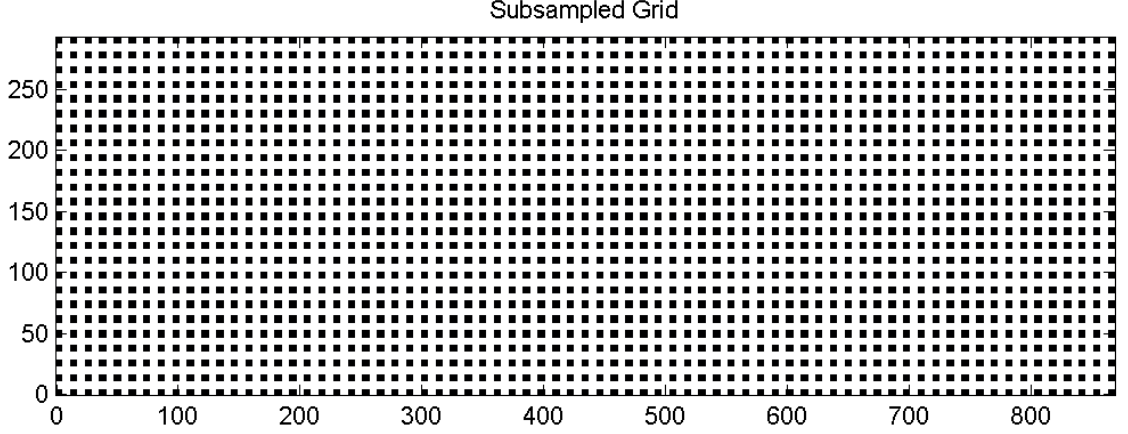
Figure 4.23: Locally-averaged patches representing controllers and sensors over which drive system is sampled and response system is coupled, shown in black. Sensors shown on subset of 3×3 grid points with a separation of 3 grid points.

$$
\frac{\partial \hat{P}}{\partial t} = \triangle \hat{P} + \hat{P}(1 - \hat{P}) - \frac{\hat{P}\hat{Z}}{\hat{P} + h} + \kappa G_n \qquad \forall x, y \in S_n, \tag{4.28}
$$

$$
\frac{\partial \hat{Z}}{\partial t} = \triangle \hat{Z} + \hat{k}\frac{\hat{P}\hat{Z}}{P + h} - \hat{m}\hat{Z},
$$

where the complete replacement term is removed in the zooplankton equation. Since the drive system is only partially sampled and local averages are taken to be the drive signal, the local driving term is,

$$
G_n(t) = \frac{1}{(dx)(dy)} \sum_{x,y \in S_n} (P(x, y, t) - \hat{P}(x, y, t)), \tag{4.29}
$$

where S_n represents a rectangular "sensor" on the domain over which the model misfit is locally averaged. A requirement for good results is that we remove the direct replacement term in Eq (4.28) since local averaging forces a small misfit from observed data. Thus, a complete replacement term eventually works *against* identical synchronization and identical synchronization is not observed. Instead, we either remove the term as shown above or we allow complete replacement until the re-

sponse output stops progressing toward drive observations. That is, rather define a temporally-varying complete replacement term which is eventually "switched off" and then couple as shown in Eq (4.28). The combination of diffusive and complete replacement coupling allows for faster synchronization from random initial conditions than by Eq (4.28) alone.

Synchronization results are shown in Figure 4.24, wherein three different arrangements of local averaging are tested. In all three cases, the synchronization manifold is asymptotically stable, however the rate of convergence to the manifold acts inversely with respect to sampling sparsity. For brevity, only globally averaged relative errors are shown and the simulation snapshots are omitted as the images look extremely similar to Figure 4.13.

These results agree with results demonstrated in [52], however we now study autosynchronization. Thus, we modify the response system Eq (4.27) as

$$
\begin{aligned}
\frac{\partial \hat{P}}{\partial t} &= \triangle \hat{P} + \hat{P}(1 - \hat{P}) - \frac{\hat{P}\hat{Z}}{\hat{P} + h} + \kappa G_n \qquad \forall x, y \in S_n, &&\text{(4.30)} \\
\frac{\partial \hat{Z}}{\partial t} &= \triangle \hat{Z} + \hat{k}\frac{\hat{P}\hat{Z}}{\tilde{P} + h} - \hat{m}\hat{Z}, \\
\frac{\partial \hat{k}}{\partial t} &= \triangle \hat{k} + s_1(\tilde{P} - \hat{P}), \\
\frac{\partial \hat{m}}{\partial t} &= \triangle \hat{m} + s_2(\tilde{P} - \hat{P})\hat{P},
\end{aligned}
$$

where $\tilde{P}$ represents complete replacement with locally-averaged observations from the drive system. We remark that diffusion is added to the parameter equations in Eq (4.30) in order that data from the driven regions, S_n will diffuse into the occluded regions. Varying sensor sizes were examined and in Figure 4.25 results are shown for a 2×2 subsampling of the domain Ω, with 1 grid point between subsequent patches.

In Figure 4.26, we notice that despite locally averaged data, the response system
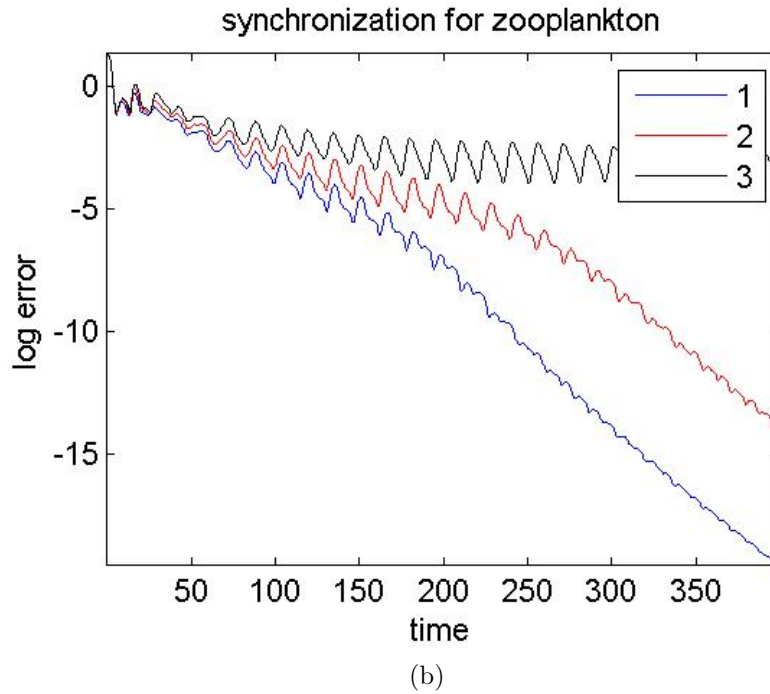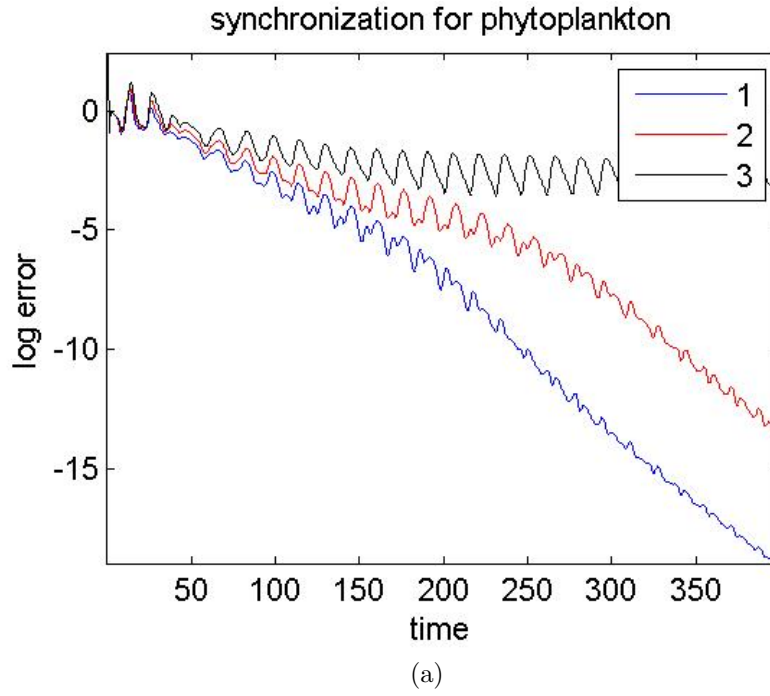
Figure 4.24: Comparison of different sampling by local averaging. Relative synchronization errors between systems for sampling over 3×3 grid points (blue) with distance of 3 grid points between sensors, 2×2 grid points (red) with distance of 2 grid points between patches, and 1×1 grid points (black) with distance of 1 grid point between patches. Phytoplankton synchronization errors in 4.24a, zooplankton synchronization errors in 4.24b.

97
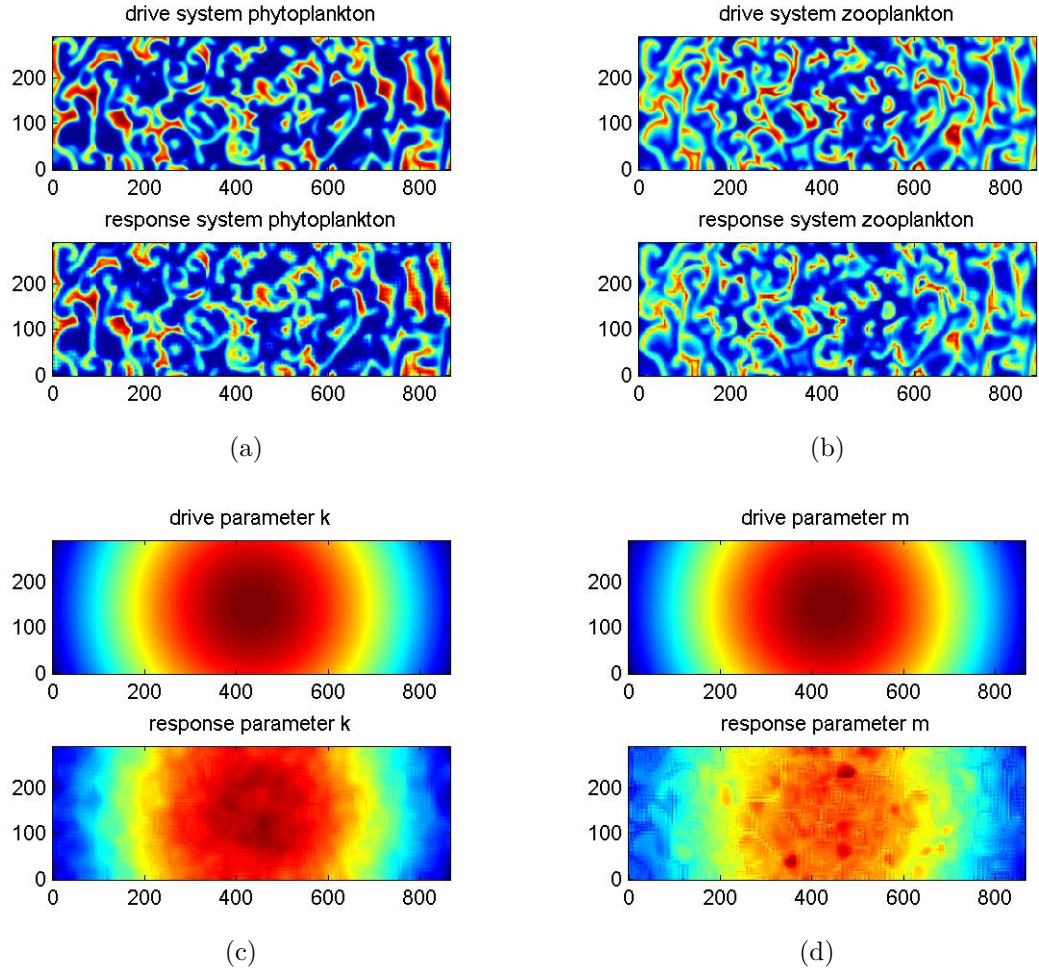
Figure 4.25: Autosynchronization results shown at $t = 2000$. Both species and both parameters shown compared with drive species and true parameters. Effect of adding diffusion to parameter equations is clearly visible in estimated parameters on bottom of Figures 4.25c and 4.25d

synchronization for species

(a)

synchronization for parameters
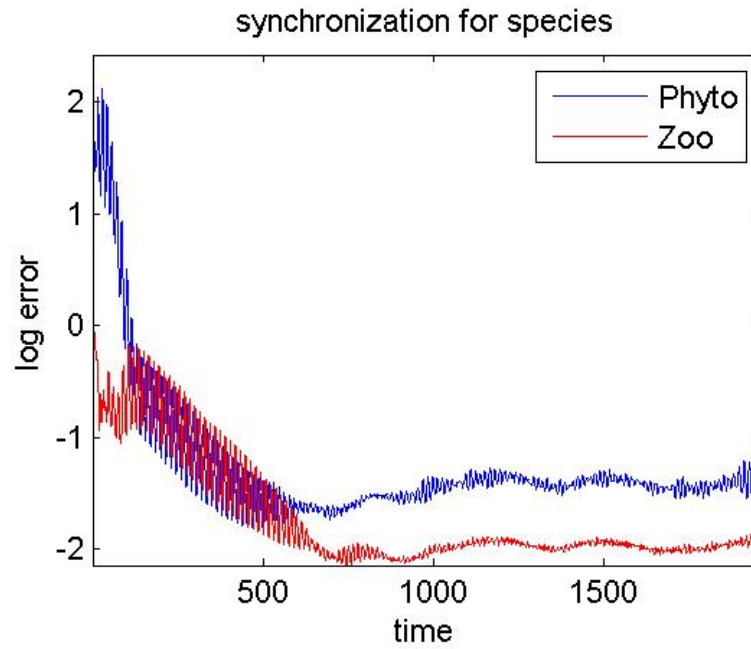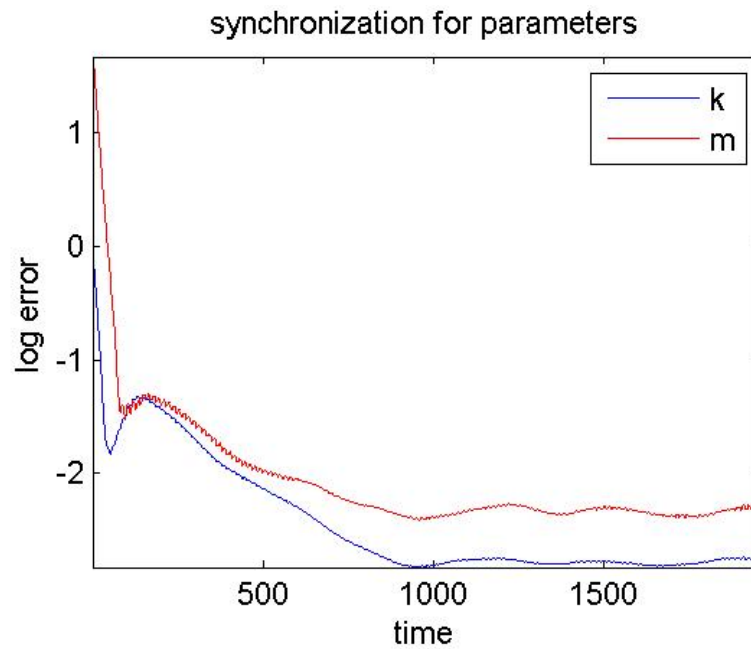
(b)

Figure 4.26: Globally-averaged relative synchronization errors shown for species and parameters. Local averaging destroys stability of the identical synchronization manifold, however spatial characteristics of parameters are still observed.

is driven toward the identical synchronization manifold. Results are clearly not as accurate as when sampling at every grid point in the domain, nor as accurate as the results for synchronization alone. Identical synchronization is not observed when the locally-averaged sampling is sparse.

We note, that we sample from sufficiently refined satellite data such that interpolation or local averaging for simulation on a finer grid is unnecessary. That is, for our application to remote sensing, we evolve ecology over the same grid on which the data are observed. Nevertheless, an important consideration for universal application of these methods is sparsity in sampling observables and local averaging of samples.

4.3.2 Temporal Subsampling

Yet another complication with satellite data is the inability to sample every timestep with which simulations are evolved. That is, although spatiotemporal dynamics are in motion, they are unobservable and can not be coupled into the response model. As the drive model continues to evolve, we ask if it is possible for the response model to synchronize with the drive when *missing* observations from the drive.

We state the response model Eq (4.26). However, we evolve the response model forward and only couple whence data is sampled in time. That is, we allow the drive and response models to oscillate independently in-between sampling, and intermittently feed samples from the drive to the response system. We experiment with several different sub-sample times to monitor how temporal sub-sampling affects synchronization.

Figure 4.27 shows the relative synchronization errors for both species when subsampling in time. Shown are results for sampling once every two time steps (blue), once every four time steps (red) and once every eight time steps (black). Temporal subsampling affects the speed of synchronization inversely with sampling rate. Regardless, by coupling only when observed, identical synchronization is still demon-

strated. The results in Figure 4.27 are obtained with the Gaussian parameters, Eq (4.20), and show that synchronization is robust to temporal subsampling.

Next, we study whether autosynchronization is also robust to temporal subsampling. We state the response model Eq (4.27) and initialize model states by Eq (4.23). Figure 4.28 shows errors obtained following autosynchronization simulations whence phytoplankton are sampled either every two, four, or eight time steps. Interestingly, the basin of attraction for the synchronization manifold seems to lose stability when varying the temporal sampling rate. To observe identical synchronization, the coupling strength κ, was changed for each simulation. Thus, for results shown in Figure 4.28, $\kappa = 0.42$ when sampling every two time steps and $\kappa = 1$ when sampling every four time steps, and $\kappa = 1.5$ when sampling every eight time steps.

Autosynchronization is now demonstrated to be robust to both spatial and temporal subsampling. That fact allows for easier use with application to systems modelled as PDEs but observable on discretized and temporally sub-sampled domains.

4.3.3 Clouds

Ocean-observing satellite imagery often includes significant amounts of cloud cover [8]. Furthermore, we have found that a *level 2* mapped and processed image may be stretched such that blank pixels are added into the domain as a consequence of projecting a sphere onto a uniform grid. The lack of data presents a challenge to data assimilation and model filtering by synchronization methods. Suppose $\omega \subset \Omega$ is the set of unobservable data. We allow for $\omega = \omega(x, y, t)$ so that the set of unobservables varies with space and time like a cloud. We couple the systems only on the compliment of ω. That is, we turn the driving signal off when the image is unobservable, allowing the two systems to oscillate independently, and switch it on after the clouds have passed. We do this only in the subregion $\omega \subset \Omega$ that is unobservable in order that data contained in the compliment of ω may continue to be driven by observables
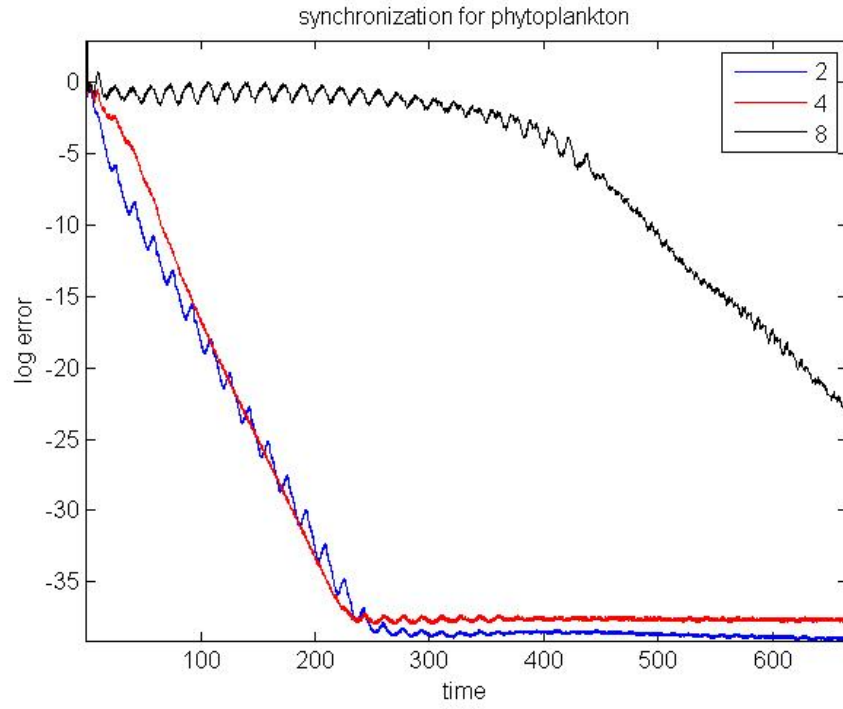
(a)
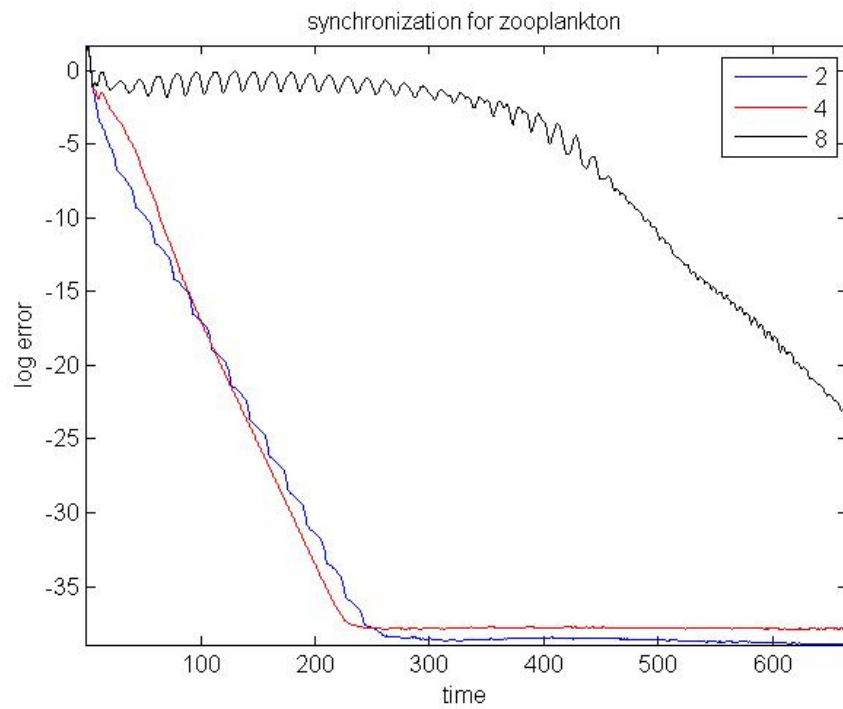
(b)

Figure 4.27: Globally-averaged relative synchronization errors shown for species for different sub-sampling cases. Sampling every two time steps in blue, every four time steps in red, and every eight time steps in black. Synchronization manifold remains stable under this subsampling, but synchronization speed decreases with increasing time between samples.
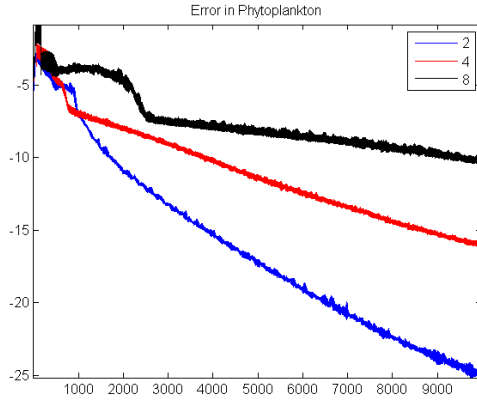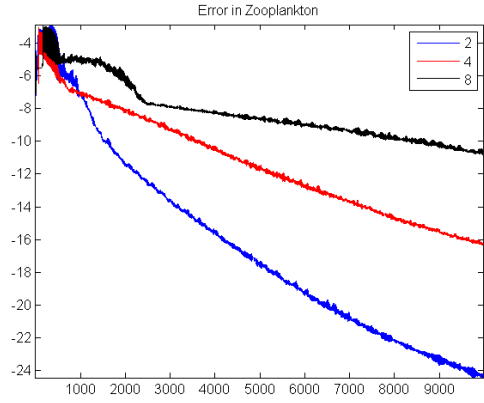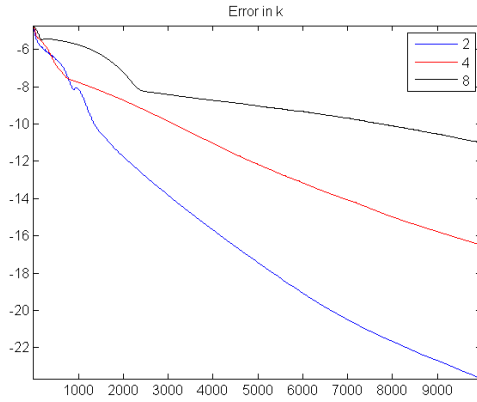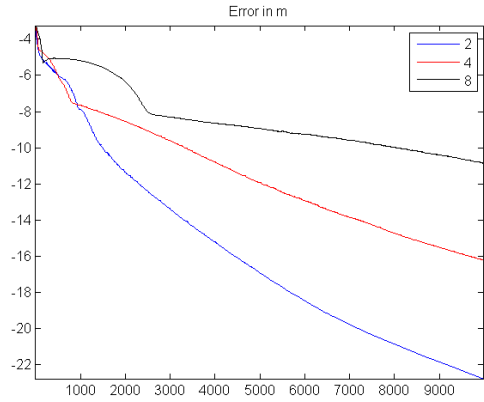
Figure 4.28: Globally-averaged relative autosynchronization errors shown. Sample every two time steps shown in blue, every four time steps shown in red, and every eight time steps shown in black. Synchronization manifold remains stable under this subsampling, but speed decreases with increasing time between samples.

toward the synchronization manifold.

Here, we build on our work in [78], where zooplankton densities and model parameters were estimated by observing solely the phytoplankton. Now we observe phytoplankton and clouds.

However, if we simulate as when sampling at every time step, the synchronization manifold is de-stabilized by incident cloud coverage. In hyperspectral image data cloud masks over certain pixels are represented by a particular assigned integer, say n. Therefore under Eq (4.25), a pixel will actually be evolved as,

$$
\begin{aligned}
\frac{\partial \hat{P}}{\partial t} &= \triangle \hat{P} + \hat{P}(1 - \hat{P}) - \frac{\hat{P}\hat{Z}}{\hat{P} + h} + \kappa(-\hat{P}), \\
\frac{\partial \hat{Z}}{\partial t} &= \triangle \hat{Z} + \hat{k}\frac{\hat{P}\hat{Z}}{n + h} - \hat{m}\hat{Z},
\end{aligned}
\tag{4.31}
$$

where n is some fixed integer value. Eq (4.31) is qualitatively different from the original response model stated and only serves to drive the response model away from the synchronization manifold. Once the cloud passes, the response model is correct and is driven toward the synchronization manifold. With a respectable amount of cloud coverage over Ω, the old approach simply does not work.

Rather, we allow the drive and response models to oscillate independently, or uncoupled, while the drive model is hidden by clouds. We represent this formally,

$$
\begin{aligned}
\frac{\partial \hat{P}}{\partial t} &= \triangle \hat{P} + \hat{P}(1 - \hat{P}) - \frac{\hat{P}\hat{Z}}{\hat{P} + h} + \kappa(H[P] - \hat{P}), \\
\frac{\partial \hat{Z}}{\partial t} &= \triangle \hat{Z} + k\frac{\hat{P}\hat{Z}}{H[P] + h} - m\hat{Z},
\end{aligned}
\tag{4.32}
$$

where $H[P]$ represents a *switching* function given by

$$H[P] = \begin{cases} \hat{P} & , \quad P = 0 \\ P & , \quad P \geq 0. \end{cases}$$

The form of response model switches off the coupling when a cloud mask is detected in the image and allows the systems to oscillate independently in the corresponding pixels, while being driven over pixels that are observed. Eq (4.32) is slightly different than temporal subsampling where models were simply not coupled for a given number of time steps. Here the models are always coupled somewhere in Ω, which is determined by time-varying clouds.

Figure 4.29 represents a partially observed dataset from Eq (4.7), with 30 randomly placed synthetic clouds evolving from left to right with circular boundary conditions resulting in $65.8\,\%$ of Ω occluded at all times. The clouds repeatedly scroll from left to right and parts of the image are always occluded, but every element in the domain is eventually driven, causing the drive and response to systems to synchronize. The response system is initialized by Eq (4.23) and we choose $\kappa = 2.6$.

Once synchronized, even hidden phytoplankton are revealed for initializing short-term forecasts, demonstrating the utility of this result. Figure 4.30 demonstrates that despite $65.8\,\%$ of the drive system hidden, the two PDE systems eventually evolve toward identical synchronization. In Figures 4.29e and 4.29f nearly all evidence of clouds is "synchronized away" from the response system and the globally averaged error between the two has been driven to be less than 2.6×10^{-12}. We remark that the choice of coupling strength, κ, varies with the amount of data occluded.

Given a model form, we have demonstrated [78] how to sample a single species toward parameter estimation and nonlinear data assimilation for a two-species PDE model. Next, we show this is true regardless of clouds. That is, by stating the

(a)　　　　　　　　　　　　　　　　　　(b)

(c)　　　　　　　　　　　　　　　　　　(d)

(e)　　　　　　　　　　　　　　　　　　(f)
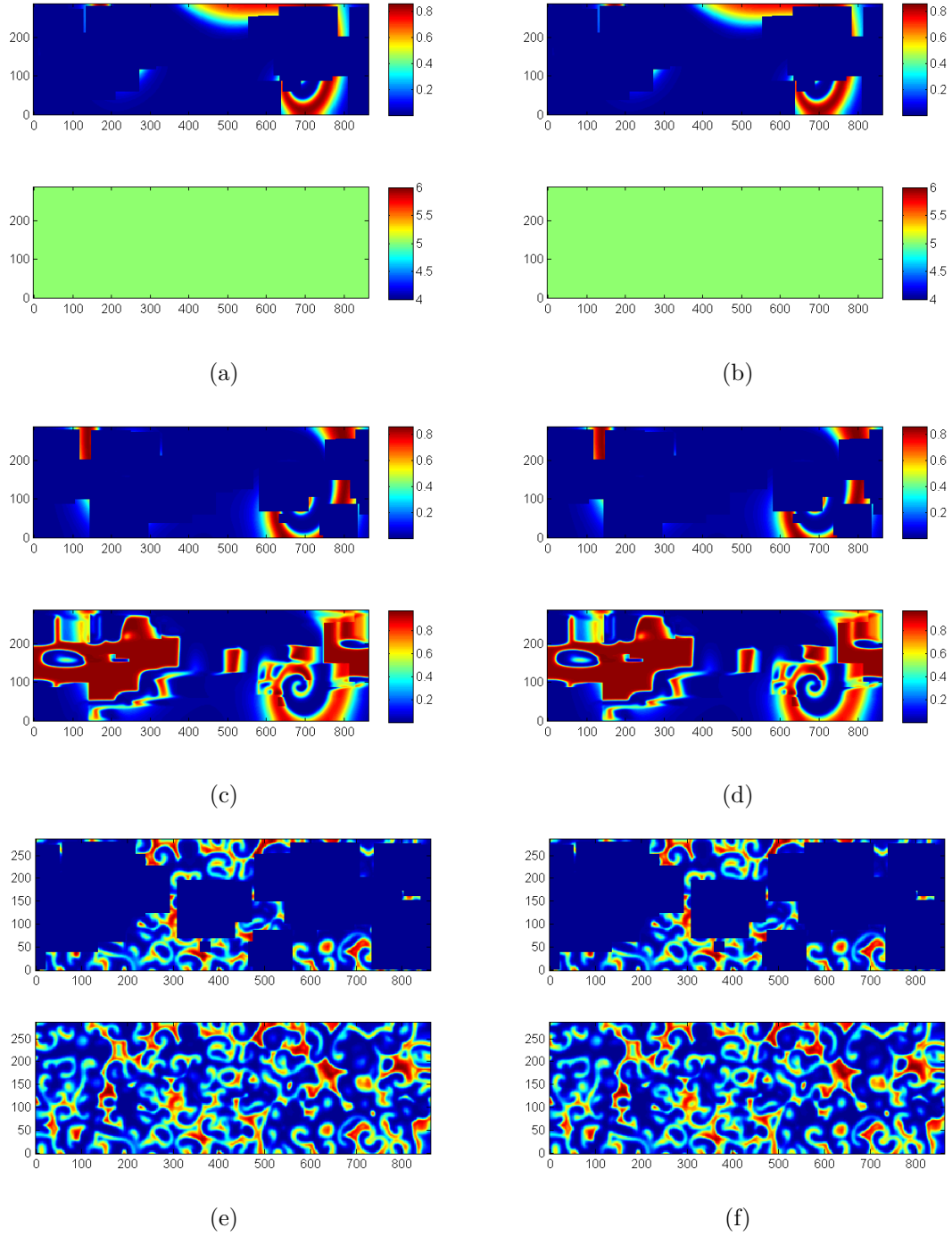
Figure 4.29: Synchronization of response system shown at $t = 0$, $t = 20$, and $t = 12000$. Here 65.8% of Ω is hidden at any point in time from clouds, however identical synchronization is observed. Each figure shows drive (top) and response (bottom) pairs. $P(x, y, 0)$ and $\hat{P}(x, y, 0)$ in 4.29a, $P(x, y, 20)$ and $\hat{P}(x, y, 20)$ in 4.29c, and $P(x, y, 12000)$ and $\hat{P}(x, y, 12000)$ in 4.29e. $Z(x, y, 0)$ and $\hat{Z}(x, y, 0)$ in 4.29b, $Z(x, y, 20)$ and $\hat{Z}(x, y, 20)$ in 4.29d, and $Z(x, y, 12000)$ and $\hat{Z}(x, y, 12000)$ in 4.29f.

106
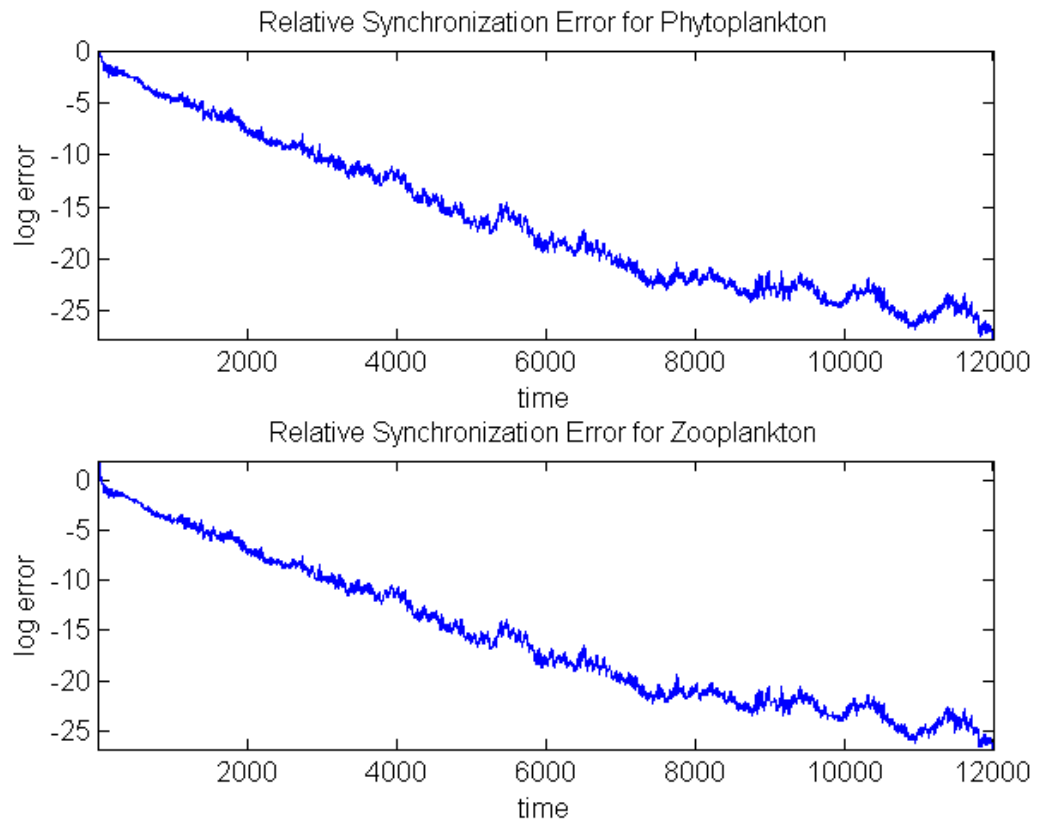
Figure 4.30: Globally-averaged relative synchronization errors. Errors given by simulation shown in Figure 4.29 decrease to less than 2.6×10^{-12} despite ever-present clouds.

response system

$$\begin{aligned}
\frac{\partial \hat{P}}{\partial t} &= \triangle \hat{P} + \hat{P}(1 - \hat{P}) - \frac{\hat{P}\hat{Z}}{\hat{P} + h} + \kappa(H[P] - \hat{P}), && (4.33)\\
\frac{\partial \hat{Z}}{\partial t} &= \triangle \hat{Z} + \hat{k}\frac{\hat{P}\hat{Z}}{H[P] + h} - \hat{m}\hat{Z},\\
\frac{\partial \hat{k}}{\partial t} &= s_1(H[P] - \hat{P})\\
\frac{\partial \hat{m}}{\partial t} &= s_2(H[P] - \hat{P})\hat{P},
\end{aligned}$$

where $k(x, y)$, $m(x, y)$, $Z(x, y, t)$, and $P(x, y, t)|_\omega$ are to be estimated by $\hat{k}(x, y)$, $\hat{m}(x, y)$, $\hat{Z}(x, y, t)$, and $\hat{P}(x, y, t)$ by sampling *only* $P(x, y, t)|_{\omega^C}$. As before, the coupling is turned off completely for the pixels on which clouds are detected.

Figures 4.31 and 4.32 demonstrate a comparison between drive and response models. In the top of Figure 4.31a, we see the observed system $P(x, y, t)|_{\omega^C}$ wherein 25.5 % of the data on Ω is not observable. Figures 4.31 and 4.32 demonstrate that phytoplankton, zooplankton, and both spatially dependent parameters $\hat{k}(x, y, t)$ and $\hat{m}(x, y, t)$ are estimated to high precision.

Figure 4.33 describes the globally-averaged relative error between the true system and the response system. Synchronization rate of convergence is slower than in Section 4.2.2 as a result of allowing the systems to oscillate independently while not driven on ω. For the results in Figures 4.31 and 4.32, we choose $\kappa = 0.625$, $s_1 = 0.2$, and $s_2 = 0.6$ for good autosynchronization results. Summarizing, we have demonstrated that it is possible to fill in missing data when hidden by clouds and, as an added bonus, estimate spatially-dependent model parameters.

Simulations are run for subsequently increasing percentages of hidden data. Figure 4.34 shows the synchronization errors for simulations after a simulation epoch of $t = 25036$. Specifically, the globally-averaged relative error between drive and response systems is plotted against the percentage of hidden data. It is clear that in-
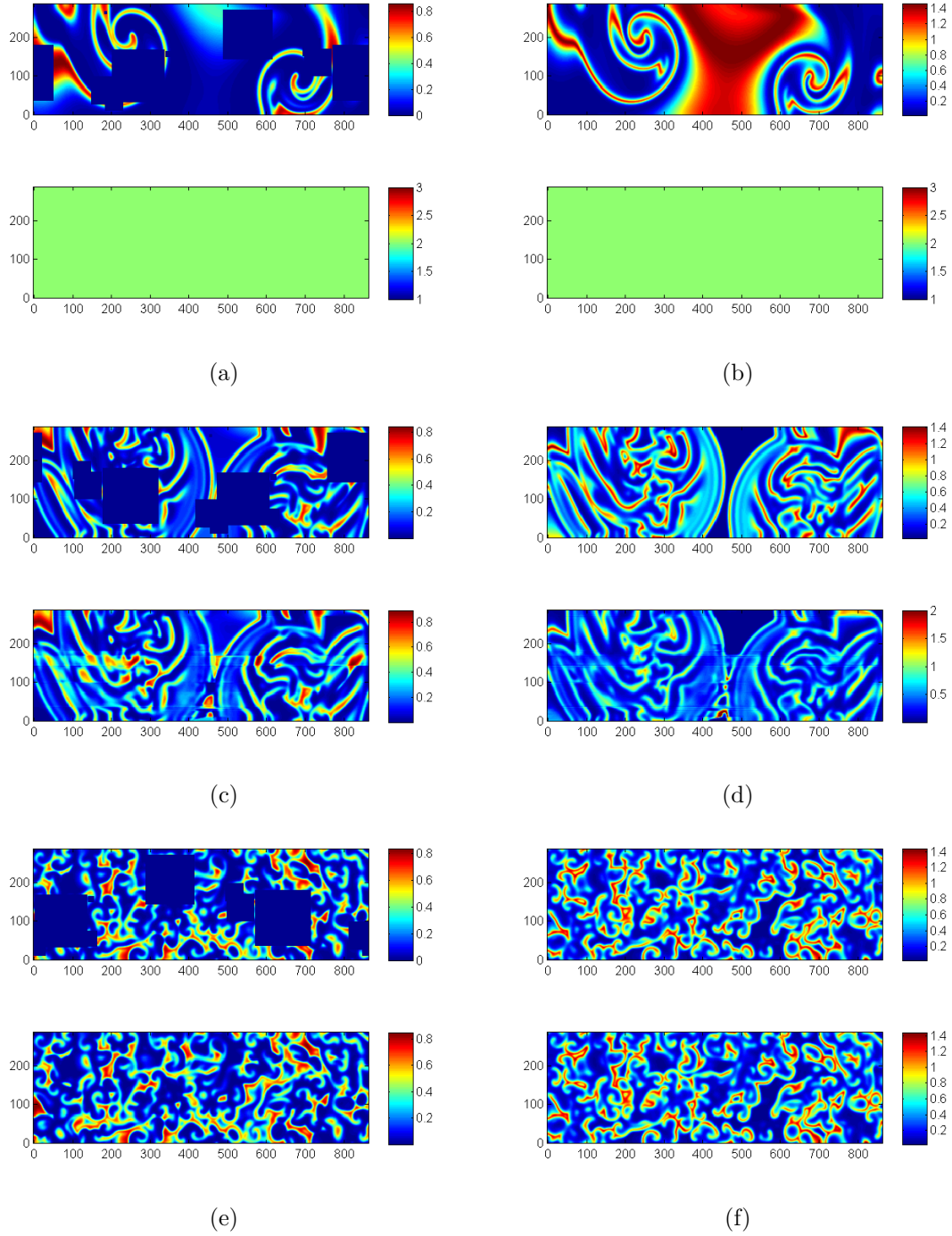
Figure 4.31: Autosynchronization of species with 25.5% of Ω is hidden at any point in time from clouds, however autosynchronization is observed. Each figure shows drive (top) and response (bottom) pairs. $P(x, y, 0)$ and $\hat{P}(x, y, 0)$ in 4.31a, $P(x, y, 200)$ and $\hat{P}(x, y, 200)$ in 4.31c, and $P(x, y, 25036)$ and $\hat{P}(x, y, 25036)$ in 4.31e. $Z(x, y, 0)$ and $\hat{Z}(x, y, 0)$ in 4.31b, $Z(x, y, 200)$ and $\hat{Z}(x, y, 200)$ in 4.31d, and $Z(x, y, 25036)$ and $\hat{Z}(x, y, 25036)$ in 4.31f.
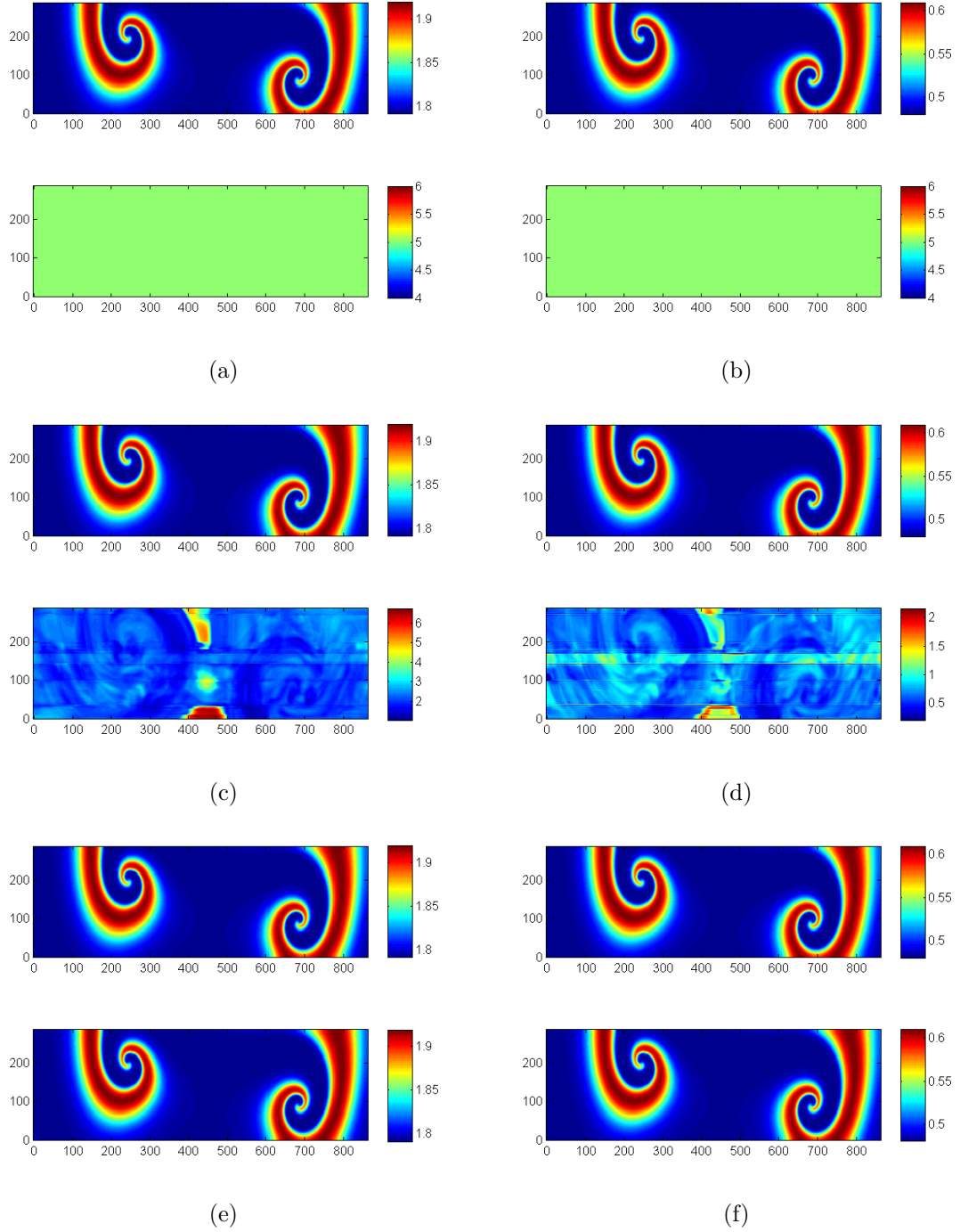
Figure 4.32: Autosynchronization of parameters with 25.5% of Ω is hidden at any point in time from clouds, however autosynchronization is observed. Each figure shows drive (top) and response (bottom) pairs. $k(x,y)$ and $\hat{k}(x,y,0)$ in 4.32a, $k(x,y)$ and $\hat{k}(x,y,200)$ in 4.32c, and $k(x,y)$ and $\hat{k}(x,y,25036)$ in 4.32e. $m(x,y)$ and $\hat{m}(x,y,0)$ in 4.32b, $m(x,y)$ and $\hat{m}(x,y,200)$ in 4.32d, and $m(x,y)$ and $\hat{m}(x,y,25036)$ in 4.32f.
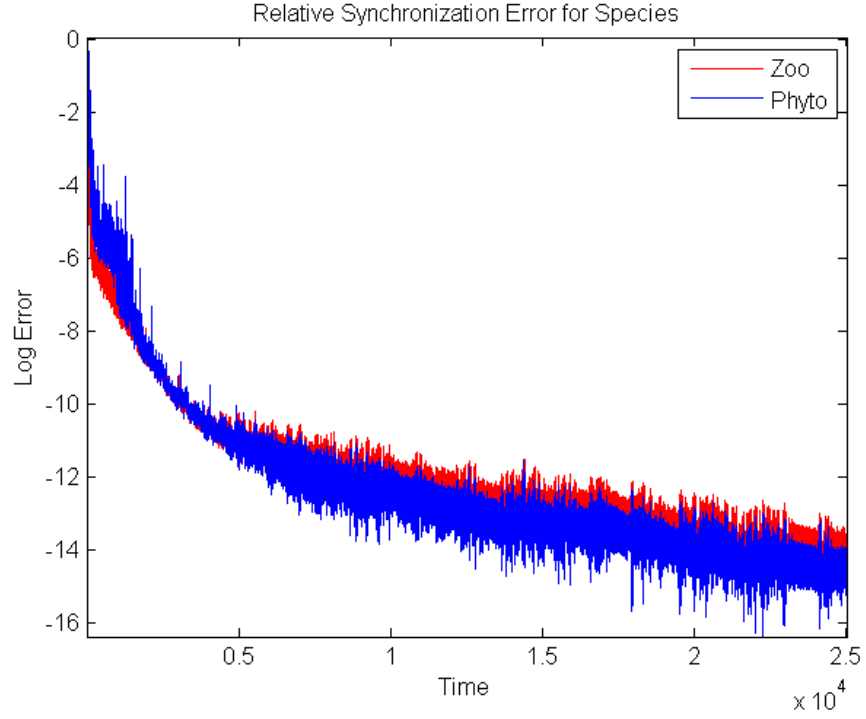
(a)
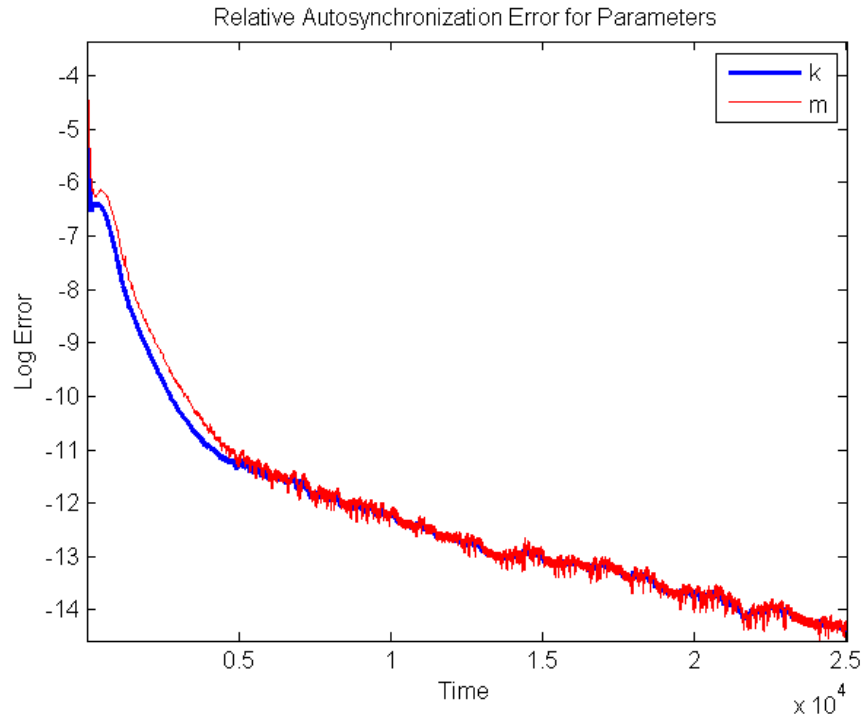
(b)

Figure 4.33: Globally-averaged relative synchronization errors. Errors given by simulation shown in Figures 4.31 and 4.32 shown to drop to within 5.7×10^{-7} despite ever-present clouds.

creasing amounts of hidden data eventually slows down the speed of synchronization, though as long as the clouds move, parameters and species are eventually observed. A counter-intuitive result is that the assimilation quality actually improves by hiding data through about 13% before worsening as a larger percentage of data is hidden. For these simulations, the same initial conditions are used throughout for consistency.

These results are a major development for use with real data. In fact the autosynchronization method is capable of data assimilation by revealing hidden phytoplankton and zooplankton densities and estimating model parameters. The technique is fairly robust to spatial subsampling, temporal subsampling, and complex spatially-dependent parameters. However, we know that plankton are somewhat subject to advection by ocean currents and such model physics should be assumed for use in specific coastal locations. Such improvements will be discussed in Chapter 6.

Moreover, this chapter is merely a demonstration of autosynchronization applied to a remote sensing problem. Results here require analytical reinforcement, including a discussion of the basin of attraction for the synchronization manifold and allowable coupling strengths to observe synchronization and parameter estimation. This is the topic of the following chapter, where we provide rigorous analysis of manifold stability.
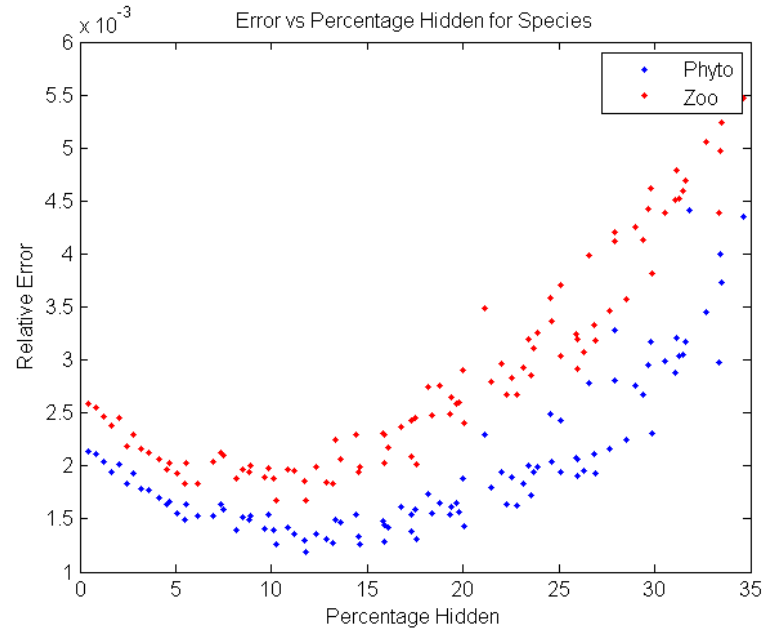
(a)
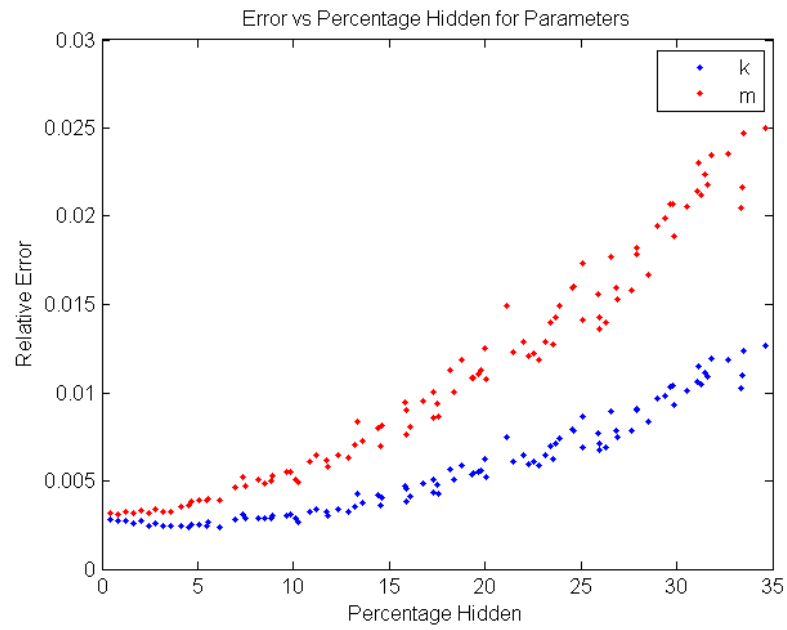
(b)

Figure 4.34: Synchronization error plotted against percentage data hidden after simulation for $t = 12000$. Species shown in Figure 4.34a and parameters in Figure 4.34b.

Chapter 5

Analysis of Synchronization

To this point, we have demonstrated a plethora of examples of two systems exhibiting identical synchronization, including coupling both species and coupling by sampling only one. While exciting, these are but heuristics and for use outside of benchmark problems a general theory is required to ensure the stability of the synchronization manifold for a particular coupling scheme. A solid proof under certain conditions that a coupling promotes an asymptotically stable synchronization manifold, would assure that subsequent observations will force a response model closer to the manifold, improving our current knowledge of the underlying dynamics.

There are classically two approaches for analyzing the stability of a synchronization manifold for chaotic systems [55]. The first method is based on the numerical approximation of Lyapunov exponents in the direction transverse to the synchronization manifold [55]. These exponents are called transverse Lyapunov exponents or conditional Lyapunov exponents (CLEs). A second method is called the Lyapunov direct method wherein an appropriate Lyapunov function is constructed [44].

The Lyapunov direct method is a direct proof for the stability of a fixed point and is thus used to prove the existence of fixed points for a variety of mathematical models ranging from simple ODEs, [83], to reaction-diffusion PDEs [83, 84]. The

method is used to prove stability of an identical synchronization manifold by a shift in coordinates such that the origin becomes the fixed point representing the manifold [44]. With respect to synchronization, the Lyapunov direct method has been used in the analysis of synchronization between coupled ODEs [44, 85] and coupled PDEs [75, 86, 87].

A drawback to the Lyapunov direct method is, to quote Strogatz, that "divine inspiration is usually required" to find such a function [88]. This led to the Lyapunov design approach, or the idea that one might work backward and design a coupling scheme to fit a desired Lyapunov function [87].

In lieu of a demonstrated Lyapunov function, the numerical approximation of Lyapunov exponents is a natural substitute. Conditional Lyapunov exponents have been used to analyze stability since the seminal work on synchronization by Pecora and Carroll [7, 50, 57, 73–75, 89]. Thus conditional Lyapunov exponents have been used to analyze the stability of the synchronization manifold for chaotic ODEs [7, 50, 57, 74, 90] and coupled PDEs that exhibit spatiotemporal chaos [73, 75].

Both methods are commonly used for parameter estimation problems within the synchronization framework. For example, the original method for estimating parameters based on synchronization, or autosynchronization, is proven robust by demonstrating a Lyapunov function [44]. Autosynchronization is also analyzed using conditional Lyapunov exponents [45]. Furthermore, a method for parameter estimation for a PDE is designed based on a Lyapunov function in [86], wherein the parameter is updated using a spectral decomposition. Also, parameters for a PDE system are estimated based on a Lyapunov design [87].

We have shown that it is possible to estimate spatially dependent parameters for a PDE system by autosynchronization using a combination of diffusive and complete replacement coupling of observed data to force the response model and parameters to synchronize with observables. Coupling strength drastically affects synchronization

115

speed and even stability [52]. We analyze the stability of the identical synchronization manifolds and discuss conditions for which synchronization is guaranteed for these systems.

We begin with some useful definitions and theorems necessary to discuss stability. We next show that the stability of a synchronization manifold can be recast into the introduced stability theory. We show that, under certain conditions, the proof in the ODE case extends immediately to the PDE case. Thus, we prove the synchronization manifold for a system of PDEs is in fact stable for certain coupling schemes used in parameter estimation by demonstrating a Lyapunov functional. We next discuss the numerical techniques used to estimate Lyapunov exponents. Finally, we analyze stability using conditional Lyapunov exponents for the cases in which we are unable to find an appropriate Lyapunov functional, considering systems of ODEs and extending to the approximation of PDEs.

5.1 Proving Stability for a Synchronization Manifold

Consider a nonlinear system

$$\dot{\mathbf{x}} = \mathbf{f}(\mathbf{x}), \tag{5.1}$$

where we wish to study the stability of the equilibria points. The study of a synchronization manifold may be recast as the study of the stability of a nonlinear system. Therefore, methods in analyzing the nonlinear system above are adequate to determine local and global stability of a synchronization manifold. We begin with some definitions and theorems pertaining to the stability of the equilibria of Eq (5.1).

Definition 5.1.1. (Perko, 127) *If* $\mathbf{f} \in C^1(E), L \in C^1(E)$ *and* ψ_t *is the flow of the differential equation (5.1), then for* $\mathbf{x} \in E$ *the derivative of the function* $L(\mathbf{x})$ *along*

116

the solution $\psi_t(\mathbf{x})$ is

$$\dot{L}(\mathbf{x}) = \frac{d}{dt}L(\phi_t(\mathbf{x}))|_{t=0} = DL(\mathbf{x})\mathbf{f}(\mathbf{x}). \tag{5.2}$$

In some sense, L acts as an energy-like function for such trajectories. In fact, trajectories can be shown to approach an equilibrium, thus answering stability questions, if L and its derivative exhibit certain properties.

Definition 5.1.2. (Alligood, Sauer, & Yorke, 305) *Let $\mathbf{x}_0$ be an equilibrium of Eq (5.1). A function $L : \mathbb{R}^n \to \mathbb{R}$ is called a* Lyapunov Function *for $\mathbf{x}_0$ if for some neighborhood E of $\mathbf{x}_0$ the following conditions hold:*

1. *$L(\mathbf{x}_0) = 0$, and $L(\mathbf{x}) > 0 \ \forall \ \mathbf{x} \neq \mathbf{x}_0$ in E, and*

2. *$\dot{L}(\mathbf{x}) \leq 0 \ \forall \ \mathbf{x} \in E$.*

The question of whether or not the identical synchronization manifold M is stable may be solved using an approach due to Lyapunov.

Theorem 5.1.3. (Perko, 127) *Let E be an open subset of $\mathbb{R}^n$ containing $\mathbf{x}_0$. Suppose that $\mathbf{f} \in C^1(E)$ and that $\mathbf{f}(\mathbf{x}_0) = 0$. Suppose further that there exists a Lyapunov function $L \in C^1(E)$. Then if $\dot{L}(\mathbf{x}) \leq 0 \ \forall \ \mathbf{x} \in E$, $\mathbf{x}_0$ is stable; if $\dot{L}(\mathbf{x}) < 0 \ \forall \ \mathbf{x} \in E \smallsetminus \{\mathbf{x}_0\}$, $\mathbf{x}_0$ is asymptotically stable; if $\dot{L}(\mathbf{x}) > 0 \ \forall \ \mathbf{x} \in E \smallsetminus \{\mathbf{x}_0\}$, $\mathbf{x}_0$ is unstable.*

Here, we demonstrate a Lyapunov functional to show the synchronization manifold is asymptotically stable for various response systems with respect to the drive system. For stability of a synchronization manifold, without loss of generality, we shift coordinates so that $L(\mathbf{0}) = 0$. If a Lyapunov functional can be found for our system, the synchronization manifold is proven stable in that domain; furthermore, if $\frac{dL}{dt}(\mathbf{0}) < 0$ then the manifold is asymptotically stable. Thus transverse perturbations will converge toward the manifold, which is requisite for our application.

5.1.1 A Lyapunov Function for an ODE

We use a simple example to introduce the method under consideration and begin with synchronization between drive and response systems when sampling both species. Therefore, we consider the ODE systems corresponding to Eq (4.7) and Eq (4.8), from Chapter 4,

$$
\begin{aligned}
\frac{dP}{dt} &= P(1-P) - \frac{PZ}{P+h}, & \text{Drive System} & \quad (5.3)\\
\frac{dZ}{dt} &= k\frac{PZ}{P+h} - mZ, & & \\
\frac{d\hat{P}}{dt} &= \hat{P}(1-\hat{P}) - \frac{\hat{P}\hat{Z}}{\hat{P}+h} + \kappa(P-\hat{P}), & \text{Response System} & \\
\frac{d\hat{Z}}{dt} &= k\frac{\hat{P}\hat{Z}}{\hat{P}+h} - m\hat{Z} + \kappa(Z-\hat{Z}). & &
\end{aligned}
$$

This system will synchronize very quickly for large enough coupling strength κ, perhaps no surprise for the ODE case. Simulation results are shown in Figure 5.1 where solutions for the two systems are plotted together with solid lines representing the drive system and dashed lines representing the response system. In Figure (b), we see log of the absolute values of the errors between drive and response systems plotted as the systems evolve. Initial conditions were taken from the drive system after transients to be $P(0) = 0.0282$, $Z(0) = 0.2$, and $\hat{Z}(0) = \hat{P}(0) = 2$. Furthermore, we let the coupling strength $\kappa = 2$.

Theorem 5.1.4. *The identical synchronization manifold $M = [P = \hat{P}, Z = \hat{Z}]$ is globally asymptotically stable for the coupling between drive and response systems in Eq (5.3) for $\kappa = 2$.*

Proof. The identical synchronization manifold for the systems Eq (5.3) can be written

(a)

(b)
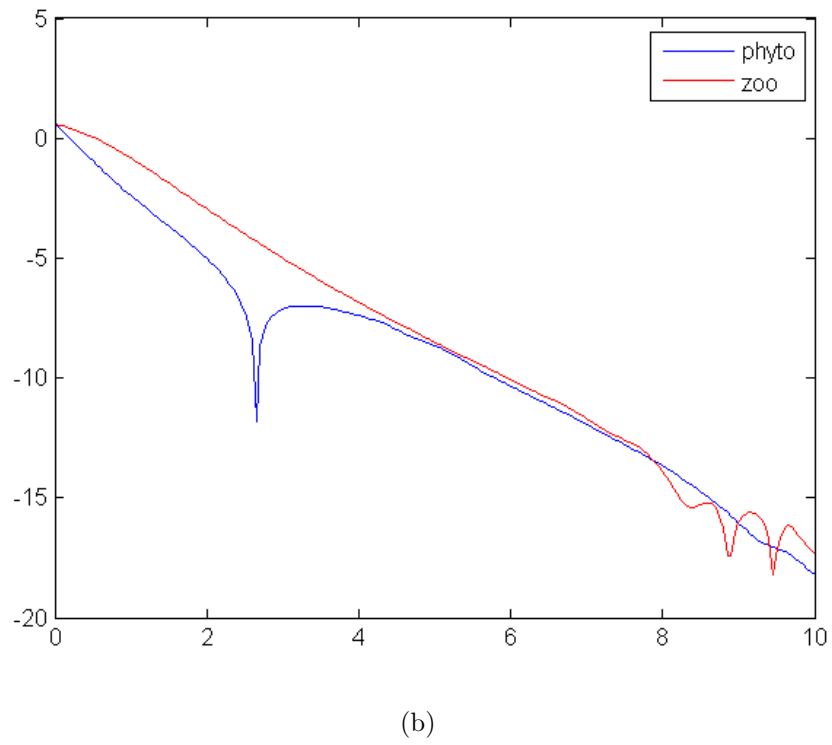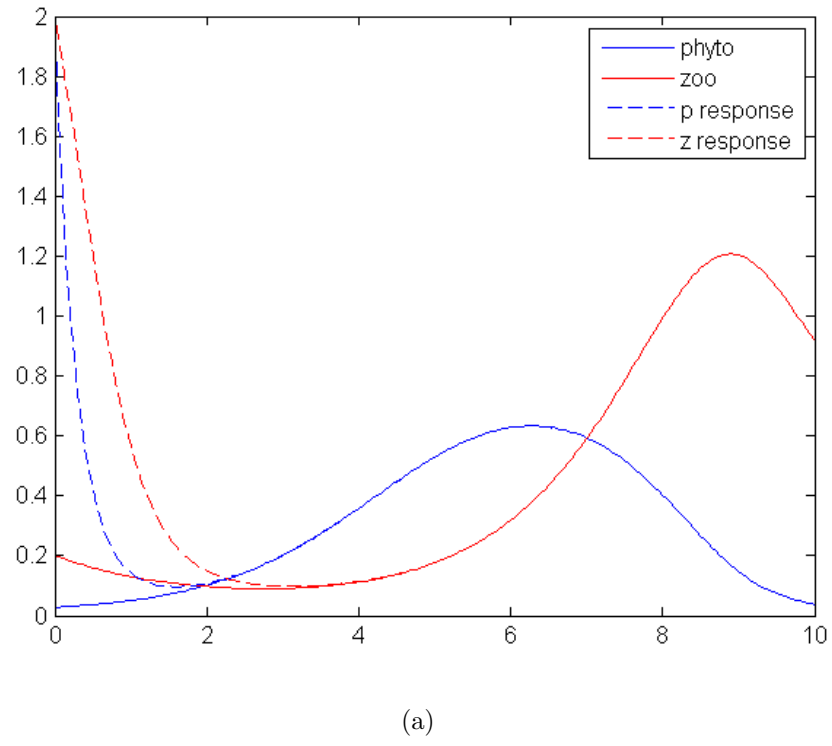
Figure 5.1: Solutions for drive and response systems plotted over time shown in (a). Log of the absolute values of errors between drive and response shown over time in (b). Coupling strength used is $\kappa = 2$.

as $M = \{P = \hat{P}, Z = \hat{Z}\}$. However, we make the change of coordinates

$$\mathbf{e} = \begin{pmatrix} e_1 \\ e_2 \end{pmatrix} = \begin{pmatrix} P - \hat{P} \\ Z - \hat{Z} \end{pmatrix} \tag{5.4}$$

such that M can now be written $M = \{0, 0\}$. That is, we simply study the stability of the origin, a question we may answer with a Lyapunov function in the new coordinate system. Therefore, we suggest the Lyapunov function

$$L(e_1, e_2) = e_1^2 + e_2^2. \tag{5.5}$$

The derivative of L with respect to time is

$$\frac{1}{2}\frac{dL}{dt} = e_1\frac{de_1}{dt} + e_2\frac{de_2}{dt}, \tag{5.6}$$

using the chain rule. And since

$$\frac{de_1}{dt} = e_1(1-\kappa) + \hat{P}^2 - P^2 + \frac{\hat{P}\hat{Z}}{\hat{P}+h} - \frac{PZ}{P+h}, \tag{5.7}$$

$$\frac{de_2}{dt} = k\left(\frac{PZ}{P+h} - \frac{\hat{P}\hat{Z}}{\hat{P}+h}\right) - e_2(m+\kappa),$$

we have that

$$\frac{1}{2}\frac{dL}{dt} = e_1^2(1-\kappa) + e_1\left(\hat{P}^2 - P^2 + \frac{\hat{P}\hat{Z}}{\hat{P}+h} - \frac{PZ}{P+h}\right) \tag{5.8}$$

$$+ e_2 k\left(\frac{PZ}{P+h} - \frac{\hat{P}\hat{Z}}{\hat{P}+h}\right) - e_2^2(m+\kappa),$$

which we would like to be strictly negative. The terms are rather messy, but we have

the freedom to choose $\kappa > 1$ large enough such that

$$|(1 - \kappa)| > e_1 \left(\hat{P}^2 - P^2 + \frac{\hat{P}\hat{Z}}{\hat{P} + h} - \frac{PZ}{P + h} \right), \tag{5.9}$$

$$|m + \kappa| > e_2 k \left(\frac{PZ}{P + h} - \frac{\hat{P}\hat{Z}}{\hat{P} + h} \right),$$

for all $t > 0$, which holds for our chosen κ. We can bound these terms in a worst-case scenario. Since $0 < P < 1$ and $0 < Z < 2$, and since the response system is clipped at $0 < \hat{P} < 2$, and $0 < \hat{Z} < 2$, we must have that $|e_1| < 2$ and $|e_2| < 2$. Thus if we choose κ large enough such that

$$|(1 - \kappa)| > 6 > -2 \left(0 - 1 + \frac{0}{0 + h} - \frac{2}{1 + h} \right), \tag{5.10}$$

$$|m + \kappa| > 8 > 4 \left(\frac{2}{1 + h} - \frac{0}{0 + h} \right), \tag{5.11}$$

an extremely liberal bound, we are assured that $\frac{dL}{dt} < 0$ for all $t > 0$. Thus, we have demonstrated a Lyapunov function for the system Eq (5.3) and by Theorem 5.1.3, are assured that the origin, corresponding to the identical synchronization manifold is asymptotically stable. □

Thus we have proven that for all initial conditions, and large enough coupling strength, we will observe synchronization between the two systems.

Consider another form of coupling between the systems as

$$\begin{aligned}
\frac{dP}{dt} &= P(1 - P) - \frac{PZ}{P + h}, && \text{Drive System} && (5.12) \\
\frac{dZ}{dt} &= k\frac{PZ}{P + h} - mZ, \\
\frac{d\hat{P}}{dt} &= \hat{P}(1 - P) - \frac{PZ}{P + h} + \kappa(P - \hat{P}), && \text{Response System} \\
\frac{d\hat{Z}}{dt} &= k\frac{PZ}{P + h} - m\hat{Z},
\end{aligned}$$

where we are coupling much more for the sake of analytic repose.

Theorem 5.1.5. *The identical synchronization manifold $M = [P = \hat{P}, Z = \hat{Z}]$ is globally asymptotically stable for the coupling between drive and response systems in Eq (5.12) for $\kappa > 1$.*

Proof. With this coupling and the change of coordinates, we find that

$$\frac{de_1}{dt} = e_1(1 - P - \kappa), \tag{5.13}$$
$$\frac{de_2}{dt} = -e_2(m + \kappa),$$

which is much easier to handle analytically. A Lyapunov function is given again by Eq (5.5) and thus

$$\frac{1}{2}\frac{dL}{dt} = e_1^2(1 - P - \kappa) - e_2^2 m, \tag{5.14}$$

which is strictly negative if $\kappa > 1$. Again, under the conditions of Theorem 5.1.3, we are guaranteed that the identical synchronization manifold is globally asymptotically stable. $\qquad\square$

Results are shown in Figure 5.2, where drive and response systems are shown to synchronize identically after a short time by choosing $\kappa = 1$.
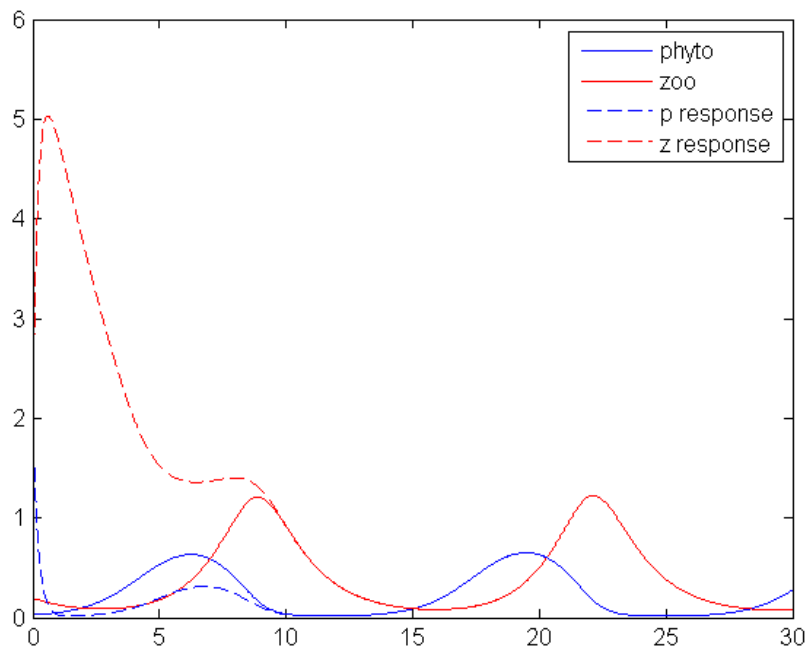
(a)
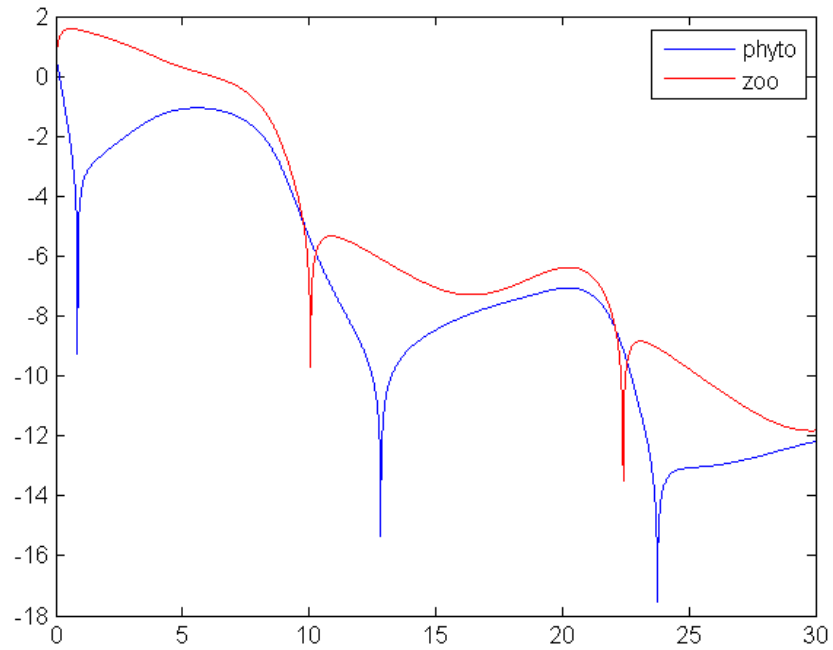
(b)

Figure 5.2: Solutions for drive and response systems plotted over time shown in (a). Log of the absolute values of errors between drive and response shown over time in (b). Coupling strength used is $\kappa = 1$.

5.1.2 A Lyapunov Functional for a PDE

We next extend the Lyapunov function from the ODE case to a Lyapunov functional for the PDE case. This provides a blueprint for proving asymptotic stability when using a certain class of Lyapunov functions. We will require the vector form of Green's Identity in this extended framework.

Theorem 5.1.6. (Marsden, 575) *Let $\Omega \subset \mathbb{R}^2$ be a simple region and let $\partial\Omega$ be its boundary. Let $\mathbf{F} = P\mathbf{i} + Q\mathbf{j}$ be a C^1 vector field on D. Then*

$$\int_{\partial\Omega} f\nabla g \cdot \mathbf{n}\, dS = \int_{\Omega} (f\nabla^2 g + \nabla f \cdot \nabla g)\ dxdy. \tag{5.15}$$

Recall the domain, Ω is a simple compact subset of $\mathbf{R}^2$ with smooth boundary, $\partial\Omega$. Now, consider the system Eq (5.12) extended as

$$
\begin{aligned}
\frac{\partial P}{\partial t} &= \triangle P + P(1-P) - \frac{PZ}{P+h}, & \text{Drive System} \quad (5.16)\\
\frac{\partial Z}{\partial t} &= \triangle Z + k\frac{PZ}{P+h} - mZ, &\\
\frac{\partial \hat{P}}{\partial t} &= \triangle \hat{P} + \hat{P}(1-P) - \frac{PZ}{P+h} + \kappa(P - \hat{P}), & \text{Response System}\\
\frac{\partial \hat{Z}}{\partial t} &= \triangle \hat{Z} + k\frac{PZ}{P+h} - m\hat{Z}, &
\end{aligned}
$$

over Ω.

Theorem 5.1.7. *The identical synchronization manifold $M = [P = \hat{P}, Z = \hat{Z}]$ is globally asymptotically stable for the coupling between drive and response reaction-diffusion PDE systems in Eq (5.16) for $\kappa > 1$.*

Proof. With the change of coordinates this system becomes

$$
\begin{aligned}
\frac{\partial e_1}{\partial t} &= \triangle e_1 + e_1 - Pe_1 - \kappa e_1,\\
\frac{\partial e_2}{\partial t} &= \triangle e_2 - me_2, \tag{5.17}
\end{aligned}
$$

because of the linearity of the Laplacian. The reaction part of the reaction-diffusion system Eq (5.17) is continuously differentiable since we enforce that $P > 0$ for all $x, y,$ and t. We introduce the Lyapunov functional $\hat{L} : C^2 \times C^2 \to \mathbb{R}$

$$\hat{L}(t) = \int_\Omega L(e_1(x, y, t), e_2(x, y, t)) \ dxdy. \tag{5.18}$$

Then,

$$\frac{\partial \hat{L}}{\partial t} = \frac{\partial}{\partial t} \int_\Omega L(e_1(x, y, t), e_2(x, y, t)) \ dxdy,$$

$$= \int_\Omega \frac{\partial L}{\partial e_1} \frac{\partial e_1}{\partial t} + \frac{\partial L}{\partial e_2} \frac{\partial e_2}{\partial t} \ dxdy,$$

$$= \int_\Omega \nabla L \cdot \begin{bmatrix} \frac{de_1}{dt} \\ \frac{de_2}{dt} \end{bmatrix} dxdy,$$

$$= \int_\Omega \nabla L \cdot \begin{bmatrix} \triangle e_1 + \frac{de_1}{dt} \\ \triangle e_2 + \frac{de_2}{dt} \end{bmatrix} dxdy,$$

$$= \int_\Omega \left(\sum_{i=1}^{2} \frac{\partial L}{\partial e_i} \right) \triangle e_i \ dxdy + \int_\Omega \frac{\partial L}{\partial t} \ dxdy,$$

where we invoke the Lebesgue Dominated Convergence Theorem to differentiate under the integral, since $|e_1| < 2$ and $|e_2| < 2$, $|L| < D = 8$. Therefore D is integrable over Ω for all t and the derivative $\frac{\partial L}{\partial t}$ exists for all $t > 0$ and all $\mathbf{x} \in \Omega$.

We have already shown that for $1 - P - \kappa < 0$, then $\frac{\partial L}{\partial t} < 0$ for all $\mathbf{x} \in \Omega, t > 0$,

which implies $\int_\Omega \dot{L} < 0$. From Green's identity, we have

$$\int_\Omega \frac{\partial L}{\partial e_i} \triangle e_i \ dxdy = \int_{\partial\Omega} \frac{\partial L}{\partial e_i} \frac{\partial e_i}{\partial \mathbf{n}} \ dxdy - \int_\Omega \nabla \left(\frac{\partial L}{\partial e_i} \right) \cdot \nabla e_i \ dxdy,$$

$$= \int_\Omega \sum_{j=1}^n \sum_{k=1}^n \left[\frac{\partial^2 L}{\partial e_i \partial e_k} \frac{\partial e_i}{\partial x_j} \frac{\partial e_k}{\partial x_j} \right] dxdy.$$

The above relies on zero-flux boundary conditions so that $\partial e_i / \partial \mathbf{n} = 0 \ \forall i$, which follows from the boundary conditions on the drive and response PDEs. If $L(\mathbf{x})$ satisfies

$$\text{1.} \quad L(\mathbf{x}) = \sum_{i=1}^n h_i(x_i), \tag{5.19}$$

$$\text{2.} \quad h_i''(\mathbf{x}) \geq 0 \quad \text{for } i = 1, 2, ...n,$$

then the matrix $\left(\frac{\partial L}{\partial e_i \partial e_k} \right)$ is positive definite $\forall i, k$ [83]. Since both conditions hold for our choice of L, we have shown that

$$\frac{\partial \hat{L}}{\partial t} < 0, \tag{5.20}$$

and the synchronization manifold $M = \{P = \hat{P}, Z = \hat{Z}\}$ is asymptotically stable. $\square$

Since this analysis presumed all possible values of the response model, $\hat{P}, \hat{Z} \in [0, 2]$ $\forall \ x, y \in \Omega$, and $\forall \ t > 0$, this is actually a global result.

Thus we have proven why identical synchronization is observed for the spatially-dependent drive-response PDE systems corresponding to Eq (5.3) and Eq (5.12). In fact, spatially-dependent parameters given by Eq (4.20), Eq (4.21), or the spiral parameters shown in Figure 4.6e will have little affect on the validity of this proof as they are bounded by the scalar values $k(x, y) < 2$ and $m(x, y) < 0.6$ on a compact domain.

5.1.3   Autosynchronization

We have shown that it is sufficient to demonstrate a Lyapunov function, although restricted to a certain class of functions, for a corresponding ODE system in order to prove asymptotic stability on M. Therefore, we now demonstrate a Lyapunov function for some autosynchronization coupling schemes and omit the PDE extension as it simply follows from Theorem 5.1.7. Therefore, consider the autosynchronization design below

$$
\begin{aligned}
\frac{\partial P}{\partial t} &= \triangle P + P(1-P) - \frac{PZ}{P+h}, & \text{Drive} \quad (5.21)\\
\frac{\partial Z}{\partial t} &= \triangle Z + k\frac{PZ}{P+h} - mZ, \\
\frac{\partial \hat{P}}{\partial t} &= \triangle \hat{P} + \hat{P}(1-P) - \frac{\hat{P}Z}{P+h} + \kappa(P - \hat{P}), & \text{Response}\\
\frac{\partial \hat{Z}}{\partial t} &= \triangle \hat{Z} + k\frac{PZ}{P+h} - \hat{m}\hat{Z}, \\
\frac{\partial \hat{m}}{\partial t} &= Z(\hat{Z} - Z),
\end{aligned}
$$

where only m is to be estimated and both species are sampled.

Theorem 5.1.8. *The identical synchronization manifold $M = [P = \hat{P}, Z = \hat{Z}, m = \hat{m}]$ is globally asymptotically stable for the coupling between drive and response reaction-diffusion PDE systems in Eq (5.21) for $\kappa > 1$.*

Proof. The corresponding ODE equations in the transformed coordinate system are

$$
\begin{aligned}
\dot{e}_1 &= e_1 - Pe_1 - \frac{Ze_1}{P+h} - \kappa e_1, \\
\dot{e}_2 &= -mZ - \hat{m}\hat{Z}, \\
\dot{e}_3 &= -Ze_2.
\end{aligned}
$$

We extend the Lyapunov function for the coupling in Eq (5.21) as,

$$L(e_1, e_2, e_3) = e_1^2 + e_2^2 + e_3^2. \tag{5.22}$$

Then

$$\frac{1}{2}\frac{\partial L}{\partial t} = e_1\dot{e}_1 + e_2\dot{e}_2 + e_3\dot{e}_3$$

$$= e_1^2\left(1 - P - \frac{Z}{P+h} - \kappa\right) - e_2(-mZ - \hat{m}\hat{Z}) + Ze_3e_2,$$

where P, $\frac{Z}{P+h}$, and κ are strictly positive. Ignoring the e_1^2 term, the rest of the equation expands as

$$-e_2(-mZ - \hat{m}\hat{Z}) + Ze_3e_2 = -e_2mZ + e_2\hat{m}Z + e_2\hat{m}\hat{Z} - e_3Z\hat{Z} + e_3Z^2,$$

$$= -mZ^2 + mZ\hat{Z} + \hat{m}Z\hat{Z} - \hat{m}Z^2 - mZ\hat{Z}\hat{m}Z\hat{Z} + mZ^2 - \hat{m}Z^2,$$

$$= 2\hat{m}Z\hat{Z} - \hat{m}\hat{Z}^2 - \hat{m}Z^2,$$

$$= -\hat{m}(Z - \hat{Z})^2,$$

$$= -\hat{m}e_2^2.$$

So the derivative of the Lyapunov function simplifies to

$$\frac{1}{2}\frac{\partial L}{\partial t} = -e_1^2\left(1 - P - \frac{Z}{P+h} - \kappa\right) - \hat{m}e_2^2, \tag{5.23}$$

which is strictly negative for $\hat{m} > 0$ and $\kappa > 1$. We restrict parameters to be non-negative so if $(1 - P - \frac{Z}{P+h} - \kappa) < 0$ then $\frac{\partial L}{\partial t} < 0$ and the synchronization manifold is asymptotically stable; we observe $\hat{m} \to m$, $\hat{P} \to P$, and $\hat{Z} \to Z$ for the ODE system. $\square$

Figure 5.3 shows the expected results based on the analysis above for $\kappa = 2.6$. Initial conditions are set to $\hat{P} = \hat{Z} = \hat{m} = 2$. Both species and the parameter are shown to synchronize identically over time.
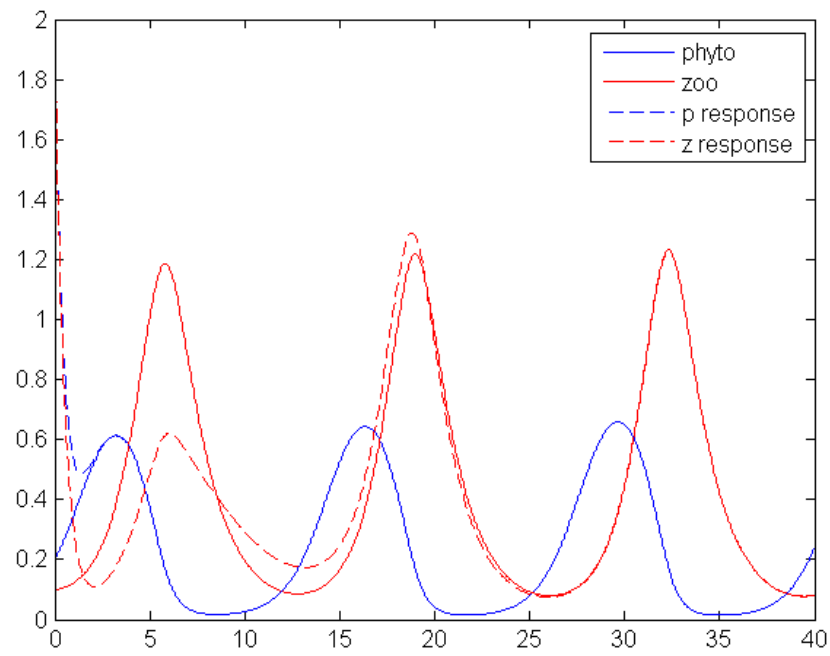
(a)
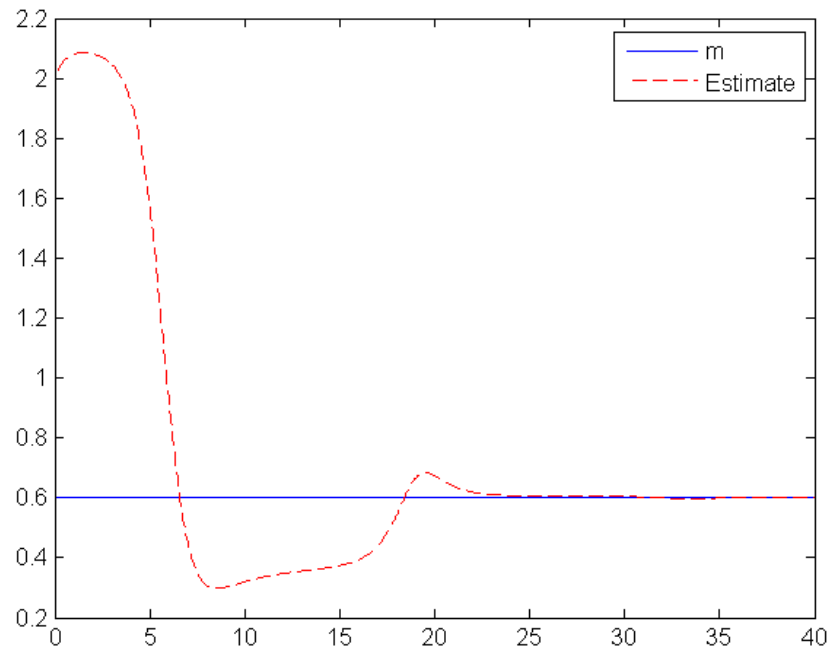
(b)

Figure 5.3: Solutions for drive and response systems plotted over time shown in (a). Drive and response parameter values m and $\hat{m}$ shown in (b). Coupling strength used is $\kappa = 2.6$.
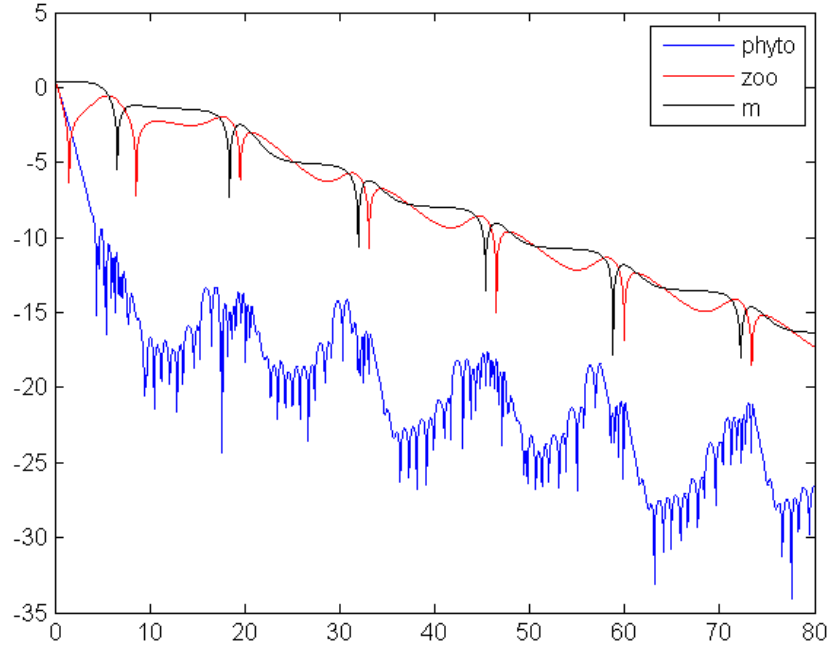
Figure 5.4: Log of the absolute values of errors between drive and response shown over time.

With the analysis shown in Section 5.1.2, we are able to quickly extend to the PDE case with spatially dependent parameters and be assured of the asymptotic stability of the synchronization manifold. Thus, the preceding analysis allows one to look for a Lyapunov function for a corresponding ODE system, a much easier task.

We see the expected results for the PDE system in Figures 5.5 and 5.6, where we used the same coupling strength as shown for the ODE in Figures 5.3 and 5.4. For this simulation, initial conditions are set to $\hat{P}(x, y, 0) = \hat{Z}(x, y, 0) = \hat{m}(x, y, 0) = 2$ to agree with the ODE simulation. The images represent drive-response pairs for phytoplankton, zooplankton, and the parameter $m(x, y)$. The first row shows initial conditions, the second row describes results at $t = 30$, and the third row represents results at $t = 95$, after which simulations were terminated since the parameter is estimated to satisfaction. The parameter $m(x, y)$ has been estimated to within a globally-averaged relative error of $1.0e^{-7}$. Figure 5.7 shows the globally-averaged

relative synchronization errors between phytoplankton, zooplankton, and the parameters on a log scale. We see phytoplankton synchronizes very rapidly with respect to the other two pairs of components.
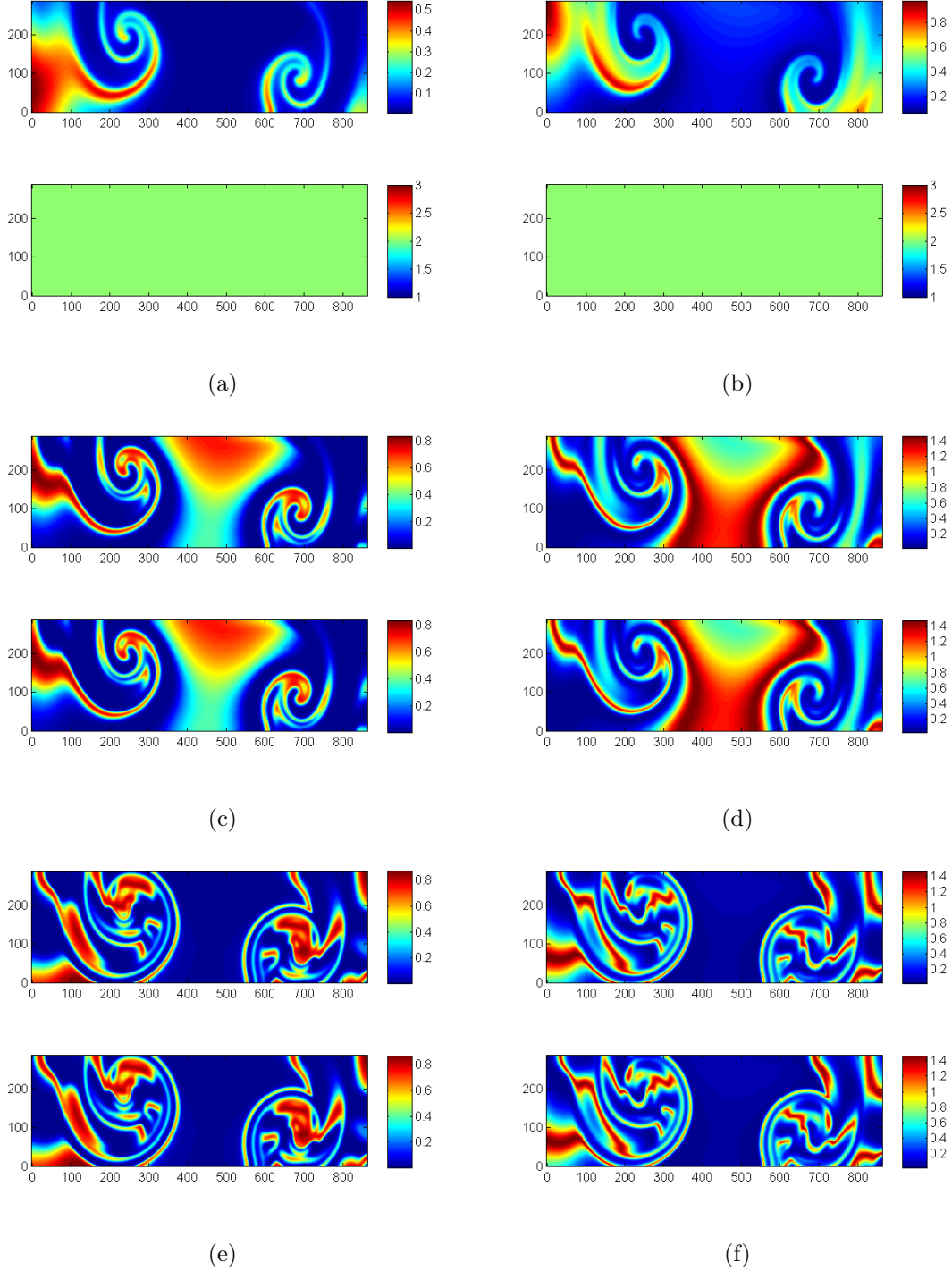
Figure 5.5: Autosynchronization of response system Eq (5.21) and spatially dependent parameter m. Figure 5.5a describes $P(x, y, 0)$ over $\hat{P}(x, y, 0)$, Figure 5.5c describes $P(x, y, 30)$ over $\hat{P}(x, y, 30)$, and Figure 5.5e describes $P(x, y, 95)$ over $\hat{P}(x, y, 95)$. Similarly, Figure 5.5b describes $Z(x, y, 0)$ over $\hat{Z}(x, y, 0)$, Figure 5.5d describes $Z(x, y, 30)$ over $\hat{Z}(x, y, 30)$, and Figure 5.5f describes $Z(x, y, 95)$ over $\hat{Z}(x, y, 95)$. Model parameters given by swirly parameters shown in Figure 4.6f. Coupling strength is set to $\kappa = 2.6$.

(a)   (b)

(c)
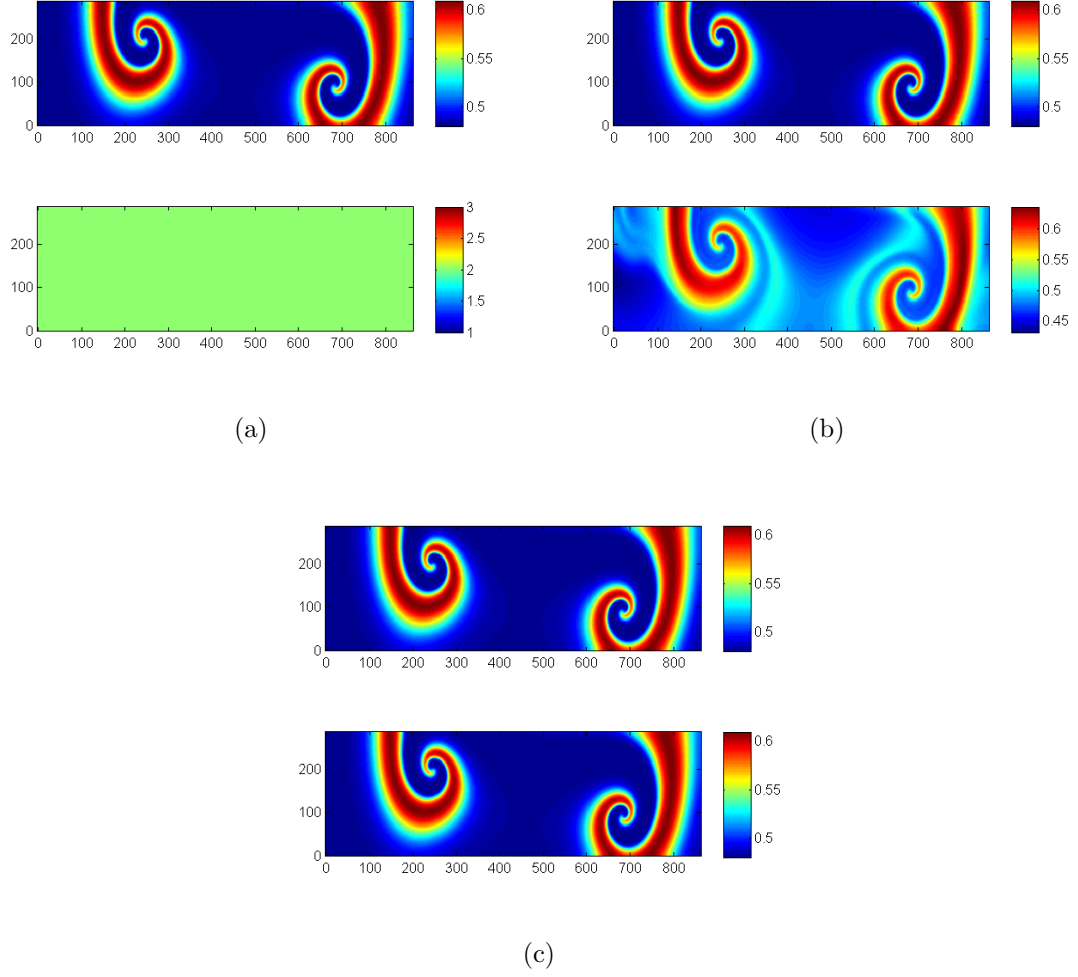
Figure 5.6: Autosynchronization of response system Eq (5.21) and spatially dependent parameter m. Figure 5.6a describes $M(x,y)$ over $\hat{M}(x,y,0)$, Figure 5.6b describes $M(x,y)$ over $\hat{M}(x,y,30)$, and Figure 5.6c describes $M(x,y)$ over $\hat{M}(x,y,95)$. Model parameters given by swirly parameters shown in Figure 4.6f. Coupling strength is set to $\kappa = 2.6$.
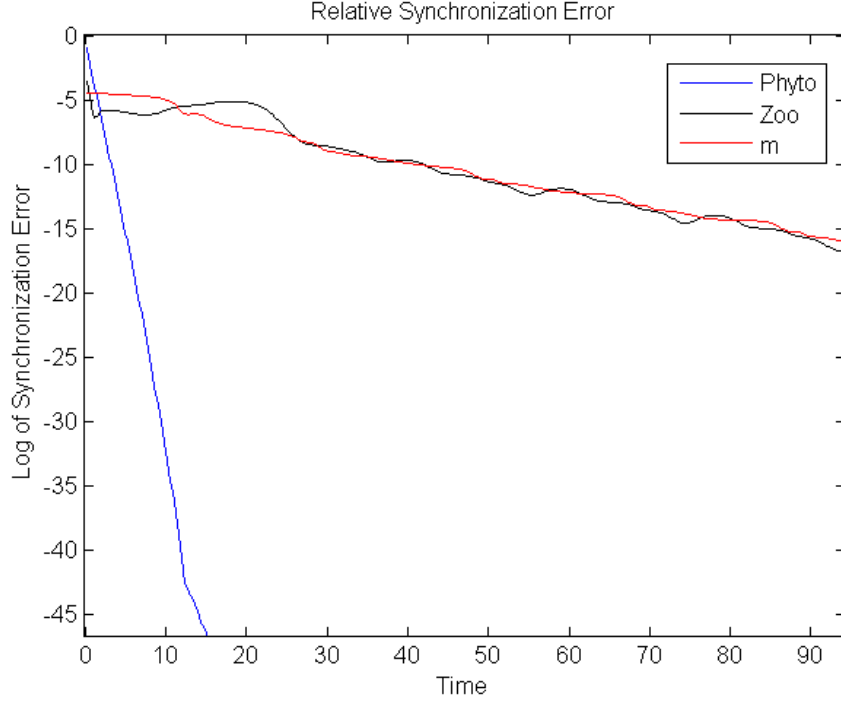
Figure 5.7: Globally averaged relative synchronization errors shown between drive and response systems. Coupling strength used is $\kappa = 2.6$. Phytoplankton shown in red, zooplankton shown in blue, parameter m shown in black.

Our choice of L obeys Eq (5.19) and we are guaranteed that the analysis extends to the PDE case by choosing,

$$\hat{L}(t) = \int_\Omega L(e_1(x, y, t), e_2(x, y, t), e_3(x, y, t)) \ dxdy, \tag{5.24}$$

thus proving asymptotic stability for the synchronization manifold $[P = \hat{P}, Z = \hat{Z}, m = \hat{m}]$ for the appropriate range of coupling strengths. This is a remarkable tool with respect to rigorously proving asymptotic stability, however is very difficult to obtain given arbitrary couplings. In fact, we have been unable to find a Lyapunov function for many of the couplings shown in Chapter 4 where only phytoplankton are sampled. Due to the complexity of the equations in the transformed coordinate system whence only sampling phytoplankton, a Lyapunov function has been elusive and therefore so has proof of stability. Thus, we next turn to empirical methods for

many of the response systems considered in Chapter 4.

5.2 Conditional Lyapunov Exponents

Since several the of above drive-response systems have proven quite difficult to analyze by the Lyapunov direct method, we now analyze instead using conditional Lyapunov exponents. Conditional Lyapunov exponents are often used to analyze the stability of a synchronization manifold [7,50,57,73–75,89]. Conditional Lyapunov exponents are also known as transverse Laypunov exponents due to the fact that they were originally to be computed in the directions transverse to the synchronization manifold [57]. Clearly a maximum exponent being negative would imply that perturbations die out and the manifold is at least locally asymptotically stable.

We begin by defining some terms relevant to computing Lyapunov exponents and derive the associated variational equations. We then briefly discuss some numerical techniques used to estimate Lyapunov exponents. The conditional Lyapunov exponents are computed for some of the coupled ODE systems from Chapter 4 and shown to be negative for the coupling strengths used. Finally, the conditional Lyapunov exponents are estimated for the n coupled ODEs representing the numerical approximation of PDEs to analyze stability in the PDE case.

5.2.1 Lyapunov Exponents

We first build some vocabulary to define a Lyapunov exponent. Consider a dynamical system

$$\dot{\mathbf{x}} = \mathbf{f}(\mathbf{x}), \tag{5.25}$$

for $\mathbf{x} \in \mathbb{R}^n$ and $\mathbf{f} : \mathbb{R}^n \to \mathbb{R}^n$.

Definition 5.2.1. (Yorke, 69) *Let* $\mathbf{f} : \mathbb{R}^n \times \mathbb{R}^n$ *, and let* $\mathbf{x} \in \mathbb{R}^n$ *. The* Jacobian

matrix *of $\boldsymbol{f}$ at $\boldsymbol{x}$, denoted $\boldsymbol{Df(x)}$, is the matrix*

$$\boldsymbol{Df(x)} = \begin{pmatrix} \frac{\partial f_1}{\partial x_1}(\mathbf{x}) & \cdots & \frac{\partial f_1}{\partial x_n}(\mathbf{x}) \\ \vdots & & \vdots \\ \frac{\partial f_n}{\partial x_1}(\mathbf{x}) & \cdots & \frac{\partial f_n}{\partial x_n}(\mathbf{x}) \end{pmatrix} \tag{5.26}$$

of partial derivatives evaluated at $\boldsymbol{x}$.

We now define the notion of a solution set of a differential equation for arbitrary times and initial conditions.

Definition 5.2.2. *(Alligood, Sauer, & Yorke, 277) Given a dynamical system, Eq (5.25), the flow ϕ is the function of time and initial condition that represents the set of solutions. That is $\phi(t, \mathbf{x}_0)$ is the value at time t of the solution with initial value $\mathbf{x}_0$.*

We use a more compact notation and denote the flow as $\phi_t(\mathbf{x}_0)$. Since the flow is itself a function, we define a map for the flow for the differential equation.

Definition 5.2.3. *(Alligood, Sauer, & Yorke, 381) The* time-τ map *of a flow $\phi_\tau(\mathbf{x}_0)$ is the mapping of the solution of a differential equation 5.25 from initial condition $\mathbf{x}_0$ to some $\mathbf{x} \in \mathbb{R}^n$ after a fixed time τ.*

Next we define the linearization about a solution trajectory or a flow with initial condition $\phi_t(\mathbf{x}_0)$. For a fixed τ, the Jacobian of the flow $D\phi_\tau(\mathbf{x}_0)$ is an $n \times n$ matrix. We derive the *variational equation* for the differential equation in the following way. Write the time derivative of the time map of the flow as

$$\frac{d}{dt}\phi_t(\mathbf{x}_0) = \mathbf{f}(\phi_t(\mathbf{x}_0)),$$

which follows by definition. Then differentiate with respect to $\mathbf{x}_0$ using the chain rule

$$\frac{d}{dt}\mathbf{D}\phi_t(\mathbf{x}_0) = \mathbf{Df}(\phi_t(\mathbf{x}_0)) \cdot \mathbf{D}\phi_t(\mathbf{x}_0).$$

Definition 5.2.4. (Alligood, Sauer, & Yorke, 382) *Given a dynamical system 5.25, and a corresponding flow $\phi_t(\mathbf{x}_0)$, the* variational equation *of 5.25 is the linear differential equation given by*

$$\frac{d}{dt}\mathbf{D}\phi_t(\mathbf{x}_0) = \mathbf{Df}(\phi_t(\mathbf{x}_0)) \cdot \mathbf{D}\phi_t(\mathbf{x}_0). \tag{5.27}$$

The variational equation tells one how the flow ϕ_t acts with respect to small variations in the initial point $\mathbf{x}_0$. The matrix $\mathbf{D}\phi_t(\mathbf{x}_0)$, if known, describes how the time-t flow map acts under small variations in the initial condition. The matrix $\mathbf{Df}(\phi_t(\mathbf{x}_0))$ is the Jacobian of the right hand side of the differential equation Eq (5.25) evaluated along a solution with initial condition $\mathbf{x}_0$. This highlights the importance of defining a time-τ flow map. The variational equation is discretized in time and the Jacobian $\mathbf{Df}(\phi_t(\mathbf{x}_0))$ acts as a matrix update. The notion of a Lyapunov exponent is often derived first for maps [6,88], thus the time-τ flow map allows for the continuous time generalization.

We next define the Lyapunov number and the corresponding Lyapunov exponent in one dimension. Denote $\phi_\tau(x_0) = x_1$, $\phi_\tau(x_1) = x_2$, and for arbitrary n, $\phi_\tau(x_n) = x_{n+1}$, so that the time-τ flow map yields an orbit of the dynamical system $\{x_0, x_1, ...x_n\}$.

Definition 5.2.5. (Alligood, Sauer, & Yorke,107) *Let $f : \mathbb{R} \to \mathbb{R}$ be a smooth function. The* Lyapunov number $r^\tau(x_0)$ *of the orbit $\{x_0, x_1, ...x_n\}$ given by the time-τ flow map is defined as*

$$r^\tau(x_0) = \lim_{n \to \infty} (|f'(x_1)| \cdots |f'(x_n)|)^{1/n},$$

138

if the limit exists.

Definition 5.2.6. (Alligood, Sauer, & Yorke,107) *The* Lyapunov exponent $\mu^\tau(x_0)$ *is defined as*

$$h^\tau(x_0) = \lim_{n \to \infty} \frac{1}{n} \left(\ln |f'(x_1)| + \cdots + \ln |f'(x_n)| \right),$$

if this limit exists. More simply we have $\ln(r^\tau(x_0)) = \mu^\tau(x_0)$.

The Lyapunov number and exponent describe the average stretching rate of two nearby initial conditions subject to a flow. Another definition frequently used [88] for a Lyapunov exponent is

$$\mu^\tau \approx \frac{1}{n} \ln \frac{\delta_n}{\delta_0},$$

where δ_0 is extremely small and δ_n is the separation of two nearby initial conditions, x_0 and $x_0 + \delta_0$, after n iterates of the time-τ flow map. Thus, intuitively, a Lyapunov exponent describes the average rate of separation between two nearby initial conditions under the flow. A negative stretching rate implies the points are moving toward each other while a positive stretching rate indicates they are evolving apart.

We now generalize the definitions to $\mathbb{R}^n$, where we are interested in the stretching rate of an infinitesimal hypersphere by the n-dimensional flow.

Definition 5.2.7. (Alligood, Sauer, & Yorke,195) *Let $\boldsymbol{f} \in C^1(\mathbf{x})$ on $\mathbb{R}^n$ and let $N \in \mathbb{R}^n$ be the unit sphere. Denote the kth longest orthogonal axis of the ellipsoid $\mathbf{D}\phi_\tau N$ to be r_k^τ. The* Lyapunov number r_k^τ *measures the contraction or expansion in a neighborhood of an orbit of $\mathbf{x}_0$ of the time-τ flow map.*

The *Lyapunov exponent* is calculated naturally from the Lyapunov number.

Definition 5.2.8. (Alligood, Sauer, & Yorke,195) *The kth* Lyapunov exponent *of $\mathbf{x}_0$ is*

$$\mu_k^\tau = \ln r_k^\tau. \tag{5.28}$$

The Lyapunov exponents for a system Eq (5.25) can be calculated by solving the variational equation. The variational equation describes how an infinitesimal hypersphere is stretched and contracted by the flow. Thus, it is necessary to simulate the variational equation forward in time as a time-τ map. After each time-τ epoch, find the square roots of the eigenvalues of the associated symmetric matrix $D\phi_\tau^T D\phi_\tau$ to obtain the average orthogonal stretching rates about a trajectory.

Recall, however that the Jacobian $\mathbf{Df}(\phi_t(\mathbf{x}_0))$ depends explicitly on the solution of the differential equation Eq (5.25). Therefore, we must concurrently solve the dynamical system Eq (5.25).

5.2.2   Numerical Estimation of Lyapunov Exponents

There are two popular methods used to produce estimates for Lyapunov exponents [6, 88, 91]. Computationally, the estimation of Lyapunov exponents is challenging since the linearized system may cause an infinitesimal hypersphere to quickly stretch in certain directions and shrink in others [6]. If an ellipsoid has both shrinking and stretching directions, for long time the ellipsoid will become quite long and thin; this results in the Jacobian growing increasingly ill-conditioned. Good methods avoid the scaling problem by normalizing before numbers become computationally problematic.

The first is found in [6], and requires that an orthonormal basis is found after every time iteration to maintain that the stretching rates are calculated in orthogonal directions. This method requires the full solution of the variational equations and yields all Lyapunov exponents for the flow. To re-orthogonalize after every iteration, the Gram-Schmidt orthogonalization method is used. We will not estimate Lyapunov exponents in this way as we require only the largest Lyapunov exponent.

The method we will use, which we will describe in some detail, is based on the power method for matrix multiplication [92], first developed in [91]. This method rather estimates the largest Lyapunov exponent such that its negativity assures sta-

bility. We begin with matrix properties necessary to apply the method.

A matrix times its transpose contains some nice properties.

Lemma 5.2.9. *Let $A \in \mathbb{R}^{n \times n}$. The matrix AA^T is a symmetric matrix with non-negative real eigenvalues.*

Proof. Suppose $A \in \mathbb{R}^{n \times n}$. Then

$$(AA^T)^T = (A^T)^T A^T,$$
$$= AA^T.$$

Furthermore, suppose $\mathbf{x}$ is a unit eigenvector of AA^T and λ is an associated eigenvalue. Then

$$AA^T \mathbf{x} = \lambda \mathbf{x}.$$

$$(5.29)$$

Therefore

$$0 \leq \|A\mathbf{x}\|^2,$$
$$= \mathbf{x}^T A^T A\mathbf{x},$$
$$= \mathbf{x}^T AA^T \mathbf{x},$$
$$= \mathbf{x}^T \lambda \mathbf{x},$$
$$= \lambda.$$

Finally, we prove the eigenvalues are real. Let $A \in \mathbb{R}^{n \times n}$ and $\mathbf{x} \in \mathbb{C}^n$ be an eigenvector of AA^T, with $\lambda \in \mathbb{C}$ as an associated eigenvalue. Then clearly $AA^T \in \mathbb{R}^n$ and we can write $\lambda = \alpha + i\beta$ with $\alpha, \beta \in \mathbb{R}$. Denote $\lambda^* = \alpha - i\beta$, the complex

conjugate of λ. Then since

$$AA^T\mathbf{x} = \lambda\mathbf{x}, \tag{5.30}$$

we multiply both sides by $(\mathbf{x}^*)^T$, to obtain

$$(\mathbf{x}^*)^T\lambda\mathbf{x} = (\mathbf{x}^*)^T(AA^T\mathbf{x}),$$

$$= ((\mathbf{x}^*)^TAA^T)\mathbf{x},$$

$$= ((AA^T)^T\mathbf{x}^*)^T\mathbf{x},$$

$$= (AA^T\mathbf{x}^*)^T\mathbf{x}. \tag{5.31}$$

Now taking the conjugate of both sides of Eq (5.30) gives

$$(AA^T\mathbf{x})^* = (\lambda\mathbf{x})^* \quad \text{so that}$$

$$AA^T\mathbf{x}^* = \lambda^*\mathbf{x}^*, \tag{5.32}$$

since AA^T is real. Finally, combining Eq (5.31) and Eq (5.32), we see that

$$(AA^T\mathbf{x}^*)^T\mathbf{x} = (\lambda^*\mathbf{x}^*)^T\mathbf{x} = (\mathbf{x}^*)^T\lambda\mathbf{x}, \quad \text{so}$$

$$(\lambda - \lambda^*)(\mathbf{x}^*)^T\mathbf{x} = 0. \tag{5.33}$$

We know $\|\mathbf{x}\|_\infty > 0$ as it is an eigenvector and at least one entry is non-zero. Furthermore, for any complex number $y = \alpha - i\beta$, $y^*y = \alpha^2 + \beta^2 \geq 0$ is real. Therefore, Eq (5.33) implies that $\lambda^* = \lambda$ so that λ is real and so is the associated eigenvector. $\square$

We next define the useful *singular value decomposition* of a matrix.

Definition 5.2.10. *Given a matrix $A \in \mathbb{R}^{m\times n}$, the* singular value decomposition

(SVD) of A is a factorization of the form

$$A = U\Sigma V^T, \tag{5.34}$$

where $U \in \mathbb{R}^{m \times m}$ and $V \in \mathbb{R}^{n \times n}$ are orthogonal matrices, and $\Sigma \in \mathbb{R}^{m \times n}$ is a diagonal matrix with the singular values, $s_1, s_2...s_n$, of A on the diagonal.

In $\mathbb{R}^2$, a matrix times a circle results in an ellipse. Therefore, the action on an infinitesimal hypersphere of initial perturbations from an initial condition $\mathbf{x}_0$ will uncover the average stretching about trajectories starting at that point; we measure of the lengths of the orthogonal axes of the resulting ellipse.

Theorem 5.2.11. (Yorke, 89) *Let $A \in \mathbb{R}^{n \times n}$ and let N be the unit hypersphere in $\mathbb{R}^n$. Let the eigenvectors and eigenvalues of AA^T be given by $s_1^2, s_2^2 \cdots s_n^2$ and $u_1, u_2 \cdots u_n$ respectively. Then the axes of the ellipse AN are $s_1 u_1, s_2 u_2 \cdots s_n u_n$.*

Therefore, we have shown that the unit hypersphere is transformed by a matrix A into a hyperellipse with semi-axes give by the square roots of the eigenvalues of AA^T. We exploit this geometry to find the rates of separation between nearby initial conditions in a flow.

Assuming infinitesimal perturbations allows for the linearization of a flow by the Jacobian, an $n \times n$ matrix. This Jacobian matrix transforms an infinitesimal circle to an ellipsoid (in two dimensions) whose semi-axes are given by the square roots of the eigenvalues of the Jacobian multiplied by its transpose. Thus, by finding these eigenvalues, we are able to estimate the Lyapunov numbers and associated Lyapunov exponents for the flow. We now discuss a numerical estimation technique.

The method we use is based on the power method for matrix multiplication. The power method is a very simple method that allows for the estimation of the largest eigenvalue of a matrix iteratively [93].

Definition 5.2.12. (Lay, 363) *The matrix $A \in \mathbb{R}^{n \times n}$ has a* strictly dominant *eigenvalue λ_1 if λ_1 is larger in absolute value than all other eigenvalues. The corresponding eigenvector is called the* dominant *eigenvector.*

So if A has strictly dominant eigenvalues, the eigenvalues may be ordered as

$$|\lambda_1| > |\lambda_2| \geq |\lambda_3| \geq \cdots \geq |\lambda_n|,$$

where the first inequality must be strict.

Theorem 5.2.13. (Golub, Van Loan, 331) *Suppose $A \in \mathbb{R}^{n \times n}$ has a strictly dominant eigenvalue λ_1. The* power method *is an iterative method for finding λ_1 and the corresponding eigenvector $\mathbf{v}_1$. Start with the initial guess $\mathbf{x}_0$, with ones in every entry of the vector. Then build a recursive sequence as*

$$\mu_n \mathbf{x}_{n+1} = \mathbf{y}_n = A\mathbf{x}_n, \; so \; that$$
$$\mathbf{x}_{n+1} = \frac{1}{\mu_n}\mathbf{y}_n,$$

where

$$\mu_n = \|\mathbf{y}_n\|_\infty.$$

Then the sequences generated will converge to the largest eigenvalue and corresponding eigenvector

$$\lim_{n \to \infty} \mathbf{x}_n = \mathbf{v_1} \quad and \quad \lim_{n \to \infty} \mu_n = \lambda_1,$$

and almost every initial guess $\mathbf{x}_0$ will work.

The method is now proven robust under the additional condition requiring that A have n distinct eigenvalues.

Proof. Suppose $A \in \mathbb{R}^{m \times m}$ has m distinct eigenvalues, including a strictly dominant

144

eigenvalue λ_1, and order them according to

$$|\lambda_1| > |\lambda_2| \geq |\lambda_3| \geq \cdots \geq |\lambda_m|.$$

Since A has rank m, there are m corresponding eigenvectors that form a linearly independent basis for the m-dimensional space. Thus, we write an initial guess $\mathbf{x}_0$, in terms of this basis as

$$\mathbf{x}_0 = c_1 \mathbf{v}_1 + c_2 \mathbf{v}_2 + \cdots + c_m \mathbf{v}_m,$$

where the eigenvectors are normalized such that $\|\mathbf{x}_j\|_\infty = 1$ for $j = 1 : m$ and such that $c_1 \neq 0$. Then the first iterate of the power method yields

$$\mathbf{y}_0 = A\mathbf{x}_0 = A\left(c_1 \mathbf{v}_1 + c_2 \mathbf{v}_2 + \cdots + c_m \mathbf{v}_m\right),$$

$$= \left(c_1 A\mathbf{v}_1 + c_2 A\mathbf{v}_2 + \cdots + c_m A\mathbf{v}_m\right),$$

$$= \left(c_1 \lambda_1 \mathbf{v}_1 + c_2 \lambda_2 \mathbf{v}_2 + \cdots + c_m \lambda_m \mathbf{v}_m\right),$$

$$= \lambda_1 \left(c_1 \mathbf{v}_1 + c_2 \frac{\lambda_2}{\lambda_1} \mathbf{v}_2 + \cdots + c_m \frac{\lambda_m}{\lambda_1} \mathbf{v}_m\right),$$

since we know $c_1 \neq 0$. Then

$$\mathbf{x}_1 = \frac{\lambda_1}{\mu_1} \left(c_1 \mathbf{v}_1 + c_2 \frac{\lambda_2}{\lambda_1} \mathbf{v}_2 + \cdots + c_m \frac{\lambda_m}{\lambda_1} \mathbf{v}_m\right).$$

Continuing recursively, the nth iterate yields

$$\mathbf{y}_{n-1} = A\mathbf{x}_{n-1},$$

$$= A \frac{\lambda_1^{n-1}}{\mu_1 \mu_2 \cdots \mu_{n-1}} \left(c_1 \mathbf{v}_1 + c_2 \left(\frac{\lambda_2}{\lambda_1}\right)^{n-1} \mathbf{v}_2 + \cdots + c_m \left(\frac{\lambda_m}{\lambda_1}\right)^{n-1} \mathbf{v}_m \right),$$

$$= \frac{\lambda_1^{n-1}}{\mu_1 \mu_2 \cdots \mu_{n-1}} \left(c_1 A\mathbf{v}_1 + c_2 \left(\frac{\lambda_2}{\lambda_1}\right)^{n-1} A\mathbf{v}_2 + \cdots + c_m \left(\frac{\lambda_m}{\lambda_1}\right)^{n-1} A\mathbf{v}_m \right),$$

$$= \frac{\lambda_1^{n-1}}{\mu_1 \mu_2 \cdots \mu_{n-1}} \left(c_1 \lambda_1 \mathbf{v}_1 + c_2 \left(\frac{\lambda_2}{\lambda_1}\right)^{n-1} \lambda_2 \mathbf{v}_2 + \cdots + c_m \left(\frac{\lambda_m}{\lambda_1}\right)^{n-1} \lambda_m \mathbf{v}_m \right),$$

$$= \frac{\lambda_1^{n}}{\mu_1 \mu_2 \cdots \mu_{n-1}} \left(c_1 \mathbf{v}_1 + c_2 \left(\frac{\lambda_2}{\lambda_1}\right)^{n} \mathbf{v}_2 + \cdots + c_m \left(\frac{\lambda_m}{\lambda_1}\right)^{n} \mathbf{v}_m \right),$$

where we rewrite as a recursion

$$\mathbf{x}_n = \frac{\lambda_1^{n}}{\mu_1 \mu_2 \cdots \mu_n} \left(c_1 \mathbf{v}_1 + c_2 \left(\frac{\lambda_2}{\lambda_1}\right)^{n} \mathbf{v}_2 + \cdots + c_m \left(\frac{\lambda_m}{\lambda_1}\right)^{n} \mathbf{v}_m \right). \tag{5.35}$$

We note that since it was assumed that $|\lambda_1| > \lambda_j$ for $j = 2 : m$, the sequence

$$\lim_{n \to \infty} c_j \left(\frac{\lambda_j}{\lambda_1}\right)^{n} \mathbf{v}_j \to 0 \text{ as } n \to \infty, \text{ for } j = 2 : m. \tag{5.36}$$

Therefore, taking the limit of Eq (5.35) gives

$$\lim_{n \to \infty} \mathbf{x}_n = \lim_{n \to \infty} \frac{c_1 \lambda_1^{n}}{\mu_1 \mu_2 \cdots \mu_n} \mathbf{v}_1. \tag{5.37}$$

By assumption, we have that for all j, $\|\mathbf{x}_j\|_\infty = 1$ and $\|\mathbf{v}_1\|_\infty = 1$, so that the largest component of the vectors in Eq (5.37) will be one. This enforces that

$$\lim_{n \to \infty} \frac{c_1 \lambda_1^{n}}{\mu_1 \mu_2 \cdots \mu_n} = 1, \tag{5.38}$$

146

otherwise a component of $\mathbf{v}_1$ would be scaled incorrectly. Eq (5.38) implies that

$$\lim_{n\to\infty} \mathbf{x}_n = \mathbf{v}_1, \qquad (5.39)$$

and we have proven that the sequence of iterates $\{\mathbf{x}_n\}$ converges to the eigenvector corresponding to the largest eigenvalue $\mathbf{v}_1$. We note that

$$\lim_{n\to\infty} \frac{c_1 \lambda_1^{n-1}}{\mu_1 \mu_2 \cdots \mu_{n-1}} = 1. \qquad (5.40)$$

Then divide Eq (5.38) by Eq (5.40), to observe that

$$\lim_{n\to\infty} \frac{c_1 \lambda_1^n \left(\mu_1 \mu_2 \cdots \mu_{n-1}\right)}{c_1 \lambda_1^{n-1} \left(\mu_1 \mu_2 \cdots \mu_n\right)} = 1,$$

which implies

$$\lim_{n\to\infty} \frac{\lambda_1}{\mu_n} = 1, \quad \text{so that} \quad \lim_{n\to\infty} \mu_n = \lambda_1,$$

and the sequence of iterates $\{c_n\}$ converges to the largest eigenvalue λ_1. $\qquad \square$

Thus, we have proven that, under certain conditions, the power method will converge to the dominant eigenvalue of a matrix. The rate of convergence to the dominant eigenvalue is determined by the ratio of the second-largest eigenvalue to the dominant eigenvalue.

Theorem 5.2.14. *The rate of convergence of the power method is linear.*

Proof. We have already shown in Eq (5.36) that for any j,

$$\left(\frac{\lambda_j}{\lambda_1}\right)^n \to 0 \text{ as } n \to \infty.$$

This rate is in proportion to $\left(\frac{\lambda_j}{\lambda_1}\right)^n < 1$. However, the slowest rate is dominated by the coefficient $\left(\frac{\lambda_2}{\lambda_1}\right)^n < 1$. This, then is the speed at which $\{\mathbf{x}^n\} \to \mathbf{v}_1$, which is linear.

In the same way, the rate of convergence of the sequence of coefficients $\{c_n\} \to \lambda_1$ is linear. $\qquad\qquad\qquad\qquad\qquad\qquad\qquad\qquad\qquad\qquad\qquad\qquad\qquad\qquad$ $\square$

Therefore a drawback to the power method is that the rate of convergence can be very slow if $\lambda_2 \approx \lambda_1$. The algorithm for the power method is described below.

Definition 5.2.15. The power method for estimating a strictly dominant eigenvalue [94] :

1. *Start with an initial vector $\mathbf{x}_0$*

2. *For $n = 0, 1, 2, \cdots$,*

   (a) *Find $A\ \mathbf{x}_n$*

   (b) *Let μ_n be an entry in $A\mathbf{x}_n$, with largest absolute value, $\mu_n = \|A\mathbf{x}_n\|_\infty$.*

   (c) *Compute $\mathbf{x}_{n+1} = \frac{1}{\mu_n} A\mathbf{x}_n$*

3. *For almost every choice of initial condition $\mathbf{x}_0$, the sequence $\{\mu_n\}$ approaches a corresponding eigenvector.*

Finally, we discuss how the power method is used to estimate a Lyapunov exponent based on the variational equations Eq (5.27). In [92], the Lyapunov exponents are found by solving Eq (5.27) and estimating

$$\mu_{\max}(T) \approx \frac{1}{T} \ln \frac{\|v(T)\|_2}{\|v_0\|_2}. \qquad\qquad (5.41)$$

We arrive at this rate of separation by applying the power method on the Jacobian in the variational equation, $\mathbf{Df}(\phi_\tau(\mathbf{x}_0))\mathbf{Df}(\phi_\tau(\mathbf{x}_0))^T$ for a given initial condition. The eigenvalues of this matrix will describe the local stretching rates in orthogonal directions that we require to estimate the largest Lyapunov exponent.

5.2.3 Conditional Lyapunov Exponents

Now that we have studied a method for estimating the largest Lyapunov exponent, we adapt this method to study the largest conditional Lyapunov exponent for a pair of coupled dynamical systems. Conditional Lyapunov exponents are used by many authors to analyze the stability of a synchronization manifold for a given coupling [7, 50, 57, 73–75, 89].

There are some discrepancies in terms of the formal definition of a conditional Lyapunov exponent. For example, in [7], they are defined to be the Lyapunov exponents of the associated system with coordinated changed to be in transverse directions to the identical synchronization manifold. However, in [50] they are defined as the Lyapunov exponents found by evaluating the Jacobian of right hand side of a response system $\mathbf{Df}(\phi_r, \phi_d)$, which because of coupling, is conditional upon both the drive and response systems. Here, we will accept the former definition based on of the work in [7].

Definition 5.2.16. *Let $\dot{\mathbf{x}} = \mathbf{f}(\mathbf{x})$ be a dynamical system with which $\dot{\mathbf{y}} = \mathbf{f}(\mathbf{y}, \mathbf{x})$ is coupled. Define the transverse coordinate $\mathbf{e} = \mathbf{x} - \mathbf{y}$ so the dynamical system in transverse space becomes $\dot{\mathbf{e}} = \mathbf{f}(\mathbf{x}) - \mathbf{f}(\mathbf{x}, \mathbf{y})$. Then the variational equations of the system are given by*

$$\dot{\mathbf{e}} = \mathbf{Df}(\mathbf{x}, \mathbf{y}) \cdot \mathbf{e}, \tag{5.42}$$

and the conditional Lyapunov exponents *are the Lyapunov exponents of the system Eq (5.42).*

The Lyapunov exponents for the new system depend on the coupling from the drive system, hence the word conditional. We first show how conditional Laypunov exponents are found when sampling phytoplankton only. We then move on to consider the autosynchronization case used in Chapter 4.

5.2.4 Synchronization

Once again, we will use a change of coordinates so that Lyapunov exponents are computed with respect to perturbations in directions traverse to the synchronization manifold. Thus, consider the drive-response system

$$
\frac{\partial P}{\partial t} = \triangle P + P(1-P) - \frac{PZ}{P+h}, \qquad \text{Drive System} \qquad (5.43)
$$

$$
\frac{\partial Z}{\partial t} = \triangle Z + k\frac{PZ}{P+h} - mZ,
$$

$$
\frac{\partial \hat{P}}{\partial t} = \triangle \hat{P} + \hat{P}(1-P) - \frac{\hat{P}\hat{Z}}{P+h} + \kappa(P-\hat{P}), \qquad \text{Response System}
$$

$$
\frac{\partial \hat{Z}}{\partial t} = \triangle \hat{Z} + k\frac{\hat{P}\hat{Z}}{P+h} - m\hat{Z},
$$

where $P(x,y,0) \neq \hat{P}(x,y,0)$, $Z(x,y,0) \neq \hat{Z}(x,y,0)$, and we do not sample zooplankton. We have already seen that this method of coupling results in identical synchronization when $\kappa = 1.25$. To estimate the conditional Lyapunov exponents for the system Eq (5.43), we work in the transverse space

$$
e_1 = P - \hat{P}, \qquad (5.44)
$$

$$
e_2 = Z - \hat{Z}.
$$

The system Eq (5.43), in the new coordinates, becomes

$$
\frac{\partial e_1}{\partial t} = P - P^2 - \frac{PZ}{P+h} - \hat{P} + \hat{P}P + \frac{\hat{P}\hat{Z}}{P+h} - \kappa e_1,
$$

$$
\frac{\partial e_2}{\partial t} = k\frac{PZ}{P+h} - mZ - k\frac{\hat{P}\hat{Z}}{P+h} + m\hat{Z},
$$

which simplifies to

$$\frac{\partial e_1}{\partial t} = e_1 - Pe_1 - \kappa e_1 + \frac{\hat{P}\hat{Z} - PZ}{P + h},$$

$$\frac{\partial e_2}{\partial t} = k\frac{PZ - \hat{P}\hat{Z}}{P + h} - me_2,$$

where we need to be a little creative to rewrite the Holling functional response term. We complete the transformation by

$$\frac{\hat{P}\hat{Z} - PZ}{P + h} = \frac{\hat{P}\hat{Z} - PZ}{P + h} + \frac{P\hat{Z} - P\hat{Z}}{P + h},$$

$$= \frac{P\hat{Z} - PZ}{P + h} + \frac{\hat{P}\hat{Z} - P\hat{Z}}{P + h},$$

$$= \frac{-\hat{P}e_2}{P + h} + \frac{-\hat{Z}e_1}{P + h}, \tag{5.45}$$

now written with respect to the new coordinate system. Similarly, we write

$$k\frac{PZ - \hat{P}\hat{Z}}{P + h} = k\frac{\hat{Z}e_1}{P + h} + k\frac{Pe_2}{P + h}. \tag{5.46}$$

Combining Eq (5.45) and Eq (5.46), the system is written

$$\frac{\partial e_1}{\partial t} = e_1 - Pe_1 - \kappa e_1 + \frac{1}{P + h}\left(-Pe_2 - \hat{Z}e_1\right), \tag{5.47}$$

$$\frac{\partial e_2}{\partial t} = k\frac{1}{P + h}\left(\hat{Z}e_1 + Pe_2\right) - me_2,$$

where we are now interested in the stability of the origin. The coupling of e_2 in the $\frac{\partial e_1}{\partial t}$ equations highlights the difficulty with using the Lyapunov function Eq (5.5) to prove the stability of the identical synchronization manifold. If these terms dropped out, we would have a much easier time of it. The Jacobian of the right hand side is

given by

$$\begin{pmatrix} 1 - P - \kappa - \frac{\hat{Z}}{P+h} & -\frac{P}{P+h} \\ \frac{k\hat{Z}}{P+h} & \frac{kP}{P+h} - m \end{pmatrix}. \tag{5.48}$$

A simulation is run and the largest Lyapunov exponent is found to be negative with results shown in Figure 5.8. The red dotted line provides a reference for zero and the maximum exponent seems to be settling down at roughly $\mu_{\mathrm{max}} = -0.3839$.
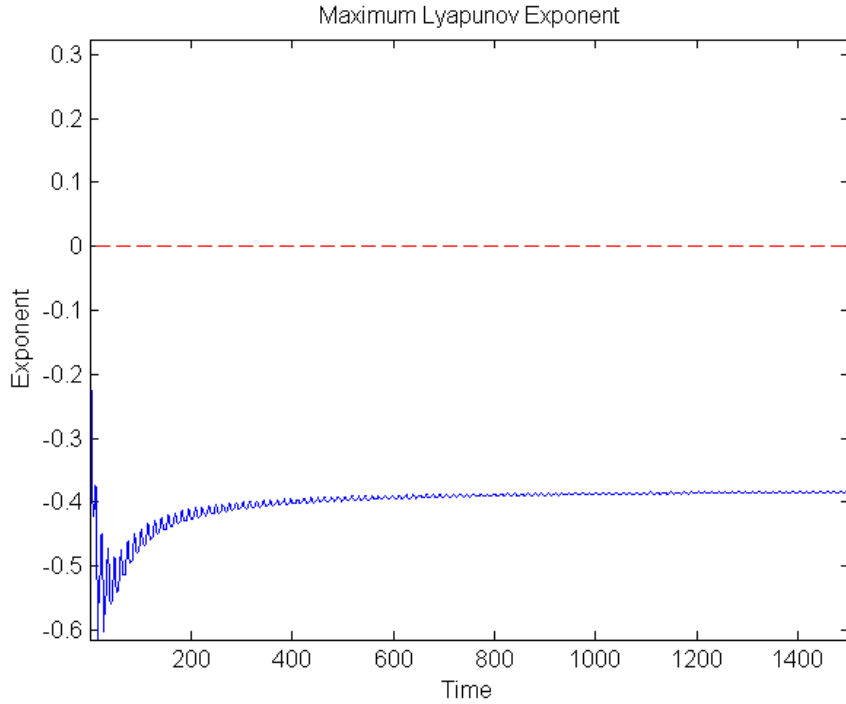
Figure 5.8: Plot shows convergence of estimation of maximum conditional Lyapunov exponent over time. The value is negative and seems to be settling to near $\mu_{\mathrm{max}} = -0.3839$. Dotted red line plotted at zero for reference.

Our numerical estimate of the largest Lyapunov exponent provides strong numerical evidence that the synchronization manifold is asymptotically stable. This holds true for all initial conditions allowable in the response system such that the manifold is evidenced to be globally asymptotically stable. Furthermore, transverse perturbations will quickly shrink back toward the manifold leading to identical synchronization

between model states.

5.2.5 Autosynchronization

We now move on to autosynchronization, considering the response system stated in Chapter 4 which only samples phytoplankton. We will use the same change in coordinates and apply conditional Lyapunov exponents to provide strong evidence for the stability of the identical synchronization manifold. Recall the response system stated for autosynchronization when sampling only phytoplankton,

$$\frac{\partial \hat{P}}{\partial t} = \triangle \hat{P} + \hat{P}(1 - P) - \frac{\hat{P}\hat{Z}}{P + h} + \kappa(P - \hat{P}),$$

$$\frac{\partial \hat{Z}}{\partial t} = \triangle \hat{Z} + \hat{k}\frac{\hat{P}\hat{Z}}{P + h} - \hat{m}\hat{Z},$$

$$\frac{\partial k}{\partial t} = s_1(P - \hat{P}),$$

$$\frac{\partial m}{\partial t} = s_2(P - \hat{P})\hat{P},$$

with the same drive system as above. We again make the change of coordinates

$$e_1 = P - \hat{P}, \tag{5.49}$$

$$e_2 = Z - \hat{Z},$$

$$e_3 = k - \hat{k},$$

$$e_4 = m - \hat{m},$$

and evolve the equations in the transverse space. We make the substitutions shown in Eq (5.45) and Eq (5.46) such that the transformed equations become

$$\frac{\partial e_1}{\partial t} = e_1 - Pe_1 - \kappa e_1 + \frac{1}{P+h}\left(-Pe_2 - \hat{Z}e_1\right), \tag{5.50}$$

$$\frac{\partial e_2}{\partial t} = \frac{1}{P+h}\left(-\hat{k}\hat{P}e_2 + \hat{k}Ze_1 + PZe_3\right) - Ze_4 - \hat{m}e_2,$$

$$\frac{\partial e_3}{\partial t} = -s_1 e_1,$$

$$\frac{\partial e_4}{\partial t} = -s_2 e_1 \hat{P},$$

The Jacobian for Eq (5.50) is

$$\begin{pmatrix} 1 - P - \kappa - \frac{\hat{Z}}{P+h} & -\frac{P}{P+h} & 0 & 0 \\ \frac{\hat{k}Z}{P+h} & \frac{\hat{k}\hat{P}}{P+h} - \hat{m} & \frac{PZ}{P+h} & -Z \\ -s_1 & 0 & 0 & 0 \\ -s_2\hat{P} & 0 & 0 & 0 \end{pmatrix}. \tag{5.51}$$

A simulation is run and the largest Lyapunov exponent is found to be negative with results shown in Figure 5.9. The red dotted line shows zero for reference and the maximum exponent seems to be settling down at roughly $\mu_{\max} = -0.0012$.
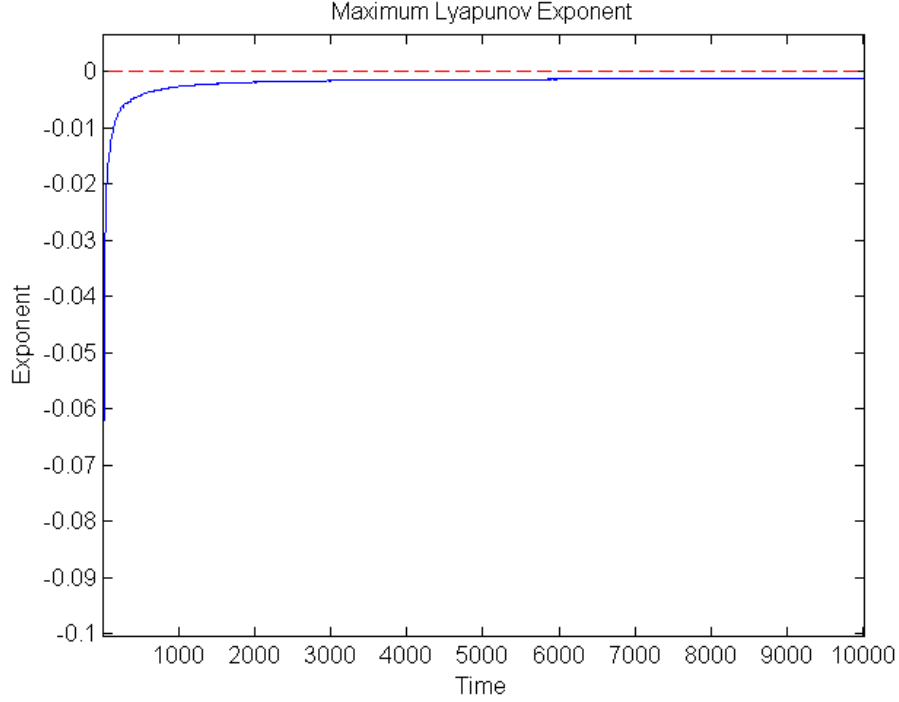
Figure 5.9: Plot shows convergence of estimation of maximum conditional Lyapunov exponent over time. The value is negative and seems to be settling to near $\mu_{\max} = -0.0012$. Dotted red line plotted at zero for reference.

Therefore, we obtain strong numerical evidence that the synchronization manifold is asymptotically stable. Again, we note that transverse perturbations will quickly shrink back toward the manifold leading to identical synchronization between both model parameters and states.

5.2.6 Conditional Lyapunov Exponents PDE Extension

Until now, we have only shown the stability of the synchronization manifold by conditional Lyapunov exponents for the ODEs with which we were unable to find a Lyapunov function and subsequently extend to the corresponding PDE. Here, we extend the system of ODEs to be a system of coupled ODEs representing the centered difference discretizations in space, approximating the corresponding reaction-diffusion PDE. Empirical evidence based on shrinking the discretizations toward zero provides

155

a heuristic argument for the stability of the identical synchronization manifold for the associated PDE when sampling only one species.

The method we use to analyze the discretized PDE is based on the method of lines. Here, we choose the centered differences in space discretization for the Laplacian. Then we choose the number of mesh points to study and find the conditional Lyapunov exponents. We explain in some detail the discretization produced from the coupled system

$$
\begin{aligned}
\frac{\partial P}{\partial t} &= \triangle P + P(1 - P) - \frac{PZ}{P + h}, && \text{Drive System} && (5.52) \\
\frac{\partial Z}{\partial t} &= \triangle Z + k\frac{PZ}{P + h} - mZ, \\
\frac{\partial \hat{P}}{\partial t} &= \triangle \hat{P} + \hat{P}(1 - P) - \frac{\hat{P}\hat{Z}}{P + h} + \kappa(P - \hat{P}), && \text{Response System} \\
\frac{\partial \hat{Z}}{\partial t} &= \triangle \hat{Z} + k\frac{\hat{P}\hat{Z}}{P + h} - m\hat{Z},
\end{aligned}
$$

where the spatial domain is given by $\Omega = [0, 300]$.

In one dimension, if we choose a mesh with m nodes in space, then we have $4m$ model equations and $2m$ equations in the transverse space. The Jacobian will be in $\mathbb{R}^{2m \times 2m}$. The forward-time centered-space discretization of Eq (5.52) gives the system

$$
\begin{aligned}
\frac{P_j^{n+1} - P_j^n}{dt} &= \frac{P_{j-1}^n - 2P_j^n + P_{j+1}^n}{dx^2} + P_j^n(1 - P_j^n) - \frac{P_j^n Z_j^n}{P_j^n + h}, && (5.53) \\
\frac{Z_j^{n+1} - Z_j^n}{dt} &= \frac{Z_{j-1}^n - 2Z_j^n + Z_{j+1}^n}{dx^2} + k\frac{P_j^n Z_j^n}{P_j^n + h} - mZ_j^n, \\
\frac{\hat{P}_j^{n+1} - \hat{P}_j^n}{dt} &= \frac{\hat{P}_{j-1}^n - 2\hat{P}_j^n + \hat{P}_{j+1}^n}{dx^2} + \hat{P}_j^n(1 - P_j^n) - \frac{\hat{P}_j^n \hat{Z}_j^n}{P_j^n + h} + \kappa(P_j^n - \hat{P}_j^n), \\
\frac{\hat{Z}_j^{n+1} - \hat{Z}_j^n}{dt} &= \frac{\hat{Z}_{j-1}^n - 2\hat{Z}_j^n + \hat{Z}_{j+1}^n}{dx^2} + k\frac{\hat{P}_j^n \hat{Z}_j^n}{P_j^n + h} - m\hat{Z}_j^n,
\end{aligned}
$$

where $j = 2 : (L/dx) - 1$, L is the length of Ω, and n is the time step. The system of equations (5.53) is valid for the interior points of the mesh and the boundary equations are settled by assuming zero flux at the boundaries.

Therefore, we write the resulting system of equations for m nodes in one dimension. The $4m$ equations describing the "left" boundary conditions, interior points, and

"right" boundary conditions are given by the following algorithm.

$$\frac{P_1^{n+1} - P_1^n}{dt} = \frac{P_2^n - P_1^n}{dx^2} + P_1^n(1 - P_1^n) - \frac{P_1^n Z_1^n}{P_1^n + h}$$

$$\frac{Z_1^{n+1} - Z_1^n}{dt} = \frac{Z_2^n - Z_1^n}{dx^2} + k\frac{P_1^n Z_1^n}{P_1^n + h} - mZ_1^n$$

$$\frac{\hat{P}_1^{n+1} - \hat{P}_1^n}{dt} = \frac{\hat{P}_2^n - \hat{P}_1^n}{dx^2} + \hat{P}_1^n(1 - P_1^n) - \frac{\hat{P}_1^n \hat{Z}_1^n}{P_1^n + h} + \kappa(P_1^n - \hat{P}_1^n)$$

$$\frac{\hat{Z}_1^{n+1} - \hat{Z}_1^n}{dt} = \frac{\hat{Z}_2^n - \hat{Z}_1^n}{dx^2} + k\frac{\hat{P}_1^n \hat{Z}_1^n}{P_1^n + h} - m\hat{Z}_1^n$$

for $j = 2 : L - 1$

$$\frac{P_j^{n+1} - P_j^n}{dt} = \frac{P_{j-1}^n - 2P_j^n + P_{j+1}^n}{dx^2} + P_j^n(1 - P_j^n) - \frac{P_j^n Z_j^n}{P_j^n + h}$$

$$\frac{Z_j^{n+1} - Z_j^n}{dt} = \frac{Z_{j-1}^n - 2Z_j^n + Z_{j+1}^n}{dx^2} + k\frac{P_j^n Z_j^n}{P_j^n + h} - mZ_j^n$$

$$\frac{\hat{P}_j^{n+1} - \hat{P}_j^n}{dt} = \frac{\hat{P}_{j-1}^n - 2\hat{P}_j^n + \hat{P}_{j+1}^n}{dx^2} + \hat{P}_j^n(1 - P_j^n) - \frac{\hat{P}_j^n \hat{Z}_j^n}{P_j^n + h} + \kappa(P_j^n - \hat{P}_j^n)$$

$$\frac{\hat{Z}_j^{n+1} - \hat{Z}_j^n}{dt} = \frac{\hat{Z}_{j-1}^n - 2\hat{Z}_j^n + \hat{Z}_{j+1}^n}{dx^2} + k\frac{\hat{P}_j^n \hat{Z}_j^n}{P_j^n + h} - m\hat{Z}_j^n$$

end

$$\frac{P_L^{n+1} - P_L^n}{dt} = \frac{P_{L-1}^n - P_L^n}{dx^2} + P_L^n(1 - P_L^n) - \frac{P_L^n Z_L^n}{P_L^n + h}$$

$$\frac{Z_L^{n+1} - Z_L^n}{dt} = \frac{Z_{L-1}^n - Z_L^n}{dx^2} + k\frac{P_L^n Z_L^n}{P_L^n + h} - mZ_L^n$$

$$\frac{\hat{P}_L^{n+1} - \hat{P}_L^n}{dt} = \frac{\hat{P}_{L-1}^n - \hat{P}_L^n}{dx^2} + \hat{P}_L^n(1 - P_L^n) - \frac{\hat{P}_L^n \hat{Z}_L^n}{P_L^n + h} + \kappa(P_L^n - \hat{P}_L^n)$$

$$\frac{\hat{Z}_L^{n+1} - \hat{Z}_L^n}{dt} = \frac{\hat{Z}_{L-1}^n - \hat{Z}_L^n}{dx^2} + k\frac{\hat{P}_L^n \hat{Z}_L^n}{P_L^n + h} - m\hat{Z}_L^n$$

These equations are solved in tandem with the Jacobian of the right hand side as part of the variational equations. For consistency we may consider rather evolving the $2m$

coupled ODEs associated with the transverse space, however build in the same way. Recall the equations Eq (5.52) in transverse space become

$$\frac{\partial e_1}{\partial t} = \triangle e_1 - Pe_1 - \kappa e_1 + \frac{1}{P+h}\left(-Pe_2 - \hat{Z}e_1\right),$$

$$\frac{\partial e_2}{\partial t} = \triangle e_2 - \frac{k}{P+h}\left(\hat{Z}e_1 + Pe_2\right) - me_2,$$

and the corresponding forward-time centered-space discretization provides the system

$$\frac{e_{1_j}^{n+1} - e_{1_j}^{n}}{dt} = \frac{e_{1_{j-1}}^{n} - 2e_{1_j}^{n} + e_{1_{j+1}}^{n}}{dx^2} - P_j^n e_{1_j}^n - \kappa e_{1_j}^n + \frac{1}{P_j^n + h}\left(-P_j^n e_{2_j}^n - \hat{Z}_j^n e_{1_j}^n\right),$$

$$\frac{e_{2_j}^{n+1} - e_{2_j}^{n}}{dt} = \frac{e_{2_{j-1}}^{n} - 2e_{2_j}^{n} + e_{2_{j+1}}^{n}}{dx^2} - \frac{k}{P_j^n + h}\left(\hat{Z}_{2_j}^n e_{1_j}^n + P_j^n e_{2_j}^n\right) - me_{2_j}^n,$$

where $j = 1 : (L/dx)$, L is the length of Ω, and n is the time step. We take the Jacobian of the right hand side of the above system of ODEs. For a mesh with m grid points, the Jacobian will have size $2m \times 2m$. The Jacobian will have a block-diagonal structure. To see this, we form three matrices

$$A = \begin{pmatrix} -\frac{1}{dx^2} + 1 - P_1^n - \kappa - \frac{\hat{Z}_1^n}{P_1^n + h} & -\frac{P_1^n}{P_1^n + h} \\ k\frac{\hat{Z}_1^n}{P_1^n + h} & -\frac{1}{dx^2} + k\frac{P_1^n}{P_1^n + h} - m \end{pmatrix},$$

$$J = \begin{pmatrix} -\frac{2}{dx^2} + 1 - P_j^n - \kappa - \frac{\hat{Z}_j^n}{P_j^n + h} & -\frac{P_j^n}{P_j^n + h} \\ k\frac{\hat{Z}_j^n}{P_j^n + h} & -\frac{2}{dx^2} + k\frac{P_j^n}{P_j^n + h} - m \end{pmatrix},$$

$$B = \begin{pmatrix} 1 - P_L^n - \kappa - \frac{\hat{Z}_L^n}{P_L^n + h} & -\frac{P_L^n}{P_L^n + h} \\ k\frac{\hat{Z}_L^n}{P_L^n + h} & -\frac{1}{dx^2} + k\frac{P_L^n}{P_L^n + h} - m \end{pmatrix},$$

$$D = \begin{pmatrix} \frac{1}{dx^2} & 0 \\ 0 & \frac{1}{dx^2} \end{pmatrix},$$

so the full Jacobian of the coupled system is given by

$$\begin{pmatrix} [A] & [D] & 0 & \cdots & 0 \\ [D] & [J] & [D] & \cdots & 0 \\ \vdots & & \ddots & & \vdots \\ 0 & \cdots & [D] & [J] & [D] \\ 0 & \cdots & 0 & [D] & [B] \end{pmatrix}. \tag{5.54}$$

Once built, we obtain the system of equations necessary to numerically solve the variational equations and subsequently estimate the dominant conditional Lyapunov exponent. The system of equation is fed into the algorithm described in [92] and the estimated Lyapunov exponent is shown in Figure 5.10 for three different choices of mesh sizes, or equivalently, different choices of m. The number of grid points are refined from $m = 150$ to $m = 300$, and then to $m = 600$. For all three we note that the largest Lyapunov exponent is estimated as negative, the requirement for stability

of the identical synchronization manifold. For $m = 150$ we estimate $\mu = -0.005$, for $m = 300$ we estimate $\mu = -0.0057$, while for $m = 600$ we estimate $\mu = -0.0063$.
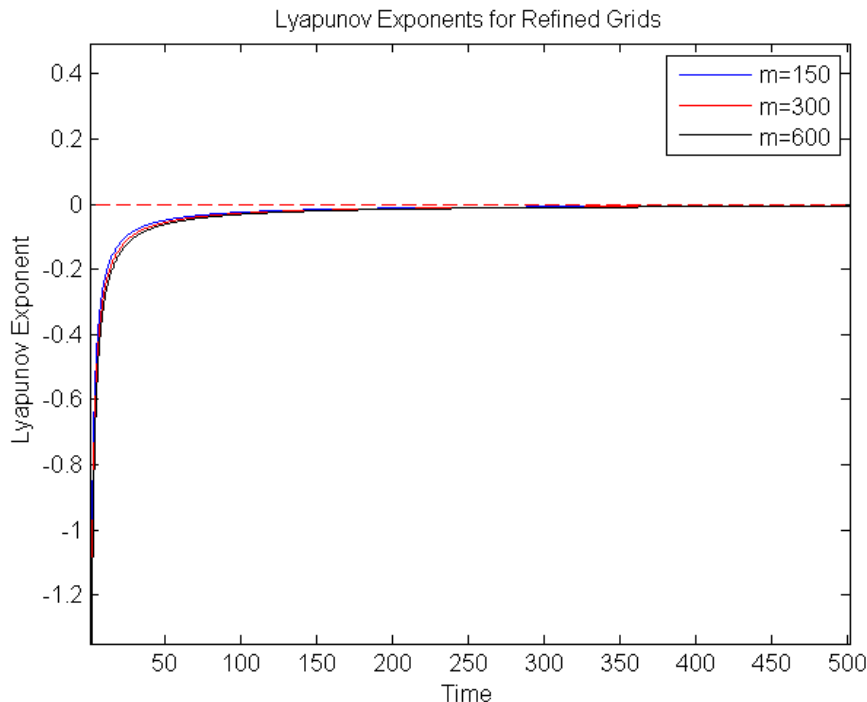
Figure 5.10: Plot shows convergence of estimation of maximum conditional Lyapunov exponent over time. The plots shown are for subsequently refined grids, including $m = 150$, $m = 300$, and $m = 600$ nodes over the fixed domain. Dotted red line plotted at zero for reference.

In summary, we have described two methods of analyzing the stability of a synchronization manifold, the Lyapunov direct method and through conditional Lyapunov exponents. We have demonstrated a Lyapunov function for some ODE representations of the equations used in Chapter 4 and then shown how to generalize those Lyapunov functions to Lyapunov functionals in the PDE setting. Therefore, we have proven the stability under certain coupling strengths of the identical synchronization manifold for certain couplings between the reaction-diffusion PDEs in Chapter 4.

We next described in detail conditional Lyapunov exponents and also the numerical techniques often used to estimate them. Conditional Lyapunov exponents were used to study the stability of the identical synchronization manifold for couplings

for which a Lyapunov function is not currently known. Since conditional Lyapunov exponents are primarily derived for ODEs, we studied the PDE by studying the behavior of the conditional Lyapunov exponents for increasingly smaller discretizations in space such that the coupled ODEs approximate the PDE. We show that the conditional Lyapunov exponent remains negative as the space discretization is refined, a strong argument for the stability of the identical synchronization manifold.

Chapter 6

Synchronization on Reaction-Diffusion-Advection PDEs

Thus far we have studied a reaction-diffusion system for ocean ecology. Although this system is capable of representing complex spatiotemporal dynamics with spiral patterns on a spatial scale consistent with satellite observations [15], a reasonable critique is that we have not yet considered advective systems. Plankton are by definition largely subject to advection by ocean currents [15]. Therefore, a natural question to consider is whether the methods proposed in chapter 4 extend to reaction-diffusion-advection systems for ocean ecology. The effect of ocean turbulence on ecological communities is an area of active research [15, 28, 95–99] and deserve consideration when modeling ecology on the mesoscale. Synchronization methods have not been studied on reaction-diffusion-advection models and this work is a first exploration of the topic.

The chapter is organized as follows: First, we define a model for advection that promotes mixing, consistent with what might be expected in coastal dynamics. Since

we might be observing river mouths and deltas our benchmark model should reproduce the sort of mixing behavior inherent in those regions. Once the model for advection is defined and discussed, we describe the new benchmark reaction-diffusion-advection system for phytoplankton-zooplankton ecology. We show that our synchronization methods can be adapted to this new situation as a first demonstration of synchronization for such systems. Finally, we consider autosynchronization for parameter estimation and demonstrate that even spatially dependent model parameters are well-estimated when observing only phytoplankton.

6.1   Double Gyre

We begin by discussing the double gyre [58–62], a popular benchmark vector field among those studying mixing, which will be used for the advection terms in our benchmark system. The non-autonomous double gyre is derived by taking the Hamiltonian gradient of the stream function given by

$$\Psi(x,y,t) = A\sin(\pi f(x,t))sin(\pi y), \tag{6.1}$$

$$f(x,t) = (\epsilon\sin(\omega t))x^2 + (1 - 2\epsilon\sin(\omega t))x.$$

That is, the double gyre is a Hamiltonian system; such systems enforce that energy is conserved on level curves. We now define the Hamiltonian gradient, as opposed to the classical gradient.

Definition 6.1.1. (Perko, 166) *[100] Given a smooth, real valued system* $\Psi(x,y)$: $\mathbb{R}^2 \to \mathbb{R}$, *the* Hamiltonian gradient, *denoted* ∇_H *is defined as*

$$\dot{x} = \frac{\partial\Psi}{\partial y}, \tag{6.2}$$

$$\dot{y} = -\frac{\partial\Psi}{\partial x}.$$

Since the double gyre is derived from a stream function, the flow is necessarily divergence free. That is, a flow field $\mathbf{v}$, derived from a stream function will satisfy

$$\nabla \cdot \mathbf{v} = 0 \tag{6.3}$$

where ∇ represents the classical gradient. Then, using Eq (6.1), the flow components for the double gyre are given by

$$\dot{x} = -A\pi \sin(\pi f(x,t)) \cos(\pi y), \tag{6.4}$$
$$\dot{y} = A\pi \cos(\pi f(x,t)) \sin(\pi y) \frac{df}{dx},$$
$$f(x,t) = (\epsilon \sin(\omega t))x^2 + (1 - 2\epsilon \sin(\omega t))x$$

where $\epsilon = 1$ and $\omega = 1$ and the domain is $M = [0,2] \times [0,1]$. Eq (6.4) is a non-autonomous vector field representing a periodic perturbation from two counter-rotating gyres of which two snapshots are shown in Figure 6.1. For our simulations, we stretch the domain, as shown in Figure 6.1, to be $\Omega = [0,900] \times [0,300]$.

(a) (b)
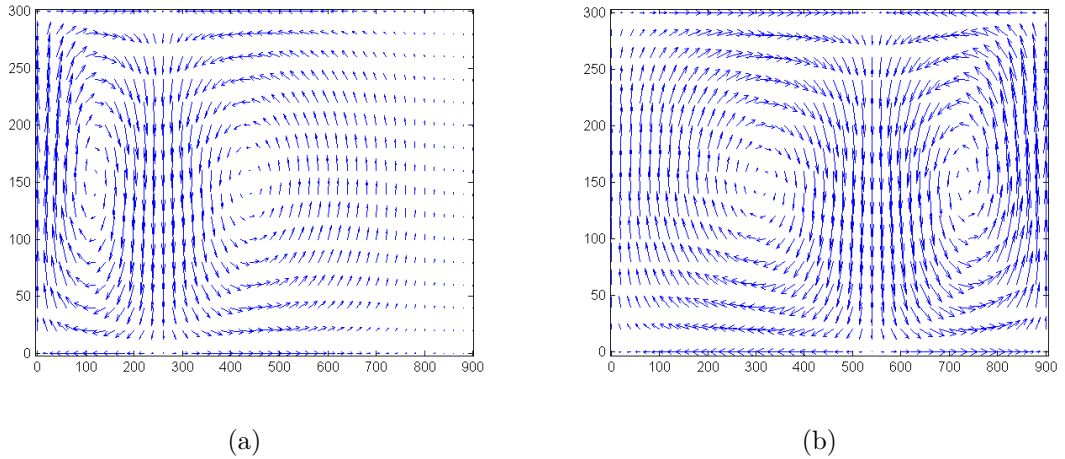
Figure 6.1: Flow field governed by Hamiltonian stream function Eq (6.1), with flow components given by Eq (6.4). Two images of non-autonomous flow shown at slightly different times.

The non-autonomous double gyre has the property that while one gyre expands, the other contracts in a back and forth motion, resulting in mixing within the domain [58–62]. The non-autonomous double gyre is a good benchmark for our techniques in providing non-autonomous vector fields representing ocean currents. The mixing properties of the double gyre are apparent in Figure 6.2 with two snapshots from a simulation of tracers. The first image, Figure (a), shows the initial conditions, with blue and red tracers placed initially on the right and left half of the domain respectively. The tracers are evolved according to Eq (6.4) and are shown to mix throughout Ω. A thorough study of these mixing properties of this system are found in many sources [58–62].

(a)   (b)
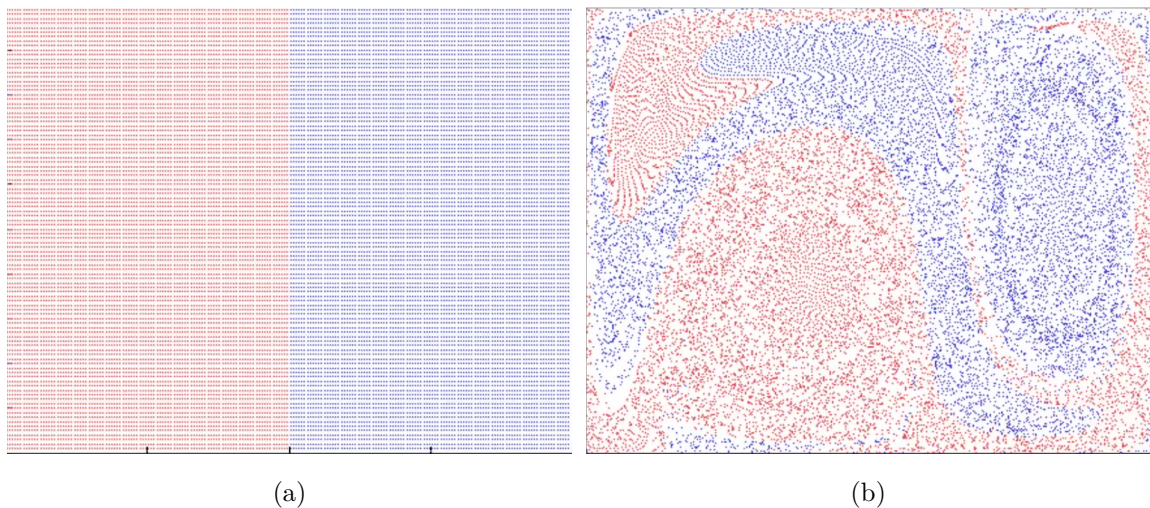
Figure 6.2: Simulation of tracers over the double gyre vector field. Initially, blue tracers on the right and red on the left, shown in (a). After a short epoch, mixing between two halves shown in (b).

With this advection model Eq (6.4) , we build a reaction-diffusion-advection system of equations based on Eq (4.7) to simulate more realistic behavior.

The new system of equations is given by

$$
\begin{aligned}
\frac{\partial P}{\partial t} &= \triangle P + \mathbf{v} \cdot \nabla P + P(1 - P) - \frac{PZ}{P + h}, \\
\frac{\partial Z}{\partial t} &= \triangle Z + \mathbf{v} \cdot \nabla Z + k\frac{PZ}{P + h} - mZ,
\end{aligned}
\tag{6.5}
$$

where $k = 2$, $m = 0.6$, and $\mathbf{v}$ is given by Eq (6.4). Figure 6.3 shows two images from a simulation of Eq (6.5) at $t = 80$ and $t = 100$, shown in Figures (a) and (b) respectively. The solution is qualitatively different than the original reaction-diffusion system, and the effects from advection are clearly visible. We now study whether synchronization is possible between two reaction-diffusion-advection systems.

(a)   (b)
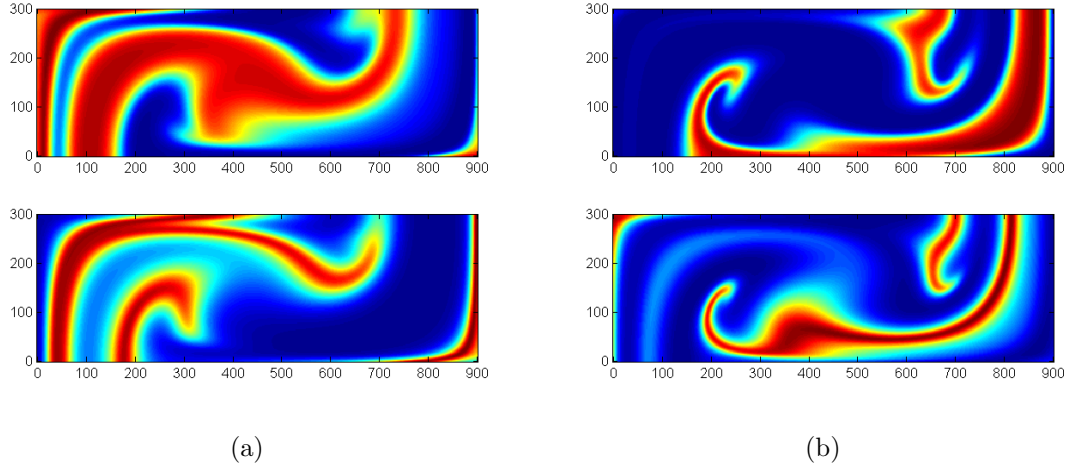
Figure 6.3: Simulation of Eq (6.5) shown at times $t = 80$ and $t = 100$. Phytoplankton shown on top, zooplankton on bottom.

6.2 Synchronization

We first study whether it is possible to observe synchronization between two reaction-diffusion-advection systems. Therefore, given the drive system Eq (6.5), we state the

response system

$$\frac{\partial \hat{P}}{\partial t} = \triangle \hat{P} + \mathbf{v} \cdot \nabla \hat{P} + \hat{P}(1 - \hat{P}) - \frac{\hat{P}\hat{Z}}{\hat{P} + h} + \kappa(P - \hat{P}), \qquad (6.6)$$

$$\frac{\partial \hat{Z}}{\partial t} = \triangle \hat{Z} + \mathbf{v} \cdot \nabla \hat{Z} + k\frac{\hat{P}\hat{Z}}{P + h} - m\hat{Z},$$

where $\mathbf{v}$ is given by Eq (6.4), and Eq (6.5) is coupled into Eq (6.6) by sampling only phytoplankton. The drive and response equations are coupled as before, where we use a combination of diffusive and complete replacement coupling. Initial conditions for the response system are $\hat{P}(x, y, 0) = 2$ and $\hat{Z}(x, y, 0) = 2$.

(a)

(b)

(c)

(d)

(e)

(f)
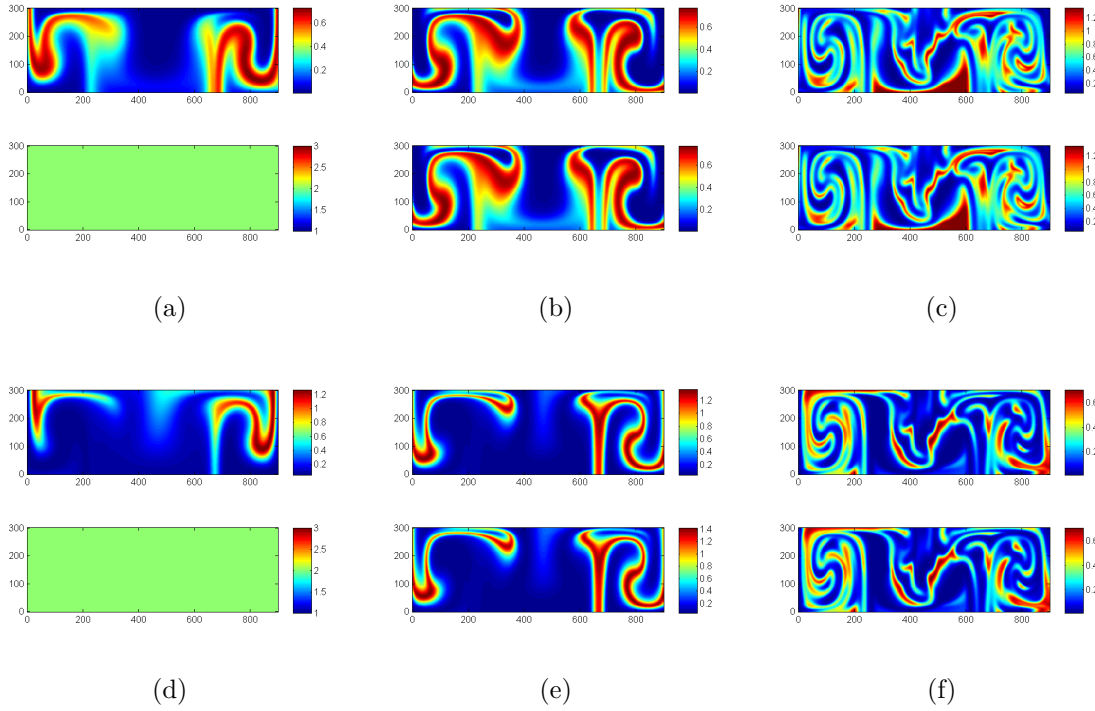
Figure 6.4: Three snapshots of simulation of Eq (6.5) - (6.6) shown at $t = 0$, $t = 30$, and $t = 171$. Phytoplankton shown on top row with drive shown above response. Zooplankton on bottom row with drive above response.
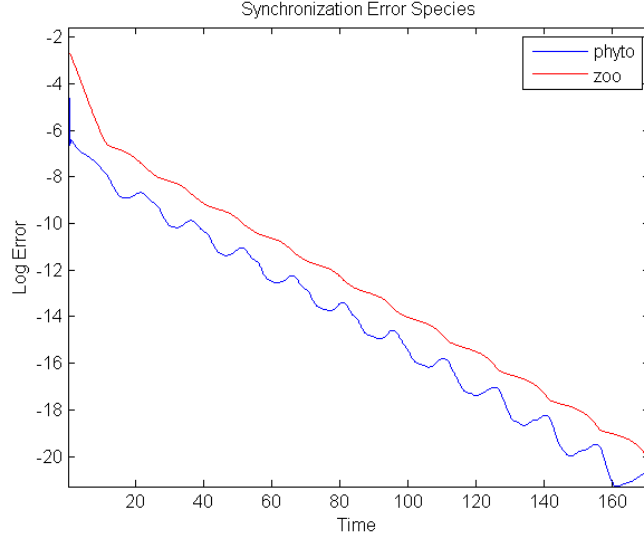
Figure 6.5: Globally-averaged relative synchronization error between drive and response systems. Error between systems is taken with respect to Frobenius norm, i.e., $e_P(t) = \|P - \hat{P}\|_F / (\|P\|_F \Omega)$. Phytoplankton vs time shown in blue, zooplankton vs time shown in red.

Figure 6.4 shows three snapshots from a simulation of the coupled drive-response systems Eq (6.5) and Eq (6.6). Figures (a) and (d) show phytoplankton and zooplankton initial conditions, respectively. Figures (b) and (e) show phytoplankton and zooplankton at $t = 30$. The images appear to coincide somewhat, however there appears to be a density mismatch between drive and response. Particularly, the density is incorrect for the zooplankton response system, apparent in Figure (e). By $t = 171$, both systems have synchronized to within 2.0×10^{-9} and we observe a first demonstration of synchronization between two reaction-diffusion-advection systems by sampling only one species.

The globally-averaged relative synchronization errors are calculated over time with

the Frobenius norm,

$$e_P(t) = \frac{1}{\Omega} \frac{\|P - \hat{P}\|_F}{\|P\|_F},$$ (6.7)

$$e_Z(t) = \frac{1}{\Omega} \frac{\|Z - \hat{Z}\|_F}{\|Z\|_F}.$$

The log of error versus time is plotted in Figure 6.5 and it is clear that the systems are synchronizing. This result alone is already great news for prediction when model parameters are estimated using in-situ measurements as one would be able to observe zooplankton and subsequently assimilate data in order to make forward predictions while allowing for advection due to ocean currents. However, we next study autosynchronization and the ability to estimate model parameters for these systems.

6.3   Autosynchronization

Given that we are aiming to adapt synchronization methods to data assimilation and parameter estimation for advective ecological models on the coastal ocean, we now use the non-autonomous benchmark system to explore autosynchronization. In order to be useful for application of remote sensing, we require access to reasonably accurate ocean current models describing advection during observation and begin by observing both species. We will further extend the system Eq (6.5) to have spatially dependent parameters. In this chapter, we will only show simulations with the spiral parameters as shown in Figures 4.6e and 4.6f, although similar results are obtained with the other parameters.

Stating a parameter estimation problem in the two-dimensional PDE setting within the framework of autosynchronization, we require a drive system

$$\mathbf{u}_t(x, y, t) = \mathbf{f}(\mathbf{u}(x, y, t), \mathbf{p}(x, y)),$$ (6.8)
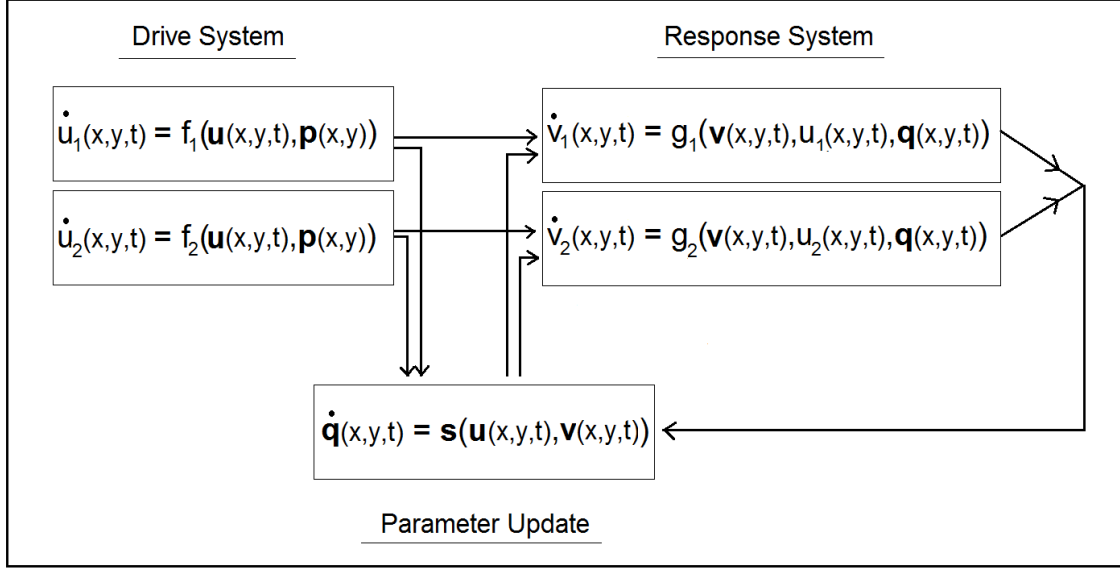
Figure 6.6: Diagram for autosynchronization of two-component PDE system.

from which we are able to sample data with (unknown to us) parameters $\mathbf{p} \in C^0(\Omega \times \Omega)$. Then we must state a response system

$$\mathbf{v}_t(x, y, t) = \mathbf{g}(\mathbf{u}(x, y, t), \mathbf{v}(x, y, t), \mathbf{q}(x, y, t)) \tag{6.9}$$

with the same model form as the drive system if $\mathbf{q} = \mathbf{p}$. Again, the goal is that when $\mathbf{u}(x, y, t)$ is coupled forward into Eq 4.12, then Eq 4.12 will synchronize with Eq 4.11 and $\mathbf{u}(x, y, t) \to \mathbf{v}(x, y, t)$. Concurrently, parameter ODEs are given by

$$\mathbf{q}_t = \mathbf{h}(\mathbf{u}(x, y, t), \mathbf{v}(x, y, t), \mathbf{q}(x, y, t)) \tag{6.10}$$

so that $(\mathbf{v}, \mathbf{q}) \to (\mathbf{u}, \mathbf{p})$ as $t \to \infty$. A box diagram for this type of simulation is shown in Figure 6.6.

Under such assumptions, we state the response system

$$\frac{\partial \hat{P}}{\partial t} = \triangle \hat{P} + \mathbf{v} \cdot \nabla \hat{P} + \hat{P}(1 - \hat{P}) - \frac{\hat{P}\hat{Z}}{\hat{P} + h} + \kappa(P - \hat{P}), \qquad (6.11)$$

$$\frac{\partial \hat{Z}}{\partial t} = \triangle \hat{Z} + \mathbf{v} \cdot \nabla \hat{Z} + \hat{k}\frac{\hat{P}\hat{Z}}{\hat{P} + h} - \hat{m}\hat{Z} + \kappa(Z - \hat{Z}),$$

$$\frac{\partial \hat{k}}{\partial t} = -s(P - \hat{P}),$$

$$\frac{\partial \hat{m}}{\partial t} = -s(Z - \hat{Z}),$$

where

$$\hat{P}(x, y, 0) \neq P(x, y, 0),$$

$$\hat{Z}(x, y, 0) \neq Z(x, y, 0),$$

$$\hat{k}(x, y, 0) \neq k(x, y),$$

$$\hat{m}(x, y, 0) \neq m(x, y),$$

and $\mathbf{v}$ is given by Eq (6.4). For good synchronization results, we choose $s_1 = s_2 = 30$, and $\kappa = 1.25$. Initial conditions for the response model are given by the constant functions

$$\hat{P}(x, y, 0) = 2,$$

$$\hat{Z}(x, y, 0) = 2,$$

$$\hat{k}(x, y, 0) = 5,$$

$$\hat{m}(x, y, 0) = 5.$$

Figure 6.7 presents results from a simulation using the stated response model, verifying that autosynchronization is observed between the two systems, even for spatially-dependent parameters. Results are at times $t = 0$, $t = 200$, and $t = 4,319$.

Figure 6.7: Three time instances of simulation shown at $t = 0$, $t = 200$, and $t = 4,319$. (a) $P(x, y, 0)$ over $\hat{P}(x, y, 0)$. (b) $P(x, y, 200)$ over $\hat{P}(x, y, 200)$. (c) Highly synchronized state $P(x, y, 4, 319)$ over $\hat{P}(x, y, 4, 319)$. (d) $Z(x, y, 0)$ over $\hat{Z}(x, y, 0)$. (e) $Z(x, y, 200)$ over $\hat{Z}(x, y, 200)$. (f) Highly synchronized state $Z(x, y, 4, 319)$ over $\hat{Z}(x, y, 4, 319)$ (g) $k(x, y, 0)$ over $\hat{k}(x, y, 0)$. (h) $k(x, y, 200)$ over $\hat{k}(x, y, 200)$. (i) Estimated state $k(x, y, 4, 319)$ over $\hat{k}(x, y, 4, 319)$. (j) $m(x, y, 0)$ over $\hat{m}(x, y, 0)$. (k) $m(x, y, 200)$ over $\hat{m}(x, y, 200)$. (l) Estimated state $m(x, y, 4, 319)$ over $\hat{m}(x, y, 4, 319)$.

173

Figure 6.8: Globally-averaged relative synchronization errors vs time for species and parameters shown on a log scale. The systems are evolved until a parameter error threshold is reached at $e_k(t) < 1.0 \times 10^{-5}$, which occurs by $t = 4,319$. Errors are calculated, including for parameters, by Eq (6.7)

Figure 6.8 shows the globally averaged relative synchronization errors between drive and response models. While convergent, these results are apparently relatively slow. However, we note that autosynchronization speed can be significantly increased by coupling in the advection terms as,

$$
\begin{aligned}
\frac{\partial \hat{P}}{\partial t} &= \triangle \hat{P} + \mathbf{v} \cdot \nabla P + \hat{P}(1 - \hat{P}) - \frac{\hat{P}\hat{Z}}{\hat{P} + h} + \kappa(P - \hat{P}), &\qquad (6.12) \\
\frac{\partial \hat{Z}}{\partial t} &= \triangle \hat{Z} + \mathbf{v} \cdot \nabla Z + \hat{k}\frac{\hat{P}\hat{Z}}{\hat{P} + h} - \hat{m}\hat{Z} + \kappa(Z - \hat{Z}), \\
\frac{\partial \hat{k}}{\partial t} &= -s(P - \hat{P}), \\
\frac{\partial \hat{m}}{\partial t} &= -s(Z - \hat{Z}),
\end{aligned}
$$

where the absence of "hats" in the advection terms denotes complete replacement from the drive system. This additional coupling results in a much faster autosynchronization speed, shown in Figure 6.9. Here, the same initial conditions, parameters, and coupling strengths were used for uniformity between simulations. Thus we have

174

shown that autosynchronization is robust to spatially dependent parameters when sampling both species, so we next explore whether autosynchronization is successful when sampling only one species.

(a)   (b)

Figure 6.9: Globally-averaged relative synchronization errors vs time for species and parameters shown on a log scale. The sytstems are evolved until the same parameter error threshold is reached, $e_k(t) < 1.0 \times 10^{-5}$, which now occurs by $t = 1,441$, a much faster rate of synchronization than shown in Figure 6.8.

6.4 Sampling One Species

We previously alluded to the fact that we require accurate knowledge of the advection governing species evolution in order to produce good results. We further require that these methods work by sampling only one species.

A box diagram describing this sort of coupling is shown in Figure 6.10 where the arrows between the second component of the system are dropped in opposition to Figure 6.6 to annotate that the second component is unknown.
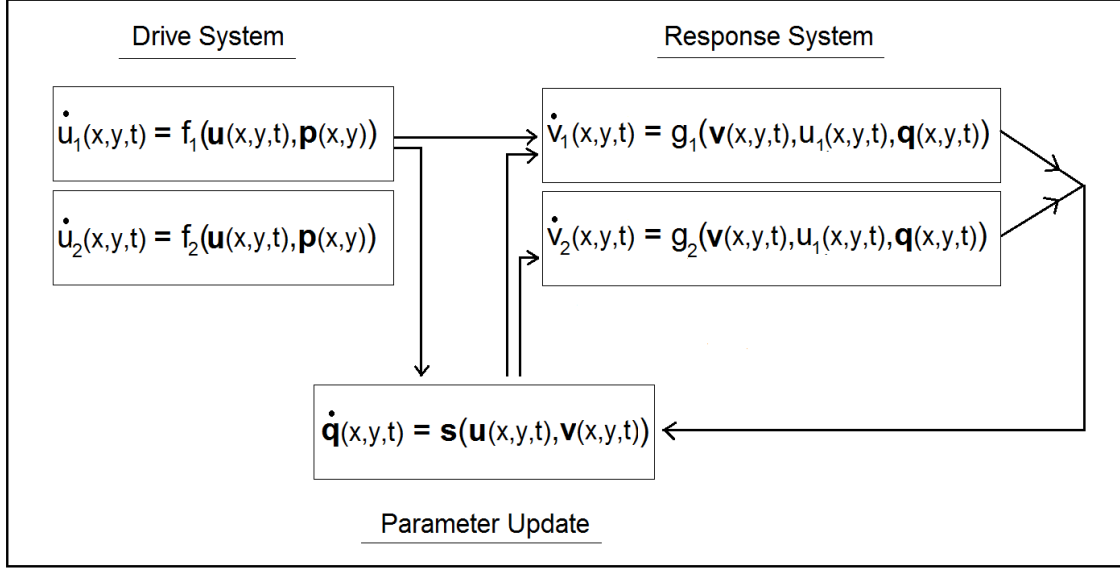
Figure 6.10: Diagram for autosynchronization of two-component PDE system by sampling only one species.

We state a new response model that requires sampling only phytoplankton as,

$$
\begin{aligned}
\frac{\partial \hat{P}}{\partial t} &= \triangle \hat{P} + \mathbf{v} \cdot \nabla \hat{P} + \hat{P}(1 - \hat{P}) - \frac{\hat{P}\hat{Z}}{\hat{P} + h} + \kappa(P - \hat{P}), && (6.13) \\
\frac{\partial \hat{Z}}{\partial t} &= \triangle \hat{Z} + \mathbf{v} \cdot \nabla \hat{Z} + \hat{k}\frac{\hat{P}\hat{Z}}{P + h} - \hat{m}\hat{Z}, \\
\frac{\partial \hat{k}}{\partial t} &= -s_1(P - \hat{P}), \\
\frac{\partial \hat{m}}{\partial t} &= -s_2(P - \hat{P})\hat{P},
\end{aligned}
$$

where $s_1 = 0.2$, $s_2 = 0.6$, and $\kappa = 1.45$. In Figure 6.11 we see the results of a simulation of the reaction-diffusion-advection system Eq (6.13) at three different times. The spatially dependent model parameters are, the spiral model parameters and advection is given by Eq (6.4). The final column in Figure 6.11 demonstrates the ability of autosynchronization to resolve both model parameters and states. These results are shown at three times, $t = 0$, $t = 200$, and $t = 2,821$.
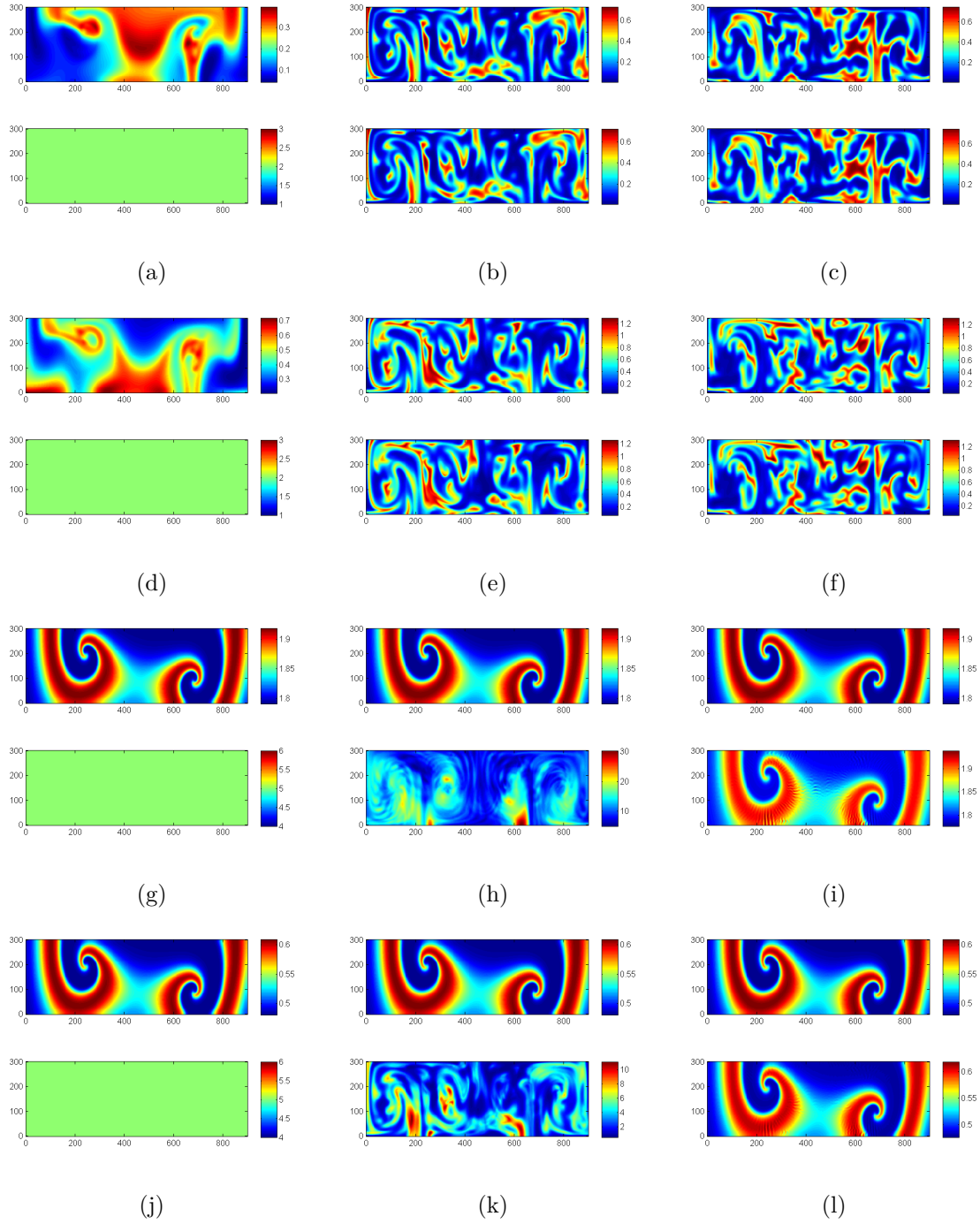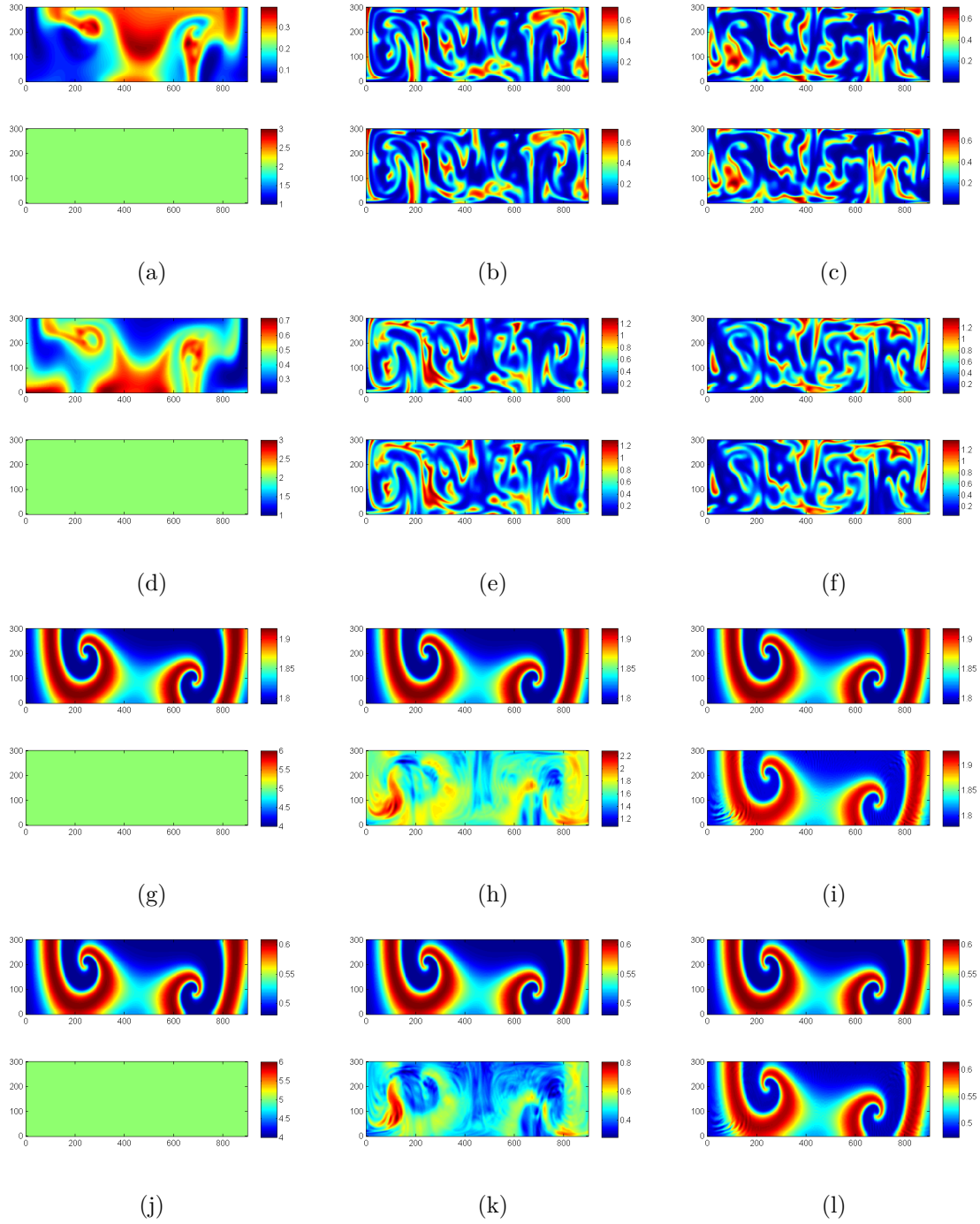
Figure 6.11: Three time instances of simulation shown at $t = 0$, $t = 200$, and $t = 2,821$.(a) $P(x,y,0)$ over $\hat{P}(x,y,0)$. (b) $P(x,y,200)$ over $\hat{P}(x,y,200)$. (c) Highly synchronized state $P(x,y,2,821)$ over $\hat{P}(x,y,2,821)$. (d) $Z(x,y,0)$ over $\hat{Z}(x,y,0)$. (e) $Z(x,y,200)$ over $\hat{Z}(x,y,200)$. (f) Highly synchronized state $Z(x,y,2,821)$ over $\hat{Z}(x,y,2,821)$ (g) $k(x,y,0)$ over $\hat{k}(x,y,0)$. (h) $k(x,y,200)$ over $\hat{k}(x,y,200)$. (i) Estimated state $k(x,y,2,821)$ over $\hat{k}(x,y,2,821)$. (j) $m(x,y,0)$ over $\hat{m}(x,y,0)$. (k) $m(x,y,200)$ over $\hat{m}(x,y,200)$. (l) Estimated state $m(x,y,2,821)$ over $\hat{m}(x,y,2,821)$.
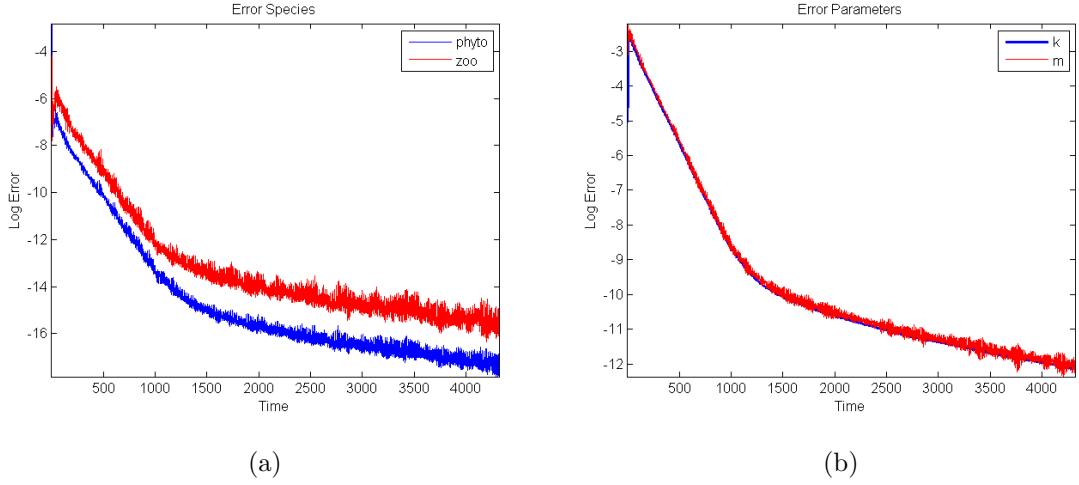
177
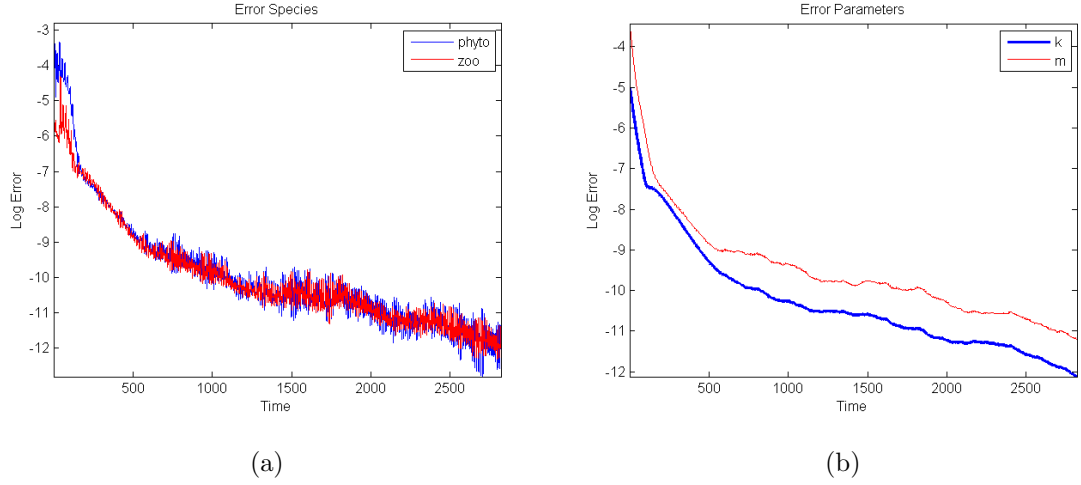
Figure 6.12: Globally-averaged relative synchronization errors vs time for species and parameters shown on a log scale. Parameter errors are shown to converge to within the synchronization threshold used in Figures 6.8 and 6.5, $e_k(t) < 1.0 \times 10^{-5}$, by $t = 2,821$. In contrast to Figure 6.8 we are sampling only one species.

Figure 6.12 shows the globally averaged relative synchronization errors between species and parameters on a log scale. Once again, we note that autosynchronization may be significantly temporally improved by complete replacement in the advection term,

$$
\begin{aligned}
\frac{\partial \hat{P}}{\partial t} &= \triangle \hat{P} + \mathbf{v} \cdot \nabla P + \hat{P}(1 - \hat{P}) - \frac{\hat{P}\hat{Z}}{\hat{P} + h} + \kappa(P - \hat{P}), \qquad (6.14) \\
\frac{\partial \hat{Z}}{\partial t} &= \triangle \hat{Z} + \mathbf{v} \cdot \nabla \hat{Z} + \hat{k}\frac{\hat{P}\hat{Z}}{P + h} - \hat{m}\hat{Z}, \\
\frac{\partial \hat{k}}{\partial t} &= -s_1(P - \hat{P}), \\
\frac{\partial \hat{m}}{\partial t} &= -s_2(P - \hat{P})\hat{P},
\end{aligned}
$$

where $s_1 = 0.2$, $s_2 = 0.6$, and $\kappa = 1.45$. Here, only phytoplankton was replaced in the advection term since we are unable to observe zooplankton.

178

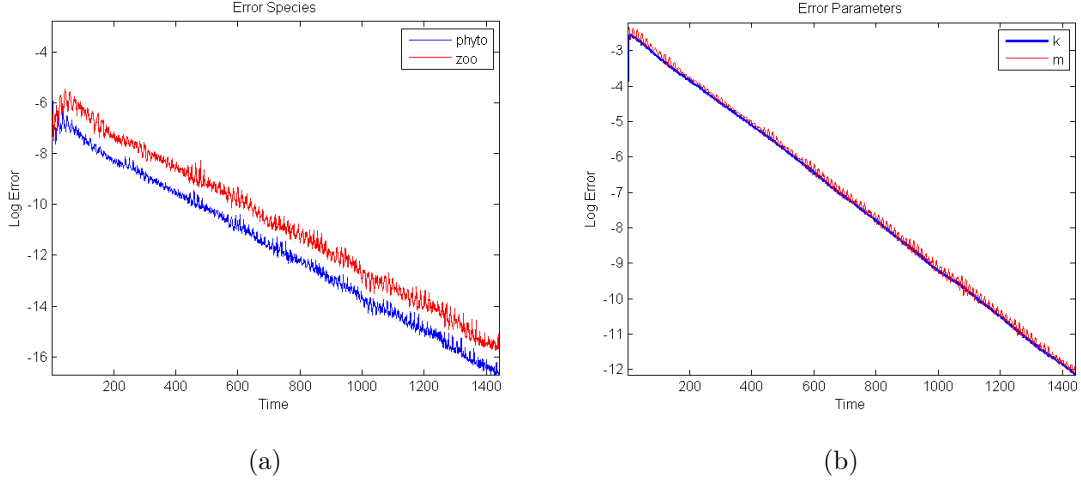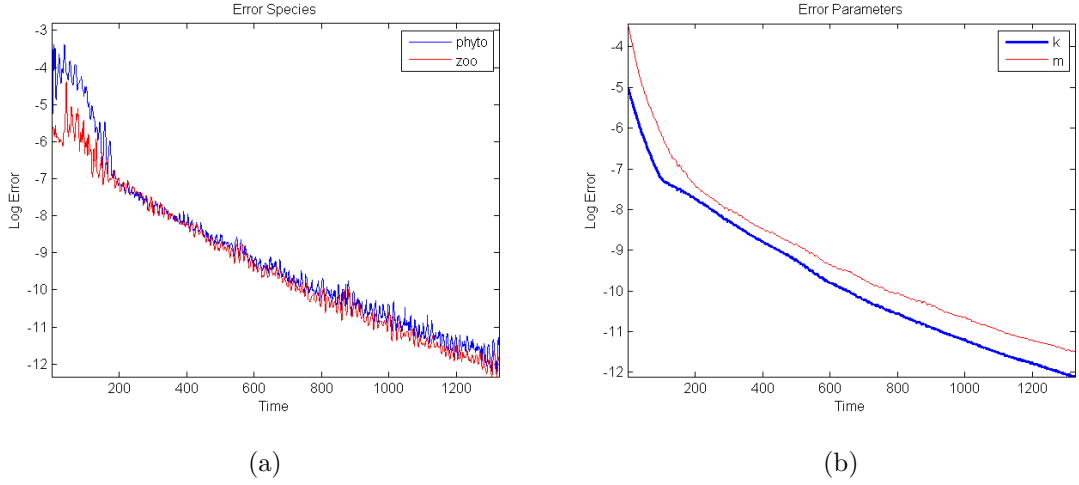Figure 6.13: Globally-averaged relative synchronization errors vs time for species and parameters shown on a log scale. Parameter errors are shown to converge to within 1.0×10^{-5} by $t = 1,326$.

Figure 6.13 shows the globally averaged relative synchronization errors for species and parameters over time. The synchronization error between the parameters $k(x,y)$ and $\hat{k}(x,y,t)$ converges to within the same values as previous results shown in Figures 6.8 and 6.9, wherein both species were sampled, in a shorter time epoch. We note that it is likely that autosynchronization speeds may be increased when sampling both species if a more thorough parameter search is performed.

The non-autonomous double gyre is introduced to be a challenging advection component in the reaction-diffusion-advection model built from the reaction-diffusion model examined in Chapter 4. Synchronization is shown to be robust to the modified systems when sampling one species. This chapter is a first demonstration of autosynchronization for spatially-dependent parameters by sampling one species between two systems of reaction-diffusion-advection equations. In fact, by showing autosynchronization is robust to sampling only one species, spatially dependent parameters, and time-dependent advection, these methods may feasibly be applied to real satellite imagery data representing ocean ecology as advected by non-autonomous currents.

179

Chapter 7

Synchronization on Coherent Sets

In this chapter we build upon the results in Chapter 6 by turning to a method to increase the rate of convergence in certain regions of the domain of a reaction-diffusion-advection system. Our goal is to improve synchronization, over a given time epoch, on large regions of the domain for model forecasts and predictions. We note in Chapter 6 that advection has significantly slowed the convergence rate when compared to the non-advective systems in Chapter 4. Therefore, we now merge synchronization with the burgeoning field of coherent sets to realize the benefits of synchronization over only appropriately-chosen subsets of the domain. Coherent sets are sets that are in some sense minimally dispersive over a finite time epoch. The main motivation is to choose subsets over the domain that are most "alike" to be those over which parameters are fit; coherent sets serve this purpose.

In this chapter we re-introduce the reaction-diffusion-advection system with which we will be working. We next describe the necessary background for extracting what are called *coherent sets* from a time-dependent dynamical system such as the double gyre. We next perform simulations to observe synchronization over only the coherent subsets of the domain. Results obtained are compared to those obtained in Chapter 6 and a discussion follows.

7.1 Model Equations

Here, for convenience, we re-state the model equations to be studied. We simulate the reaction-diffusion-advection system of equations,

$$
\frac{\partial P}{\partial t} = \triangle P + \mathbf{v} \cdot \nabla P + P(1-P) - \frac{PZ}{P+h}, \qquad \text{Drive} \qquad (7.1)
$$

$$
\frac{\partial Z}{\partial t} = \triangle Z + \mathbf{v} \cdot \nabla Z + k\frac{PZ}{P+h} - mZ,
$$

$$
\frac{\partial \hat{P}}{\partial t} = \triangle \hat{P} + \mathbf{v} \cdot \nabla P + \hat{P}(1-\hat{P}) - \frac{\hat{P}\hat{Z}}{\hat{P}+h} + \kappa(P - \hat{P}), \qquad \text{Response}
$$

$$
\frac{\partial \hat{Z}}{\partial t} = \triangle \hat{Z} + \mathbf{v} \cdot \nabla \hat{Z} + \hat{k}\frac{\hat{P}\hat{Z}}{P+h} - \hat{m}\hat{Z},
$$

$$
\frac{\partial \hat{k}}{\partial t} = -s_1(P - \hat{P}),
$$

$$
\frac{\partial \hat{m}}{\partial t} = -s_2(P - \hat{P})\hat{P},
$$

where $s_1 = 0.2$, $s_2 = 0.6$, and $\kappa = 1.45$. The advection is governed by the non-autonomous double gyre,

$$
\dot{x} = -A\pi \sin(\pi f(x,t)) \cos\left(\pi \frac{y}{300}\right), \qquad (7.2)
$$

$$
\dot{y} = A\pi \cos(\pi f(x,t)) \sin\left(\pi \frac{y}{300}\right) \frac{df}{dx},
$$

$$
f(x,t) = (\epsilon \sin(\omega t)) \left(\frac{x}{450}\right)^2 + (1 - 2\epsilon \sin(\omega t)) \frac{x}{450},
$$

where $\epsilon = 0.25$, $A = 5$, $\omega = 2\pi/50$, and the domain is $\Omega = 300 \times 900$. We enforce initial conditions,

$$P(x, y, 0) \neq \hat{P}(x, y, 0),$$

$$Z(x, y, 0) \neq \hat{Z}(x, y, 0),$$

$$k(x, y, 0) \neq \hat{k}(x, y, 0),$$

$$m(x, y, 0) \neq \hat{m}(x, y, 0),$$

and desire that $\hat{P} \to P, \hat{Z} \to Z, \hat{k} \to k$, and $\hat{m} \to m$. In this chapter, we only sample one species, $P(x, y, t)$. We first demonstrate the approach on the synchronization problem by assuming $\hat{k} = k$ and $\hat{m} = m$. Next, we demonstrate the approach on the full parameter and state estimation problem.

7.2 Coherent Pairs

We choose the double gyre as a benchmark component of the reaction-diffusion-advection equations to simulate offshore chaotic transport. Transport in fluid systems is a complex problem and an area of active research [58–62]. Recently, a probabilistic approach based on transfer operators has been developed to study transport in chaotic dynamical systems [63]. In Chapter 6, we present a first demonstration of autosynchronization between reaction-diffusion-advection systems, and here we improve upon those results. Information about the underlying dynamics allows for more efficient observation of the entire system through synchronization and autosynchronization.

We exploit a probabilistic method for determining maximally coherent or minimally dispersive sets over finite-time epochs, first demonstrated in [63]. Let $M \subset \mathbb{R}^d$ be a compact smooth manifold. Let $f(x, t)$, with $x \in M$ and $t \in \mathbb{R}$, be a non-autonomous vector field. We require that f is smooth enough such that there exists

a flow map $\Phi(x, t, \tau) : M \times \mathbb{R} \times \mathbb{R} \to M$ describing the final location of a point x at a time t subject to the flow for time τ.

Definition 7.2.1. (Froyland, Santitissakeekorn, & Monahan, 2) *Two sets A_t and $A_{t+\tau}$ are called a (ρ, t, τ)-coherent pair if*

$$\rho_\mu(A_t, A_{t+\tau}) = \frac{\mu(A_t \cap \Phi(A_{t+\tau}, t+\tau; -\tau))}{\mu(A_t)} \geq \rho_0, \tag{7.3}$$

and $\mu(A_t) = \mu(A_{t+\tau})$, where μ is a reference probability measure at time t. Furthermore, the sets must be resistant to small noise perturbations.

To clarify resistance to small noise perturbations, coherent sets are time-evolving almost-invariant sets, or sets that mostly hold together. There may be strong mixing within coherent sets but weak mixing between them. The reference probability μ describes the mass distribution of the quantity under scrutiny over the time interval $[t, t+\tau]$.

Two coherent sets are shown in Figure 7.1 for the time-dependent double gyre, Eq (7.2). The coherent sets were uncovered by seeding the domain with initial points and flowing the initial points for $t = 50$. That is the separate regions are minimally dispersive such that the blue subset exhibits very little mixing with the red subset over the time epoch.
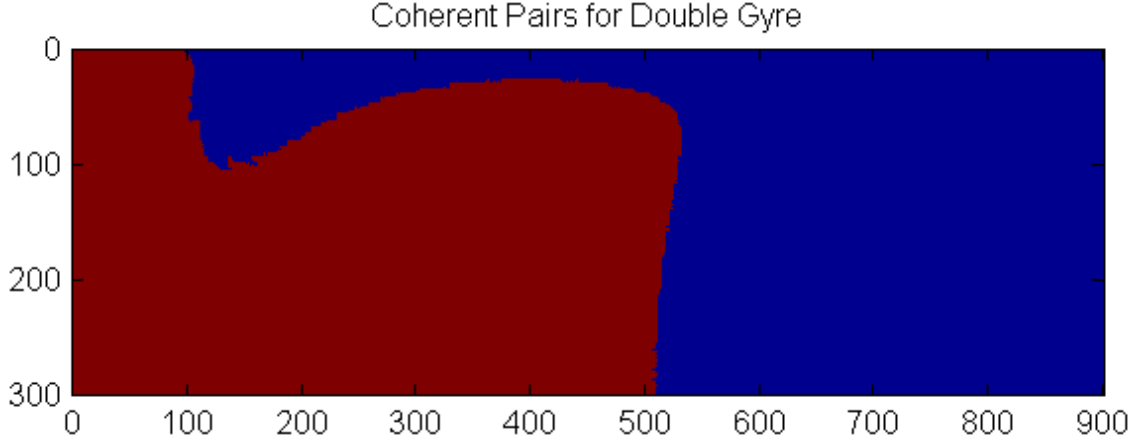
Figure 7.1: Figure represents an extraction of two coherent pairs extracted from the non-autonomous double gyre Eq (7.2) over a simulation time of $t = 50$.

The two sets shown in Figure 7.1 serve as the sets over which we couple the systems Eq (7.1). This partition of the domain was provided with thanks from Tian Ma. The sets are evolved in time according to Eq (7.2) in order to keep track of the coherent pairs. We exploit this knowledge of the underlying dynamics toward improving synchronization by observing synchronization over only coherent regions.

7.3 Model as Ordinary Differential Equation

We first note that, since there is little mixing between the two sets, an ODE model over the coherent set might be an appropriate simplification. Here, the biomass is averaged over each coherent pair during observation. The total biomass of both species is averaged over the coherent sets, providing a measure of the average biomass. The average biomass is fed into the ODE drive-response system corresponding to Eq (7.1),

$$\frac{dP}{dt} = P(1-P) - \frac{PZ}{P+h}, \qquad \text{Drive} \qquad (7.4)$$

$$\frac{dZ}{dt} = k\frac{PZ}{P+h} - mZ,$$

$$\frac{d\hat{P}}{dt} = \hat{P}(1-\hat{P}) - \frac{\hat{P}\hat{Z}}{\hat{P}+h} + \kappa(P-\hat{P}), \qquad \text{Response}$$

$$\frac{d\hat{Z}}{dt} = k\frac{\hat{P}\hat{Z}}{P+h} - m\hat{Z}$$

where $\kappa = 5$. To clarify, Figure 7.2 describes a schematic diagram for the coupling in these systems, where $|\Omega|$ denotes the Lebesgue measure [80], of Ω.
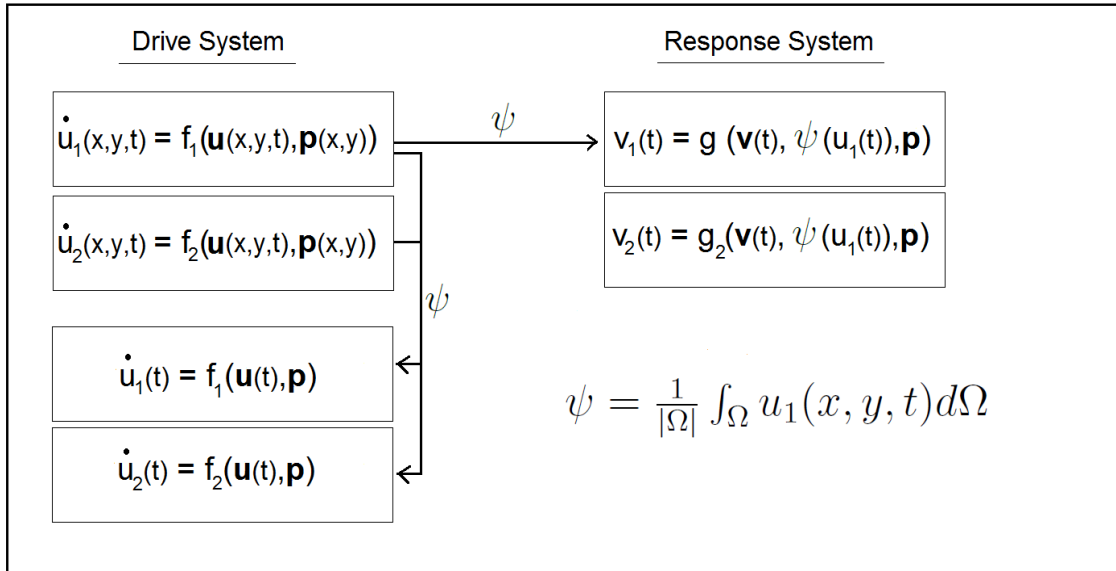
Figure 7.2: The coupling between drive and response systems wherein the drive PDE is simplified to and ODE and drives response ODE system. Here ψ is the averaging filter.

Intuitively, we expect an ODE representation of the system to synchronize reasonably well over a given time epoch if there is little mixing out of the region over which the system is represented as an ODE. Simulation results are described in Figure 7.3,

where two approaches are compared. First, we assume the observed system can be represented as an ODE over the entire domain and feed the average phytoplankton biomass into the system Eq (7.4).

The synchronization error is plotted in red and is shown to oscillate some distance from the identical manifold, likely due to the oversimplification of the observed dynamics. Next, we average the biomass over each region separately and inform a different ODE with same model form over individual coherent sets. The synchronization error between ODE from observed data over the coherent set is plotted in blue. We note that the synchronization error is most often smaller when coupled over only coherent regions. As a preliminary demonstration of the efficacy of synchronization over coherent sets, we observe an improvement over our previous work.
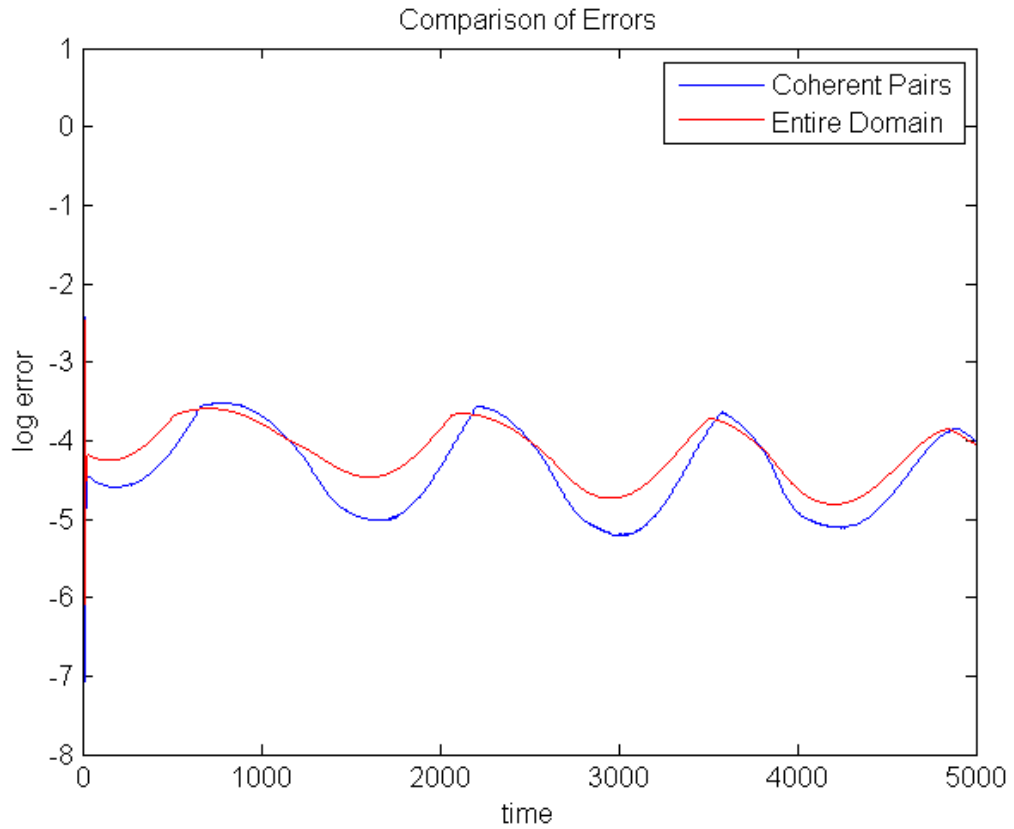
Figure 7.3: The coupling between drive and response systems wherein drive PDE is averaged to ODE and drives response ODE system. Here ψ from Figure 7.2 is the averaging filter.

7.4 Synchronization Over Coherent Sets

We now study the synchronization problem, where we synchronize over only coherent sets and compare results to synchronization over the entire domain at once. As noted, we now assume $\hat{k} = k$ and $\hat{m} = m$, such that we are testing synchronization first. Results are shown in Figure 7.4, where globally-averaged synchronization errors are compared. In Figure , the synchronization error is plotted over only the coherent sets in red. The error plotted in blue represents previous synchronization results obtained in Chapter 6. Thus, synchronization is more efficient when performed over the coherent sets as opposed to the entire domain as in Chapter 6.

Phytoplankton Errors

(a)

Zooplankton Errors
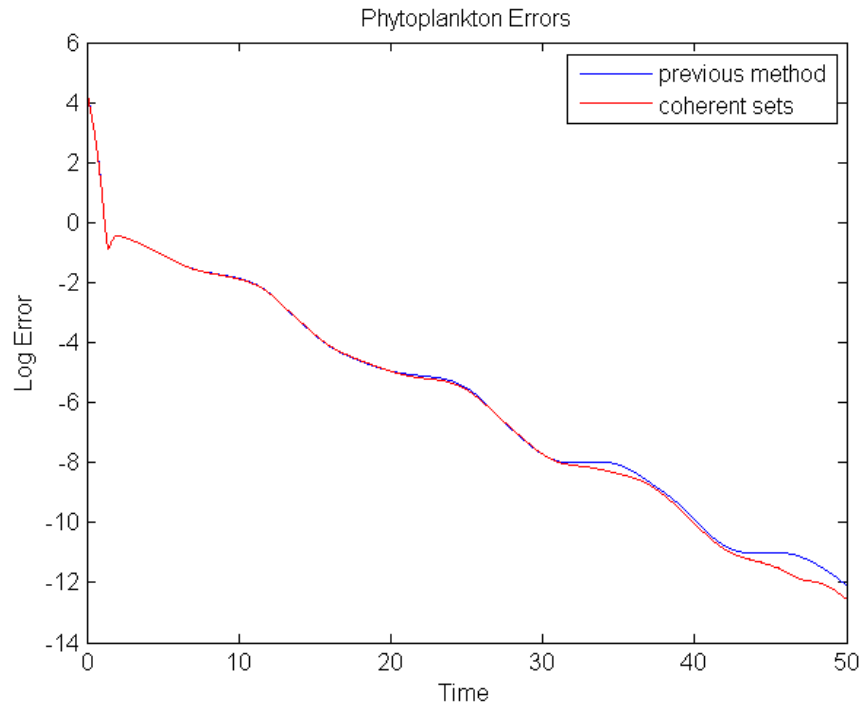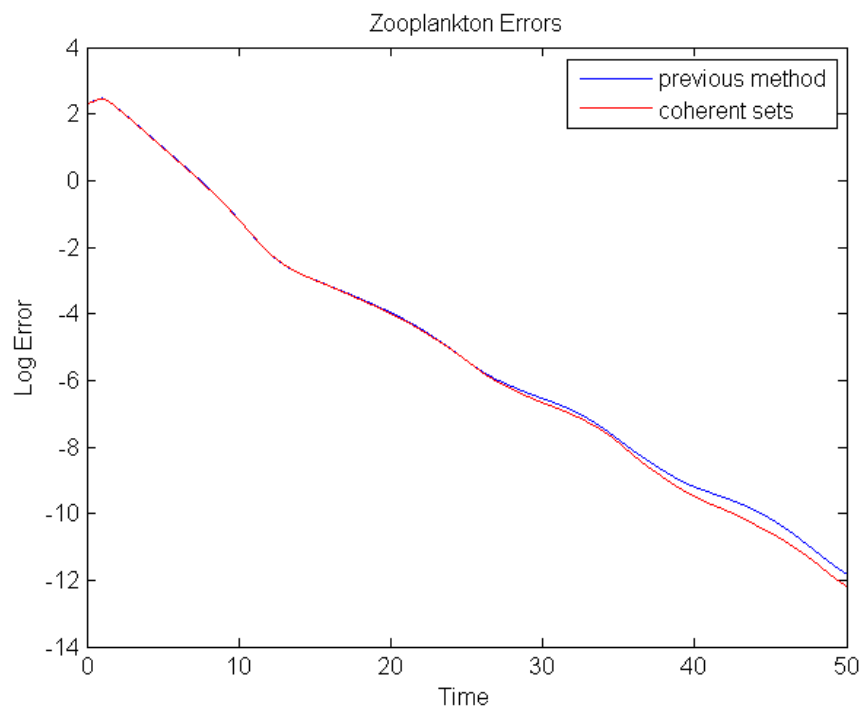
(b)

Figure 7.4: Comparison of methods from Chapter 6 with synchronization over coherent sets. Figure 7.4a compares the previous method, shown in blue, with the coherent sets method, shown in red, for phytoplankton. Figure 7.4b shows the same results for zooplankton.

188

7.5 Autosynchronization Over Coherent Sets

We next study the parameter estimation problem, where we autosynchronize over only coherent sets and compare results to those obtained in Chapter 7. Here, we simulate the full drive-response system Eq (7.1), where parameters and model states are to be estimated. Initial conditions for the drive system are arbitrarily,

$$\hat{P}(x, y, 0) = 2,$$
$$\hat{Z}(x, y, 0) = 2,$$
$$\hat{k}(x, y, 0) = 3,$$
$$\hat{m}(x, y, 0) = 3,$$

and the parameters, $k(x, y)$ and $m(x, y)$, are given by the Gaussian equations Eq(4.20).

Results are shown in Figure 7.5, where globally-averaged parameter errors are compared. In Figure 7.5, the synchronization error is plotted over only the coherent sets in red. The error plotted in blue represents previous synchronization results obtained in Chapter 6. Autosynchronization is more efficient when performed over the coherent sets as opposed to the entire domain as in Chapter 6.

The results in Figure 7.5, although preliminary, are very promising with respect to estimation over regions that might include chaotic mixing. Thus, we have demonstrated a potential method to improve the rate of convergence for model state and parameter estimation for reaction-diffusion-advection systems by exploiting the knowledge of coherent sets in the advective dynamics.
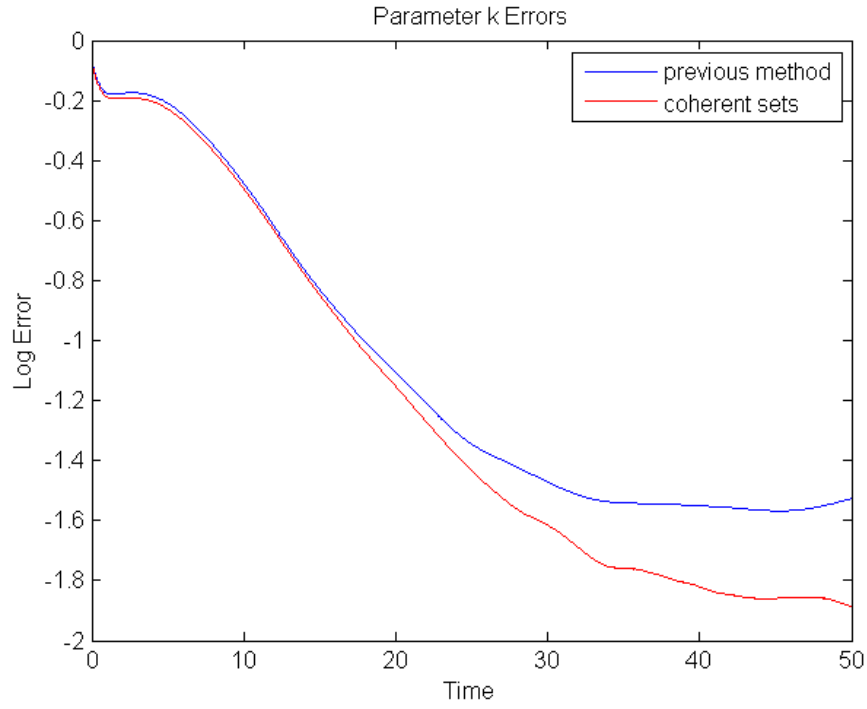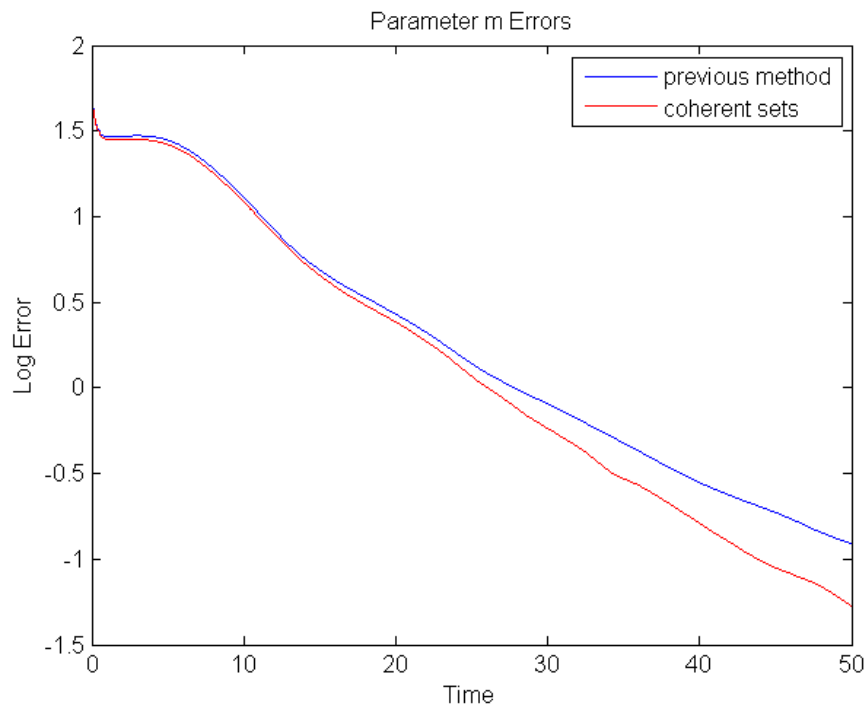
Figure 7.5: Comparison of methods from Chapter 6 with synchronization over coherent sets. Figure 7.4a compares the previous method, shown in blue, with the coherent sets method, shown in red, for phytoplankton. Figure 7.4b shows the same results for zooplankton.

We have briefly introduced the idea of merging synchronization techniques with the emergence of coherent pairs in a non-autonomous dynamical system. This is made possible by the physical assumption of advection in our ecological models and the seminal work [63] to uncover coherent pairs in a dynamical system over a finite time epoch. We have briefly demonstrated that the rates of convergence of both synchronization and autosynchronization are improved by coupling over coherent pairs. This is an exciting development toward improving our methods for fitting parameters and estimating model states for oceanic ecology informed by remote sensing data.

Chapter 8

Concluding Remarks and Future Work

In this thesis, we have explored and developed the theory of autosynchronization for a system of PDEs. We emphasize here the improvements upon past synchronization methods in that we treat autosynchronization as a means of parameter estimation of parameters that exist in a function space. We assume prior knowledge of the model form of the observed system, but have no prior knowledge of the parameters. By sampling at every time step, we observe identical synchronization between the response and drive systems, akin to preceding work [52]. As a first attempt, we provide a model form for adaptive parameters in the response system such that we observe identical synchronization between response model parameters and drive model parameters, or autosynchronization. Our techniques are implemented on a benchmark model and estimates converge to true parameters. Thus, autosynchronization is observed for PDEs with scalar parameters.

Next, we considered the same system of PDEs wherein the parameters were spatially dependent. We provided a scheme with which we observe autosychronization of spatially dependent parameters. We next confirm our results against several different

192

functional forms for model parameters.

We markedly improved upon these results once more with an autosynchronization scheme that requires sampling of only one species (phytoplankton). We note that in order to evolve a system of PDEs for forecasting, we require initial conditions for both species; this is a complication when working with remote sensing data with which we only observe one of the species in the full system. This concern was addressed by providing a response system to observe autosynchronization and estimate the full state of zooplankton using only phytoplankton data. These methods are plausible for use in remote sensing problems.

A drawback of this technique with application to hyperspectral satellite data is that data may be noisy; this is where filtering techniques have a built-in advantage. Data may also be occluded because of cloud cover, or spatial limitations on sampling over the domain. Cloudy data are first studied with results indicating autosynchronization despite clouds when systems are allowed to oscillate uncoupled while occluded. Samples are taken to be local averages representing a subset of the domain. By driving only on coarse subset of the original domain, we show that autosynchronization is robust to spatial subsampling as long as subsampling is not too coarse. However, we have not had the same success for autosynchronization with large amounts of simply connected occluded data. Since there is little hope to synchronize PDEs without large quantities of data relative to the domain, we require techniques to "fill in" missing data.

Another complication with applying these techniques to satellite imagery is temporal data resolution. There may be several days between successive images and autosynchronization requires ample data observations. The need for frequent observables is perhaps the main drawback to this method. However, autosynchronization may be advantageous for parameter estimation or model state estimation in situations where spatiotemporal data are abundant, and especially where parameters are

expected to vary spatially. Temporal sparsity in observables is shown to slow the rate of synchronization and parameter estimation, but does not destroy stability of the synchronization manifold.

We have proven the global stability of the synchronization manifold for a range of coupling strengths and shown that these methods will result in parameter and state estimation when observables are governed by physics that are accurately represented by the assumed model form. Proofs are found for several of the systems, but are not yet discovered for the coupled systems resulting in autosynchronization when sampling one species. In the absence of the Lyapunov direct method, we have analyzed the stability for the synchronization manifold by conditional Lyapunov exponents. Conditional Lyapunov exponents were initially estimated for the system of ODEs, and were then estimated on the representative coupled ODEs approximating the coupled PDEs.

We have demonstrated autosynchronization under the additional assumption of reaction-diffusion-advection PDEs by studying a complex flow field that is characteristic of the type of mixing typical in coastal ocean currents. The same results are next demonstrated by sampling one species.

Finally, we have merged the fields of synchronization and coherent pairs in order to improve synchronization over spatiotemporal phenomena. It was demonstrated that the ODE representation, or average biomass, of the species over a coherent subset of the domain will synchronize more efficiently than the ODE representation of ecology over the entire domain. We have observed more efficient synchronization when coupling over only coherent pairs as opposed to coupling over the entire domain as in Chapter 6. Finally, we compared the autosynchronization results from Chapter 6 with autosynchronization over only coherent pairs and found the latter to be more efficient over the same time epoch. These results are encouraging for use in application, particularly our target application of remote sensing toward ocean forecasting. Given

ocean currents and forecasts, and coupled with this sort of analysis of the ocean current dynamics, more accurate model estimates are expected over coherent regions.

This work is a first demonstration of many different phenomena with respect to synchronization and there remains abundant future work in the field. Future work is aimed at studying how much data can be occluded from the observable set before autosynchronization completely fails. Clearly, results obtained are not as accurate when the locally-averaged sampling is sparse. We note, however, that our satellite data is sufficiently fine such that interpolation or local averaging for simulation on a finer grid is unnecessary. That is, for our application to remote sensing, we evolve ecology over the same grid on which the data are observed.

Additional future study includes synchronization over finite datasets. Naively, one might run the drive-response simulation until samples are depleted, at which time the models are no longer coupled. We aim to build methods to observe the most efficient synchronization possible over a finite epoch.

Furthermore, proofs on synchronization using the Lyapunov direct method are needed to study the synchronization manifold for the coupling in Chapter 6. We aim to extend the Lyapunov functions for reaction-diffusion systems to reaction-diffusion-advection systems. For the cases in which Lyapunov functions are ambitious, our goal is to study stability using conditional Lyapunov exponents.

There is much work to be done in the merging of coherent pairs and synchronization, and even model forecasting. For example, more than two coherent pairs can be uncovered such that the domain might be sub-divided several times into more-coherent pairs [101]. This might result in even more accurate synchronization over hierarchical coherent regions. Furthermore, we aim to study whether a reaction-diffusion system will perform well enough over smaller coherent regions such that we need not include advection in the synchronization between systems.

Finally, we aim to apply these methods to observe the most accurate forecasts

possible with a finite set of sampled data. At this point the techniques are ready for use on real observed data, particularly coastal algal blooms. The main goal of this work is to build tools for forecasts based on observed satellite data and available ocean currents. We aim to forecast geophysical quantities of interest such as algal bloom events. Knowing that plankton are subject to the ocean currents [15], we are confident that biomass in one coherent region will not mix with biomass in another coherent region. Thus, we aim to use coherent regions analysis as a method to improve synchronization and also as a method of forward prediction.

Perhaps the most exciting future work is to model fit and forecast over regions for which we have no data for ocean currents. We assume reaction-diffusion-advection dynamics over the domain, but ocean currents would be inferred from time-adjacent images using a technique called *optical flow* [102]. Techniques for inferring vector fields from time-adjacent images based on physical assumptions more appropriate for fluid flow have recently been developed [103], resulting in accurate reconstruction of ocean-like phenomena such as gyres and eddys. Subsequently, our full methods would be appropriate for use in any region observable by satellite-mounted remote sensing instruments. With vector fields in hand, coherent regions might be uncovered and models and parameters might be estimated, producing previously unavailable model forecasts.

Here, we observe over every point in the grid as would be available from satellite data, however it has been shown that synchronization is possible by sub-sampling the grid [52]. Further, we will be interested to allow k and m to vary spatially as functions, $k(x, y)$ and $m(x, y)$ as they also account for phytoplankton dynamics.

Our interest in this PDE model stems from our work in remote sensing, to build a better understanding of our ocean's ecology. Particularly, we aim to predict short-term behavior of coastal algal blooms. Such a system may in principle be modeled by estimating parameters directly from observed data in the field. This additional

data could then be used to validate model predictions informed by remote sensing data. However, hyperspectral satellite imagery provides the observed data to which we would synchronize a response model in hopes of autosynchronization providing good parameter estimates for forecasting. Since phytoplankton are largely affected by spatial inhomogeneities in the ocean such as nitrogen runoff, regions of hypoxia, or upwelling, to name a few parameter inhomogeneity-inducing effects, we wish to allow model parameters to vary spatially. These considerations are especially important since our models will be built over coastal domains where large changes in ocean biology occur spatially, leading naturally to spatially dynamic parameters.

Bibliography

[1] M.J.R. Fasham. Modelling the marine biota. *The Global Carbon Cycle*, pages 457–504, 1993.

[2] JE Truscott and J Brindley. Ocean plankton populations as excitable media. *Bulletin of Mathematical Biology*, 56(5):981–998, 1994.

[3] Marten Scheffer, Sergio Rinaldi, Yuri A Kuznetsov, and Egbert H van Nes. Seasonal dynamics of daphnia and algae explained as a periodically forced predator-prey system. *Oikos*, pages 519–532, 1997.

[4] Eckart Steffen, Horst Malchow, and Alexander B Medvinsky. Effects of seasonal perturbations on a model plankton community. *Environmental Modeling & Assessment*, 2(1-2):43–48, 1997.

[5] L. Backer and D. McGillicuddy. Harmful algal blooms. *Oceanography*, 19(2):94, 2006.

[6] Kathleen T Alligood, Tim D Sauer, and James A Yorke. *Chaos: an introduction to dynamical systems*. Springer, 1996.

[7] Louis M Pecora, Thomas L Carroll, Gregg A Johnson, Douglas J Mar, and James F Heagy. Fundamentals of synchronization in chaotic systems, concepts, and applications. *Chaos: An Interdisciplinary Journal of Nonlinear Science*, 7(4):520–543, 1997.

[8] Seelye Martin. *An introduction to ocean remote sensing*. Cambridge University Press, 2004.

[9] Orbit ground tracks. `http://www.aerospaceweb.org/question/spacecraft/q0282.shtml`. [Online; accessed 25-Feb-2013].

[10] European space agency: Types of orbits. `http://www.esa.int/Our_Activities/Launchers/Types_of_orbits`. [Online; accessed 25-Feb-2013].

[11] Floyd F Sabins and Remote Sensing. Principles and interpretation. *Remote sensing, San Francisco*, 1987.

[12] Genearl botany - university of miami online course material. `http://www.bio.miami.edu/dana/226/226F09_11.html`. [Online; accessed 3-May-2013].

[13] Manly hydraulics laboratory. `http://mhl.nsw.gov.au/projects/berowra/chloro.php`. [Online; accessed 3-May-2013].

[14] Hico database. `http://hico.coas.oregonstate.edu/datasearch/data-search-basic.php`. [Online; accessed 5-Nov-2012].

[15] A. Medvinski, S. Petrovskii, I. Tikhonova, H Malchow, and B. Li. Spatiotemporal complexity of plankton and fish dynamics. *SIAM Review*, 44(3):311–370, 2002.

[16] Amit Huppert, Bernd Blasius, and Lewi Stone. A model of phytoplankton blooms. *The American Naturalist*, 159(2):156–171, 2002.

[17] Peter M Cox, Richard A Betts, Chris D Jones, Steven A Spall, and Ian J Totterdell. Acceleration of global warming due to carbon-cycle feedbacks in a coupled climate model. *Nature*, 408(6809):184–187, 2000.

[18] Robert J Charlson, James E Lovelock, Meinrat O Andreae, Stephen G Warren, et al. Oceanic phytoplankton, atmospheric sulphur, cloud albedo and climate. *Nature*, 326(6114):655–661, 1987.

[19] Phillip Williamson and John Gribbin. How plankton change the climate(jgofs). *New Scientist*, 129(1760):48–52, 1991.

[20] Andrew M Edwards and John Brindley. Zooplankton mortality and the dynamical behaviour of plankton population models. *Bulletin of mathematical biology*, 61(2):303–339, 1999.

[21] Jan A Freund, Sebastian Mieruch, Bettina Scholze, Karen Wiltshire, and Ulrike Feudel. Bloom dynamics in a seasonally forced phytoplankton–zooplankton model: trigger mechanisms and timing effects. *Ecological complexity*, 3(2):129–139, 2006.

[22] JE Truscott and J. Brindley. Ocean plankton populations as excitable media. *Bulletin of Mathematical Biology*, 56(5):981–998, 1994.

[23] AP Martin. Phytoplankton patchiness: the role of lateral stirring and mixing. *Progress in Oceanography*, 57(2):125–174, 2003.

[24] Clinton J Dawes. *Marine botany*. Wiley, 1998.

[25] JH Steele and EW Henderson. A simple plankton model. *American Naturalist*, pages 676–691, 1981.

[26] JS Wroblewski. A model of the spring bloom in the north atlantic and its impact on ocean optics. *Limnology and oceanography*, 34(8):1563–1571, 1989.

[27] MJR Fasham, HW Ducklow, and SM McKelvie. A nitrogen-based model of plankton dynamics in the oceanic mixed layer. *Journal of Marine Research*, 48(3):591–639, 1990.

[28] H Malchow, N Shigesada, et al. Nonequilibrium plankton community structures in an ecohydrodynamic model system. *Nonlinear Processes in Geophysics*, 1(1):3–11, 1994.

[29] JE Truscott, J. Brindley, JE Truscott, and J. Brindley. Equilibria, stability and excitability in a general class of plankton population models. *Philosophical Transactions of the Royal Society of London. Series A: Physical and Engineering Sciences*, 347(1685):703–718, 1994.

[30] A.M. Edwards and J. Brindley. Oscillatory behaviour in a three-component plankton population model. *Dynamics and stability of Systems*, 11(4):347–370, 1996.

[31] L. Matthews and J. Brindley. Patchiness in plankton populations. *Dynamics and Stability of Systems*, 12(1):39–59, 1997.

[32] A.M. Edwards and J. Brindley. Zooplankton mortality and the dynamical behaviour of plankton population models. *Bulletin of Mathematical Biology*, 61(2):303–339, 1999.

[33] H. Malchow, B. Radtke, M. Kallache, A.B. Medvinsky, D.A. Tikhonov, and S.V. Petrovskii. Spatio-temporal pattern formation in coupled models of plankton dynamics and fish school motion. *Nonlinear analysis. Real world applications*, 1(1):53–67, 2000.

[34] A.M. Edwards and M.A. Bees. Generic dynamics of a simple plankton population model with a non-integer exponent of closure. *Chaos, Solitons & Fractals*, 12(2):289–300, 2001.

[35] H. Malchow, FM Hilker, RR Sarkar, and K. Brauer. Spatiotemporal patterns in an excitable plankton system with lysogenic viral infection. *Mathematical and computer modelling*, 42(9):1035–1048, 2005.

[36] J.A. Freund, S. Mieruch, B. Scholze, K. Wiltshire, and U. Feudel. Bloom dynamics in a seasonally forced phytoplankton–zooplankton model: trigger mechanisms and timing effects. *Ecological complexity*, 3(2):129–139, 2006.

[37] R.K. Upadhyay, N. Kumari, and V. Rai. Exploring dynamical complexity in diffusion driven predator–prey systems: Effect of toxin producing phytoplankton and spatial heterogeneities. *Chaos, Solitons & Fractals*, 42(1):584–594, 2009.

[38] S. Schiff and T. Sauer. Kalman filter control of a model of spatiotemporal cortical dynamics. *BMC Neuroscience*, 9(Suppl 1):O1, 2008.

[39] JD Annan, JC Hargreaves, NR Edwards, and R. Marsh. Parameter estimation in an intermediate complexity earth system model using an ensemble kalman filter. *Ocean Modelling*, 8(1):135–154, 2005.

[40] E.A. Wan and R. Van Der Merwe. The unscented kalman filter for nonlinear estimation. In *Adaptive Systems for Signal Processing, Communications, and Control Symposium 2000. AS-SPCC. The IEEE 2000*, pages 153–158. IEEE, 2000.

[41] TG Muller and J. Timmer. Parameter identification techniques for partial differential equations. *International journal of bifurcation and chaos in applied sciences and engineering*, 14:2053–2060, 2004.

[42] T.G. Müller and J. Timmer. Fitting parameters in partial differential equations from partially observed noisy data. *Physica D: Nonlinear Phenomena*, 171(1-2):1–7, 2002.

[43] IM Navon. Practical and theoretical aspects of adjoint parameter estimation and identifiability in meteorology and oceanography. *Dynamics of Atmospheres and Oceans*, 27(1):55–79, 1998.

[44] U. Parlitz. Estimating model parameters from time series by autosynchronization. *Physical Review Letters*, 76(8):1232–1235, 1996.

[45] U. Parlitz, L. Junge, and L. Kocarev. Synchronization-based parameter estimation from time series. *Physical Review E*, 54.

[46] T. Stojanovski, L. Kocarev, and U. Parlitz. A simple method to reveal the parameters of the lorenz system. *International Journal of Bifurcation and Chaos*, 6(12B):2645–2652, 1996.

[47] W. Yu, G. Chen, J. Cao, J. Lu, and U. Parlitz. Parameter identification of dynamical systems from time series. *Physical Review E*, 75.

[48] D. Yu and U. Parlitz. Estimating parameters by autosynchronization with dynamics restrictions. *Physical Review E*, 77(066221):066221–1–7, 2008.

[49] F. Sorrentino and E. Ott. Using synchronization of chaos to identify the dynamics of unknown systems. *Arxiv preprint arXiv:0909.2926*, 2009.

[50] J.C. Quinn, P.H. Bryant, D.R. Creveling, S.R. Klein, and H.D.I. Abarbanel. Parameter and state estimation of experimental chaotic systems using synchronization. *Physical Review E*, 80(1):016201, 2009.

[51] J. Schumann-Bischoff, J. Schröder-Schetelig, S. Luther, and U. Parlitz. Estimating parameters and hidden variables of cardiac cell models from time series.

[52] S. Berg, S. Luther, and U. Parlitz. Synchronization based system identification of an extended excitable system. *Chaos*, 21(3):3104, 2011.

[53] J. Schumann-Bischoff and U. Parlitz. State and parameter estimation using unconstrained optimization. *Physical Review E*, 84(5):056214, 2011.

[54] H.D.I. Abarbanel, D.R. Creveling, R. Farsian, and M. Kostuk. Dynamical state and parameter estimation. *SIAM Journal on Applied Dynamical Systems*, 8(4):1341–1381, 2009.

[55] L. Kocarev, Z. Tasev, and U. Parlitz. Synchronization spatiotemporal chaos of partial differential equations. *Physical Review Letters*, 79(1):51–54, 1997.

[56] L.M. Pecora and T.L. Carroll. Synchronization in chaotic systems. *Physical review letters*, 64(8):821–824, 1990.

[57] Louis M Pecora and Thomas L Carroll. Driving systems with chaotic signals. *Physical Review A*, 44(4):2374, 1991.

[58] Thomas Peacock and George Haller. Lagrangian coherent structures: The hidden skeleton of fluid flows. *Physics Today*, 66(2):41–47, 2013.

[59] Gary Froyland and Kathrin Padberg. Almost-invariant sets and invariant manifolds connecting probabilistic and geometric descriptions of coherent structures in flows. *Physica D: Nonlinear Phenomena*, 238(16):1507–1523, 2009.

[60] Steven L Brunton and Clarence W Rowley. Fast computation of finite-time lyapunov exponent fields for unsteady flows. *Chaos: An Interdisciplinary Journal of Nonlinear Science*, 20(1):017503–017503, 2010.

[61] Doug Lipinski and Kamran Mohseni. A ridge tracking algorithm and error estimate for efficient computation of lagrangian coherent structures. *Chaos: An Interdisciplinary Journal of Nonlinear Science*, 20(1):017504–017504, 2010.

[62] Shawn C Shadden, Francois Lekien, and Jerrold E Marsden. Definition and properties of lagrangian coherent structures from finite-time lyapunov exponents in two-dimensional aperiodic flows. *Physica D: Nonlinear Phenomena*, 212(3):271–304, 2005.

[63] Gary Froyland, Naratip Santitissadeekorn, and Adam Monahan. Transport in time-dependent dynamical systems: Finite-time coherent sets. *arXiv preprint arXiv:1008.1613*, 2010.

[64] Yunus A Cengel and Michael A Boles. Thermodynamics: an engineering approach, 2002.

[65] Esa earthnet online. `https://earth.esa.int/web/guest/missions/esa-operational-eo-missions/envisat/instruments/meris`. [Online; accessed 20-Feb-2013].

[66] National aeronautics and space administration. `http://modis.gsfc.nasa.gov/`. [Online; accessed 20-Feb-2013].

[67] The ocean color home page. `http://oceancolor.gsfc.nasa.gov/`. [Online; accessed 20-Feb-2013].

[68] Manuel Gimond. Description and verification of an aquatic optics monte carlo model. *Environmental Modelling & Software*, 19(12):1065–1076, 2004.

[69] C.S. Holling. Some characteristics of simple types of predation and parasitism. *The Canadian Entomologist*, 91(7):385–398, 1959.

[70] Richard L Burden and J Douglas Faires. Numerical analysis, brooks/cole. *Pacific Grove, CA*, 2000.

[71] Randall LeVeque. *Finite Difference Methods for Ordinary and Partial Differential Equations*. SIAM, 2007.

[72] Keith W Morton and David Francis Mayers. *Numerical solution of partial differential equations: an introduction*. Cambridge university press, 2005.

[73] Ljupčo Kocarev, Žarko Tasev, Toni Stojanovski, and Ulrich Parlitz. Synchronizing spatiotemporal chaos. *Chaos: An Interdisciplinary Journal of Nonlinear Science*, 7(4):635–643, 1997.

[74] Louis M Pecora and Thomas L Carroll. Master stability functions for synchronized coupled systems. *Physical Review Letters*, 80(10):2109–2112, 1998.

[75] Anmar Khadra, Xinzhi Liu, and Xuemin Shen. Impulsive control and synchronization of spatiotemporal chaos. *Chaos, Solitons Fractals*, 26(2):615–636, 2005.

[76] Kres?imir Josić. Invariant manifolds and synchronization of coupled dynamical systems. *Physical Review Letters*, 80(14):3053–3056, 1998.

[77] Jie Sun, Erik M Bollt, and Takashi Nishikawa. Constructing generalized synchronization manifolds by manifold equation. *SIAM Journal on Applied Dynamical Systems*, 8(1):202–221, 2009.

[78] S. Kramer and E. Bollt. Spatially dependent parameter estimation and nonlinear data assimilation by autosynchronization of a system of partial differential equations. *Accepted for publication, Chaos*.

[79] Ljupčo Kocarev, Ulrich Parlitz, Toni Stojanovski, and Predrag Janjic. Controlling spatiotemporal chaos in coupled nonlinear oscillators. *Physical Review E*, 56(1):1238–1241, 1997.

[80] Halsey Lawrence Royden and Patrick Fitzpatrick. *Real analysis*, volume 4. Prentice Hall New York, 2010.

[81] Robert V Thomann. *Mathematical modeling of phytoplankton in Lake Ontario*, volume 1. National Environmental Research Center, 1975.

[82] Jann Paul Mattern, Katja Fennel, and Michael Dowd. Estimating time-dependent parameters for a biological ocean model using an emulator approach. *Journal of Marine Systems*, 96:32–47, 2012.

[83] S.B. Hsu. A survey of constructing lyapunov functions for mathematical models in population biology. *Taiwanese Journal of Mathematics*, 9(2):pp–151, 2005.

[84] M Guedda and M Kirane. A lyapunov function for a reaction-diffusion system. *Applied Mathematics Letters*, 10(3):95–97, 1997.

[85] Ute Feldmann. On proofs of synchronization-the outweighing approach. 1996.

[86] Gregory S Duane, Dongchuan Yu, and Ljupco Kocarev. Identical synchronization, with translation invariance, implies parameter estimation. *Physics Letters A*, 371(5):416–420, 2007.

[87] M. Krstic and A. Smyshlyaev. Adaptive control of pdes. *Annual Reviews in Control*, 32(2):149–160, 2008.

[88] Steven Strogatz. Nonlinear dynamics and chaos: with applications to physics, biology, chemistry and engineering. 2001.

[89] Daniel R Creveling, Philip E Gill, and Henry DI Abarbanel. State and parameter estimation in nonlinear systems as an optimal tracking problem. *Physics Letters A*, 372(15):2640–2644, 2008.

[90] K Pyragas. Conditional lyapunov exponents from time series. *PHYSICAL REVIEW-SERIES E-*, 56:5183–5188, 1997.

[91] Alan Wolf, Jack B Swift, Harry L Swinney, and John A Vastano. Determining lyapunov exponents from a time series. *Physica D: Nonlinear Phenomena*, 16(3):285–317, 1985.

[92] D. Meiss, James. *Differential Dynamical Systems*. SIAM, 2007.

[93] Gene H Golub and Charles F Van Loan. *Matrix computations*, volume 3. JHUP, 2012.

[94] David C Lay. Linear algebra and its applications, 1997.

[95] Trevor Platt. Local phytoplankton abundance and turbulence. In *Deep Sea Research and Oceanographic Abstracts*, volume 19, pages 183–187. Elsevier, 1972.

[96] James A Yoder, Steven G Ackleson, Richard T Barber, Pierre Flament, and William M Balch. A line in the sea. *Nature*, 371(6499):689–692, 1994.

[97] EE Holmes, MA Lewis, JE Banks, and RR Veit. Partial differential equations in ecology: spatial interactions and population dynamics. *Ecology*, pages 17–29, 1994.

[98] Peter JS Franks. Spatial patterns in dense algal blooms. *Limnology and Oceanography*, 42(5):1297–1305, 1997.

[99] Edward R Abraham. The generation of plankton patchiness by turbulent stirring. *Nature*, 391(6667):577–580, 1998.

[100] Lawrence Perko. *Differential equations and dynamical systems*, volume 7. Springer, 2000.

[101] T. Ma and E. Bollt. Relatively coherent sets as a hierarchical partition method. *Accepted for publication, International Journal of Bifurcation and Chaos.*

[102] Berthold KP Horn and Brian G Schunck. Determining optical flow. *Artificial intelligence*, 17(1):185–203, 1981.

[103] A. Luttman, E. Bollt, R. Basnayake, S. Kramer, and N. Tufillaro. A stream function framework for estimating fluid flow from digital imagery. *submitted Chaos.*